
Engineering new Zr-MOFs for the structure determination of site-isolated metal complexes

A thesis presented to

The School of Physics, Chemistry, and Earth Sciences

at

The University of Adelaide

in fulfillment of the requirements for

The Degree of

Doctor of Philosophy in Chemical Science

by

Pol Gimeno I Fonquernie



THE UNIVERSITY
of ADELAIDE

Adelaide, Australia

August 2023

Declaration

I certify that this work contains no material which has been accepted for the award of any other degree or diploma in my name, in any university or other tertiary institution and, to the best of my knowledge and belief, contains no material previously published or written by another person, except where due reference has been made in the text. In addition, I certify that no part of this work will, in the future, be used in a submission in my name, for any other degree or diploma in any university or other tertiary institution without the prior approval of the University of Adelaide and where applicable, any partner institution responsible for the joint award of this degree.

The author acknowledges that copyright of published works contained within the thesis resides with the copyright holder(s) of those works.

I give permission for the digital version of my thesis to be made available on the web, via the University's digital research repository, the Library Search and also through web search engines, unless permission has been granted by the University to restrict access for a period of time.

Pol Gimeno I Fonquernie, 15/08/2023

Acknowledgements

Completing my PhD thesis has been a journey filled with challenges and accomplishments, and I owe my success to the unwavering support and guidance of many individuals. I am deeply grateful to each of them for their contributions and encouragement throughout this academic endeavour.

First and foremost, I extend my heartfelt gratitude to my principal supervisor, Prof. Christopher Sumbly. Working under his mentorship has been an absolute honour. I have learned invaluable insights into organometallic chemistry, scientific writing, and X-ray crystallography. His passion for X-ray crystallography sparked my own interest in the field, and his constant guidance and unwavering support have been instrumental in shaping the direction of my research.

I also want to express my sincere appreciation to my co-supervisor, Prof. Christian Doonan. Christian's exceptional support and invaluable guidance throughout the project have played a pivotal role in shaping the trajectory of my research. His insights and advice have been instrumental in advancing my understanding of the subject matter. Moreover, I would like to extend my thanks to my other co-supervisor, Dr Jason Price, for his assistance with the synchrotron data collection and experiments.

I would also like to acknowledge the support for my research of an Australian Institute Nuclear Science and Engineering Postgraduate Research Award (AINSE-PGRA).

Other researchers I would like to thank are Dr Jack Evans for his support and computational studies, Dr Witold Bloch, and Dr Michael Huxley for providing insights into previous work that was very helpful for the development of the project, and Dr Weibin Liang for preliminary data collected for the work included in chapter 2.

I also want to thank the entire Sumbly-Doonan group. It has been great to work in such a supportive and friendly environment. I would like to specially acknowledge Dr Jorge Albalad, who was key in the early stages of the project and a crucial source of support during the COVID-19 pandemic. Also, my heartfelt thanks go to Steven Tsoukatos for his immense support and with whom I have built a great friendship.

I am indebted to the staff at the MX beamlines of the Australian Synchrotron for their invaluable support and assistance during the synchrotron experiments. Additionally, I am grateful to the staff at Adelaide Microscopy, especially Ken Neubauer and Ashley Slattery, for their assistance

with SEM and TEM experiments. Special thanks go to Matt Bull for maintaining the NMR and other equipment and for his help in utilizing these characterisation tools.

I owe a debt of gratitude to my friends, Xavi and Mireia, who have been pillars of support during my time in Australia. Your friendship has made this journey far from home much more bearable.

My heartfelt thanks go to my high school teacher, Lucía Valentín, who ignited my passion for chemistry and set me on this academic path. I am also grateful to my Bachelor's and Master's degree thesis supervisor, Dr. Jose Giner Planas, for his guidance, recommendations, and support that paved the way for me to pursue my PhD.

The COVID-19 pandemic presented unforeseen challenges, and I am deeply appreciative of the support I received during these difficult times. My housemates and friends, Aaron and Tianyi, have made Australia feel like home, and their constant help and encouragement have been truly invaluable.

I extend my appreciation to my friends back in Spain, especially the members of the English and Pias Republic group: Raquel, Paola, Rendós, Cruz, Peraire, Carlos, Borja, Cume, Pere, Fer, Maldo, Pablo, and Peri. Your unwavering support during the tough moments of my candidature, especially throughout the COVID-19 crisis, has meant the world to me.

To my family, I am eternally grateful. To my brother Oskar, my cousin Marc, my grandmas Nuri and Marivi, my step-brother Max, and my step-mum Elisabeth, thank you for your unending support.

Lastly, I want to express my deepest gratitude to my parents, Toni and Rosana. Your love, dedication, and unwavering belief in me have been the driving force behind my accomplishments. Your support, both emotionally and financially, has allowed me to pursue my dreams, and I wouldn't be the person I am today without you. Thank you for raising me in a way that nurtured my curiosity and passion for learning.

To all those who have contributed to my journey, directly or indirectly, your support and involvement have been invaluable. I am genuinely grateful for the incredible network of individuals who have played a significant role in shaping my academic pursuits. Thank you for being part of this rewarding experience.

Abstract

Transient, coordinatively unsaturated metal sites found in biological systems and important industrial catalysts have intrigued scientists for their role in facilitating selective chemical reactions. Researchers aim to synthetically mimic and study these sites for new chemical transformations and to facilitate selective small molecule binding. Metal-organic frameworks (MOFs), due to their robust and crystalline structures, offer a platform to trap and study these entities by single crystal X-ray diffraction (SCXRD). However, many MOFs lack the properties, along with the chemical and thermal stability, needed for reliable X-ray diffraction based characterization of metal complexes located at binding sites within their structures. This thesis aims to synthesize chemically robust Zirconium-based MOFs with free bis-pyrazole sites for coupled post-synthetic metalation and SCXRD. These Zr-MOFs can act as crystalline sponge materials, with the bis-pyrazole groups being used to site-isolate and facilitate SCXRD characterisation of mononuclear and dinuclear transition metal complexes.

Leveraging significant prior art in the formation of MOFs from pyrazole carboxylate linkers, the work described in the thesis investigated the synthesis of chemically and thermally stable Zr-MOFs from bis-pyrazole and tetrakis-pyrazole carboxylate linkers. The initial linker that was studied for developing new crystalline sponges with Zr-based nodes, 1,1'-methylenebis(1H-pyrazole-4-carboxylic acid), gave MOFs that did not fully meet the targeted aims of the thesis, although, the study provided important insights into the synthesis of Zr-MOFs for this type of linker. In chapter 2, the templated synthesis of zirconium(IV)-based 2D-metal-organic frameworks (2D-MOFs) using the aforementioned di-topic linker is reported. This gave two different but structurally related 2D-MOFs depending on whether a templating metal ion was used in the synthesis or not. Without the template, a close packed 3D solid comprising 2D MOF was formed, whereas using a synthetic approach with a Cu(I) template provided a more open 3D solid comprising related 2D layers. Chemical delamination of this latter material produced stable and polydisperse 2D-MOF nanosheets that were capable of post-synthetic metalation (PSMet). However, the delamination process unavoidably caused a loss of long-range order, preventing the study of resulting metal complexes by SCXRD.

To address these limitations and pursue the goal of generating robust crystalline sponges, a tetratopic linker, 1,1,2,2-tetrakis[4-(4-carboxyphenyl)-1H-pyrazol-1-yl]ethane (TCPE), was employed for the study presented in Chapter 3. This linker led to the synthesis of a new Zr-MOF,

UAM-1001, which enable structure determination of unusually distorted dimeric complexes trapped within the pre-organised metalation site. The chapter reports the synthesis and characterisation of the crystalline sponge UAM-1001, by first preparing a more flexible MOF (UAM-1000) and then post-synthetically bracing the structure to ensure PSMet could occur without loss of crystallinity. The study explored PSMet of UAM-1001 with different metal salts, revealing the ability to accommodate of both monomeric and dimeric metal complexes, depending on the choice of metal salt and its coordination geometry. The semi-rigid and preorganised arrangement of the donor groups enforced notably shorter metal-metal distances for some of the dinuclear complexes.

Chapter 4 presents an in-depth study into the formation of Zr-MOFs from tetratopic linkers containing free bis-pyrazole units, combining experimental and computational analyses, to understand how these MOFs are formed and the effect of linker length and synthetic conditions on the resulting topology. MOFs with three different topologies (*scu*, *flu*, and *sqc*) are encountered as the overall length and width (insertion of a spacer in the arm) of the linker are modified. Only one of the original three MOFs (UAM-1001, *sqc* topology, chapter 3) could be post-synthetically metalated. Using the same TPCE linker that was studied previously to form UAM-1000/1001, a fourth MOF could be synthesised by changing the modulator. This material, UAM-1002, has a different topology to UAM-1001, and is only able to form mononuclear complexes due to spatial isolation of the bis-pyrazole sites.

Finally, a short study, which covers a small body of work, is presented in chapter 5, to highlight how changing the positioning of the donor groups on the arms of the organic linker can also affect the topology of the MOF. The resulting material, UAM-1006, has the same *scu* topology of UAM-1002, but is formed as a “closed” phase.

In summary, this thesis has focused on the synthesis of chemically and thermally robust and highly porous crystalline sponges for site-isolating and investigating the structures and chemistry occurring at transition metal complexes anchored to the MOF. It has reported several new Zr-based MOFs, including two new MOFs that serve the targeted purpose. One of these MOFs is capable of trapping either mononuclear or dinuclear complexes (the former with a vacant non-coordinating site near the metal), while a second MOF is set-up to provide spatially isolated bidentate binding sites. These new materials significantly expand the library of MOFs capable of acting as crystalline sponges for metal complexes but combined the work highlights the challenges of forming such materials. The crystalline sponges identified are being used to investigate

chemistry occurring at metal sites within the confined, chemically controlled environment of the MOF pores by SCXRD.

Contents

CHAPTER 1: Introduction	1
1.1. Trapping and studying reactive metal complexes	2
1.2. Metal-organic frameworks (MOFs)	5
1.2.1. MOF stability	6
1.2.2. MOF topology.....	8
1.2.3. MOF post synthetic modification	9
1.2.4. Linker flexibility.....	15
1.3. Use of MOFs as crystalline sponges.....	17
1.4. Contextual Statement.....	26
1.5. References.....	31
CHAPTER 2: Templated synthesis of zirconium(IV)-based metal-organic layers (MOLs) with accessible chelating sites.....	39
2.1. Statement of authorship	42
2.2. Introduction	44
2.3. Experimental Section	46
2.3.1. Materials and Methods.....	46
2.3.2. Synthetic protocols.....	46
2.3.3. Single crystal X-ray crystallography	48
2.4. Results and discussion	50
2.5. Conclusions.....	54
2.6. References.....	55
CHAPTER 3: Atomic scale elucidation of unusually distorted dimeric complexes confined in a new Zr-based Metal-organic Framework.....	59
3.1. Statement of authorship	62
3.2. Introduction	64
3.3. Experimental Section	66
3.3.1. Materials and methods.....	66
3.3.2. Synthetic protocols.....	67
3.4. Results and discussion	69
3.4.1. Synthesis of UAM-1000.....	69
3.4.2. “Locking” UAM-1000 to form UAM-1001	71
3.4.3. Isolation of distorted dimeric complexes in UAM-1001.....	72

3.4.4.	UV-vis spectroscopic studies and reactivity	76
3.5.	Conclusions	78
3.6.	References	79
CHAPTER 4: Topological control of post-synthetic metalation sites in Zirconium-based metal-organic frameworks		83
4.1.	Statement of authorship.....	86
4.2.	Introduction.....	88
4.3.	Experimental Section.....	90
4.3.1.	Materials and methods	90
4.3.2.	Molecular simulations	91
4.3.3.	Single Crystal X-ray Diffraction	91
4.3.4.	Synthetic protocols	92
4.4.	Results and discussion	94
4.4.1.	Linker synthesis and preferred conformation	94
4.4.2.	MOF synthesis and structures	96
4.4.3.	Topologies of UAM-10, UAM-11, UAM-1002 and UAM-1000	99
4.4.4.	Post-synthetic metalation of the MOFs	102
4.5.	Conclusions	105
4.6.	References	106
CHAPTER 5: Effect of linker “geometry mismatch” on MOF topology.....		111
5.1.	Introduction.....	113
5.2.	Experimental Section.....	115
5.2.1.	Materials and methods	115
5.2.2.	Synthetic protocols	115
5.2.3.	Single-crystal X-ray crystallography.....	115
5.3.	Results and discussion	116
5.4.	Conclusions	120
5.5.	Supplementary information	121
5.5.1.	Alternative images of the structure of UAM-1006	121
5.5.2.	Table of X-ray crystallography data collection and refinement parameters.....	123
5.6.	References	124
CHAPTER 6: Conclusions and Future Directions		125
Appendixes.....		133
I.	Appendix 1: Supplementary Information for Chapter 2	135
I.I.	Main text supporting characterization	135

I.II.	Fourier Transform Infrared Spectroscopy (FTIR) spectra.....	145
I.III.	Nuclear Magnetic Resonance (NMR) data.....	146
I.IV.	Single crystal X-ray crystallography	147
I.V.	References.....	151
II.	Appendix 2: Supplementary Information for Chapter 3	153
II.I.	Main Text Supporting Characterisation	153
II.II.	Other Supplementary Information	165
II.III.	Single Crystal X-ray Crystallography.....	168
II.IV.	References.....	176
III.	Appendix 3: Supplementary Information for Chapter 4	177
III.I.	Main text supporting data.....	177
III.II.	Fourier Transform Infrared Spectroscopy (FTIR) spectra.....	191
III.III.	Adsorption experiments.....	193
III.IV.	Single crystal X-ray crystallography	195

Abbreviations

DMF	Dimethyl formamide
THF	Tetrahydrofuran
MeCN	Acetonitrile
EtOH	Ethanol
MeOH	Methanol
DEF	Diethylformamide
AcH	Acetic Acid (occasionally AA)
TFA	Trifluoroacetic acid
BA	Benzoic Acid
EDX	Electron dispersive X-ray
PSM	Post-synthetic modification
PSMet	Post-synthetic metalation
MicroED	Microcrystal electron diffraction
IR	Infrared
MOL	Metal-organic layer
MOF	Metal-organic framework
NMR	Nuclear magnetic resonance
PXRD	Powder X-ray diffraction
SCXRD	Single crystal X-ray diffraction
SEM	Scanning electron microscopy
TEM	Transmission electron microscopy
TGA	Thermogravimetric analysis

CHAPTER 1: Introduction

1.1. Trapping and studying reactive metal complexes

Under controlled conditions, coordinatively unsaturated metal sites are found in biological systems, for example in metalloproteins and metalloenzymes.¹⁻⁵ The reactive, vacant metal sites possessed by these biomacromolecules enable molecular transport and chemical transformations by facilitating the binding of substrates and stabilizing reactive intermediates. Taking inspiration from these biological systems, chemists have attempted to prepare new synthetic mimics with comparable reactivity and selectivity.⁶ These studies aim to develop new chemical transformations or exploit the chemistry of the coordinatively unsaturated metal sites to efficiently bind certain molecules.

Coordinatively unsaturated metal centres are also extensively encountered in the field of catalysis.⁷⁻¹⁰ They are important intermediates in homogeneous catalytic cycles catalysed by organometallic complexes or, more recently, nanoparticles.¹¹ Due to the industry's preference for using heterogeneous catalysts, chemists have sought ways to heterogenise reactive organometallic complexes and nanoparticles by anchoring them onto solid supports.^{12, 13} This approach has not only allowed for the utilisation of reactive metals in catalysis but also in adsorption and separation processes.¹⁴ By doping porous supports with reactive metals in the form of organometallic complexes and nanoparticles, the adsorption of small molecules can be enhanced, the affinity for specific molecules can be tuned, and separation processes can be facilitated. This has enabled these materials to be used for separation or remediation of undesirable or toxic chemicals.^{15, 16}

Given the fundamental interest in these species, and the importance of reactive or coordinatively unsaturated metal complexes in biochemical transformations, homogeneous and heterogeneous catalysis, and adsorption/separation, chemists have looked to find ways to characterise and explore their reactivity. Matrix isolation is one technique used to study and stabilize reactive or short-lived chemical species. It involves trapping these species within a solid or cryogenic matrix at low temperatures (Figure 1.1).^{17, 18} This minimises their reactivity and preserves their structure such that their *spectroscopic* properties can be analysed. However, it does not typically provide detailed *structural* information about the coordinatively unsaturated or transient species, which needs to be inferred from other studies, often on precursors to the reactive species. By contrast, single-crystal X-ray diffraction is a powerful technique used to determine the atomic structure of crystalline materials. It has been particularly useful in providing structural information about coordination and organometallic complexes, including catalysts, but its application is typically limited to cases where the molecule is stable and successful

crystallization can be achieved. Spectroscopic techniques can also be applied to characterise these solid-state samples. Unfortunately, as the crystallization process is time-consuming and requires the complex to remain stable for a specific duration, application to studying transient species like coordinatively unsaturated intermediates or reactive complexes, which have relatively short lifetimes, is nearly impossible. These species undergo decomposition or dimerization reactions in the time taken to form the single crystals (or indeed well before this).

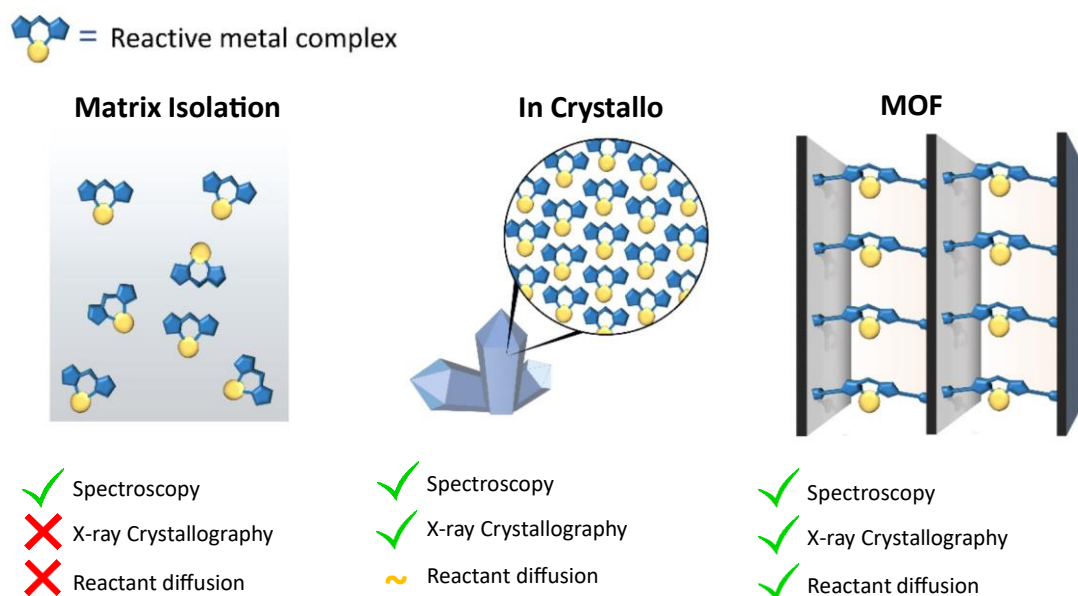


Figure 1.1. The formation of reactive metal complexes in solution results in decomposition due to a lack of site-isolation. The site-isolation imposed by the crystalline lattice within a single crystal can allow highly reactive species to be stabilised, however the lack of permanent porosity limits their application in small molecule activation. Metal-organic Frameworks provide a robust, permanently porous matrix within which highly reactive complexes can be generated and studied, including their reactivity with small molecules. Figure adapted from ref ¹⁹.

One approach to overcoming the aforementioned challenges has been to study the reactivity of reactive species “in crystallo”.²⁰⁻²⁵ This involves crystallising the precursor species and conducting the reactions to generate the reactive or coordinatively unsaturated species within the protective environment of a crystal lattice (Figure 1.1). This prevents the desired reactive species from undergoing decomposition or dimerization reactions and allows it to be characterized using single-crystal X-ray diffraction (SCXRD). Following this approach, several examples of reactive species have been characterised, including a nitride complex that was successfully observed by SCXRD through the photolysis of the crystal at 95 K.²⁰ To facilitate chemical transformations beyond photolysis “in crystallo”, the crystals used must possess the ability to allow molecular diffusion whilst maintaining their crystalline structure. This necessitates

a certain level of structural flexibility and, as molecular crystals are typically dense materials with little to no prospect of allowing the required egress or ingress of small molecules (gases or ligands), bulky supporting ligands or anions are needed to generate channels or pores. This approach has facilitated, for example, the observation of reactive σ -alkane complexes through the hydrogenation of an alkene complex.^{21, 23, 25-28}

The ultimate extension of this concept involves the use of metal-organic frameworks (MOFs), which provide a rigid, three-dimensionally interconnected framework (Figure 1.1).²⁹ Unlike molecular crystals, MOF crystals are generally robust with respect to chemical processing, including solvent removal, and possess pores suitable for the transport of large guest molecules. This unique combination of chemical robustness, porosity, and the ability to maintain crystallinity makes MOFs excellent candidates to be used as “crystalline sponges” for trapping reactive metal complexes and studying chemical processes involving these entities using X-ray crystallography. This thesis explores the synthesis of new MOF-based crystalline sponges and the utilisation of these materials to provide structural insight into coordination chemistry as a prelude to studying reactive and coordinatively unsaturated complexes.

1.2. Metal-organic frameworks (MOFs)

Metal-organic frameworks (MOFs) are highly tuneable, crystalline materials composed of metal nodes linked by organic linkers (Figure 1.2).²⁹ These materials have garnered significant interest from chemists and materials scientists due to their incomparable properties, including large surface areas, high degree of chemical tunability, and crystallinity. These combined properties have led to them being considered and investigated for a wide range of applications such as gas storage and separation,³⁰⁻³² drug delivery,³³ catalysis,³⁴⁻³⁸ and sensing.³⁹⁻⁴¹

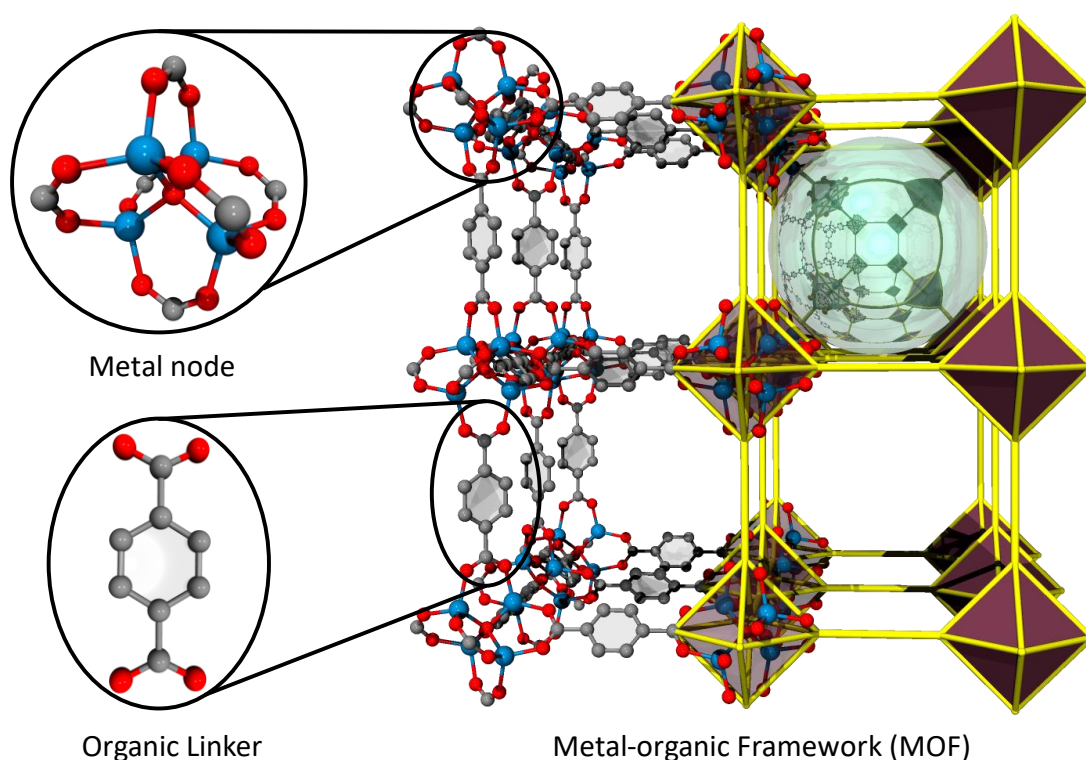


Figure 1.2. Schematic representation of the formation of a metal-organic framework (MOF) from a metal node and an organic linker. In the ball and stick representations of the node and linker the colour scheme is oxygen (red), carbon (grey) and zinc (blue). In the MOF structure, the organic linkers are simplified to yellow sticks and the metal nodes with a maroon polyhedron. The reflective green ball represents the free chemical space in the MOF.

The properties of MOFs are strongly influenced by both the linker and the metal node. For instance, choosing a linker with a hydrophobic group, such as a carborane, will impart high hydrophobicity to the MOF.⁴² Similarly, utilizing a photoactive linker will confer photoactivity to the MOF.⁴³ Moreover, the number and arrangement of functional groups in the linker controls the resulting topology of the MOF. In addition to the linker, the metal node also plays a crucial role in determining the structure and properties of the MOF. Different metal nodes exhibit distinct connectivities, thereby influencing the overall structure of the MOF.⁴⁴ The formation of the metal

node is determined by a combination of the metal used, linker donor chemistry, and reaction conditions. Furthermore, the choice of metal node affects the stability of the MOF, as different metals can interact with the functional groups of the same linker with varying bond strength and kinetic stability, thereby influencing the overall stability of the resulting MOF.⁴⁵ When designing new MOFs as crystalline sponges for characterisation of reactive or coordinatively unsaturated metal sites, several parameters must be carefully considered. These include stability, topology, ability to facilitate post-synthetic modification (PSM) and linker flexibility. Each of these factors will be further explored in the subsequent sections of this introduction, providing a comprehensive understanding of their significance in MOF design and for use as a crystalline sponge.

1.2.1. MOF stability

The stability of MOFs is primarily determined by the coordination bond formed between the metal and the organic linker.⁴⁵⁻⁴⁷ This interaction also influences the crystallization process that occurs during the synthesis. The crystallization process used to form MOFs needs to be controlled, providing the components sufficient time and energy to arrange themselves in the most stable conformation and, importantly for application as a crystalline sponge, to grow crystals of sufficient size. A strong metal-linker interaction ensures a stable MOF, but this can also impact the ability for error correction and crystallisation. For example, during the MOF formation process, if the linker and metal react too quickly an amorphous powder can be formed instead of a crystalline MOF structure. This is why MOFs were commonly, and especially during the development of the area, synthesized using ligands and metals with moderately strong bonds.⁴⁸ ⁴⁹ These interactions allowed for a favourable crystallization process, resulting in the formation of large crystals that could be characterized using single crystal X-ray analysis. However, with some exceptions, these materials exhibit relatively poor chemical and thermal stability.

Attempts to synthesize MOFs with harder metal ions like Zr(IV) or Al(III) that could lead to more stable MOFs was not reported until 2008, when Lillerud and coworkers reported the synthesis of the first examples of Zr-MOFs.⁵⁰ The reaction of ZrCl₄ with 1,4-benzenedicarboxylate (BDC), 4,4'-biphenyl-dicarboxylate (BPDC), and terphenyl dicarboxylate (TPDC) yielded three new MOFs with identical topologies, namely UiO-66, UiO-67, and UiO-68, respectively. However, the crystal size was too small for SCXRD characterization and therefore, structural determination was obtained using powder X-ray diffraction. One year later, in 2009, Kitagawa and colleagues introduced the coordination modulation approach, which has been employed to overcome the trade-off between the desirable improvement in stability and the loss or lack of crystallinity.^{51, 52} The modulation approach consists in the addition of monocarboxylic

acids to the MOF reaction mixture that competes with the linker to bind to the metal nodes. This competition slows down the reaction of the linker, allowing for the growth of larger crystals. This method has enabled the synthesis and structure determination by single crystal X-ray crystallography of more robust MOFs, such as those based on Zr(IV),⁵³ Ti(IV),⁵⁴ or Al(III)^{55, 56} nodes, and is critical for the research in this thesis where high quality single crystals are needed. The hard Lewis acidity of these cations, combined with the carboxylate functional groups, forms a very strong metal-linker interaction, resulting in the formation of highly stable materials. Zr-MOFs have been extensively studied, as the use of modulators has facilitated the formation of larger crystals compared to Al-MOFs or Ti-MOFs. Additionally, Zr-MOFs exhibit high thermal and chemical stabilities, typically withstanding temperatures up to 350°C and displaying chemical stability across a pH range from 1 to 11. Due to their exceptional stability and ability to form large crystals, Zr-MOFs have gained popularity and have been widely utilized in various applications.^{53,}

57

Recently, there has been a growing interest in synthesizing highly stable MOFs using low-valent metals.⁵⁸ These metals exhibit reduced Lewis acidity, which enables them to form strong interactions with N-donor groups such as azolates. Milner and colleagues conducted a comparison of the robustness of carboxylate, salicylate, and azolate MOFs by subjecting them to various stability tests, including exposure to air, acids, bases, nucleophiles, electrophiles, oxidants, and reductants.⁵⁹ The study revealed that carboxylate MOFs exhibited greater stability towards acids, electrophiles, and oxidants, whereas azolate MOFs demonstrated higher stability towards bases, nucleophiles, and reductants (Table 1.1). In contrast, salicylate MOFs, in general, exhibited lower overall robustness compared to the other two MOFs. While they were not stable in air, they demonstrated significant stability when exposed to reductants. It is important to note that while this field is expanding, this thesis exclusively focuses on the synthesis of high-valent carboxylate-based MOFs.

Table 1.1. Summary of robustness scores for different families of MOFs. Values represent the degree of preservation of crystallinity, with 1 indicating crystallinity is preserved and 0 representing full loss of crystallinity. Table adapted from ref ⁵⁹.

MOF	Air	Acids	Bases	Nucleophiles	Electrophiles	Oxidants	Reductants
Carboxylate	0.93	0.55	0.13	0.56	0.69	0.71	0.25
Salicylate	0.60	0.25	0.5	0.77	0.41	0.46	0.78
Azolate	0.97	0.49	0.63	0.78	0.53	0.44	0.53
	0 - 0.20	0.20 - 0.40	0.40 - 0.60	0.60 - 0.80	0.80 - 1.00		

1.2.2. MOF topology

MOFs can exhibit a wide range of topologies, giving rise to diverse pore structures and channel shapes that have significant implications for their properties.⁶⁰⁻⁶² The control of MOF topology is essential for achieving desired characteristics and properties, particularly where the MOF is being used as a crystalline sponge for metal complexes. A MOF with the same metal cluster and organic linker can exhibit different properties depending on its topology.⁶³ Topology control also becomes crucial in MOFs that incorporate linkers with free functional groups. When these functional groups are metalated via post-synthetic modification (PSM), the arrangement of these complexes is influenced by the underlying topology. If the linkers are in (too) close proximity due to the framework topology, it can lead to short metal-metal interactions or indeed steric clashes between these complexes, the latter of which may reduce the yield of the PSM step.⁶⁴ Conversely, isolated metal sites can ensure quantitative metalation and the ability to access the coordination environment by reactants and solvent. Extensive research has been conducted to understand and predict MOF topologies, with the building block approach developed by Yaghi and coworkers playing a key role.⁶⁰⁻⁶² This approach involves the systematic assembly of metal ions or clusters as nodes and organic ligands as linkers to construct the desired framework (as outlined above). It emphasizes the use of well-defined building units that can be combined in a modular fashion to form MOFs with specific topologies. The selection of these building blocks is based on their coordination chemistry and compatibility with each other, and by considering factors such as size, geometry, and coordination preferences, researchers can predict the topologies that can be achieved. For example, the concept of MOF isoreticulation has been employed to form MOFs with larger void spaces and higher porosity.^{65, 66} By designing a linker with the same shape and connectivity, a MOF with the same topology, but with larger pores, can be formed, enabling enhanced gas adsorption or the diffusion of larger molecules through the MOF structure, for example.

Despite having the same arrangement and connectivity, the functionalization of a linker can also give rise to a different topology. Farha and coworkers⁶⁷ observed that modifying an organic linker with a bulky substituent could influence the resulting topology. They synthesized a Zr-MOF named NU-903 using 1,2,4,5-tetrakis(4-carboxyphenyl)benzene (TCPB) as the linker, which resulted in an *scu* topology. However, by brominating the central benzene ring and reacting the resulting linker with the same Zr salt, they obtained a different MOF, NU-1008, with a *csq* topology. Furthermore, the same group also observed that the synthetic conditions could also influence the resulting topology (Figure 1.3). By reacting 1,4-dibromo-2,3,5,6-tetrakis(4-

carboxyphenyl)benzene with $ZrCl_4$ using different solvents and modulators, four different MOFs with distinct topologies could be synthesized.⁶⁸ This highlights that the choice of modulators and solvents for the synthesis of high-valent MOFs can also impact the resulting topology.

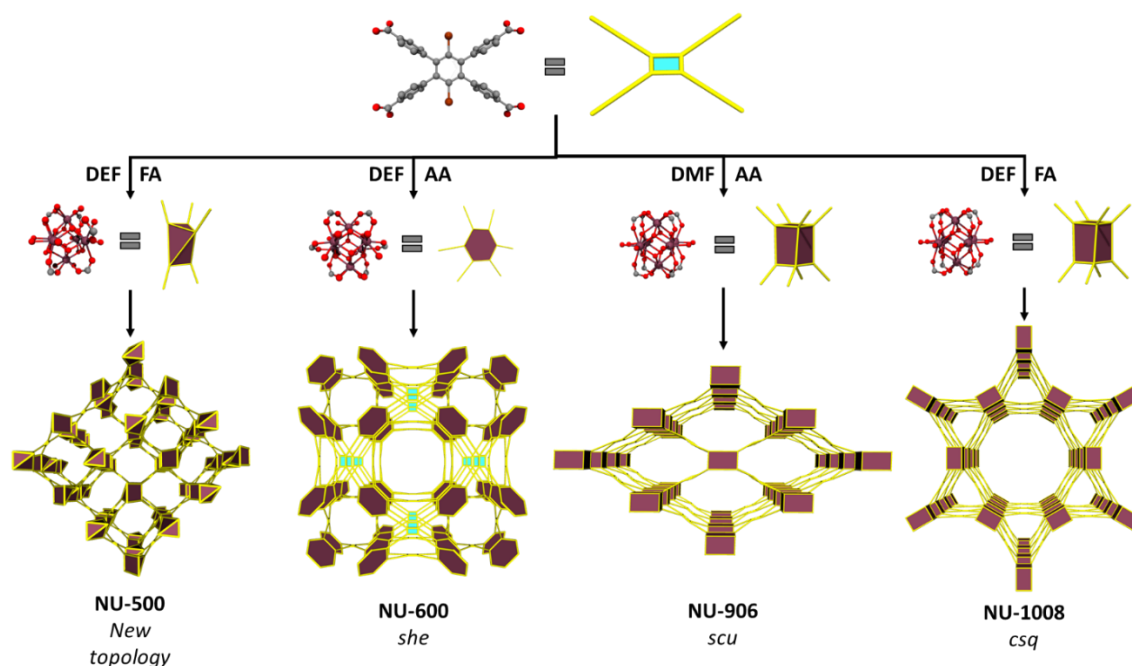


Figure 1.3. Synthetic conditions can affect MOF structure. The solvent or the modulator can affect the connectivity of the metal node and therefore the MOF topology that forms. The figure shows the synthesis of four different MOFs from a same linker and zirconium hexanuclear cluster. Figure adapted from ref ⁶⁸.

Despite all these advances into controlling MOF topology, MOF structure remains hard to predict as there are several factors, such as control over the metal cluster that will form, linker functionality and synthetic conditions, that can influence the resulting topology. Nonetheless, these principles and literature precedent can guide the design and choice of MOF components to achieve MOFs with the required stability, connectivity, and pore structures.

1.2.3. MOF post synthetic modification

In addition to controlling the structure and properties of MOFs by combining suitable metal nodes with organic linkers, MOFs can also undergo modifications after the framework formation step through a process called post-synthetic modification (PSM).⁶⁹⁻⁷² PSM plays a significant role in MOF chemistry allowing for better control over the formation of a functionalized MOF. It is worth noting PSM of MOFs does not usually alter the MOF topology, and thereby allows access to families of MOFs with the same topology but often quite chemically distinct pore environments. Moreover, PSM offers the advantage of introducing chemical functionality that requires considerably milder conditions compared to those used in the assembly of MOFs. The

synthesis of MOFs typically involves the use of high boiling point solvents like DMF or DEF at temperatures ranging from 80 to 120 °C and in certain cases, the inclusion of monocarboxylic acids as modulators acids to favour the crystallization process. These conditions impose limitations on the incorporation of linker functional groups or requires the use of secondary metal complexes that can withstand the synthesis conditions.

PSM provides a solution to this limitation by enabling the inclusion, post-synthesis of the framework structure, of functional groups or metal centres that may not be stable or fail to crystallize under solvothermal synthesis conditions. An example of such an approach is demonstrated by Doonan *et al.*, who synthesized a Zn-MOF containing pyridylimine organic groups that would not be stable under solvothermal conditions.⁷³ Amine groups present within the synthesized Zn-MOF were reacted with a pyridine aldehyde to form the desired pyridylimine group. Subsequently, this functionalized MOF was able to be reacted with a Pd(II) precursor to form a Pd(II) complex within the MOF structure. The possibilities for PSM of MOFs are diverse and can be categorized into three main types: covalent modifications, coordinative modifications, and post-synthetic metalations (PSMet), with the latter approach particularly important for using MOFs as crystalline sponges to characterise the structures of metal complexes. Selected examples are presented to show the versatility of the chemistry.

1.2.3.1. Covalent modifications

Several covalent transformations, including amide coupling,^{74, 75} imine condensation,⁷⁶ urea formation,⁷⁷ N-alkylation,⁷⁸ bromination,⁷⁵ reduction,⁷⁹ click reactions,⁸⁰ protonation⁸¹ and ozonolysis reactions,⁸² have been applied to MOFs to increase their functionality or their adsorption properties. For instance, Kronast *et al.* synthesized a version of UiO-66 with free amino-alcohol groups to act as molecular gates, selectively tuning the adsorption properties for CO₂ over N₂.⁸³ The Zr-MOF was first synthesized using 2-allyl-1,4-dicarboxylic-acid to form UiO-66-allyl. The allyl groups were then reacted with dimethyl-dioxirane to form an epoxide group and later with ammonia to form the amino-alcohol group (UiO-66-amino-alcohol). In a different example, MasPOCH and coworkers used an ozonolysis reaction to decompose some linkers of a Zr-MOF and increase its porosity.⁸⁴ By employing a mixed ligand approach, they synthesized a Zr-MOFs using 4,4'-azobenzene dicarboxylic acid (H₂azo) and 4,4'-stilbene dicarboxylic acid (H₂sti). Reaction with ozone gas resulted in the lysis of the alkene group, removing the H₂sti linkers to make a linker defect and thus increasing the pore size of the MOF.

1.2.3.2. Coordinative modifications

Coordinative modifications in MOFs primarily involve linker exchange or linker insertions. In the case of linker insertions, monocarboxylic acids or solvent molecules coordinated to the metal nodes are substituted with multitopic linkers (Figure 1.4). This technique is commonly observed in MOFs featuring a paddlewheel metal node, where the axial positions of the paddlewheel are typically occupied by solvent molecules that can be exchanged with multitopic linkers. For instance, Suh and coworkers conducted an insertion of di(4-pyridyl)-1,2,4,5-tetrazine (DPT) into a Zn-MOF to enhance its porosity.⁸⁵ The original Zn-MOF consisted of Zn-paddlewheel nodes with water molecules occupying the axial positions. By substituting these water molecules with DPT, the pore aperture of the MOF was increased. This insertion technique has also been successfully applied to Zr-MOFs with unsaturated clusters. The common Zr_6 -node has the capability to accommodate up to 12 carboxylate groups. However, under specific crystallization conditions or due to the shape of the linker, Zr-nodes with 10, 8, 6, 5, or 4 carboxylates can be formed, leaving some positions occupied by monocarboxylic acids and/or solvent molecules. Zhou and coworkers demonstrated that in such cases, secondary linkers could be inserted into the Zr-MOF by exchanging the solvent molecules or monocarboxylic acids with organic linkers.^{57, 86} This approach allowed for the insertion of different linkers into PCN-700, thereby fine-tuning its pore aperture. PCN-700, comprising 8-connected Zr-nodes, facilitated the insertion of ditopic linkers of varying lengths. By inserting FA (fumarate), BDC (1,4-benzenedicarboxylate), NDC (2,6-naphthalene dicarboxylate), and BPDC (4,4'-biphenyldicarboxylate) into PCN-700, the channel width of the MOF was tuned from 12.7 Å to 19.2 Å.

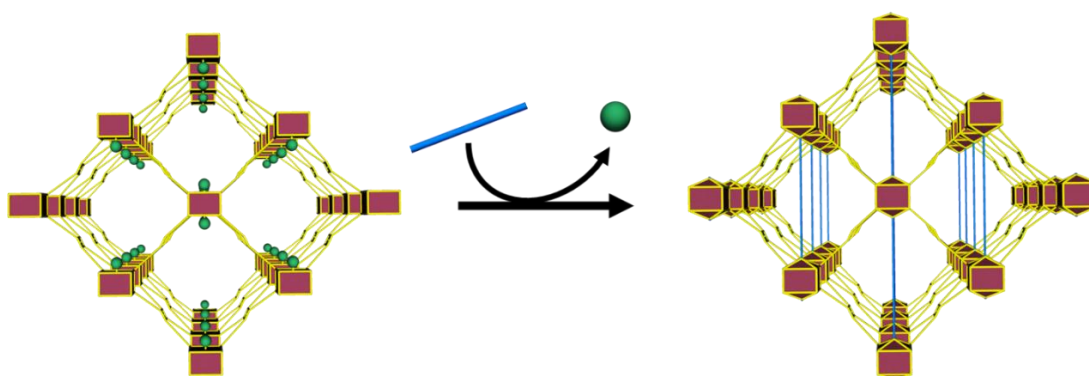


Figure 1.4. Representation of a linker insertion PSM of a MOF. MOF metal nodes are represented as maroon polyhedra. The organic linkers of the parent MOF are represented in yellow and the inserted linkers as blue sticks. The green balls represent monocarboxylic acids or solvent molecules.

Linker exchange, also known as solvent-assisted linker (SALE), involves the partial or complete ligand exchange within a MOF (Figure 1.5). The synthetic procedure for linker exchange is similar to that of linker insertion, as it entails a heterogeneous reaction between the parent MOF crystals and a concentrated solution of the desired linker(s) for exchange. However, in this case, the MOFs do not contain any solvent molecules or monocarboxylic acids to be exchanged, resulting in the original MOF linker being the one subject to exchange. For instance, UiO-66 is formed by a 12-connected Zr-cluster and BDC. Through a ligand exchange approach, Fei *et al.* successfully replaced a portion of the BDC ligands with 2,3-dimercaptoterephthalate (tcat).⁸⁷ This ligand exchange introduced free SH groups into UiO-66, which, through a subsequent post-synthetic modification (PSM), allowed for the incorporation of a Pd(II) centre. Importantly, the direct reaction of tcat with $ZrCl_4$ did not yield the UiO-66 structure formed through the PSM approach. Furthermore, it is worth noting that unlike linker insertion, linker exchange is typically not a quantitative process. While it provides the desired functionality within the framework, non-quantitative exchange in most cases limits using single-crystal X-ray diffraction (SCXRD) to study the resulting linker environment or metal sites.

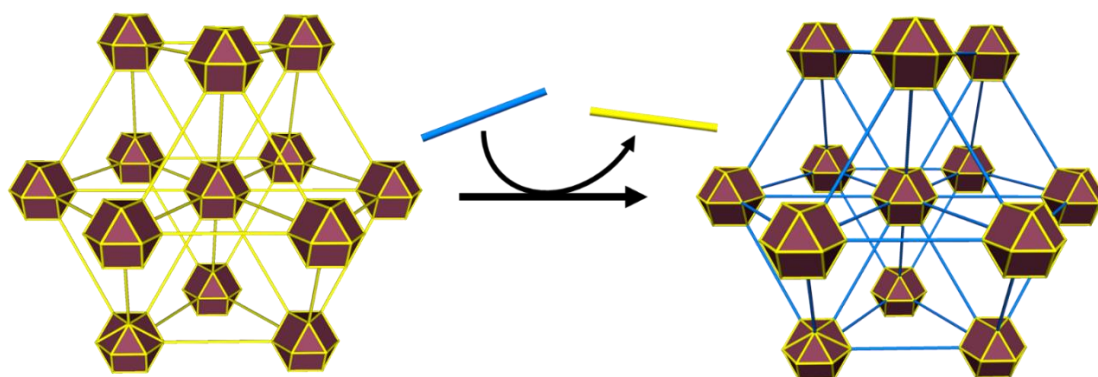


Figure 1.5. Schematic representation of a linker exchange/solvent-assisted linker exchange (SALE) PSM of a MOF. MOF metal nodes are represented as maroon polyhedra. The organic linkers of the parent MOF are represented as yellow sticks and the exchanged linkers as blue sticks.

1.2.3.3. Post synthetic metalation

Post-synthetic metalation (PSMet) is a process first reviewed by Evans *et al.* a several years ago. It encompasses various processes that involve the insertion of a secondary, typically non-structural metal into a MOF.⁸⁸ These processes can be achieved through some of the aforementioned modifications, such as ligand exchange with a metallolinker or by modifying a linker to incorporate a functional group capable of accommodating a secondary metal. However,

while all these other processes fit the broader definition, this section of the thesis will specifically address chemistry where a metal complex is incorporated into the parent framework. These processes can be further categorized into three groups: anchoring the metal complexes to the metal node, anchoring them to the linker, or stabilizing them within the pores of the MOF.

In the first group, the direct anchoring of metal complexes to the metal node of the MOF is typically achieved when the MOF possesses metal nodes that are not fully saturated (Figure 1.6). An illustrative example is the post synthetic metalation of the mesoporous Zr-MOF NU-1000, where different metals have been anchored to the node. For instance, chromium(III) has been directly attached to the node and utilized as a catalyst for ethylene oligomerization.⁸⁹ In a different example, $\text{Ir}(\text{CO})_2$ and $\text{Ir}(\text{C}_2\text{H}_4)_2$ complexes were inserted into the same node for ethylene hydrogenation and dimerization.⁹⁰

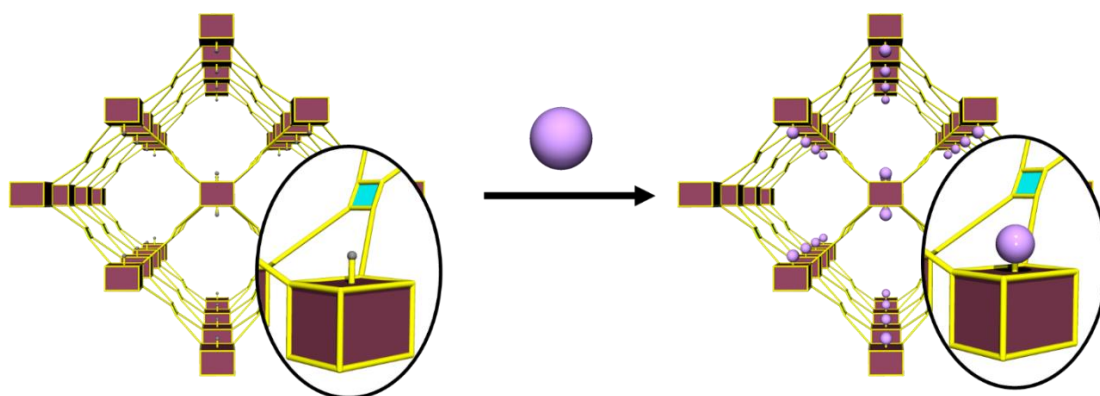


Figure 1.6. Schematic representation of PSMet of the metal nodes of a MOF. MOF metal nodes are represented as maroon polyhedra. The organic linkers of the parent MOF are represented as yellow sticks. Grey balls represent an anchoring site for a metal complex and purple balls represent the added metal ion or complex.

In the second group, and as used in this thesis, the metal complexes are attached to the linker of the MOF (Figure 1.7). This requires the linker to possess free functional groups capable of coordinating to the metal complex, along with additional metal donor groups that enable its incorporation into the MOF framework. To achieve this, it is common to synthesize organic linkers with two different types of functional groups (mixed donor linkers), where only one donor preferentially binds to the metal nodes while the other remains non-coordinated. Since MOFs are typically synthesized with carboxylate linkers to form the nodes, linkers containing carboxylates and slightly softer functional groups, such as nitrogen donor groups (e.g., pyridines, porphyrins, or pyrazoles), have been developed so that the metal node selectively binds to the carboxylates and the nitrogen donor group remains non-coordinated. An example is UiO-67bipy, a Zr-MOF containing free 2,2'-bipyridine donors that allows for the incorporation of metal complexes.⁹¹ The

relatively softer nature of the nitrogen donors compared to the oxygen donors enables selective binding of the carboxylates to the Zr atoms while leaving the bipyridines non-coordinated during the MOF synthesis step. Similarly, MOF-525 is a Zr-MOF containing a porphyrin linker that has been successfully used for post-synthetic metalation.⁹² In an example, Co(II) was anchored to the porphyrin groups to enhance the photocatalytic conversion of CO₂.⁹³ There are also a few examples of MOFs with free phosphorus donor groups,^{94, 95} but they are limited due to synthetic challenges, susceptibility to oxidation and generally lower stability.

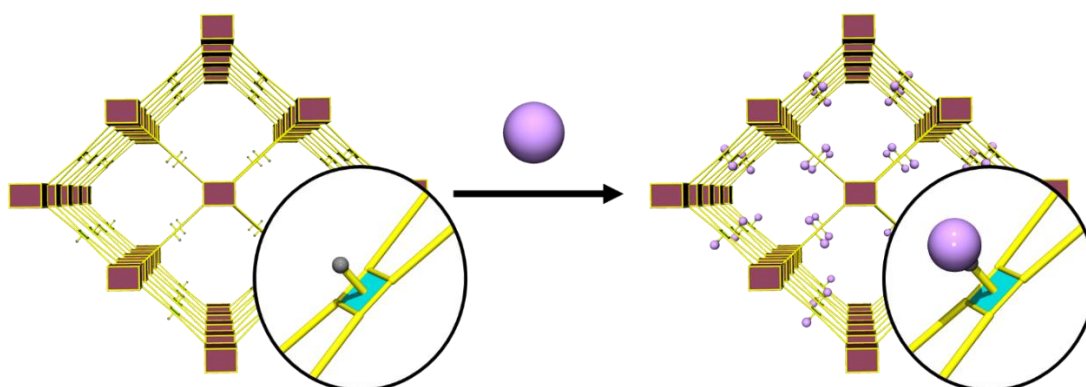


Figure 1.7. Schematic representation of PSMet of the organic linker of a MOF. MOF metal nodes are represented as maroon polyhedra. The organic linkers of the parent MOF are represented as yellow sticks. Grey balls represent a free functional group that can accommodate a metal centre and purple balls represent the added metal ion or complex.

Lastly, in the third group, metal complexes can be added within the pores of the MOF. This involves encapsulating the metal complex within the void spaces of the MOF structure, providing stability, and preventing its diffusion or leaching (Figure 1.8). This can be readily achieved if the MOF is anionic and has free cations in the pores. In those cases, cationic organometallic complexes can be introduced in MOFs via cation exchange. For instance, Crabtree's catalyst was encapsulated inside the pores of a Cr-MOF (MIL-101(Cr)) by cation exchange. The functionalized MOF was then active for the heterogeneous hydrogenation of non-functionalized alkenes either in solution or in the gas phase.⁹⁶

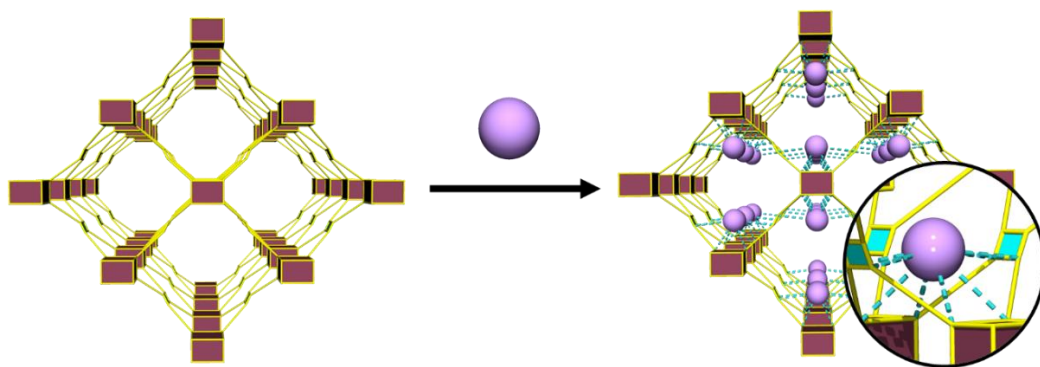


Figure 1.8. Schematic representation of PSMet at the pores of a MOF. MOF metal nodes are represented as maroon polyhedra. The organic linkers of the parent MOF are represented as yellow sticks. Purple balls represent a metal complex and dashed blue sticks weak interactions of the metal ion or complex with the MOF.

1.2.4. Linker flexibility

The binding of a metal post-synthetically (PSMet) and the complexation or dissociation of ligands to or from that metal centre can induce a change in the metal geometry. To synthesize a MOF platform capable of anchoring metal complexes with different metal environments, and acting as a crystalline sponge, the linker must possess a degree of flexibility to accommodate these varying environments and metal geometries. This requirement is strongly at odds with the common approach to MOF synthesis whereby the organic linkers used to form MOFs are typically rigid. This rigidity aids in the crystallization process by limiting the degrees of freedom of the linker. In contrast, flexible linkers can adopt many conformations and thereby many different phases are possible with minimal differences in the conditions. Consequently, the synthesis of phase pure high-valent MOFs, such as Zr-MOFs, with flexible linkers is uncommon. Additionally, when considering the synthesis of Zr-MOFs that incorporate functional groups capable of accommodating secondary metals, the options are primarily limited to porphyrin and 2,2'-bipyridine linkers.^{63, 97-102} While better able to facilitate the synthesis of the resulting MOF, the rigidity of these functional groups can restrict the types of metal environments they can support. For example, porphyrin linkers cannot coordinate organometallic complexes with a tetrahedral geometry. On the other hand, 2,2'-bipyridines can isolate a wider range of metal environments because they only possess two N-donor atoms, unlike porphyrins. However, when 2,2'-bipyridines chelate metal complexes, they can become distorted and this distortion can, in some cases, affect the stability of the metal complex or the crystallinity of the MOF.

Although the synthesis of high-valent MOFs with flexible linkers has not been widely reported, the synthesis of a Mn-based MOF (MnMOF-1) containing a free bis-pyrazole functional

group has demonstrated the ability to accommodate secondary metals with a broad range of metal coordination environments.^{103, 104} Compared to 2,2'-bipyridine, the bis-pyrazole group offers a few advantages. When the bis-pyrazole group chelates a metal, it forms a more conformationally mobile 6-membered ring instead of a 5-membered ring like the bipyridine group. Furthermore, the sp^3 carbon of the methylene bridge imparts flexibility to the chelating group, enabling it to adjust its conformation based on the metal, its geometry, and co-ligands, and facilitate better binding of the metal centre.

1.3. Use of MOFs as crystalline sponges

Metal-organic frameworks (MOFs) are crystalline materials commonly characterized using single-crystal X-ray diffraction (SCXRD) in their as-synthesized state to obtain information about the framework structure and topology. However, the characterization of post-synthetic modifications (PSM) in MOFs using SCXRD is often challenging due to factors such as thermal motion of pendant groups, low conversions, and crystallographic disorder. These factors lead to averaged electron density, making it difficult or sometimes impossible to model the product of PSM accurately. Despite these challenges, there are examples in the literature that demonstrate the process and highlight the advantages determining the structure of molecules and studying chemical transformations occurring within MOF pores.

MOFs can serve as crystalline matrices for structurally characterizing and studying the reactivity of pore guests. The concept of using MOFs in this manner was introduced by Fujita's group in 2010 as the "crystalline sponge" method (Figure 1.9).¹⁰⁵ The approach involves the synthesis of flexible MOFs known as sponge crystals, which have the ability to include guests and accommodate structural changes while maintaining crystallinity. This allows for the loading of the MOF pores with a molecule of interest, enabling its structural determination using SCXRD without the requirement of forming traditional crystals. Using different sponge crystals, Fujita and coworkers successfully determined the absolute structure of chiral natural products,¹⁰⁶⁻¹¹⁰ volatile substrates,^{111, 112} chiral molecules,^{113, 114} and monitored chemical transformations using this approach.¹¹⁵ One of the limitations of these systems was that their stability in polar media was limited. Recently, Gelder et al. developed a series of water-stable lanthanide MOFs (RUM-1 to -3) capable of hosting both hydrophobic and hydrophilic guests.¹¹⁶

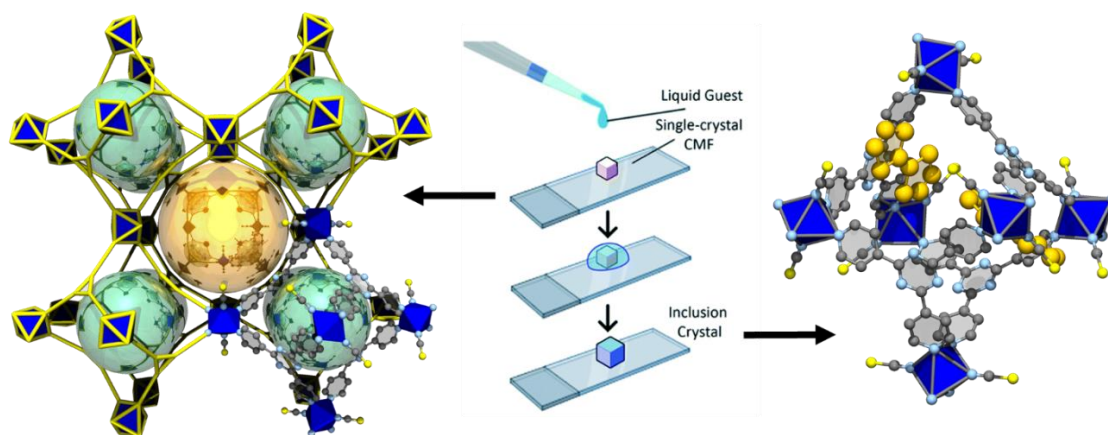


Figure 1.9. Summary of the crystalline sponge method developed by Fujita for enabling the structural determination of a guest molecule. Left: A schematic representation of a crystalline sponge synthesized by Fujita. Middle: Representation of a standard procedure for guest loading. Right: Representation of a pore of the crystalline sponge crystal loaded with a guest molecule. The blue polyhedra represent metal clusters, and the yellow sticks depict the organic linker. The colour scheme for the balls is as follows: carbon (grey), nitrogen (light blue), sulfur (yellow), and the guest molecule (orange). Figure adapted from refs ^{105, 117}.

Another approach to the crystalline sponge method, called coordinative alignment, was developed by Yaghi and coworkers.¹¹⁸ They synthesized a chiral Al-MOF (MOF-520) containing formate groups that could be replaced through PSM by other molecules with four common functional groups, such as primary alcohols, phenols, vicinal diols, and carboxylic acids (Figure 1.10). These molecules varied in complexity from methanol to plant hormones. The main functional group is coordinatively bound to the framework, but the unique environment of the chiral pore enables weak interactions with other functional groups of the guest molecules, aligning them in a specific manner and facilitating their characterization using SCXRD. Moreover, the chirality of the MOF provides specific stabilization for chiral molecules, allowing for the determination of their absolute configuration.

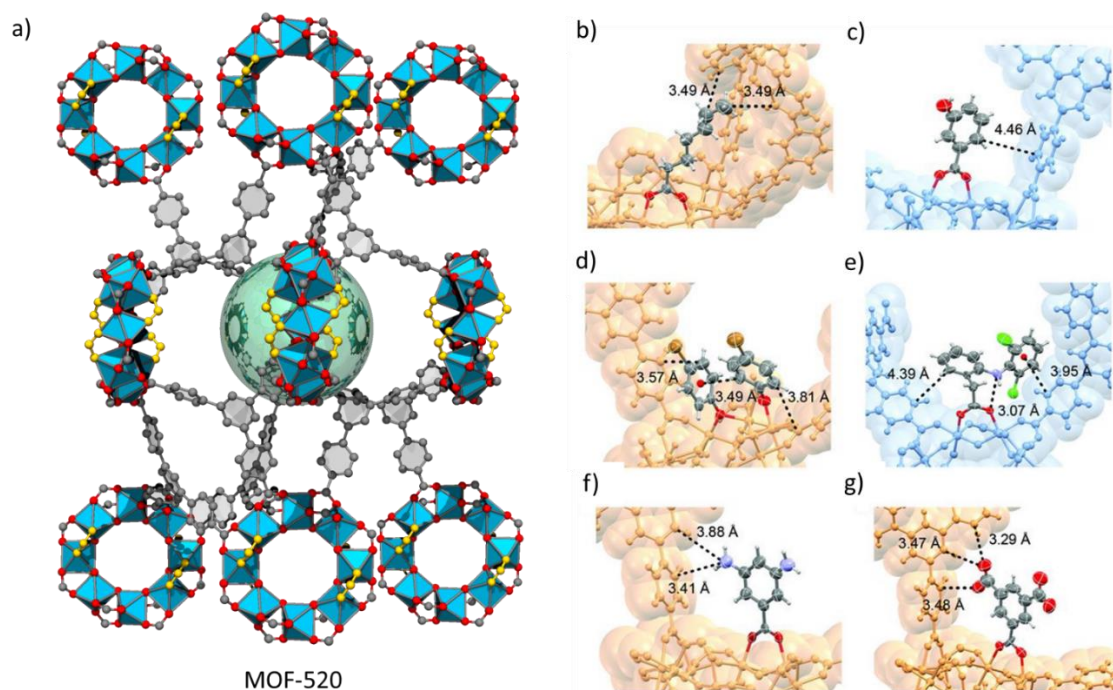


Figure 1.10. Summary of the coordinative alignment method developed by Yaghi. (a) Schematic representation of the MOF platform with the formate groups highlighted in yellow. The colour scheme used is as follows: carbon (grey), oxygen (red), and blue polyhedra representing the aluminium clusters. The remaining figures (b-g) depict crystal structures of different molecules coordinated to the MOF after displacement of the formate groups. The molecules shown are: (b) heptanoic acid, (c) 3-hydroxybenzoic acid, (d) 4-bromophenol, (e) diclofenac, (f) 3,5-diaminobenzoic acid, and (g) trimesic acid. Figure adapted from ref ¹¹⁸.

In addition to serving as crystalline matrices, SCXRD characterization of MOFs has provided insights into the interaction of gas molecules with different regions of the framework, which is crucial for designing MOFs as absorbent materials for gas adsorption and separation processes. Several studies have investigated the preferential binding sites of gas molecules in MOFs through SCXRD analysis.^{119, 120} Most studies have focused on the adsorption of CO₂ and H₂O molecules, as they form stronger interactions with the framework compared to molecules like CH₄ or N₂ which can be partially exchanged by water molecules during crystal mounting.¹²¹ Despite these challenges, Long and coworkers were able to visualize the adsorption of CO, CH₄, N₂, O₂, Ar, and P₄ in a Co-MOF using a custom-made system (Figure 1.11).¹²² At low pressure, they observed the interaction of guest molecules with the Co(II) open metal sites, while at higher pressure, they observed secondary and tertiary binding sites in the MOF. Terasaki and Yaghi took a further step by combining gas adsorption measurements with *in situ* X-ray diffraction to generate isotherms of individual pores.^{123, 124} Their approach allowed for the determination of

individual gas uptake capacity, surface area, and accessible pore volume, as well as the impact of pore geometry on the uptake and distribution of different adsorbates within the sample.

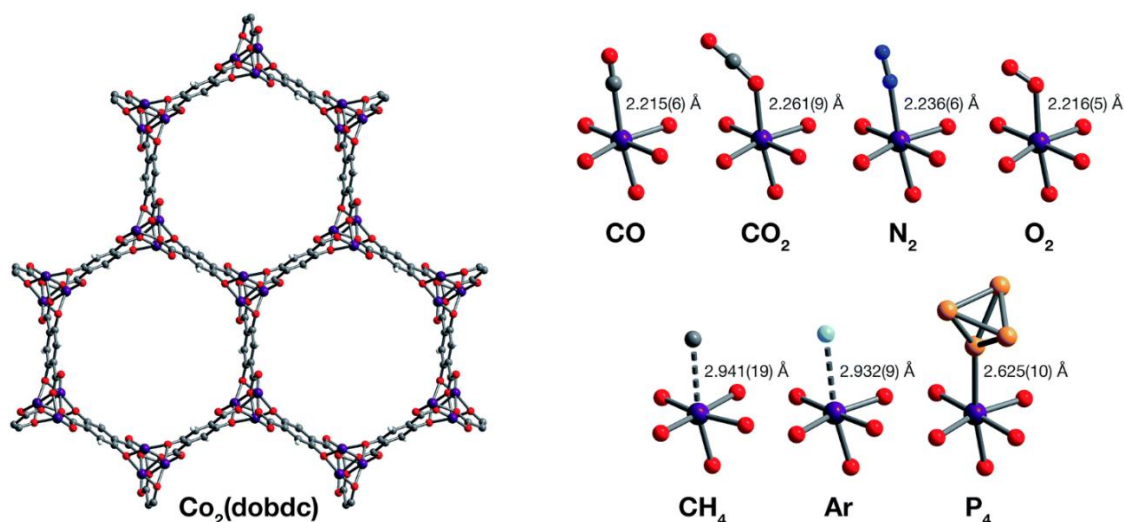


Figure 1.11. Representation of the interaction of small molecules with the Co open metal sites of $\text{Co}_2(\text{dobdc})$. The image of the left shows a crystallographic representation of the MOF and on the right, crystallographic representations of each of the molecules interacting with the cobalt node. Colour scheme: carbon (grey), oxygen (red), cobalt (purple), nitrogen (dark blue), argon (light blue) and phosphorus (yellow). Figure adapted from ref ¹²².

SCXRD in MOFs has also been instrumental in characterizing covalent transformations within the organic linker of the MOF. While NMR spectroscopy is the preferred method for routine structural elucidation of organic moieties in MOFs, it falls short in providing information sensitive to functional groups or metal complexes that might decompose during sample digestion. In such cases, SCXRD enables the characterization of long-range order without any sample digestion needed. For example, Forgan and coworkers utilized SCXRD to elucidate the bromination of alkyne groups in Zr- and Hf-MOFs. The MOFs were synthesized using 4,4'-ethynyldibenzoic acid, and subsequently, bromine was introduced, reacting with the alkyne groups.¹²⁵ SCXRD analysis revealed a change in the hybridization of the alkyne groups and induced lattice contraction. In another study, Maspoch and coworkers reported the first SC-to-SC transformation of a MOF through solid/gas phase reactivity.⁸² They synthesized a UiO-66 type MOF incorporating pendant olefin groups using 2-ethylenebenzene-1,4-dicarboxylic acid as the organic linker. By exposing the MOF to ozone gas, the olefin groups reacted to form metastable trioxolane groups (Figure 1.12). SCXRD characterization played a crucial role since NMR analysis would have resulted in the fragmentation of the trioxolanes into a mixture of solvated species, hindering a direct study of the reaction evolution. Building upon this work, they further reacted the oxolane groups with Me_2S

or H_2O_2 to yield aldehydes or carboxylic acids, respectively, and these products were also characterized through SCXRD.

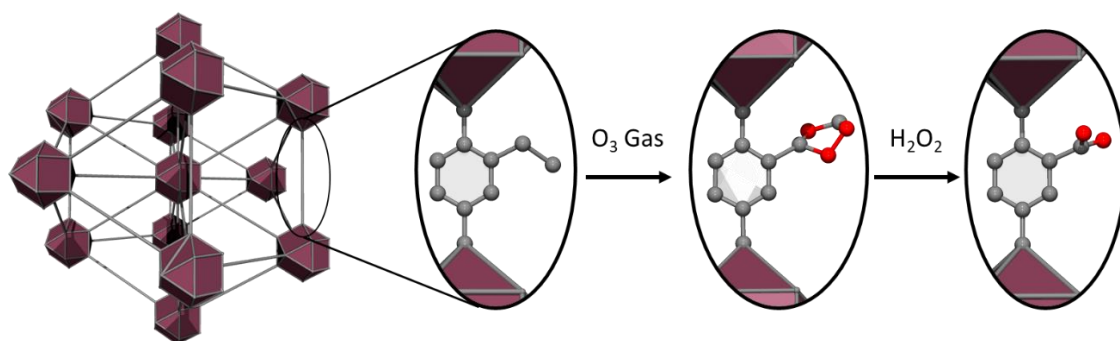


Figure 1.12. Representations showing covalent PSM of the organic linker in a UiO-66 type MOF. Left: Topological structure of the UiO-66 type MOF synthesized using 2-ethylenebenzene-1,4-dicarboxylic acid as the organic linker, with an enlargement showing the organic linker in a ball-and-stick representation. Middle: Similar enlargement showing the trioxolane groups formed from the reaction of the ethylene moiety and ozone. Right: Representation showing the carboxylate groups formed from the reaction of the trioxolane groups with hydrogen peroxide. The colour scheme used is as follows: carbon (grey), oxygen (red), and maroon polyhedra represent the Zr clusters. Figure adapted from ref ⁸².

X-ray crystallography of MOFs bound species can also offer valuable insights into catalytically active complexes, playing a crucial role in understanding the mechanisms of catalysed reactions and facilitating the development of new catalysts. The inherent crystallinity of MOFs, coupled with their pore nanoconfinement, allows for the structural elucidation of reactive metal complexes through SCXRD. For instance, Humphrey and colleagues successfully isolated AuCl and CuBr complexes anchored to a Co-MOF (PCM-101) containing phosphine vacant sites.⁹⁴ This MOF catalysed the hydroaddition of 4-pentyn-1-ol to tetrahydro-2-methyl-2-furanol. Interestingly, SCXRD analysis of the metalated MOFs revealed the presence of a $[\text{Cu}_2\text{Br}_2]$ dimer in the case of CuBr-metalated PCM-101 with a shorter Cu-Cu distance (2.91 Å) when compared to the average reported in literature (Figure 1.13).

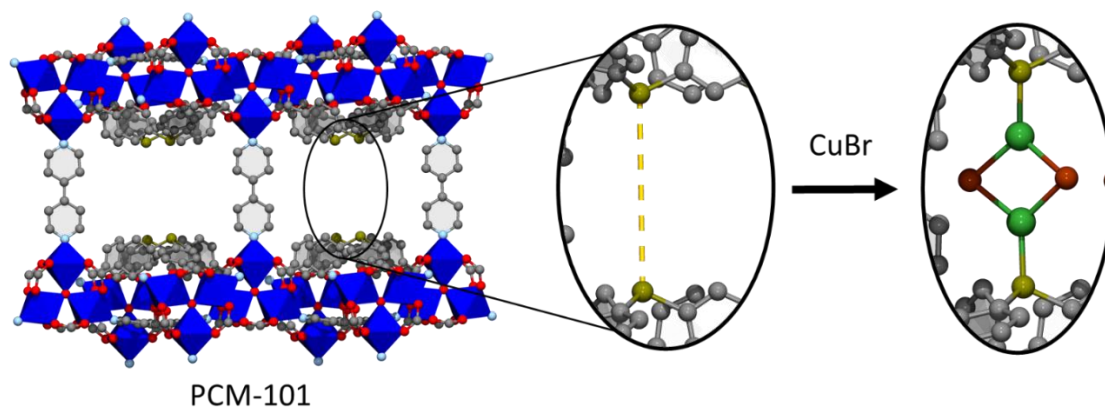


Figure 1.13. Isolation of a $[Cu_2Br_2]$ complex in a MOF (PCM-101). The close proximity of vacant phosphine sites in PCM-101 allow the formation of a $[Cu_2Br_2]$ complex upon metalation with CuBr. The colour scheme used is as follows: carbon (grey), oxygen (red), nitrogen (light blue), copper (green) bromine (brown), phosphorus (green-yellow) and cobalt clusters (blue polyhedral). Figure adapted from ref ⁹⁴.

Pardo and coworkers also made significant contributions in this area by anchoring naked $[Pd_4]^{2+}$ clusters within the cavities of an anionic MOF ($Ni_2[Ni_4(Cu_2(L)_2)_3]$) (Figure 1.14a).¹²⁶ To form the metal clusters, Ni(II) cations in the pores were exchanged with Pd(II), with these being stabilized by the pore chemistry. Subsequently, the Pd(II) centres were reduced in situ to form $[Pd_4]^{2+}$ metal clusters (Figure 1.14b). SCXRD analysis revealed the formation of an uncommon quasi-linear $[Pd_4]^{2+}$ metal cluster stabilized within the MOF. Following a similar procedure, $[Pt_2]^0$,¹²⁷ $[Pt]^{1+}$,¹²⁸ Pd(II)/Au(III),¹²⁹ and $[Ag_2]^0$ ¹³⁰ metal clusters were also successfully stabilized and characterized using SCXRD.

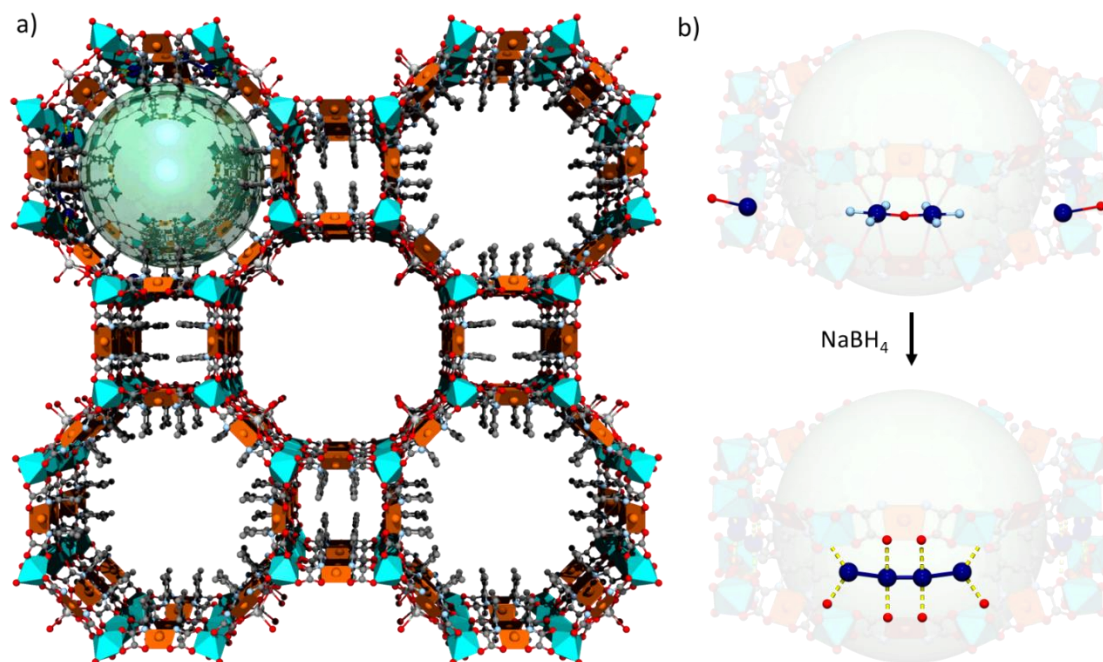


Figure 1.14. Isolation of $[Pd_4]^{2+}$ clusters within the cavities of an anionic MOF ($Ni_2[Ni_4(Cu_2(L)_2)_3]$). (a) Crystallographic representation of $Ni_2[Ni_4(Cu_2(L)_2)_3]$. (b) Reaction scheme showing the reduction of the Pd(II) centres anchored in the pores to form $[Pd_4]^{2+}$ clusters upon reduction with $NaBH_4$. The colour scheme used is as follows: carbon (grey), oxygen (red), nitrogen (light blue), palladium (dark blue) nickel cluster (light blue polyhedron) and copper cluster (orange polyhedron). Dashed yellow lines represent weak electrostatic interactions. Figure adapted from ref ¹²⁶.

Finally, the Sumbly-Doonan group have made significant advancements in this area by not only providing crystallographic insights into catalytically active metal complexes anchored within MOFs but also capturing structures of trapped reaction intermediates. Their research focused on the Mn-based MOF called MnMOF-1, which was reported by the same group in 2014. MnMOF-1 comprises the dicarboxylate ligand mdp (mdp = 4,4'-(methylenebis(3,5-dimethyl-1H-pyrazole-1,4-diyl))dibenzoic acid) (Figure 1.15a) and trinuclear Mn(II) nodes (Figure 1.15b).¹³¹ The linker mdp contained two carboxylates and a bis-pyrazole unit, allowing coordination to both harder carboxylates and softer bis-pyrazole units due to the intermediate hardness of Mn(II). This resulted in a trinuclear manganese cluster with bridging carboxylates and capping bis-pyrazole units. Within this structure one bis-pyrazole unit remained available for post-synthetic metalation (Figure 1.15c).

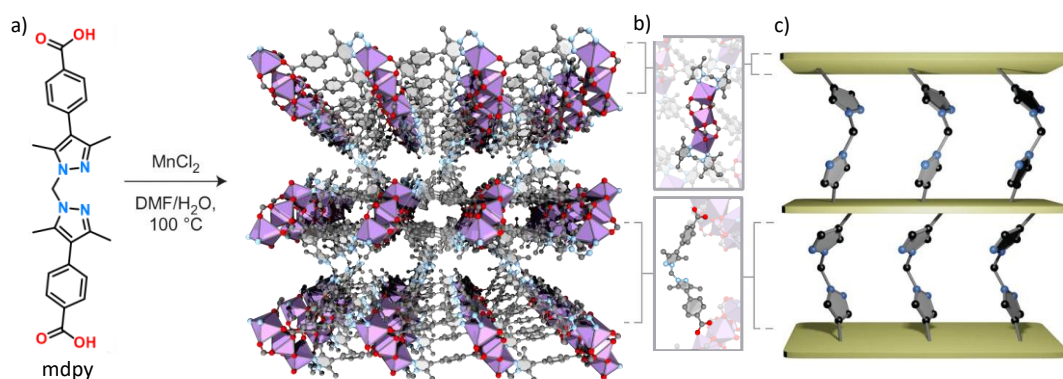


Figure 1.15. Schematic representation of the synthesis and crystal structure of MnMOF-1. (a) Synthesis of MnMOF-1 and a perspective view of the single-crystal X-ray structure of this material along the *c* axis. The colour scheme used is as follows: carbon (grey), oxygen (red), nitrogen (light blue), manganese cluster (purple polyhedron). (b) Enlargements of the trinuclear Mn(II) nodes of MnMOF-1 showing the coordination environment of the three Mn centres and one complete molecule of the pillaring ligand flanked by two trinuclear Mn(II) nodes, highlighting the pillaring ligand moiety. (c) Schematic representation of MnMOF-1 with the layers represented as mustard coloured planes and chemical detail highlighting the bis-pyrazole coordinating site. Figure adapted from ref ¹³¹.

The flexible chelating site provided by the central sp³ carbon in the bis-pyrazole unit facilitated the quantitative metalation of various metal complexes (Cu(II), Zn(II), Co(II), Mn(I), and Rh(I)) without losing crystallinity.^{103, 132} Additionally, the lower symmetry of MnMOF-1 compared to other MOFs and the limited rotational freedom of the bis-pyrazole units enabled the visualization by SCXRD of both the initial metal coordination environment and after chemical transformations occurring at the coordination environment of the metal centres.^{104, 133} In one example, MnMOF-1 was metalated with CoCl₂·6H₂O, resulting in the isolation of an octahedral Co(II) aqua complex metal complex anchored to the free bis-pyrazole groups of MnMOF-1.¹³¹ When these crystals were solvent exchanged and/or heated, the Co(II) complex underwent dehydration, transforming into a tetrahedral CoCl₂ complex. This transformation occurred through a SC-to-SC transformation, allowing for the SCXRD characterization of the tetrahedral CoCl₂ complex. MnMOF-1 also facilitated the isolation and structural characterisation of reaction intermediates formed by the interaction of a reagent with a metal complex. For instance, a Rh(I) biscarbonyl complex was anchored to MnMOF-1, followed by exposure to MeI, resulting in the identification of an acetyl intermediate bound to the Rh metal centre through SCXRD (Figure 1.16a).¹³⁴ Similarly, MnMOF-1 was metalated with Mn(I)N₃ in a two-step process, and then the crystals were exposed to ethyl-propiolate, leading to the formation of a triazolone product bound to the metal centre, which could also be characterized via SCXRD (Figure 1.16b).¹³⁵ These examples highlight the potential of using MOFs as platforms to study reaction chemistry, reaction mechanisms and to

develop new catalysts. Furthermore, they emphasize the importance of designing MOFs with functional groups that have a balance of structural flexibility and rigidity, and importantly, limited rotational freedom at the site of reactivity, to enable SCXRD characterization of both the metal centre and its environment.

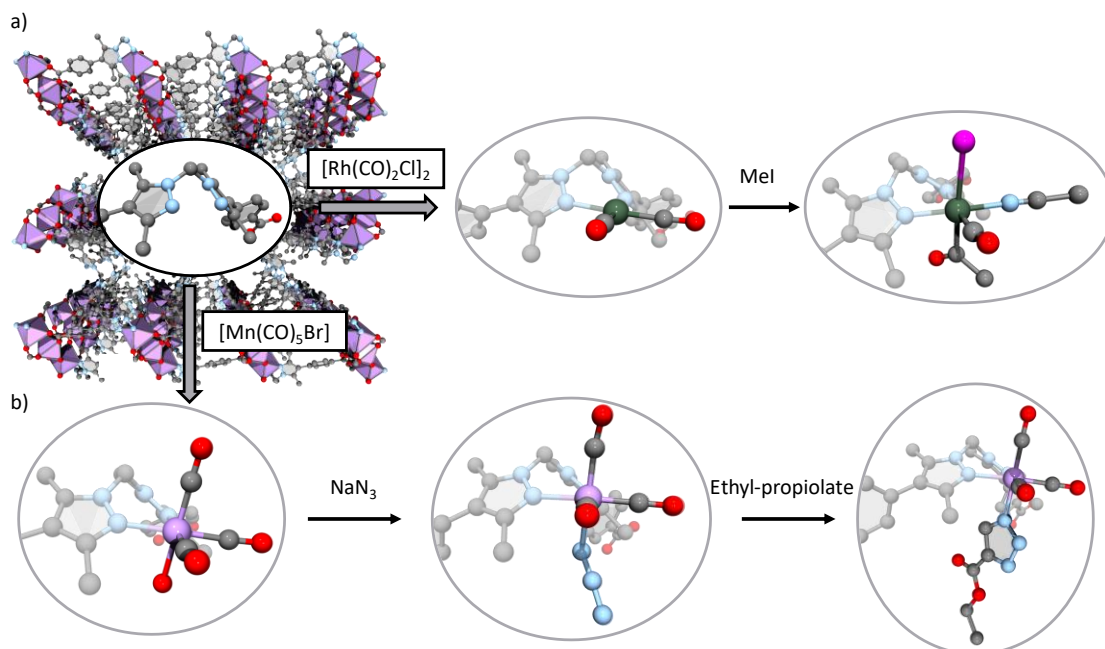


Figure 1.16. Overview of several chemical transformations occurring in the free bis-pyrazole groups of MnMOF-1. (a) Representation of MnMOF-1 bispyrazolyl units metalated with a Rh(I)bis(carbonyl) complex and the subsequent reaction with CH_3I to give an acetyl intermediate complex. (b) Introduction of Mn(I) pentacarbonyl complex into MnMOF-1 and the subsequent transformations with NaN_3 and ethyl-propiolate to isolate a triazolate intermediate bound to the Mn(I) centre. Figure adapted from refs ^{134, 135}.

1.4. Contextual Statement

As outlined above, despite all MOFs being, by definition, crystalline materials very few can act as generally applicable crystalline sponges. In particular, the lack of chemically and thermally stable MOFs that allow reliable X-ray characterization of metal complexes at binding sites presents a challenge to expanding the crystalline sponge approach. This lack of suitable robust crystalline sponges is mainly due to these MOFs being synthesised from a combination of high connected clusters and rigid linkers with phenyl rings that can freely rotate, generating disorder if coordinating groups are introduced. In these cases, for example for MOFs like UiO-67-bpy, the coordination environment of post-synthetically added metal centres is averaged out, making it difficult to characterize them using SCXRD. Therefore, this thesis focuses on studying the synthesis of new, chemically robust MOFs with free vacant sites that enable post-synthetic metalation and subsequent SCXRD to elucidate the chemistry of these metalated sites.

To achieve this goal, we decided to use a linker design approach that involved mixed donors, like the approach used previously in our group, and as used by Humphrey and coworkers in their work anchoring AuCl and Cu₂Br₂ to the free phosphine groups of the organic linker. This approach was preferred over anchoring the metal complexes directly to the metal cluster or isolating it within the pockets of the MOF as these positions typically exhibit a high degree of conformational freedom and/or high crystallographic symmetry which hinders their crystallographic elucidation.

To ensure the chemical and thermal stability of the framework, priority was given to the synthesis of stable high valent metal carboxylate MOFs rather than low valent metal MOFs. This was due to our focus being on isolating and structurally characterising low valent metal complexes, their intermediates, and products within the MOFs for catalytic applications. This choice of MOF target was made because a mixed donor linker requires a relatively hard donor and a relatively softer donor; thus, requiring the metal node to selectively form from the hard donor groups would leave the softer donors vacant for PSMet with the desired soft metal ions and incorporation of low valent complexes. Among the various high valent metals used for MOF synthesis, we chose to work with Zr-MOFs due to their favourable balance between chemical and thermal stability and crystallinity.

Finally, to facilitate post-synthetic metalation (PSMet), it was also necessary to have a free coordinating site, typically one that chelates to the secondary metal to order the complex. The selection of the functional group was based on three main considerations to maximize the

chances of ensuring crystallinity after PSMet. Firstly, lower symmetry MOFs are preferred to reduce the likelihood of the metal guest being disordered due to its location on a special position. Secondly, flexible organic linkers were chosen to allow for versatile geometries and changes in bite angles at the secondary metal centre without compromising the long-range order of the framework. Lastly, the ability to synthesize linkers in a few steps was important to maximize yields and enable the efficient synthesis of different linkers. Considering these factors, the use of linkers containing bis-pyrazole units, as previously reported within the research group, was determined to be the best choice. These linkers typically occupy lower symmetry sites and have less rotation freedom in the context of MOFs compared to other functional groups such as bipyridines, reducing the chances of crystallographic disorder.

Hence, the overall aim of this thesis was to synthesize new Zr-MOFs containing free bis-pyrazole units that enable post-synthetic metalation and subsequent allow SCXRD to be applied to elucidate the chemistry of these metalated sites. This required:

1. Synthesis of different organic linkers containing free bis-pyrazole groups and their reaction with Zr(IV) metal salts to form a family of Zr-MOFs.
2. PSMet of these Zr-MOFs and characterization by SCXRD to evaluate if they can act as sponge crystals and allow the elucidation of the chemistry occurring at these metalated sites.

Due to its ease of synthesis and a short linker length that should favour crystallization, 1,1'-methylenebis(1H-pyrazole-4-carboxylic acid) was our first linker of choice for developing new chemically and thermally robust crystalline sponges, which led to the study presented in chapter 2. While not directly achieving all the targeted aims of the thesis, Chapter 2 presents the templated synthesis of zirconium(IV)-based 2D-metal-organic frameworks (2D-MOFs), which followed by chemical delamination can provide access to metal-organic layers (MOLs) with accessible chelating sites. It was found that the angular shape of this short di-topic linker favoured the formation of 2D-MOFs when reacted with Zr. In the absence of a templating agent, the layered structure formed (UAM-1) is closely packed with the bis-pyrazole units adopting an anti-conformation that prevents their delamination and PSMet. However, the addition of copper(I) iodide to the reaction media gives rise to a pre-organized 'syn'-conformation of the pyrazole moieties, yielding a layered MOF pillared by CuI dimers, UAM-2. These dimers form a 'weak link' that can be readily displaced with mildly acidic solutions to provide efficient delamination. The resulting polydisperse nanosheets are stable and can undergo quantitative PSMet. This chapter presents the templating synthetic approach, allied with chemical delamination, as a useful method

to form 2D-MOF nanosheets. Importantly, this strategy provides chemical control over the delamination process without subjecting the material to significant mechanical stress. These new Zr-based 2D-MOFs could potentially be used for catalysis applications, as they possess no barrier to substrate diffusion due to the absence of channels or pores. Unfortunately, however, metal leaching from the bis-pyrazole site was pronounced in the case of labile metals. In respect of the overall goal of generating robust crystalline sponges, the need for delamination of those layers for PSMet also leads to a loss of crystallinity, which prevented the study of the resulting metal complexes by SCXRD. For this reason, we decided to increase the connectivity of the linker to force the formation of 3D Zr-MOFs that could retain crystallinity. The tetra-topic linker 1,1,2,2-tetrakis[4-(4-carboxyphenyl)-1H-pyrazol-1-yl]ethane (TCPE) was our choice and this led to the study presented in chapter 3.

Chapter 3 presents the synthesis of a new Zr-MOF that allows atomic-scale elucidation of unusually distorted dimeric complexes. This MOF, UAM-1001, is synthesized in a two-step process. The first step involves the direct reaction of TCPE and a Zr salt to form the parent MOF (UAM-1000). In the second step, the insertion of a secondary linker via PSM is performed. The insertion of the secondary linkers is necessary because UAM-1000 shows a high degree of flexibility that, upon PSMet, leads to loss of its crystallinity. With the addition of the bracing secondary linker, the degree of flexibility of UAM-1001 is about right for use of the material as a crystalline sponge, with the syn-conformation of the bis-pyrazole groups in UAM-1001 being locked by the MOF topology. With some of the targeted characteristics for a crystalline sponge being present, we set out to characterise the PSMet chemistry with different metal salts. In particular, it was observed that the proximity of adjacent bis-pyrazole units allows the accommodation of monomeric and dimeric metal complexes depending on the choice of metal salt (metal coordination geometry and presence of bridging ligands). UAM-1001 was metalated with PdCl₂, Cu(NO₃)₂, CuCl₂, CoCl₂, NiCl₂, and [Rh(CO)₂Cl]₂. Monomeric complexes were isolated in the case of PdCl₂ and Cu(NO₃)₂. However, due to the close proximity of the adjacent bis-pyrazole units, only 50% of the bis-pyrazole units could be metalated. On the other hand, dinuclear complexes were isolated with CuCl₂, CoCl₂, NiCl₂, and [Rh(CO)₂Cl]₂. The isolated Ni(II) and Rh(I) dimers exhibited an octahedral geometry with minor distortions compared to similar discrete complexes reported in the literature. In contrast, the Cu(II) and Co(II) dinuclear complexes showed a trigonal bipyramidal geometry in the case of Cu(II) and a mixture of trigonal bipyramidal and square pyramidal dimers in the case of Co(II). These two complexes exhibited significant distortions compared to other similar discrete complexes reported in the literature. The

ability to isolate dinuclear complexes was particularly interesting as there are very few MOF platforms that can isolate dimeric complexes whilst allowing SCXRD characterization. There was an additional level of interest as dinuclear metal complexes are important components of metalloenzyme active sites and show an interesting array of photophysical and magnetic properties. The results of this chapter also highlight the importance of MOF topology in the ability to isolate metal complexes in MOFs; the encountered topology brings two bis-pyrazole groups into close proximity and provides a distinct PSMet site compared to that seen in MnMOF-1. Finally, the topology of UAM-1001 is somewhat unusual, being only the second example of a MOF that crystallizes with the *sqc* topology. To understand this, we undertook a study on the formation of Zr-MOFs from tetratopic linkers containing bis-pyrazole units and that work is presented in chapter 4.

Chapter 4 presents an extensive study on the formation of Zr-MOFs from tetratopic linkers containing free bis-pyrazole units, combining experimental and computational studies to understand how the MOFs are formed. Note that the computational studies were done by Dr. Jack D. Evans. The experimental part of the work focuses on two aspects: firstly, the effect of linker length on the MOF topologies that are formed, and finally, the effect of synthetic conditions on the resulting topology. This study is crucial because the topology of UAM-1001 gives rise to a tetrapyrazole binding site that can bind dinuclear complexes, and we wanted to understand if this could be perturbed to contract or relax this PSMet site. A secondary interest related to the paucity of studies on the synthesis of Zr-MOFs with flexible linkers. There are many studies that show that, when using rigid linkers under the same conditions, the length of the linker does not affect the topology of the MOF. However, relatively few studies have been done using flexible linkers, as they have different accessible conformations that can potentially lead to the formation of MOFs with different topologies. Thus, in this work, three different but related linkers were reacted with a Zr salt under the same conditions, resulting in three different MOF structures and topologies. This highlights the fact that changing the length or the width of the linker, if the linker is flexible, can make a pronounced difference in its conformation and, therefore, can influence the topology of the resulting MOFs. Furthermore, by changing the synthetic conditions, a different topology from UAM-1001, UAM-1002, could be obtained with the same linker. The different distribution of the bis-pyrazole units in UAM-1002 disfavours formation of dinuclear complexes like those seen in UAM-1001, allowing only site-isolated single-atom metal complexes to be formed upon PSMet. PSMet of UAM-1002 induces a big change in the conformation of the TCPE bringing the Zr clusters very close to each other. This allows the capping formate groups of the

Zr-cluster to partially detach to bridge the cluster. This increases the connectivity of the Zr-cluster from 8 to 10-connected. This increase in connectivity of the Zr-cluster is not enough to allow detailed structural elucidation of the anchored metal complexes like in UAM-1001. However, solvent exchanging the crystals to toluene allows the ordering of the structure and hence detailed structural elucidation of the metal complex. These findings highlight that the TCPE linker is too flexible in certain MOF topologies to allow SCXRD characterization after PSMet, and a slight rigidification is needed to more reliably enable atomic-scale elucidation of the post-synthetically metalated metal complexes. In cases where rigidification is not enough, a solvent that orders the structure might still overcome the ligand flexibility enabling atomic-scale elucidation of the post-synthetically metalated metal complexes.

Finally, chapter 5 presents a short study on how the substitution pattern and hence angular shape of the linker can also affect the MOF topology formed. Instead of using a para-substituted linker like TCPE, we examined the effect of using a meta-substituted linker, 1,1,2,2-tetrakis[4-(3-carboxyphenyl)-1H-pyrazol-1-yl]ethane, to form Zr-MOFs. This gives rise to a new MOF (UAM-1006) where adjacent bis-pyrazole groups are similarly close, potentially allowing for use of this material as a crystalline sponge and the possibility of isolating dimeric complexes. This work further shows how the linker shape can affect the MOF topology and thereby the distribution of the free metal sites in the pores of the MOF formed.

1.5. References

1. Zastrow, M. L. and Pecoraro, V. L. *Coord. Chem. Rev.*, **2013**, 257, 2565-2588.
2. Permyakov, E. A. *Encyclopedia*, **2021**, 1, 261-292.
3. Vallee, B. L. and Williams, R. J. *PNAS*, **1968**, 59, 498-505.
4. Rosati, F. and Roelfes, G. *ChemCatChem*, **2010**, 2, 916-927.
5. Wittwer, M., Markel, U., Schiffels, J., Okuda, J., Sauer, D. F. and Schwaneberg, U. *Nat. Catal.*, **2021**, 4, 814-827.
6. Bullock, R. M., Chen, J. G., Gagliardi, L., Chirik, P. J., Farha, O. K., Hendon, C. H., Jones, C. W., Keith, J. A., Klosin, J., Minteer, S. D., Morris, R. H., Radosevich, A. T., Rauchfuss, T. B., Strotman, N. A., Vojvodic, A., Ward, T. R., Yang, J. Y. and Surendranath, Y. *Science*, **2020**, 369, eabc3183.
7. McFarland, E. W. and Metiu, H. *Chem. Rev.*, **2013**, 113, 4391-4427.
8. Roduner, E. *Chem. Soc. Rev.*, **2014**, 43, 8226-8239.
9. Schlögl, R. *Angew. Chem. Int. Ed.*, **2015**, 54, 3465-3520.
10. Chen, Y., Yekta, S. and Yudin, A. K. *Chem. Rev.*, **2003**, 103, 3155-3212.
11. Astruc, D. *Chem. Rev.*, **2020**, 120, 461-463.
12. Sarkar, S., Guibal, E., Quignard, F. and SenGupta, A. K. *J. Nanopart. Res.*, **2012**, 14, 1-24.
13. McMorn, P. and Hutchings, G. J. *Chem. Soc. Rev.*, **2004**, 33, 108.
14. Goh, P. S., Ismail, A. F., Sanip, S. M., Ng, B. C. and Aziz, M. *Sep. Purif. Technol.*, **2011**, 81, 243-264.
15. Wu, J., Xu, F., Li, S., Ma, P., Zhang, X., Liu, Q., Fu, R. and Wu, D. *Adv. Mater.*, **2019**, 31, 1802922.
16. Zhu, L., Shen, D. and Luo, K. H. *J. Hazard. Mater.*, **2020**, 389, 122102.
17. Bondybey, V. E., Smith, A. M. and Agreiter, J. *Chem. Rev.*, **1996**, 96, 2113-2134.
18. Pagacz-Kostrzewa, M., Bumażnik, D., Coussan, S. and Sałdyka, M. *Molecules*, **2022**, 27, 3897.
19. Young, R. J., Huxley, M. T., Pardo, E., Champness, N. R., Sumbly, C. J. and Doonan, C. *J. Chem. Sci.*, **2020**, 11, 4031-4050.
20. Das, A., Reibenspies, J. H., Chen, Y.-S. and Powers, D. C. *J. Am. Chem. Soc.*, **2017**, 139, 2912-2915.

21. Martínez-Martínez, A. J., Tegner, B. E., McKay, A. I., Bukvic, A. J., Rees, N. H., Tizzard, G. J., Coles, S. J., Warren, M. R., Macgregor, S. A. and Weller, A. S. *J. Am. Chem. Soc.*, **2018**, *140*, 14958-14970.
22. Chadwick, F. M., McKay, A. I., Martínez-Martínez, A. J., Rees, N. H., Kramer, T., Macgregor, S. A. and Weller, A. S. *Chem. Sci.*, **2017**, *8*, 6014-6029.
23. Chadwick, F. M., Rees, N. H., Weller, A. S., Kramer, T., Iannuzzi, M. and Macgregor, S. A. *Angew. Chem. Int. Ed.*, **2016**, *55*, 3677-3681.
24. Chadwick, F. M., Kramer, T., Gutmann, T., Rees, N. H., Thompson, A. L., Edwards, A. J., Buntkowsky, G., Macgregor, S. A. and Weller, A. S. *J. Am. Chem. Soc.*, **2016**, *138*, 13369-13378.
25. Chadwick, F. M., Rees, N. H., Weller, A. S., Krämer, T., Iannuzzi, M. and Macgregor, S. A. *Angew. Chem. Int. Ed.*, **2016**, *128*, 3741-3745.
26. Pike, S. D., Chadwick, F. M., Rees, N. H., Scott, M. P., Weller, A. S., Kramer, T. and Macgregor, S. A. *J. Am. Chem. Soc.*, **2015**, *137*, 820-833.
27. Chadwick, F. M., Krämer, T., Gutmann, T., Rees, N. H., Thompson, A. L., Edwards, A. J., Buntkowsky, G., Macgregor, S. A. and Weller, A. S. *J. Am. Chem. Soc.*, **2016**, *138*, 13369-13378.
28. Chadwick, F. M., McKay, A. I., Martínez-Martínez, A. J., Rees, N. H., Krämer, T., Macgregor, S. A. and Weller, A. S. *Chem. Sci.*, **2017**, *8*, 6014-6029.
29. Furukawa, H., Cordova, K. E., O'Keeffe, M. and Yaghi, O. M. *Science*, **2013**, *341*, 1230444.
30. Li, H., Wang, K., Sun, Y., Lollar, C. T., Li, J. and Zhou, H.-C. *Mater. Today*, **2018**, *21*, 108-121.
31. Tsivadze, A. Y., Aksyutin, O. E., Ishkov, A. G., Knyazeva, M. K., Solovtsova, O. V., Men'Shchikov, I. E., Fomkin, A. A., Shkolin, A. V., Khozina, E. V. and Grachev, V. A. *Russ. Chem. Rev.*, **2019**, *88*, 925-978.
32. Jia, T., Gu, Y. and Li, F. *J. Environ. Chem. Eng.*, **2022**, *10*, 108300.
33. Taylor-Pashow, K. M. L., Della Rocca, J., Xie, Z., Tran, S. and Lin, W. *J. Am. Chem. Soc.*, **2009**, *131*, 14261-14263.
34. Kumar, S., Mohan, B., Tao, Z., You, H. and Ren, P. *Catal. Sci. Technol.*, **2021**, *11*, 5734-5771.
35. Dhakshinamoorthy, A., Asiri, A. M. and García, H. *Trends Chem.*, **2020**, *2*, 454-466.
36. Wei, Y. S., Zhang, M., Zou, R. and Xu, Q. *Chem. Rev.*, **2020**, *120*, 12089-12174.

37. Reddy, C. V., Reddy, K. R., Harish, V. V. N., Shim, J., Shankar, M. V., Shetti, N. P. and Aminabhavi, T. M. *Int. J. Hydrogen Energy*, **2020**, *45*, 7656-7679.
38. Zhang, T., Chen, Z., Walsh, A. G., Li, Y. and Zhang, P. *Adv. Mater.*, **2020**, *32*, 2002910.
39. Kajal, N., Singh, V., Gupta, R. and Gautam, S. *Environ. Res.*, **2022**, *204*, 112320.
40. Lu, K., Aung, T., Guo, N., Weichselbaum, R. and Lin, W. *Adv. Mater.*, **2018**, *30*, 1707634.
41. Lustig, W. P., Mukherjee, S., Rudd, N. D., Desai, A. V., Li, J. and Ghosh, S. K. *Chem. Soc. Rev.*, **2017**, *46*, 3242-3285.
42. Gan, L., Chidambaram, A., Fonquernie, P. G., Light, M. E., Choquesillo-Lazarte, D., Huang, H., Solano, E., Fraile, J., Vinas, C., Teixidor, F., Navarro, J. A. R., Stylianou, K. C. and Planas, J. G. *J. Am. Chem. Soc.*, **2020**, *142*, 8299-8311.
43. Huang, R., Peng, Y., Wang, C., Shi, Z. and Lin, W. *Eur. J. Inorg. Chem.*, **2016**, *2016*, 4358-4362.
44. Kalmutzki, M. J., Hanikel, N. and Yaghi, O. M. *Sci. Adv.*, **2018**, *4*, eaat9180.
45. Ding, M., Cai, X. and Jiang, H.-L. *Chem. Sci.*, **2019**, *10*, 10209-10230.
46. Burtch, N. C., Jasuja, H. and Walton, K. S. *Chem. Rev.*, **2014**, *114*, 10575-10612.
47. Yuan, S., Qin, J.-S., Lollar, C. T. and Zhou, H.-C. *ACS Cent. Sci.*, **2018**, *4*, 440-450.
48. James, S. L. *Chem. Soc. Rev.*, **2003**, *32*, 276.
49. Rowsell, J. L. C. and Yaghi, O. M. *Microporous Mesoporous Mater.*, **2004**, *73*, 3-14.
50. Cavka, J. H., Jakobsen, S., Olsbye, U., Guillou, N., Lamberti, C., Bordiga, S. and Lillerud, K. P. *J. Am. Chem. Soc.*, **2008**, *130*, 13850-13851.
51. Tsuruoka, T., Furukawa, S., Takashima, Y., Yoshida, K., Isoda, S. and Kitagawa, S. *Angew. Chem. Int. Ed.*, **2009**, *121*, 4833-4837.
52. Diring, S., Furukawa, S., Takashima, Y., Tsuruoka, T. and Kitagawa, S. *Chem. Mater.*, **2010**, *22*, 4531-4538.
53. Bai, Y., Dou, Y., Xie, L. H., Rutledge, W., Li, J. R. and Zhou, H. C. *Chem. Soc. Rev.*, **2016**, *45*, 2327-2367.
54. Li, L., Wang, X. S., Liu, T. F. and Ye, J. *Small methods*, **2020**, *4*, 2000486.
55. Guo, Y., Zhang, J., Dong, L.-Z., Xu, Y., Han, W., Fang, M., Liu, H.-K., Wu, Y. and Lan, Y.-Q. *Eur. J. Chem.*, **2017**, *23*, 15518-15528.
56. Fan, W., Wang, K.-Y., Welton, C., Feng, L., Wang, X., Liu, X., Li, Y., Kang, Z., Zhou, H.-C., Wang, R. and Sun, D. *Coord. Chem. Rev.*, **2023**, *489*, 215175.
57. Yuan, S., Zou, L., Li, H., Chen, Y. P., Qin, J., Zhang, Q., Lu, W., Hall, M. B. and Zhou, H. C. *Angew. Chem. Int. Ed.*, **2016**, *55*, 10776-10780.

58. Sikma, R. E., Balto, K. P., Figueroa, J. S. and Cohen, S. M. *Angew. Chem. Int. Ed.*, **2022**, *61*, e202206353.
59. Wang, Z., Bilegsaikhan, A., Jerozal, R. T., Pitt, T. A. and Milner, P. J. *ACS Appl. Mater. Interfaces*, **2021**, *13*, 17517-17531.
60. Chen, Z., Hanna, S. L., Redfern, L. R., Alezi, D., Islamoglu, T. and Farha, O. K. *Coord. Chem. Rev.*, **2019**, *386*, 32-49.
61. Jiang, H., Alezi, D. and Eddaoudi, M. *Nat. Rev. Mater.*, **2021**, *6*, 466-487.
62. Yaghi, O. M., O'Keeffe, M., Ockwig, N. W., Chae, H. K., Eddaoudi, M. and Kim, J. *Nature*, **2003**, *423*, 705-714.
63. Deria, P., Yu, J., Balaraman, R. P., Mashni, J. and White, S. N. *Chem. Commun.*, **2016**, *52*, 13031-13034.
64. Sikma, R. E., Kunal, P., Dunning, S. G., Reynolds, J. E., 3rd, Lee, J. S., Chang, J. S. and Humphrey, S. M. *J. Am. Chem. Soc.*, **2018**, *140*, 9806-9809.
65. Pachfule, P., Garai, B. and Banerjee, R. *Inorg. Chem.*, **2016**, *55*, 7200-7205.
66. Guillermin, V., Kim, D., Eubank, J. F., Luebke, R., Liu, X., Adil, K., Lah, M. S. and Eddaoudi, M. *Chem. Soc. Rev.*, **2014**, *43*, 6141-6172.
67. Lyu, J., Zhang, X., Otake, K.-I., Wang, X., Li, P., Li, Z., Chen, Z., Zhang, Y., Wasson, M. C., Yang, Y., Bai, P., Guo, X., Islamoglu, T. and Farha, O. K. *Chem. Sci.*, **2019**, *10*, 1186-1192.
68. Chen, Y., Zhang, X., Mian, M. R., Son, F. A., Zhang, K., Cao, R., Chen, Z., Lee, S.-J., Idrees, K. B., Goetjen, T. A., Lyu, J., Li, P., Xia, Q., Li, Z., Hupp, J. T., Islamoglu, T., Napolitano, A., Peterson, G. W. and Farha, O. K. *J. Am. Chem. Soc.*, **2020**, *142*, 21428-21438.
69. Wang, Z. and Cohen, S. M. *Chem. Soc. Rev.*, **2009**, *38*, 1315.
70. Tanabe, K. K. and Cohen, S. M. *Chem. Soc. Rev.*, **2011**, *40*, 498-519.
71. Kalaj, M. and Cohen, S. M. *ACS Cent. Sci.*, **2020**, *6*, 1046-1057.
72. Mandal, S., Natarajan, S., Mani, P. and Pankajakshan, A. *Adv. Funct. Mater.*, **2021**, *31*, 2006291.
73. Doonan, C. J., Morris, W., Furukawa, H. and Yaghi, O. M. *J. Am. Chem. Soc.*, **2009**, *131*, 9492-9493.
74. Tanabe, K. K., Wang, Z. and Cohen, S. M. *J. Am. Chem. Soc.*, **2008**, *130*, 8508-8517.
75. Wang, Z. and Cohen, S. M. *Angew. Chem. Int. Ed.*, **2008**, *47*, 4699-4702.
76. Haneda, T., Kawano, M., Kawamichi, T. and Fujita, M. *J. Am. Chem. Soc.*, **2008**, *130*, 1578-1579.

-
77. Dugan, E., Wang, Z., Okamura, M., Medina, A. and Cohen, S. M. *Chem. Commun.*, **2008**, 3366.
78. Seo, J. S., Whang, D., Lee, H., Jun, S. I., Oh, J., Jeon, Y. J. and Kim, K. *Nature*, **2000**, *404*, 982-986.
79. Morris, W., Doonan, C. J., Furukawa, H., Banerjee, R. and Yaghi, O. M. *J. Am. Chem. Soc.*, **2008**, *130*, 12626-12627.
80. Goto, Y., Sato, H., Shinkai, S. and Sada, K. *J. Am. Chem. Soc.*, **2008**, *130*, 14354-14355.
81. Wang, X.-S., Ma, S., Sun, D., Parkin, S. and Zhou, H.-C. *J. Am. Chem. Soc.*, **2006**, *128*, 16474-16475.
82. Albalad, J., Xu, H., Gándara, F., Haouas, M., Martineau-Corcós, C., Mas-Ballesté, R., Barnett, S. A., Juanhuix, J., Imaz, I. and MasPOCH, D. *J. Am. Chem. Soc.*, **2018**, *140*, 2028-2031.
83. Kronast, A., Eckstein, S., Altenbuchner, P. T., Hindelang, K., Vagin, S. I. and Rieger, B. *Eur. J. Chem.*, **2016**, *22*, 12800-12807.
84. Guillerm, V., Xu, H., Albalad, J., Imaz, I. and MasPOCH, D. *J. Am. Chem. Soc.*, **2018**, *140*, 15022-15030.
85. Burnett, B. J. and Choe, W. *Dalton Trans.*, **2012**, *41*, 3889.
86. Yuan, S., Chen, Y. P., Qin, J. S., Lu, W., Zou, L., Zhang, Q., Wang, X., Sun, X. and Zhou, H. C. *J. Am. Chem. Soc.*, **2016**, *138*, 8912-8919.
87. Fei, H. and Cohen, S. M. *J. Am. Chem. Soc.*, **2015**, *137*, 2191-2194.
88. Evans, J. D., Sumbly, C. J. and Doonan, C. J. *Chem. Soc. Rev.*, **2014**, *43*, 5933-5951.
89. Goetjen, T. A., Zhang, X., Liu, J., Hupp, J. T. and Farha, O. K. *ACS Sustain. Chem. Eng.*, **2019**, *7*, 2553-2557.
90. Yang, D., Odoh, S. O., Wang, T. C., Farha, O. K., Hupp, J. T., Cramer, C. J., Gagliardi, L. and Gates, B. C. *J. Am. Chem. Soc.*, **2015**, *137*, 7391-7396.
91. Li, L., Tang, S., Wang, C., Lv, X., Jiang, M., Wu, H. and Zhao, X. *Chem. Commun.*, **2014**, *50*, 2304-2307.
92. Morris, W., Voloskiy, B., Demir, S., Gándara, F., McGrier, P. L., Furukawa, H., Cascio, D., Stoddart, J. F. and Yaghi, O. M. *Inorg. Chem.*, **2012**, *51*, 6443-6445.
93. Zhang, H., Wei, J., Dong, J., Liu, G., Shi, L., An, P., Zhao, G., Kong, J., Wang, X., Meng, X., Zhang, J. and Ye, J. *Angew. Chem. Int. Ed.*, **2016**, *128*, 14522-14526.
94. Dunning, S. G., Nandra, G., Conn, A. D., Chai, W. R., Sikma, R. E., Lee, J. S., Kunal, P., Reynolds, J. E., Chang, J. S., Steiner, A., Henkelman, G. and Humphrey, S. M. *Angew. Chem. Int. Ed.*, **2018**, *57*, 9295-9299.
-

95. Sawano, T., Lin, Z., Boures, D., An, B., Wang, C. and Lin, W. *J. Am. Chem. Soc.*, **2016**, *138*, 9783-9786.
96. Grigoropoulos, A., McKay, A. I., Katsoulidis, A. P., Davies, R. P., Haynes, A., Brammer, L., Xiao, J., Weller, A. S. and Rosseinsky, M. J. *Angew. Chem.*, **2018**, *130*, 4622-4627.
97. Feng, D., Chung, W.-C., Wei, Z., Gu, Z.-Y., Jiang, H.-L., Chen, Y.-P., Darensbourg, D. J. and Zhou, H.-C. *J. Am. Chem. Soc.*, **2013**, *135*, 17105-17110.
98. Feng, D., Gu, Z. Y., Li, J. R., Jiang, H. L., Wei, Z. and Zhou, H. C. *Angew. Chem. Int. Ed.*, **2012**, *51*, 10307-10310.
99. Jiang, H.-L., Feng, D., Wang, K., Gu, Z.-Y., Wei, Z., Chen, Y.-P. and Zhou, H.-C. *J. Am. Chem. Soc.*, **2013**, *135*, 13934-13938.
100. Wang, Z., Zhang, J.-H., Jiang, J.-J., Wang, H.-P., Wei, Z.-W., Zhu, X., Pan, M. and Su, C.-Y. *J. Mater. Chem. A*, **2018**, *6*, 17698-17705.
101. Bai, C., Jian, S., Yao, X. and Li, Y. *Catal. Sci. Technol.*, **2014**, *4*, 3261.
102. Gonzalez, M. I., Bloch, E. D., Mason, J. A., Teat, S. J. and Long, J. R. *Inorg. Chem.*, **2015**, *54*, 2995-3005.
103. Huxley, M. T., Coghlan, C. J., Bloch, W. M., Burgun, A., Doonan, C. J. and Sumbly, C. J. *Philos. Trans. Royal Soc. A*, **2017**, *375*, 20160028.
104. Peralta, R. A., Huxley, M. T., Young, R. J., Linder-Patton, O. M., Evans, J. D., Doonan, C. J. and Sumbly, C. J. *Faraday Discuss.*, **2021**, *225*, 84-99.
105. Inokuma, Y., Arai, T. and Fujita, M. *Nat. Chem.*, **2010**, *2*, 780-783.
106. Wada, N., Kersten, R. D., Iwai, T., Lee, S., Sakurai, F., Kikuchi, T., Fujita, D., Fujita, M. and Weng, J.-K. *Angew. Chem. Int. Ed.*, **2018**, *57*, 3671-3675.
107. Mitsuhashi, T., Kikuchi, T., Hoshino, S., Ozeki, M., Awakawa, T., Shi, S.-P., Fujita, M. and Abe, I. *Org. Lett.*, **2018**, *20*, 5606-5609.
108. De Poel, W., Tinnemans, P. T., Duchateau, A. L. L., Honing, M., Rutjes, F. P. J. T., Vlieg, E. and De Gelder, R. *Cryst. Growth Des.*, **2018**, *18*, 126-132.
109. Urban, S., Brkljača, R., Hoshino, M., Lee, S. and Fujita, M. *Angew. Chem. Int. Ed.*, **2016**, *55*, 2678-2682.
110. Kersten, R. D., Lee, S., Fujita, D., Pluskal, T., Kram, S., Smith, J. E., Iwai, T., Noel, J. P., Fujita, M. and Weng, J.-K. *J. Am. Chem. Soc.*, **2017**, *139*, 16838-16844.
111. Zigon, N., Kikuchi, T., Ariyoshi, J., Inokuma, Y. and Fujita, M. *Asian J. Chem.*, **2017**, *12*, 1057-1061.
112. Yoshioka, S., Inokuma, Y., Duplan, V., Dubey, R. and Fujita, M. *J. Am. Chem. Soc.*, **2016**, *138*, 10140-10142.

-
113. Sairenji, S., Kikuchi, T., Abozeid, M. A., Takizawa, S., Sasai, H., Ando, Y., Ohmatsu, K., Ooi, T. and Fujita, M. *Chem. Sci.*, **2017**, *8*, 5132-5136.
114. Yan, K., Dubey, R., Arai, T., Inokuma, Y. and Fujita, M. *J. Am. Chem. Soc.*, **2017**, *139*, 11341-11344.
115. Duplan, V., Hoshino, M., Li, W., Honda, T. and Fujita, M. *Angew. Chem. Int. Ed.*, **2016**, *55*, 4919-4923.
116. Poel, W., Tinnemans, P., Duchateau, A. L. L., Honing, M., Rutjes, F. P. J. T., Vlieg, E. and Gelder, R. *Eur. J. Chem.*, **2019**, *25*, 14999-15003.
117. Albalad, J., Sumbly, C. J., Maspocho, D. and Doonan, C. J. *CrystEngComm*, **2021**, *23*, 2185-2195.
118. Lee, S., Kapustin, E. A. and Yaghi, O. M. *Science*, **2016**, *353*, 808-811.
119. Rowsell, J. L. C., Spencer, E. C., Eckert, J., Howard, J. A. K. and Yaghi, O. M. *Science*, **2005**, *309*, 1350-1354.
120. Carrington, E. J., Vitórica-Yrezábal, I. J. and Brammer, L. *Acta Crystallogr. B: Struct. Sci. Cryst. Eng. Mater.*, **2014**, *70*, 404-422.
121. Miller, R. G., Warren, M. R., Allan, D. R. and Brooker, S. *Inorg. Chem.*, **2020**, *59*, 6376-6381.
122. Gonzalez, M. I., Mason, J. A., Bloch, E. D., Teat, S. J., Gagnon, K. J., Morrison, G. Y., Queen, W. L. and Long, J. R. *Chem. Sci.*, **2017**, *8*, 4387-4398.
123. Cho, H. S., Yang, J., Gong, X., Zhang, Y.-B., Momma, K., Weckhuysen, B. M., Deng, H., Kang, J. K., Yaghi, O. M. and Terasaki, O. *Nat. Chem.*, **2019**, *11*, 562-570.
124. Sung Cho, H., Deng, H., Miyasaka, K., Dong, Z., Cho, M., Neimark, A. V., Ku Kang, J., Yaghi, O. M. and Terasaki, O. *Nature*, **2015**, *527*, 503-507.
125. Marshall, R. J., Griffin, S. L., Wilson, C. and Forgan, R. S. *J. Am. Chem. Soc.*, **2015**, *137*, 9527-9530.
126. Fortea-Perez, F. R., Mon, M., Ferrando-Soria, J., Boronat, M., Leyva-Perez, A., Corma, A., Herrera, J. M., Osadchii, D., Gascon, J., Armentano, D. and Pardo, E. *Nat. Mater.*, **2017**, *16*, 760-766.
127. Mon, M., Rivero-Crespo, M. A., Ferrando-Soria, J., Vidal-Moya, A., Boronat, M., Leyva-Pérez, A., Corma, A., Hernández-Garrido, J. C., López-Haro, M., Calvino, J. J., Ragazzon, G., Credi, A., Armentano, D. and Pardo, E. *Angew. Chem.*, **2018**, *130*, 6294-6299.
128. Rivero-Crespo, M. A., Mon, M., Ferrando-Soria, J., Lopes, C. W., Boronat, M., Leyva-Pérez, A., Corma, A., Hernández-Garrido, J. C., López-Haro, M., Calvino, J. J.,
-

- Ramos-Fernandez, E. V., Armentano, D. and Pardo, E. *Angew. Chem. Int. Ed.*, **2018**, *57*, 17094-17099.
129. Adam, R., Mon, M., Greco, R., Kalinke, L. H. G., Vidal-Moya, A., Fernandez, A., Winpenny, R. E. P., Doménech-Carbó, A., Leyva-Pérez, A., Armentano, D., Pardo, E. and Ferrando-Soria, J. *J. Am. Chem. Soc.*, **2019**, *141*, 10350-10360.
130. Tiburcio, E., Zheng, Y., Mon, M., Martin, N., Ferrando Soria, J., Armentano, D., Leyva Perez, A. and Pardo, E. *Inorg. Chem.*, **2022**, *61*, 11796-11802.
131. Bloch, W. M., Burgun, A., Coghlan, C. J., Lee, R., Coote, M. L., Doonan, C. J. and Sumbly, C. J. *Nat. Chem.*, **2014**, *6*, 906-912.
132. Bloch, W. M., Burgun, A., Doonan, C. J. and Sumbly, C. J. *Chem. Commun.*, **2015**, *51*, 5486-5489.
133. Peralta, R. A., Huxley, M. T., Evans, J. D., Fallon, T., Cao, H., He, M., Zhao, X. S., Agnoli, S., Sumbly, C. J. and Doonan, C. J. *J. Am. Chem. Soc.*, **2020**, *142*, 13533-13543.
134. Burgun, A., Coghlan, C. J., Huang, D. M., Chen, W., Horike, S., Kitagawa, S., Alvino, J. F., Metha, G. F., Sumbly, C. J. and Doonan, C. J. *Angew. Chem. Int. Ed.*, **2017**, *56*, 8412-8416.
135. Huxley, M. T., Burgun, A., Ghodrati, H., Coghlan, C. J., Lemieux, A., Champness, N. R., Huang, D. M., Doonan, C. J. and Sumbly, C. J. *J. Am. Chem. Soc.*, **2018**, *140*, 6416-6425.

CHAPTER 2: Templated
synthesis of zirconium(IV)-
based metal-organic layers
(MOLs) with accessible
chelating sites

Templated synthesis of zirconium(IV)-based metal-organic layers (MOLs) with accessible chelating sites

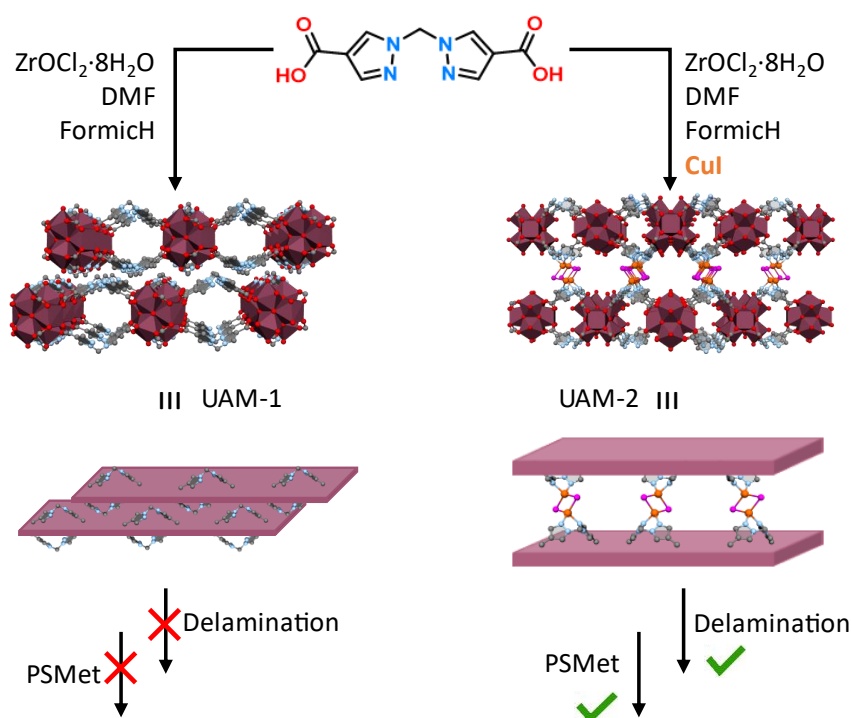
Pol Gimeno-Fonquernie,^a Weibin Liang,^{a†} Jorge Albalad,^a Andrew Kuznicki,^c Jason R. Price,^b Eric D. Bloch,^c Christian J. Doonan^{a*} and Christopher J. Sumbly^{a*}

^a Centre for Advanced Nanomaterials and Department of Chemistry, The University of Adelaide, Adelaide, SA 5000, Australia.
Email: christian.doonan@adelaide.edu.au; christopher.sumbly@adelaide.edu.au

^b ANSTO Melbourne, The Australian Synchrotron, 800 Blackburn Rd, Clayton, Vic 3168, Australia.

^c Department of Chemistry & Biochemistry, University of Delaware, Newark, DE 19716, USA

[†]Current address: School of Chemical and Biomolecular Engineering, Sydney Nano Institute, The University of Sydney, New South Wales, 2006, Australia.



2.1. Statement of authorship

Statement of Authorship

Title of Paper	Templated synthesis of zirconium(IV)-based metal-organic layers (MOLs) with accessible chelating sites		
Publication Status	<input checked="" type="checkbox"/> Published	<input type="checkbox"/> Accepted for Publication	
	<input type="checkbox"/> Submitted for Publication	<input type="checkbox"/> Unpublished and Unsubmitted work written in manuscript style	
Publication Details	Gimeno-Fonquernie, P., Liang, W., Albalad, J., Kuznicki, A., Price, J. R., Bloch, E. D., Doonan, C. J. and Sumby, C. J. <i>Chem. Commun.</i> , 2022, 58, 957-960.		

Principal Author

Name of Principal Author (Candidate)	Pol Gimeno I Fonquernie		
Contribution to the Paper	Design and development of the project. Preparation of samples and data collection. Analysis and interpretation of X-ray crystallography data and SEM-EDX data. Preparation, drafting and final version of manuscript.		
Overall percentage (%)	70%		
Certification:	This paper reports on original research I conducted during the period of my Higher Degree by Research candidature and is not subject to any obligations or contractual agreements with a third party that would constrain its inclusion in this thesis. I am the primary author of this paper.		
Signature		Date	10 - 07 - 2023

Co-Author Contributions

By signing the Statement of Authorship, each author certifies that:

- i. the candidate's stated contribution to the publication is accurate (as detailed above);
- ii. permission is granted for the candidate to include the publication in the thesis; and
- iii. the sum of all co-author contributions is equal to 100% less the candidate's stated contribution.

Name of Co-Author	Weibin Liang		
Contribution to the Paper	Assisted with preparation of preliminary data and data collection.		
Signature		Date	11 July 2023

Name of Co-Author	Jorge Albalad		
Contribution to the Paper	Assisted with conception of the project and drafting of the manuscript.		
Signature		Date	11/7/2023

Please cut and paste additional c

Name of Co-Author	Andrew Kuznicki		
Contribution to the Paper	Assisted with preparation of preliminary data and data collection.		
Signature			12JUL2023

Name of Co-Author	Jason R. Price		
Contribution to the Paper	Assisted with collection, analysis and interpretation of X-ray crystallography data.		
Signature			15/8/2023

Name of Co-Author	Eric D. Bloch		
Contribution to the Paper	Assisted with conception of the project and drafting of the manuscript.		
Signature			2 Aug 2023

Name of Co-Author	Christian J. Doonan		
Contribution to the Paper	Assisted with conception of the project, experiment design and drafting of the manuscript.		
Signature			31/7/2023

Name of Co-Author	Christopher J. Sumbly		
Contribution to the Paper	Assisted with conception of the project experiment design, drafting of the manuscript and analysis of X-ray crystallography data.		
Signature			24/7/2023

2.2. Introduction

The study of metal-organic frameworks (MOFs) has provided insight into gas adsorption and catalytic processes in solid-state materials,^{1, 2} paving the way for applications in gas storage,^{3, 4} molecular separations,⁵ and in heterogeneous catalysis.⁶⁻⁸ Amongst a wide range of MOF materials that can be prepared through the reticular molecular building block (MBB) approach,⁹⁻¹¹ zirconium(IV)-based MOFs have attracted significant attention as strong Zr-O bonds, coupled with their highly-connected metal nodes, have engendered materials with chemically and thermally stable structures.¹² Many of these robust materials, such as UiO-6x (x = 6, 7, and 8),¹³ NU-1000,¹⁴ and PCN-22x (x = 2, 3, and 4),^{15, 16} are typically prepared from relatively rigid, planar ligands. The robust platform provided by these Zr-based MOFs has enabled post-synthetic metalation (PSMet) of non-coordinated donor groups, such as porphyrin moieties,¹⁵ within the linker backbone, and grafting of reactive metal species to their framework structures.^{16, 17} The intrinsic stability of Zr-based MOFs has also facilitated the synthesis of robust metal-organic layers (MOLs) that can be pillared to generate size-selective catalytic materials with controlled layer-layer distances,¹⁸ or exfoliated to form colloiddally stable nanosheets.¹⁹

In contrast to this wide body of work with rigid linkers, the synthesis of Zr-based MOFs from flexible ligands is beset by challenges that often preclude formation of crystalline materials.²⁰⁻²² Limiting the conformational freedom of a dicarboxylate linker, by introducing conjugation or inhibiting torsional rotation, is a strategy that has been used to facilitate the formation of MOFs with zirconium(IV) oxo-clusters.¹¹ For linkers possessing internal coordinating groups, the challenge of synthesising Zr-based MOFs from flexible linkers can be overcome by employing a metal ion to pre-organise and rigidify the linker.²³ As an example, a scorpionate linker was preorganised by the use of a secondary Cu(I) metal source,²³ which was subsequently removed with an acid treatment to allow the resulting material to undergo PSMet.

Herein, we use a templating approach to synthesise stable Zr-based MOLs with accessible chelating sites. In this case, the formation of a Cu(I) dimer controls the formation of the Zr-based MOLs with preorganised bis-pyrazole units (Figure 2.1). Synthesis without the structure-directing copper(I) iodide gives a close-packed layered material with an 'anti'-arrangement between the pyrazole donors (University of Adelaide Material-1, UAM-1, $[\text{Zr}_6\text{O}_4(\text{OH})_4(\text{HCOO})_4(\text{L})_4]$, where L = bis(4-carboxypyrazol-1-yl)methane), whereas addition of copper(I) iodide gives rise to a pre-organised 'syn'-

arrangement of the pyrazole moieties that yields a layered MOF pillared by CuI dimers, UAM-2, $[\text{Zr}_6\text{O}_4(\text{OH})_4(\text{HCOO})_4(\text{L})_4(\text{CuI})_4]$. These dimers form a ‘weak-link’ that can be readily displaced with mild acid solutions to provide efficient delamination. The resulting polydisperse nanosheets are stable and can undergo quantitative PSMet.

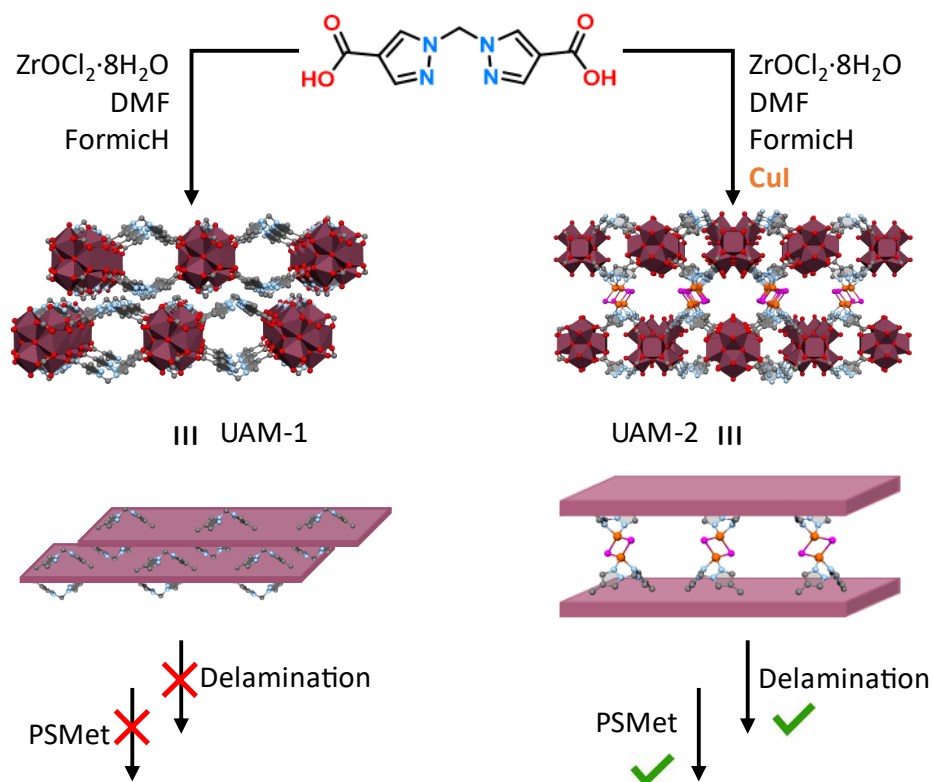


Figure 2.1. Non-templated and templated synthesis of Zr-based MOFs, showing the resulting structures and schematic representations. In the absence of templating metal ions (left), the bis-pyrazole groups of the linker adopt an ‘anti’ conformation, resulting in a dense, efficiently packed 2D-MOL (UAM-1). In the presence of templating copper(I) iodide (right), the bis-pyrazole moieties are preorganised into a ‘syn’ conformation that renders the layers part of a 3D-MOF structure bridged by “weak link” Cu_2I_2 pillaring clusters (UAM-2). Only UAM-2 can be delaminated and post-synthetically metalated.

2.3. Experimental Section

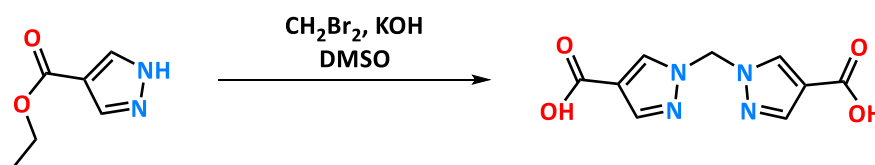
2.3.1. Materials and Methods

Unless otherwise stated, all chemicals were obtained from commercial sources and used as received. Acetonitrile (MeCN) was dried from CaH₂ under N₂ and degassed with Ar prior to use. The chemicals CuI, CuCl₂ anhydrous, CoCl₂ anhydrous, ZrOCl₂·8H₂O and PdCl₂ were obtained from commercial sources and used without further purification.

PXRD data were collected on a Bruker Advanced D8 diffractometer (capillary stage) using Cu K α radiation ($\lambda = 1.5456 \text{ \AA}$, 40 kW/40 mA, $2\theta = 2\text{--}52.94^\circ$, φ rotation = 20 rotations/min, at 1 s exposure per step with 5001 steps, and using 0.8 mm glass capillaries). FTIR spectra were collected on a Shimadzu IR spirit using ATR mode. Nuclear Magnetic Resonance (NMR) spectra were collected on a Agilent DD2 500 MHz NMR with a 5mm OneNMR probe. Solid samples were digested in NaOD/D₂O at 80 °C. SEM images were collected and EDX analysis performed on a FEI Quanta 450 field-emission scanning electron microscope. TEM images were performed on a Tecnai G2 Spirit 120 kV. Gas adsorption measurements were performed on a Micromeritics 3-Flex surface area and pore size analyser. Activation of samples was carried out as described in the captions to Figure I.9 and Figure I.11. Geometric surface area was calculated in Materials Studio using the accessible solvent surface @1.84 Å.

2.3.2. Synthetic protocols

2.3.2.1. Synthesis of 1,1'-methylenebis(1H-pyrazole-4-carboxylic acid) (H₂L)



Ethyl 1H-pyrazole-4-carboxylate (5.2 g, 0.037 mmol) and finely powdered potassium hydroxide (8.25 g, 0.147 mmol) were dissolved in 30 mL of DMSO, and the resulting solution was stirred for 1 h at 60 °C. After that, a solution of dibromomethane (1.3 mL, 0.019 mmol) in 10 mL of DMSO was added dropwise before being left to stir overnight at 60 °C. The solution was then poured into 200 mL of distilled water and was washed with chloroform (5 x 30 mL), and the combined organic phases were discarded. The aqueous phase was then acidified to pH= 3 with a 4 M HCl solution to precipitate H₂L as a white solid, washed with water (2 x 50 mL), and dried under vacuum for 24 h. Yield: 4.2 g (94%). FTIR ν_{\max} (Nujol, cm⁻¹): 1670, 1565, 1421, 1367,

1245; ^1H NMR (500 MHz, $\text{DMSO-}d_6$): 12.49 (s, 2H, COOH), 8.50 (s, 2H, CH_2 pyrazole), 7.84 (s, 2H, CH_2 pyrazole), 6.46 (s, 2H, N- CH_2 -N).

Note that a similar procedure has recently been reported by N. P. Burlutskiy et al.²⁴

2.3.2.2. Synthesis of UAM-1

A solution of $\text{ZrOCl}_2 \cdot 8\text{H}_2\text{O}$ (32 mg, 0.10 mmol) and formic acid (0.6 mL, 15.90 mmol, 171 mol. eq.) in 1 mL of DMF was sonicated for 30 min. Separately, H_2L (25 mg, 0.11 mmol) was dissolved in 0.9 mL of DMF and sonicated until solution. Then, the ligand solution was added to the metal precursor one, and the resulting mixture was transferred to a solvothermal scintillation vial and heated at 120 °C for 48 h. Single-crystals of UAM-1 were separated by filtration and washed with DMF (4 x 5 mL), acetone (3 x 5 mL), and dried under vacuum for 24 h.

2.3.2.3. Synthesis of UAM-2

$\text{ZrOCl}_2 \cdot 8\text{H}_2\text{O}$ (25 mg, 0.08 mmol), H_2L (25 mg, 0.11 mmol) and CuI (25 mg, 0.13 mmol) were dissolved in 1.5 mL of DMF and sonicated for 30 min. Formic acid (0.8 mL, 21.10 mmol, 273 mol. eq.) was then added to the solution, and the resulting mixture was transferred to a solvothermal scintillation vial and heated at 120 °C for 48 h. Microcrystalline UAM-2 was collected by filtration and washed with DMF (4 x 5 mL), acetone (3 x 5 mL) and dried under vacuum for 24 h.

To obtain single crystals suitable for X-ray crystallography, the procedure was slightly modified as follows. The same quantities of reagents and solvent were thoroughly mixed, transferred to a non-solvothermal vial (with pressure regulation), and heated at 140 °C for 48 h. Single crystals of UAM-2 were collected by filtration, and washed with DMF (3 x 5 mL).

2.3.2.4. Synthesis of UAM-2·HCl

UAM-2 (50 mg, 0.025 mmol) was soaked in a 5 mL stock solution of HCl in DMF (1.3 mL 4 M HCl in 29.7 mL DMF) and heated to 60 °C for 48 h to induce the acid-triggered chemical delamination of the sample. UAM-2·HCl was then collected by centrifugation and thoroughly washed with DMF (4 x 5 mL). For characterisation, the sample was washed with acetone (3 x 5 mL) and dried under reduced pressure overnight.

2.3.2.5. Synthesis of UAM-2·ns

UAM-2·HCl (50 mg, 0.026 mmol) was neutralised with a 0.05 M ammonium formate solution in MeOH (5 x 5 mL). The solution was left to stand at room temperature for 16 h and the supernatant was exchanged with fresh DMF twice over 24 h.

2.3.2.6. General protocol for the post-synthetic metalation of UAM-1 and UAM-2

The different phases of UAM-1 or UAM-2-ns (50 mg, 0.028 mmol) were soaked in 3 mL of dry acetonitrile. An excess of metal salt (~20 mg of PdCl₂, CuCl₂, or CoCl₂) was added, and the solution was heated to 60 °C for 2 h, 5 h or 24 h. The sample was then washed by decantation with dry acetonitrile (4 x 4 mL).

2.3.3. **Single crystal X-ray crystallography**

2.3.3.1. General procedures

Single crystals were mounted in Paratone-N oil on a MiTeGen micromount. Single-crystal X-ray data were typically collected at 100 K on the MX1 or MX2 beamlines of the Australian Synchrotron using the Blue-ice software interface,²⁵ $\lambda = 0.71073 \text{ \AA}$ (0.6888 Å in the case of the provided structure of UAM-1). Absorption corrections were applied using multiscan methods using XDS,^{26, 27} the structures solved using SHELXS or SHELXT,^{28, 29} and refined by full-matrix least squares on F² by SHELXL,³⁰ interfaced through the program X-Seed or OLEX.^{31, 32} In general, all atoms were refined anisotropically and hydrogens atoms were included as invariants at geometrically estimated positions, unless specified otherwise in additional details in supporting information. Where noted, the data was treated with the SQUEEZE routine available in Platon³³ or using the solvent masking feature of Olex. Figures were produced using the software Diamond. X-ray experimental data is given in Table I.5. CIF data have been deposited with the Cambridge Crystallographic Data Centre, CCDC reference numbers CCDC 2119441 and 2119442.

2.3.3.2. Specific Data and Refinement Details

UAM-1. There was significant ambiguity in the correct unit cell and symmetry (Bravais lattice and space group) needed to solve the structure of UAM-1. Many data collections and structure solutions were tried but significant residual electron density remained around the Zr atoms of the Zr-oxo cluster. This residual electron density was consistent with the structure being disordered but, despite recognising this, it remained difficult to get a chemical sensible model of the structure in the space groups identified. To identify the correct symmetry, we collected data at energies around the Zr adsorption edge (which is close to the standard Mo K α wavelength). Using this data, which was collected in low angle and high angle runs before being merged (using corrected scattering factors), we were able to identify an orthorhombic *Amm*2 space group. Structure solution and close examination of the layer structure of the well resolved layer allowed

us to identify to distinct positions of the second layer, which were refined with a 50:50 disorder model using a TWIN refinement (TWIN law -1 0 0 0 -1 0 0 0 -1).

Refinement of a sensible structural model required the use of SIMU/RIGU commands for the Zr-oxo cluster of the disordered layer, and the associated linker pyrazole rings. The pyrazole rings of L are all anti in the structure, and this gives 4-connected layers with a spacing of the Zr-oxo clusters consistent with the primary layer. A significant number of DFIX restraints were used to maintain chemically sensible bond lengths and angles for the pyrazole carboxylates and a disordered formate anion (50:50 disorder). A DMF solvate molecule was refined with isotropic displacement parameters. A solvent mask was calculated and 498 electrons were found in a volume of 3022 Å³ in 1 void per unit cell. This is consistent with the presence of 1.5[C₃H₇NO] (DMF) per Asymmetric Unit which account for 480 electrons per unit cell.

UAM-2. Due to the high symmetry structure the exact formulation of the Zr-oxo cluster cannot be determined (OH and O groups occupy the same positions) and the formate modulators, that were identified by digestion of the sample and NMR spectroscopy, cannot be located. Additionally, a highly disordered Zr formate cluster was identified in the structure of crystals of UAM-2 made via the second procedure (bulk crystals made by the primary procedure do not have the second cluster that stabilises the growth of larger single crystals). A solvent mask was calculated and 4310 electrons were found in a volume of 807 Å³ in 1 void per unit cell. This is consistent with the presence of 1[Zr₆C₁₂H₁₆O₃₂] (a disordered Zr formate cluster) per Unit Cell which account for 4672 electrons per unit cell.

2.4. Results and discussion

Despite having flexibility conferred by an sp^3 methylene spacer, the linker H_2L undergoes reaction with $ZrOCl_2 \cdot 8H_2O$ in DMF, using formic acid as a modulator, to afford colourless cubic crystals of UAM-1 (Figure I.1a). The resulting crystals were suitable for single crystal X-ray diffraction (SCXRD), which revealed a layered structure composed of Zr_6 secondary building units (SBUs) bound to eight bridging L linkers and four formate modulating agents that complete the coordination sphere around the clusters.³⁴ NMR data of UAM-1 digested with NaOD/ D_2O quantitatively proved the presence of these formate modulators in the SBU (Figure I.2). The angular shape of the linker extends the MOL along the bc crystallographic plane, undulating about the plane of the Zr_6 SBUs to form a corrugated 4-connected layer (Figure 2.2a). An absence of strong directional interactions perpendicular to the layers means that the B layer is disordered over two sites and the interlayer packing is dominated by π - π interactions between the aromatic pyrazole rings of vicinal linkers (oriented 'anti' to maximize the interactions, Figure I.3 and Figure I.4). The phase purity of UAM-1 was confirmed by powder X-ray diffraction (PXRD) (Figure 2.2d).

Having previously demonstrated the importance of a pre-organised metal binding site for PSMet in MOFs,³⁵⁻³⁷ we introduced a templating agent during the synthesis to pre-orientate the pyrazole groups in L into a 'syn' disposition. Reaction of H_2L and $ZrOCl_2 \cdot 8H_2O$ in DMF, again using formic acid as a modulator, but in the presence of copper(I) iodide, afforded cubic, pale-yellow coloured crystals (Figure I.5) of UAM-2. SCXRD revealed UAM-2 to have a 3D structure wherein the Zr-based SBUs share eight linkers that are in turn bridged by Cu_2I_2 clusters (Figure 2.2b). Like UAM-1, the angular linkers form a four-connected 2D network extending alternately above and below the plane containing the Zr-SBUs. However, in this case, the Cu_2I_2 clusters (Cu-I distances: 2.553 and 2.693 Å; Cu-I-Cu 56.21°) force a 'syn' arrangement of the bis-pyrazole moieties, which connects the MOLs into a 3D MOF network. Phase purity for UAM-2 was confirmed by PXRD (Figure 2.2d), Energy Dispersive X-ray (EDX) data was consistent with a quantitative CuI incorporation at the bis-pyrazole sites (Cu:Zr ratio 2:3) (Table I.1), and 1H -NMR digestions showed formate modulators saturate the Zr-SBU (Figure I.6).

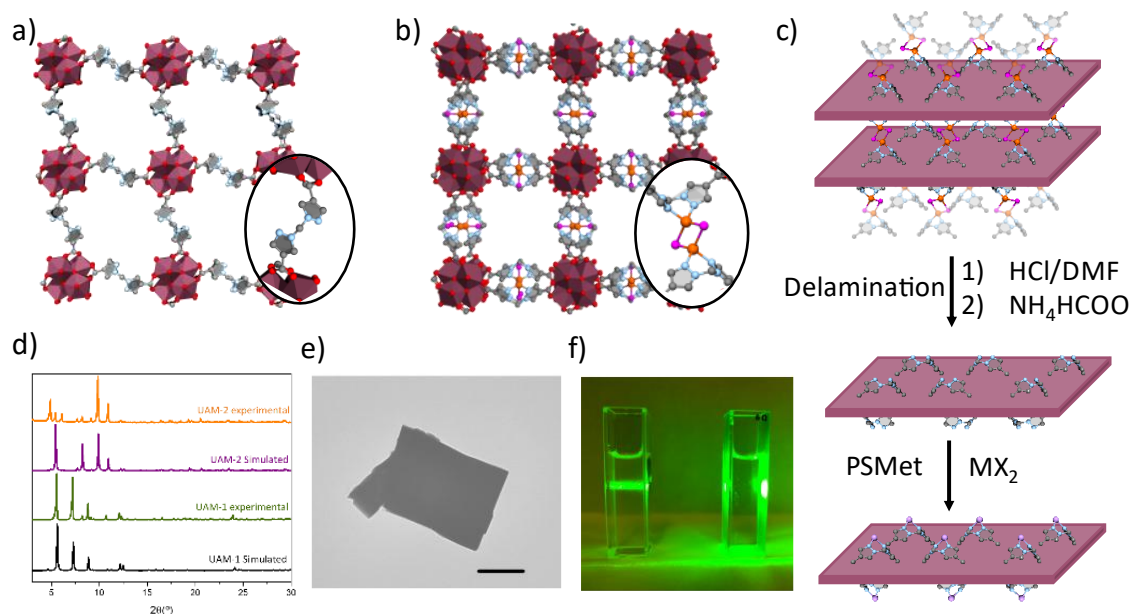


Figure 2.2. a) A view of one of the layers in UAM-1 (in the bc plane) with an inset showing the ‘anti’ disposition of the bis-pyrazole groups. b) A view of the related layers in UAM-2 (in the ab plane) with an inset showing the ‘syn’ disposition of the bis-pyrazole groups and the linking CuI dimers. c) A scheme showing the processing to achieve UAM-2 delamination and post-synthetic metalation. d) PXRD data for UAM-1 simulated (black), UAM-1 experimental (green), UAM-2 simulated (purple) and UAM-2 experimental (orange). e) TEM image of UAM-2·ns (scale bar size $1 \mu\text{m}$). f) UAM-2·ns (left) and UAM-1·us (right) dispersions in ethanol showing the Tyndall effect upon laser irradiation for UAM-2·ns.

The packing of MOLs within UAM-1 and UAM-2 is very different, providing distinct pore networks and chemical and physical properties. Thermogravimetric analysis (TGA) data of both materials showed a steady mass loss that we attributed to trapped solvent that cannot be removed under vacuum, as evidenced by the ^1H NMR analysis of digested UAM-2 that shows the presence of DMF (Figure I.6). UAM-1 possesses comparatively higher thermal stability, with a decomposition step at $375 \text{ }^\circ\text{C}$ (Figure I.7), whereas UAM-2 undergoes a two-step decomposition that commences at $250 \text{ }^\circ\text{C}$, attributable to the Cu_2I_2 pillars in the structure (Figure I.8). The corrugated shape of the MOLs in UAM-1 leads to a close-packed structure along the a axis, with distinct channels (9.7 by 3.8 \AA) perpendicular to the layers. A 77 K N_2 isotherm measured on a UAM-1 sample activated from methanol (MeOH) demonstrated that the material is permanently porous (experimental $S_{\text{BET}} = 417 \text{ m}^2/\text{g}$; predicted geometric $S_{\text{BET}} = 637 \text{ m}^2/\text{g}$) (Figure I.9). In contrast, the 3D connectivity and the additional spacing between the layers in UAM-2, implies a greater pore volume and surface area (predicted geometric $S_{\text{BET}} = 1792 \text{ m}^2/\text{g}$). However, as shown by the TGA data, the CuI bridges are not stable to solvent removal, leading to a partial delamination of UAM-2 evidenced by PXRD (Figure I.10). Consequently, experimental 77 K N_2 adsorption

isotherms of UAM-2 were significantly lower, with experimental $S_{\text{BET}} = 341 \text{ m}^2/\text{g}$ (Figure I.11).

Both UAM-1 and UAM-2 possess a bis(pyrazolyl)methane moiety, known to undergo facile and quantitative post-synthetic metalation.^{38, 39} Due to the close-packed nature of UAM-1, particularly around the π -stacked bis-pyrazole sites, we anticipated that the accessibility to the chelating sites would be limited. Indeed, the post-synthetic metalation (PSMet) of bulk UAM-1 was unsuccessful, as confirmed by EDX analysis of the material after metalation (Table I.2). Given that layered MOFs, especially those packed through van der Waals or π -stacking interactions, can be readily exfoliated,⁴⁰⁻⁴⁴ we turned our attention to mechanical and chemical methods to form MOLs that could make the pyrazole sites on the linkers accessible. Despite only possessing interlayer π -stacking, UAM-1 resisted chemical (dilute acid treatment at 65 °C for 48 h) and mechanical (ultrasonication for 2 h) delamination in multiple solvents, as evidenced by PXRD and Scanning Electron Microscopy (SEM) (Figure I.12, Figure I.1b). After both treatments, the crystals still showed a well-defined polyhedral shape, rather than the expected formation of a lamellar dispersion. Furthermore, the PXRD patterns for UAM-1 after ultrasonication (UAM-1·us) and treatment with acid and base (UAM-1·abt) did not show significant changes compared to the pristine material. As a result, PSMet of these samples was again unsuccessful, as evidenced by EDX analysis (Table I.3).

Based on previous work,²³ we anticipated that the Cu_2I_2 clusters that bridge the MOLs comprising UAM-2 could also serve as exfoliation points and generate vacant coordination sites, since the Cu-I and Cu-N bonds are significantly weaker than the Zr-O bonds of the framework. Indeed, these Cu_2I_2 clusters show visible signs of decomposition when as-synthesised, pale-yellow crystals of UAM-2 develop a blue colouration (presumably due to oxidation to Cu(II) upon immersion in wet DMF for 10 minutes). This observation motivated us to pursue a combined demetalation and delamination strategy for UAM-2 that could overcome the limitations observed in UAM-1 and unveil a pre-organised, 'syn' arrangement of the bis-pyrazole site (Figure 2.2c). Crystals of UAM-2 were soaked in a dilute HCl solution (0.05 M) in DMF at 65 °C for 48 h to afford the delaminated product UAM-2·HCl as a dispersion that displayed the characteristic Tyndall effect when irradiated with a visible laser beam (Figure 2.2f, Figure I.13a-b). EDX analysis of the sample confirmed that all the bis-pyrazole sites were fully demetalated, as no residual Cu or I signals were detected (Table I.1). Instead, EDX analysis of UAM-2·HCl revealed the

presence of chloride anions in an *ca.* 3:2 Zr:Cl ratio, which is consistent with the protonation of the pyrazole groups. Potential loss of the formate anions was dismissed, as digestion $^1\text{H-NMR}$ analysis shows quantitative retention at the Zr-O cluster (Figure I.14). Next, UAM-2·HCl was washed with an ammonium formate solution in methanol (0.05 M) that afforded the deprotonation of the coordinative bis-pyrazolate moieties within the structure. The effectiveness of this strategy was demonstrated by a quantitative loss of the chloride EDX signal (Table I.3) for neutralised UAM-2 nanosheets (UAM-2·ns).

To provide evidence for the formation of UAM-2 nanosheets, we carried out Transmission Electron Microscopy (TEM) (Figure 2.2e, Figure I.13c) imaging of the supernatant, which showed the formation of well-defined layers. Remarkably, UAM-2·ns still showed some long-range order, as shown by selected area electron diffraction analysis (Figure I.13d). However, random orientation and inefficient packing of the dry bulk sample led to the material being amorphous, as shown by PXRD (Figure I.10) and non-porous (Figure I.15). After successfully affording quantitative delamination of UAM-2, presumably now with 'syn' oriented bis-pyrazole sites (locked by the Zr-O coordination), we revisited PSMet, which we anticipated would be more facile for UAM-2·ns. Indeed, following brief sonication of UAM-2·ns in acetonitrile to achieve a good dispersion, we achieved a quantitative metalation (Table I.4) of the MOLs with CoCl_2 , CuCl_2 and PdCl_2 under the same conditions employed for UAM-1 (heating for 2 h at 65 °C). The PSMet process was quantified by EDX analysis of the dispersed samples, indicating a 100% bis-pyrazole site occupancy (based on Zr:L:M ratio) for all the metal salts after just 2 hours of incubation time. The degree of metalation remained constant in further tests, after 5 h and 24 h, suggesting that cation exchange at the Zr-based SBUs did not occur under these conditions.

2.5. Conclusions

In summary, a combined templating and chemical delamination strategy to prepare MOF nanosheets that can be post-synthetically metalated has been presented. A new 3D MOF UAM-2, comprised of Zr-based layers, was synthesised by pre-organising the bis-pyrazole groups of the organic linker into a 'syn' conformation using CuI. The Cu₂I₂ clusters that pillar the layers could be quantitatively removed with an acid-base treatment, leading to delamination of the MOLs, and the bis-pyrazole sites in the exposed layers could be post-synthetically metalated with CoCl₂, CuCl₂ and PdCl₂, as evidenced by TEM, PXRD and EDX. The synthesis of a MOF in the absence of templating CuI gave another layered material, UAM-1, where the bis-pyrazole groups were oriented in an 'anti' conformation and extensive π -stacking prevented exfoliation. The templating synthetic approach, allied with chemical delamination has been shown to be a useful approach to form MOL nanosheets. Importantly, the strategy provides chemical control over the delamination process without subjecting the material to significant mechanical stress. Additionally, this delamination process yields coordinating groups poised for PSMet reactions, thus providing opportunities for exploring separations and catalysis.

2.6. References

1. Easun, T. L., Moreau, F., Yan, Y., Yang, S. and Schröder, M. *Chem. Soc. Rev.*, **2017**, *46*, 239-274.
2. Young, R. J., Huxley, M. T., Pardo, E., Champness, N. R., Sumbly, C. J. and Doonan, C. *J. Chem. Sci.*, **2020**, *11*, 4031-4050.
3. Mason, J. A., Veenstra, M. and Long, J. R. *Chem. Sci.*, **2014**, *5*, 32-51.
4. Li, H., Wang, K., Sun, Y., Lollar, C. T., Li, J. and Zhou, H.-C. *Mater. Today*, **2018**, *21*, 108-121.
5. Qian, Q., Asinger, P. A., Lee, M. J., Han, G., Mizrahi Rodriguez, K., Lin, S., Benedetti, F. M., Wu, A. X., Chi, W. S. and Smith, Z. P. *Chem. Rev.*, **2020**, *120*, 8161-8266.
6. Yang, D. and Gates, B. C. *ACS Catal.*, **2019**, *9*, 1779-1798.
7. Wasson, M. C., Buru, C. T., Chen, Z. J., Islamoglu, T. and Farha, O. K. *Appl. Catal. A: Gen.*, **2019**, *586*, 117214.
8. Wei, Y. S., Zhang, M., Zou, R. and Xu, Q. *Chem. Rev.*, **2020**, *120*, 12089-12174.
9. Kalmutzki, M. J., Hanikel, N. and Yaghi, O. M. *Sci. Adv.*, **2018**, *4*, eaat9180.
10. Yaghi, O. M., O'Keeffe, M., Ockwig, N. W., Chae, H. K., Eddaoudi, M. and Kim, J. *Nature*, **2003**, *423*, 705-714.
11. Chen, Z., Hanna, S. L., Redfern, L. R., Alezi, D., Islamoglu, T. and Farha, O. K. *Coord. Chem. Rev.*, **2019**, *386*, 32-49.
12. Bai, Y., Dou, Y., Xie, L. H., Rutledge, W., Li, J. R. and Zhou, H. C. *Chem. Soc. Rev.*, **2016**, *45*, 2327-2367.
13. Cavka, J. H., Jakobsen, S., Olsbye, U., Guillou, N., Lamberti, C., Bordiga, S. and Lillerud, K. P. *J. Am. Chem. Soc.*, **2008**, *130*, 13850-13851.
14. Mondloch, J. E., Bury, W., Fairen-Jimenez, D., Kwon, S., Demarco, E. J., Weston, M. H., Sarjeant, A. A., Nguyen, S. T., Stair, P. C., Snurr, R. Q., Farha, O. K. and Hupp, J. T. *J. Am. Chem. Soc.*, **2013**, *135*, 10294-10297.
15. Morris, W., Voloskiy, B., Demir, S., Gándara, F., McGrier, P. L., Furukawa, H., Cascio, D., Stoddart, J. F. and Yaghi, O. M. *Inorg. Chem.*, **2012**, *51*, 6443-6445.
16. Feng, D., Gu, Z. Y., Li, J. R., Jiang, H. L., Wei, Z. and Zhou, H. C. *Angew. Chem. Int. Ed.*, **2012**, *51*, 10307-10310.
17. Gonzalez, M. I., Bloch, E. D., Mason, J. A., Teat, S. J. and Long, J. R. *Inorg. Chem.*, **2015**, *54*, 2995-3005.

18. Qiao, G.-Y., Yuan, S., Pang, J., Rao, H., Lollar, C. T., Dang, D., Qin, J.-S., Zhou, H.-C. and Yu, J. *Angew. Chem. Int. Ed.*, **2020**, *59*, 18224-18228.
19. Leubner, S., Bengtsson, V. E. G., Synnatschke, K., Gosch, J., Koch, A., Reinsch, H., Xu, H., Backes, C., Zou, X. and Stock, N. *J. Am. Chem. Soc.*, **2020**, *142*, 15995-16000.
20. Furukawa, H., Gándara, F., Zhang, Y.-B., Jiang, J., Queen, W. L., Hudson, M. R. and Yaghi, O. M. *J. Am. Chem. Soc.*, **2014**, *136*, 4369-4381.
21. Wißmann, G., Schaate, A., Lilienthal, S., Bremer, I., Schneider, A. M. and Behrens, P. *Microporous Mesoporous Mater.*, **2012**, *152*, 64-70.
22. Schulz, M., Gehl, A., Schlenkrich, J., Schulze, H. A., Zimmermann, S. and Schaate, A. *Angew. Chem. Int. Ed.*, **2018**, *57*, 12961-12965.
23. Sun, C., Skorupskii, G., Dou, J. H., Wright, A. M. and Dinca, M. *J. Am. Chem. Soc.*, **2018**, *140*, 17394-17398.
24. Burlutskiy, N. P. and Potapov, A. S. *Molecules*, **2021**, *26*, 413.
25. McPhillips, T. M., McPhillips, S. E., Chiu, H. J., Cohen, A. E., Deacon, A. M., Ellis, P. J., Garman, E., Gonzalez, A., Sauter, N. K., Phizackerley, R. P., Soltis, S. M. and Kuhn, P. J. *Synchrotron Radiat.*, **2002**, *9*, 401-406.
26. Cowieson, N. P., Aragao, D., Clift, M., Ericsson, D. J., Gee, C., Harrop, S. J., Mudie, N., Panjikar, S., Price, J. R., Riboldi-Tunnicliffe, A., Williamson, R. and Caradoc-Davies, T. J. *Synchrotron Radiat.*, **2015**, *22*, 187-190.
27. Aragao, D., Aishima, J., Cherukuvada, H., Clarken, R., Clift, M., Cowieson, N. P., Ericsson, D. J., Gee, C. L., Macedo, S., Mudie, N., Panjikar, S., Price, J. R., Riboldi-Tunnicliffe, A., Rostan, R., Williamson, R. and Caradoc-Davies, T. T. *J. Synchrotron Radiat.*, **2018**, *25*, 885-891.
28. Sheldrick, G. M. *Acta Crystallogr. Sect. A: Found. Crystallogr.*, **2008**, *64*, 112-122.
29. Sheldrick, G. M. *Acta Crystallogr. Sect. A: Found. Crystallogr.*, **2015**, *71*, 3-8.
30. Sheldrick, G. M. *Acta Crystallogr. Sect. C: Cryst. Struct. Commun.*, **2015**, *71*, 3-8.
31. Barbour, L. J. *Supramol. Chem.*, **2001**, *1*, 189-191.
32. Dolomanov, O. V., Bourhis, L. J., Gildea, R. J., Howard, J. A. K. and Puschmann, H. J. *Appl. Crystallogr.*, **2009**, *42*, 339-341.
33. Spek, A. L. *Acta Crystallogr. C*, **2015**, *71*, 9-18.
34. Wei, R., Gaggioli, C. A., Li, G., Islamoglu, T., Zhang, Z., Yu, P., Farha, O. K., Cramer, C. J., Gagliardi, L., Yang, D. and Gates, B. C. *Chem. Mater.*, **2019**, *31*, 1655-1663.
35. Bloch, W. M., Burgun, A., Coghlan, C. J., Lee, R., Coote, M. L., Doonan, C. J. and Sumbly, C. J. *Nat. Chem.*, **2014**, *6*, 906-912.

-
36. Burgun, A., Coghlan, C. J., Huang, D. M., Chen, W., Horike, S., Kitagawa, S., Alvino, J. F., Metha, G. F., Sumbly, C. J. and Doonan, C. J. *Angew. Chem. Int. Ed.*, **2017**, *56*, 8412-8416.
 37. Peralta, R. A., Huxley, M. T., Evans, J. D., Fallon, T., Cao, H., He, M., Zhao, X. S., Agnoli, S., Sumbly, C. J. and Doonan, C. J. *J. Am. Chem. Soc.*, **2020**, *142*, 13533-13543.
 38. Bloch, W. M., Burgun, A., Doonan, C. J. and Sumbly, C. J. *Chem. Commun.*, **2015**, *51*, 5486-5489.
 39. Peralta, R. A., Huxley, M. T., Young, R. J., Linder-Patton, O. M., Evans, J. D., Doonan, C. J. and Sumbly, C. J. *Faraday Discuss.*, **2021**, *225*, 84-99.
 40. Li, Y.-Z., Fu, Z.-H. and Xu, G. *Coord. Chem. Rev.*, **2019**, *388*, 79-106.
 41. Duan, J., Li, Y., Pan, Y., Behera, N. and Jin, W. *Coord. Chem. Rev.*, **2019**, *395*, 25-45.
 42. Zhao, M., Huang, Y., Peng, Y., Huang, Z., Ma, Q. and Zhang, H. *Chem. Soc. Rev.*, **2018**, *47*, 6267-6295.
 43. Ashworth, D. J. and Foster, J. A. *J. Mater. Chem. A*, **2018**, *6*, 16292-16307.
 44. Sakamoto, R., Takada, K., Pal, T., Maeda, H., Kambe, T. and Nishihara, H. *Chem. Commun.*, **2017**, *53*, 5781-5801.

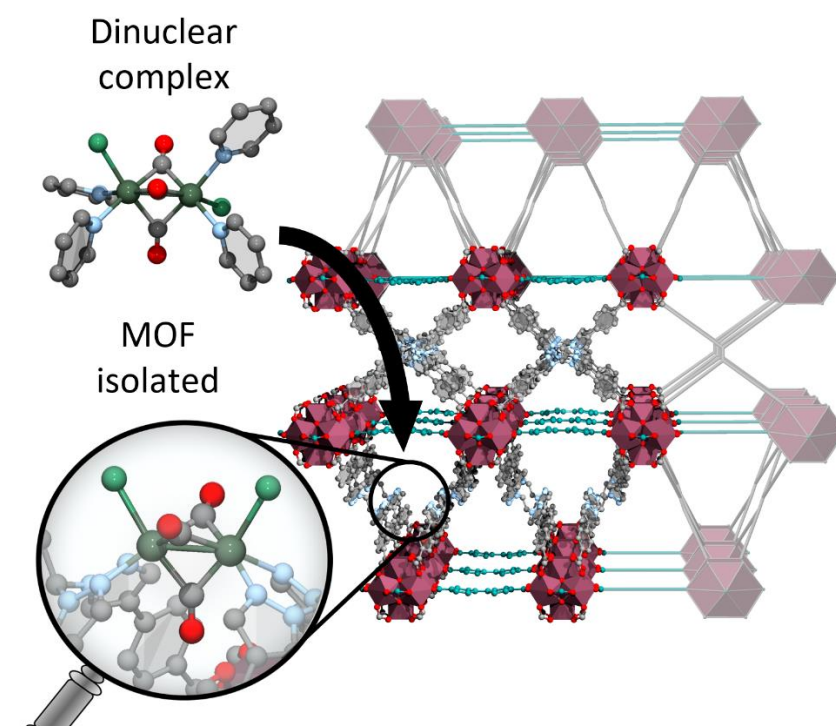
CHAPTER 3: Atomic scale
elucidation of unusually
distorted dimeric complexes
confined in a new Zr-based
Metal-organic Framework

Atomic scale elucidation of unusually distorted dimeric complexes confined in a new Zr-based Metal-organic Framework

Pol Gimeno-Fonquernie,^a Jorge Albalad,^{a†} Jack D. Evans,^a Jason R. Price,^b Christian J. Doonan^{a} and Christopher J. Sumby^{a*}*

^a Centre for Advanced Nanomaterials and Department of Chemistry, The University of Adelaide, Adelaide, SA 5000, Australia.

^b ANSTO Melbourne, The Australian Synchrotron, 800 Blackburn Rd, Clayton, Vic 3168, Australia.



3.1. Statement of authorship

Statement of Authorship

Title of Paper	Atomic scale elucidation of unusually distorted dimeric complexes confined in a new Zr-based Metal-organic Framework		
Publication Status	<input type="checkbox"/> Published	<input type="checkbox"/> Accepted for Publication	<input type="checkbox"/> Unpublished and Unsubmitted work written in manuscript style
	<input checked="" type="checkbox"/> Submitted for Publication		
Publication Details			

Principal Author

Name of Principal Author (Candidate)	Pol Gimeno I Fonquernie		
Contribution to the Paper	Design and development of the project. Preparation of samples and data collection. Analysis and interpretation of X-ray crystallography data and SEM-EDX data. Preparation, drafting and final version of manuscript.		
Overall percentage (%)	70%		
Certification:	This paper reports on original research I conducted during the period of my Higher Degree by Research candidature and is not subject to any obligations or contractual agreements with a third party that would constrain its inclusion in this thesis. I am the primary author of this paper.		
Signature		Date	13 - 07 - 2023

Co-Author Contributions

By signing the Statement of Authorship, each author certifies that:

- i. the candidate's stated contribution to the publication is accurate (as detailed above);
- ii. permission is granted for the candidate to include the publication in the thesis; and
- iii. the sum of all co-author contributions is equal to 100% less the candidate's stated contribution.

Name of Co-Author	Jorge Albalad		
Contribution to the Paper	Assisted with conception of the project and drafting of the manuscript.		
Signature		Date	17/7/2023

Name of Co-Author	Jack D. Evans		
Contribution to the Paper	Design and development of the computational studies.		
Signature		Date	28/7/23.

Please cut and paste additional co-author panels here as required.

Name of Co-Author	Jason R. Price
Contribution to the Paper	Assisted with collection, analysis and interpretation of X-ray crystallography data.
Signature	Signed on behalf of Jason R. Price 15/8/2023

Name of Co-Author	Christian J. Doonan
Contribution to the Paper	Assisted with conception of the project, experiment design and drafting of the manuscript.
Signature	31/7/2023

Name of Co-Author	Christopher J. Sumby
Contribution to the Paper	Assisted with conception of the project experiment design, drafting of the manuscript and analysis of X-ray crystallography data.
Signature	24/7/2023

3.2. Introduction

The close proximity of metal atoms in dimeric complexes can give rise to metal cooperativity, which can result in unique magnetic, optical, and chemical properties.¹⁻³ In biological systems, this phenomenon is harnessed by numerous metalloenzymes, which incorporate multiple metals within their active pockets, resulting in enhanced substrate binding, increased turnover frequency, and improved product selectivity.^{4, 5} Inspired by the intricacy of natural systems, scientists have directed their focus towards the investigation of dinuclear complexes and small metal clusters in synthetic systems (Figure 3.1).⁶⁻¹⁰

Metal-organic Frameworks (MOFs)¹¹⁻¹³ are open pore networks that can be tailored to site isolate and stabilise reactive metal complexes and provide structural insight into their properties by single-crystal X-ray diffraction (SCXRD). The inherent crystallinity of MOFs and the ability to incorporate secondary metals by post-synthetic metalation (PSMet)¹⁴ has allowed “matrix isolation” and detailed structure elucidation of unprecedented, often highly reactive, organometallic species trapped inside the pores that in turn could be employed as catalysts.¹⁵⁻¹⁹ Despite the success of this approach, it is broadly limited to mononuclear species due to the several challenges of forming MOFs that allow the SCXRD characterization of dimeric complexes.²⁰⁻²²

The atomic scale elucidation of binuclear complexes and small metal clusters (2 – 10 metals) in MOFs requires of a high occupancy of the species, low crystallographic disorder or retention of the long-range order after PSMet. To achieve this goal, MOFs with a high density and appropriate arrangement of ligating groups to accommodate small metal clusters are required. An illustrative example of this concept was reported by Pardo et al.²³ They synthesized a bimetallic anionic MOF with small pockets characterized by a high density of oxygen donor groups. Through a two-step post-synthetic metalation (PSMet) process, various metal clusters were successfully incorporated into the MOF and their structures successfully determined via SCXRD. This unique environment facilitated the isolation of unconventional “naked” metal clusters, including a novel linear Pd₄ mixed-valence cluster,²⁴ Pt₂ dimers,²⁵ and recently, Ag₂²⁶ species.

In a different example, using designed bifunctional linkers, Humphrey and coworkers were able to synthesize a MOF with high density of metal-free phosphine functional groups (PCM-101). The close proximity of the phosphine groups allowed the formation of a Cu₂Br₂ dimers that could be characterized by SCXRD.²⁷ The same group was also able to isolate an Au₂Cl₂ dimer complex in a different MOF (ACM-1) containing *cis*-diarsine pockets.²⁸

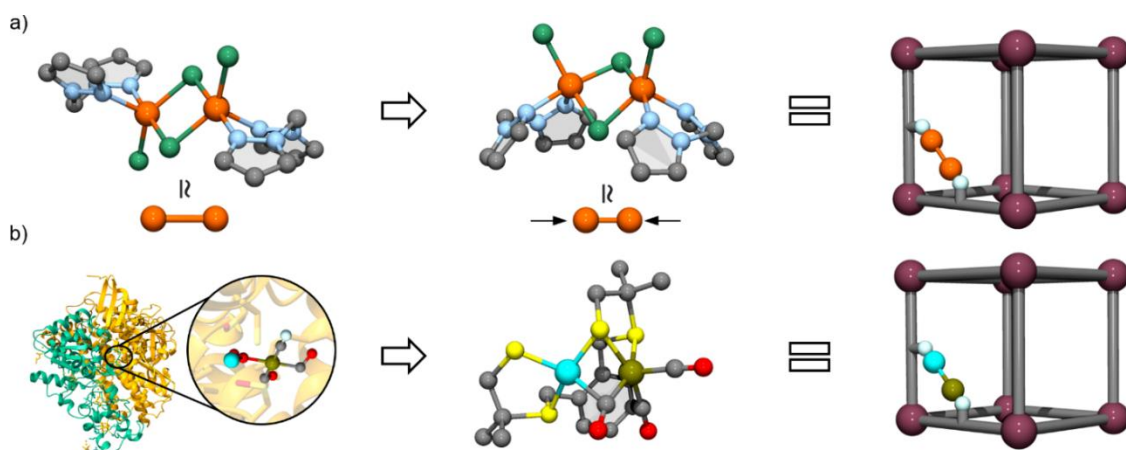


Figure 3.1. Representations of some of the uses of MOFs in the isolation of binuclear complexes or small metal clusters, for a) access new species, by forcing geometric distortions by anchoring them to the MOF and b) site isolate modelling enzyme active sites. a) Left to right, shows a structural model of a molecular dimeric complex, a structural model of a distorted dimeric complex that can only be accessed by isolating it in a MOF. b) Left to right, shows a metalloenzyme active site, a structural model of that site and a schematic of a potential MOF-tethered species.

Although the aforementioned systems represent significant advances, the MOFs presented can only accommodate dimeric species and clusters with specific characteristics due to their donor environments and structure metrics. Thus, to stabilise and isolate new dimeric complexes, new designed MOF platforms, ideally possessing a degree of structural flexibility and large pore apertures to provide access, are required. Inspired by our previous work on pyrazole containing linkers, we hypothesized that the synthesis of a high connectivity Zr-based MOF using a bifunctional linker (1,1,2,2-tetrakis[4-(4-carboxyphenyl)-1H-pyrazol-1-yl]ethane, L1H₄) would yield a stable and structurally flexible open framework material with a high density of pyrazole donors. Furthermore, we anticipated that a high density of soft/borderline nitrogen donors would facilitate PSMet with mono- and binuclear metal complexes, and coupled with the inherent structural flexibility, would allow characterisation of the added complexes by SCXRD.

Herein, we report the synthesis of a stable Zr-based MOF ($[\text{Zr}_6(\mu_3\text{-OH})_8(\text{OH})_4(\text{DMF})_4(\text{L1})_2]$, University of Adelaide Material-1000, UAM-1000) with a high density of free bis-pyrazole units poised to support binuclear metal species (Figure 3.1). We found that the framework flexibility and distance between chelating pyrazole moieties could be controlled post-synthetically by ‘bracing’ the structure with a biphenyl-4,4’-dicarboxylic acid (BPDC) linker (yielding UAM-1001). The more rigid UAM-1001 allowed “matrix isolation” and detailed structural elucidation of a number of post-synthetically added dimeric species, $[\text{Co}_2\text{Cl}_4]$, $[\text{Cu}_2\text{Cl}_4]$, $[\text{Ni}_2\text{Cl}_3(\text{H}_2\text{O})_2]\text{Cl}$ and $[\text{Rh}_2(\text{CO})_3\text{Cl}_2]$, bound within a tetradentate binding site formed from two linkers. Notably, this novel coordination environment gives rise to significant geometric distortions,

and unprecedented bond lengths, for the metal dimers compared to analogous molecular species. This work shows the potential for MOFs to support precisely characterised multinuclear metal complexes capable of carrying out reactions that are facilitated by cooperative substrate binding or multiple electron transfers.

3.3. Experimental Section

3.3.1. Materials and methods

Unless otherwise stated, all chemicals were obtained from commercial sources and used as received. 1,1,2,2-Tetrakis[4-(4-carboxyphenyl)-1H-pyrazol-1-yl]ethane (L1H₄) was synthesized following an already reported procedure.^{29, 30} Acetonitrile (MeCN) was dried from CaH₂ under N₂ and tetrahydrofuran (THF) and toluene were dried from sodium under N₂. All solvents were degassed with Ar prior to use. Solid MOF samples were digested in DCI/DMSO-*d*₆ at 80 °C for 16 h.

Powder X-ray Diffraction (PXRD) data were collected on a Bruker Advanced D8 diffractometer (capillary stage) using Cu K α radiation (λ = 1.5456 Å, 40 kW/40 mA, 2 θ = 2–52.94°, ϕ rotation= 20 rotations/min, at 1 s exposure per step with 5001 steps, and using 0.5 mm glass capillaries). Fourier Transform Infrared Spectroscopy (FTIR) spectra were collected on a Shimadzu IR spirit using ATR mode (Spectral range: 7800 – 350 cm⁻¹). Nuclear Magnetic Resonance (NMR) spectra were collected at 25 °C in deuterated solvents on an Agilent DD2 500 MHz NMR with a 5 mm OneNMR probe, using tetramethylsilane (TMS) signals as the internal reference standard. Scanning Electron Microscopy (SEM) images were collected, and Energy Dispersive X-ray (EDX) analysis performed on a FEI Quanta 450 field-emission scanning electron microscope, operating at 10.0 – 20.0 kV and under ultra-high vacuum (10⁻⁷ – 10⁻¹² hPa) conditions. Gas adsorption measurements were performed on a Micromeritics 3-Flex surface area and pore size analyser. Prior to gas adsorption, the MOF materials underwent solvent exchange to dry MeCN at 25°C by washing with dry MeCN (4 \times) over 24 h. The materials were activated from dry MeCN by heating at 120°C under vacuum for 4 hours. Thermogravimetric analysis data was collected on an STA 449 F3 Jupiter analyser from 45 °C – 700 °C at 5 °C/min under 21% O₂, 79% N₂.

The CP2K software package³¹ was used to perform density functional theory (DFT) based structural optimisations of UAM-1000 and UAM-1001. Representative low symmetry structures were refined from crystal structures. The uncoordinated Zr environments present in UAM-1000 were coordinated with water and OH ligands. The exchange-correlation energy was

assessed in the Perdew–Burke–Ernzerhof (PBE) approximation,³² and the dispersion interactions were modelled using the DFT-D3 approach.³³ Five different grids and a high plane-wave cut-off for the electronic density of 800 Ry (70 Ry relative cut-off) was used to provide high accuracy.

Valence electrons were treated by double-zeta valence polarized basis sets and norm-conserving Goedecker–Teter–Hutter pseudo-potentials, all adapted for PBE (DZVP-GTH-PBE) for H, C, O and N or optimized for solids (DZVP-MOLOPT-SR-GTH) for Zr.³⁴ Cell and atom positions were optimised with no constraints to a convergence criteria of $4.5\text{E-}05$ hartrees bohr⁻¹ max force and $3.0\text{E-}5$ hartrees bohr⁻¹ root-mean-square forces. Surface areas were simulated based on the optimised structure for a probe radius of 1.82 Å (equivalent to the size of N₂) using the Zeo++ program.^{35, 36}

3.3.2. Synthetic protocols

3.3.2.1. Synthesis of UAM-1000

ZrCl₄ (15 mg, 0.064 mmol) and trifluoroacetic acid (0.2 mL, 2.61 mmol, 41 mol. eq.) were dissolved in 1 mL of DMF and sonicated for 30 min. Separately, L1H₄ (10 mg, 0.013 mmol) was dissolved in 1 mL of DMF and the solution was then added to the metal solution. The resulting mixture was transferred to a solvothermal scintillation vial and heated at 120 °C for 72 h. Colourless crystals UAM-1000 were collected by filtration and washed with DMF (4 x 5 mL).

3.3.2.2. Synthesis of UAM-1001

UAM-1001 was synthesized following a slightly modified already reported procedure.^[21a] Briefly, crystals of UAM-1000 (50 mg) were treated with a solution of BPDC in DMF (0.03 M, 10 mL) at 75 °C for 24 h. The crystals were collected by filtration and washed with fresh DMF (2 x 10 mL) (yield: quantitative).

3.3.2.3. Post-synthetic metalation of UAM-1000 and UAM-1001

Synthesis of UAM-1000[Cu(NO₃)₂H₂O]. UAM-1000 crystals (50 mg, 0.028 mmol) were soaked in 3 mL of dry acetonitrile. An excess of Cu(NO₃)₂·3H₂O (~5 mg) was added, and the solution was heated to 40 °C for 16 h. The sample was then washed by decantation with dry acetonitrile (4 x 4 mL) and with dry toluene (4 x 4 mL). The green crystals (55 mg, 95%) were left in solution for characterization by SCXRD. SEM-EDX molar ratio 3.0(Zr):0.9(Cu).

Synthesis of UAM-1000[PdCl₂]. UAM-1000 crystals (50 mg, 0.028 mmol) were soaked in 3 mL of dry acetonitrile. An excess of PdCl₂ (~5 mg) was added, and the solution was left at 25 °C for 16 h. The sample was then washed by decantation with dry acetonitrile (4 x 4 mL) and with

dry toluene (4 x 4 mL). The orange crystals (54 mg, quantitative) were left in solution for characterization by SCXRD. SEM-EDX molar ratio 3.0(Zr):1.0(Pd):2(Cl).

Synthesis of UAM-1001[Cu(NO₃)₂H₂O]. UAM-1001 crystals (50 mg, 0.028 mmol) were soaked in 3 mL of dry acetonitrile. An excess of Cu(NO₃)₂·3H₂O (~5 mg) was added, and the solution was heated to 40 °C for 16 h. The sample was then washed by decantation with dry acetonitrile (4 x 4 mL) and with dry toluene (4 x 4 mL). The green crystals (55 mg, quantitative) were left in solution for characterization by SCXRD. SEM-EDX molar ratio 3.0(Zr):0.9(Cu).

Synthesis of UAM-1001[PdCl₂]. UAM-1001 crystals (50 mg, 0.028 mmol) were soaked in 3 mL of dry acetonitrile. An excess of PdCl₂ (~5 mg) was added, and the solution was left at 25 °C for 16 h. The sample was then washed by decantation with dry acetonitrile (4 x 4 mL) and with dry toluene (4 x 4 mL). The orange crystals (54 mg, quantitative) were left in solution for characterization by SCXRD. SEM-EDX molar ratio 3.0(Zr):1.0(Pd):2(Cl).

Synthesis of UAM-1001[Rh₂(CO)₃Cl₂]. UAM-1001 crystals (50 mg, 0.028 mmol) were soaked in 3 mL of dry acetonitrile. An excess of [Rh(CO)₂Cl]₂ (~5 mg) was added, and the solution was left at 40 °C for 16 h. The sample was then washed by decantation with dry acetonitrile (4 x 4 mL) and with dry toluene (4 x 4 mL). The pale-yellow crystals (60 mg, quantitative) were left in solution for characterization by SCXRD. SEM-EDX molar ratio 3.0(Zr):1.9(Rh):2.0(Cl). FT-IR (Nujol, cm⁻¹) 1860.

Synthesis of UAM-1001[Ni₂(Cl₃)(H₂O)₂]Cl. UAM-1001 crystals (50 mg, 0.028 mmol) were soaked in 3 mL of ethanol. An excess of NiCl₂·6H₂O (~5 mg) was added, and the solution was heated to 60 °C for 16 h. The sample was then washed by decantation with ethanol (2 x 4 mL) and with dry toluene (4 x 4 mL). The pale-green crystals (58 mg, quantitative) were left in solution for characterization by SCXRD. SEM-EDX molar ratio 3.0(Zr):1.9(Ni):4.0(Cl).

Synthesis of UAM-1001[Co₂Cl₄]. UAM-1001 crystals (50 mg, 0.028 mmol) were soaked in 3 mL of dry THF under argon. An excess of CoCl₂ (~5 mg) was added, and the solution was heated to 60 °C for 16 h. The sample was then washed by decantation with dry THF (2 x 4 mL) and with dry toluene (4 x 4 mL). The blue crystals (52 mg, quantitative) were left in solution for characterization by SCXRD. SEM-EDX molar ratio 3.0(Zr):1.5(Co):3.2(Cl).

Synthesis of UAM-1001[Cu₂Cl₄]. UAM-1001 crystals (50 mg, 0.028 mmol) were soaked in 3 mL of dry THF under argon. An excess of CuCl₂ (~5 mg) was added, and the solution was heated to 60 °C for 16 h. The sample was then washed by decantation with dry THF (2 x 4 mL)

and with dry toluene (4 x 4 mL). The yellow crystals (52 mg, quantitative) were left in solution for characterization by SCXRD. SEM-EDX molar ratio 3.0(Zr):1.8(Cu):3.9(Cl).

3.4. Results and discussion

3.4.1. Synthesis of UAM-1000

Employing bifunctional organic linkers is a common strategy for synthesizing MOFs with metal-free groups primed for PSMet.^{14, 20} Specifically, donors of different hardness allows for the selective coordination of one donor type to the node metal, generating a MOF with metal-free functional groups.^{18, 37} For our L1H₄ linker, we anticipated that a hard Zr(IV) node metal would yield a MOF with high thermal and chemical stability and, due to the higher connectivity of the Zr node, engender a framework with a high density of free bis-pyrazole units. In addition, we hypothesized that careful linker design could provide a 3D pore environment suited to stabilising binuclear complexes. Firstly, our previous studies indicated that a tetra-carboxylate linker is required to generate a 3D MOF as flexible ditopic pyrazole carboxylate linkers produced 2D Metal-organic Layers (MOLs) with Zr(IV) exclusively.³⁸ Secondly, this work also revealed the carboxylate donors could not be directly appended to the pyrazole rings as this restricts rotation of the pyrazoles and causes torsional strain upon metal chelation, thus preventing single-crystal to single-crystal (SC-SC) PSMet. Considering these design criteria, our linker of choice was 1,1,2,2-tetrakis[4-(4-carboxyphenyl)-1H-pyrazol-1-yl]ethane (L1H₄)(Figure 3.2).²⁹ Reaction of L1H₄ with ZrCl₄ using a trifluoroacetic acid (TFA) modulator in dimethylformamide (DMF) yielded colourless octahedral crystals suitable for SCXRD (Figure II.1). The MOF structure consists of an octahedral Zr₆ cluster capped by eight μ_3 -OH ligands with eight of the twelve edges of the octahedral cluster connected to L1 carboxylate donors, and the remaining Zr coordination sites occupied by a mixture of DMF and OH molecules. The 3D structure has a *sqc* topology forming diamond-shaped channels that are accessible along the *a* and *b* axes (Figure 3.2). The resultant MOF has the formula of [Zr₆(μ_3 -OH)₈(OH)₄(DMF)₄(L1)₂] (UAM-1000).

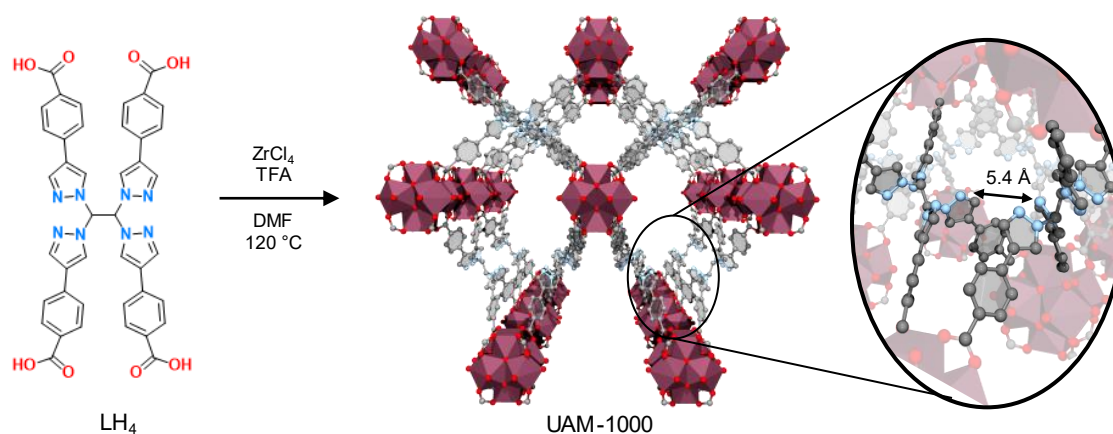


Figure 3.2. Synthesis and structural representations of UAM-1000. Synthesis of UAM-1000 from LH_4 and $ZrCl_4$ (left), and a perspective view of the SCXRD structure of this material along the a/b axis (tetragonal unit cell). Coloured spheres represent O (red), N (blue) and C (black), and the Zr centres are shown as green polygons. DMF molecules and hydrogen atoms have been omitted for clarity. An enlargement of the node region of the framework (right) showing the proximity of adjacent bis-pyrazole units.

UAM-1000 exhibits excellent thermal and chemical stability, comparable to other reported Zr-based MOFs. Thermogravimetric analysis (TGA) analysis of a sample of UAM-1000, activated under vacuum at room temperature, reveals thermal stability up to 400 °C (Figure II.2). Crystallinity of UAM-1000 is retained after being soaked in water at pH 1 and pH 11 for 72 h, as evidenced by PXRD data showing no appreciable loss of long-range order (Figure 3.3b). UAM-1000 also has a high degree of structural flexibility provided by the ethyl spacer between the bis-pyrazole units. PXRD data for activated UAM-1000 (UAM-1000·act) reveals a loss of crystallinity that can be attributed to a partial collapse of the framework (Figure 3.3d). Despite partial collapse, a 77K N_2 adsorption isotherm of UAM-1000·act shows the material to be porous to nitrogen with a type I isotherm, a Brunauer–Emmett–Teller (BET) surface area of 391 m^2g^{-1} (Figure 3.3c) and a total pore volume of 0.13 cm^3g^{-1} (Density Functional Theory (DFT) calculations of the structure reveal an estimated surface area of 1826 m^2g^{-1}). The parent structure of UAM-1000 can be recovered by resolution of UAM-1000·act at room temperature (Figure II.3). This indicates UAM-1000·act may represent a closed phase and does not suggest decomposition of the framework structure. As predicted, the hard Zr(IV) metal centres bind to the carboxylate donors but not the relatively soft pyrazole donors yielding an open framework structure replete with metal-free bis-pyrazole donors. For an individual bis-pyrazole moiety, these are arranged in a ‘syn’ conformation, near a second unit, to form a tetradentate site where the two entities are ca. 5.4 Å apart and predisposed to being post-synthetically metalated (Figure 3.2). To evaluate coordinating ability of the bis-pyrazole units, we attempted the PSMet of UAM-1000 with copper(II) nitrate ($Cu(NO_3)_2$) and palladium(II) chloride ($PdCl_2$). Soaking UAM-1000 crystals in a

solution of $\text{Cu}(\text{NO}_3)_2 \cdot 3\text{H}_2\text{O}$ or PdCl_2 gave an almost instant colour change of the crystals from colourless to green or orange suggesting the successful metalation of the bis-pyrazole units. The metalation was confirmed by Scanning Electron Microscopy Energy Dispersive X-ray (SEM-EDX) analysis (Table II.1). To confirm the metalation was occurring at the bis-pyrazole units we attempted SCXRD characterization. Despite $\text{UAM-1000} \cdot \text{Cu}(\text{NO}_3)_2$ and $\text{UAM-1000} \cdot \text{PdCl}_2$ retaining long range order, as evidenced by PXRD (Figure II.4), the crystals were no longer suitable for SCXRD. Attempts to preserve single crystal quality by metalating at lower temperatures or using less concentrated solutions to slow down the metal diffusion into UAM-1000 were unsuccessful.

3.4.2. “Locking” UAM-1000 to form UAM-1001

The lower connectivity of the Zr-based node in UAM 1000, the partial structure collapse upon activation, and loss the crystal integrity upon metalation, prompted us to rigidify the framework by inserting a secondary linker to brace the structure (Figure 3.3a).³⁹ Following a similar procedure to Zhou *et al.*^{40, 41} for the insertion of secondary linkers into MOFs, we soaked UAM-1000 crystals in a 0.03 M biphenyl-4,4'-dicarboxylic acid (BPDC) solution at 80 °C for 18 h to form UAM-1001. BPDC insertion into UAM-1000 was confirmed by ¹H-NMR spectroscopy, showing a BPDC:L1 1:1 molar ratio (Figure II.5), and SCXRD (Figure 3.3a). Furthermore, the rigidification of UAM-1000 was evidenced by reduction in the flexibility of UAM-1001. PXRD analysis of activated UAM-1001 ($\text{UAM-1001} \cdot \text{act}$, formed by heating UAM-1001 in dry acetonitrile at 120 °C for 4 h) shows that crystallinity is preserved and the structure is little changed upon activation (Figure 3.3d). UAM-1001 is also porous to nitrogen, showing a type I isotherm profile and giving a BET surface area of 2324 m^2g^{-1} and a total pore volume of 0.85 cm^3g^{-1} (Figure 3.3c) (DFT calculations of the structure reveal an estimated surface of 1773 m^2g^{-1}).

Despite the additional bracing acting to rigidify the MOF, PSMet of UAM-1001 with the metal salts ($\text{Cu}(\text{NO}_3)_2 \cdot 3\text{H}_2\text{O}$, PdCl_2) under the same conditions used for PSMet of UAM-1000 gratifyingly led to the same degree of metalation as evidenced by SEM-EDX analysis (Table II.2). Pleasingly, and contrary to UAM-1000, UAM-1001 crystals were still suitable for SCXRD, thereby allowing study of the chemical environment of the metal centre in the bis-pyrazole moieties. With a careful choice of the metal centre, including those with the propensity to form metal-metal bonds; counterions; and co-ligands, the proximity of the adjacent bis-pyrazole groups should allow for the incorporation of binuclear complexes and potentially clusters.

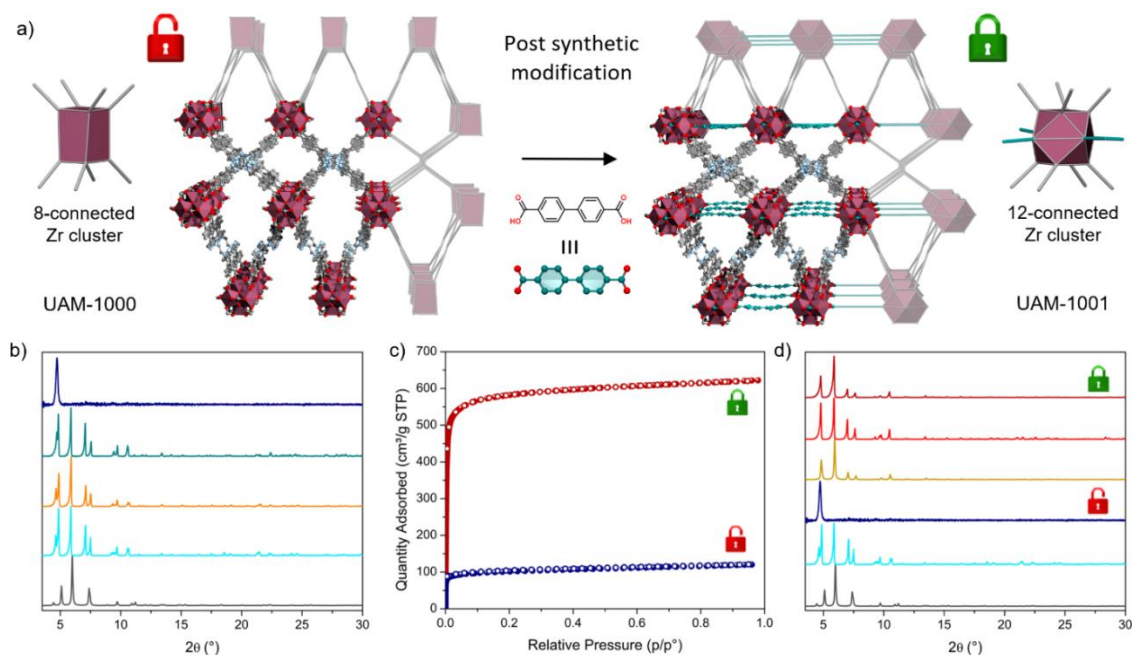


Figure 3.3. a) Synthesis and structural representation of UAM-1001. b) Experimental PXRD plots for UAM-1000 as made (light blue), UAM-1000 after being soaked in water pH11 (orange), UAM-1000 after being soaked in water pH1 (green) versus simulated UAM-1000 (black). c) 77 K N₂ isotherm data of UAM-1000 (blue) and UAM-1001 (red). Filled circles represent adsorption, open circles represent desorption. d) PXRD plots for UAM-1000 simulated (black), UAM-1000 as made (light blue), UAM-1000·act (dark blue), UAM-1001 simulated (gold), UAM-1001 as made (light red) and UAM-1001·act (dark red).

3.4.3. Isolation of distorted dimeric complexes in UAM-1001

We decided to start the study of isolation of dimeric complexes in UAM-1001 by anchoring a dinuclear species that had N-donor ligands that matched the structure metrics of the bis-pyrazole moieties in UAM-1001. Our dimer of choice was a Ni₂ complex (like that seen in [Ni₂Cl₃(tzcn)₂PF₆]⁴² where both Ni(II) centres have an octahedral geometry and three chloride ligands are shared (Figure 3.4a). SCXRD analysis of UAM-1001 metalated with NiCl₂·6H₂O reveals the formation of a similar pale green coloured complex where each Ni(II) metal centre is coordinated by two pyrazole donors, a water molecule and three bridging chlorides in an octahedral geometry (UAM-1001[Ni₂Cl₃(H₂O)₂Cl] (Figure 3.4a). SEM-EDX analysis supported 100% metalation of the bis-pyrazole units and two Cl ligands per Ni centre, placing one in the pore (Table II.2). Comparison of UAM-1001[Ni₂Cl₃(H₂O)₂Cl] with [Ni₂Cl₃(tzcn)₂PF₆] (Table II.3) reveals a shorter Ni-Ni distance and a smaller Ni-Cl-Ni bond angle that evidences that the framework is slightly squeezing the dimer. Notably, this is the shortest Ni-Ni distance reported for a [Ni₂μCl₃] complex to the date (Figure 3.4e, Figure II.6).

UAM-1001 can also accommodate other octahedral dimers where in solution the N-donor ligands are not in the same disposition. [Rh₂Py₄Cl₂(μ-CO)₃]⁴³ (Figure 3.4b) is a Rh(I) octahedral

dimer where the Rh(I) coordinate two pyridine (Py) molecules, a capping chloride and three carbon monoxide (CO) bridging molecules. SCXRD analysis of pale yellow crystals of UAM-1001 metalated with $[\text{Rh}(\text{CO})_2\text{Cl}]_2$ (UAM-1001 $[\text{Rh}_2\text{CO}_3\text{Cl}_2]$) reveals the formation of a similar Rh(I) dimer where each Rh(I) metal centre is coordinated by two pyrazole donors, two chloride atoms and three CO bridging carbons in an octahedral geometry (Figure 3.4b). The formation of the dimer was confirmed by Fourier-Transform Infrared Spectroscopy (FT-IR) that reveals a stretching band at 1860 cm^{-1} (Figure II.7), consistent with the presence of bridging CO ligands.⁴⁴ SEM-EDX analysis also supported 100% metalation of the bis-pyrazole units (Table II.2). Comparison of UAM-1001 $[\text{Rh}_2\text{CO}_3\text{Cl}_2]$ with $[\text{Rh}_2\text{Py}_4\text{Cl}_2(\mu\text{-CO})_3]$ (Table II.4) reveals similar bond lengths and angles with a Rh-Rh distance of 2.5 \AA . The shorter Rh-Rh distance compared to the Ni dimer (3.0 \AA) allows the accommodation of this species without shortening the Rh-Rh distance. However, in this case, the arrangement of the bis-pyrazole units in UAM-1001 forces the chloride ions to be in a *syn*-disposition compared to the *anti*-arrangement of the complex in solution; this places the Cl counterions on the same face of the dimer and may have implications for further reactivity.

Metalation of UAM-1001 with dinuclear complexes possessing a different metal geometry leads to even greater changes in the coordination environment observed in the MOF. SCXRD analysis of UAM-1001 metalated with CuCl_2 (UAM-1001 $[\text{Cu}_2\text{Cl}_4]$) reveals the formation of a yellow Cu(II) dimer where each Cu(II) metal centre is coordinated by two pyrazole donors, two capping chloride atoms and two bridging chloride atoms in distorted trigonal bipyramidal geometry (Figure 3.4c). SEM-EDX analysis supported 100% metalation of the bis-pyrazole units (Table II.2). Comparison of UAM-1001 $[\text{Cu}_2\text{Cl}_4]$ with a CuCl_2 dimer with a similar set of ligands ($[\text{CuCl}_2\text{bpm}]_2$)⁴⁵ (Figure 3.4c, Table II.5) reveals a dramatic change in the Cu-Cu distance from 3.5 \AA in $[\text{CuCl}_2\text{bpm}]_2$ to 3.1 \AA in UAM-1001 $[\text{Cu}_2\text{Cl}_4]$. The axial N-Cu- μCl bond angle is also dramatically distorted, changing from 178.19° to 165.37° in the discrete dinuclear complex compared to the MOF-bound structure. As with the Rh dimer, the capping chlorides change from an *anti*-conformation in solution to a *syn*-conformation in the framework. Comparison of the Cu-Cu distance with other dimers with a $[\text{N}_2\text{CuCl}(\mu\text{Cl})_2]$ coordination environment reveals UAM-1001 $[\text{Cu}_2\text{Cl}_4]$ to have the shortest Cu-Cu distance reported for directly comparable systems (Figure 3.4f, Figure II.8).

Similar Co(II) dinuclear complexes, such as $[\text{CoCl}_2\text{bpm}]_2$ ⁴⁶ (Figure 3.4d) have been isolated; however, despite this analogous behaviour for discrete complexes, a very different outcome was encountered when metalating UAM-1001 with CoCl_2 (UAM-1001 $[\text{Co}_2\text{Cl}_4]$). SCXRD

analysis of UAM-1001[Co₂Cl₄] reveals the formation of a mixture of two different CoCl₄ dimers, one with both the Co(II) centres in a distorted trigonal bipyramidal geometry (*trbipy*-UAM-1001[Co₂Cl₄]) and the second with both the Co(II) centres in a square pyramidal geometry (*sqpy*-UAM-1001[Co₂Cl₄]). SCXRD and SEM-EDX data are consistent with ca. 80% metalation of the bis-pyrazole units (Table II.2) and the blue coloration of the crystals is consistent with a 5-coordinate Co(II) centre and an absence of coordinated water (Figure II.9). Comparison of *trbipy*-UAM-1001[Co₂Cl₄] with [CoCl₂bpm]₂ reveals again that the capping chloride atoms are now forced into a *syn*-conformation and that the Co-Co distance has notably reduced from 3.70 Å to 3.06 Å (Table II.6). This is the shortest Co-Co distance, by a significant margin, reported for a [N₂CoCl(μCl)] complex of this type (Figure 3.4g, Figure II.10). The Cl-Co-μCl bond angle formed between the capping and bridging chloride also undergoes a noticeable change from 113.8° to 150.7°.

Attempts to form a square planar dinuclear complex in UAM-1001 were not successful. SCXRD analysis of UAM-1001 metalated with PdCl₂ (UAM-1001[PdCl₂]) reveals the formation of a mononuclear complex with a square planar Pd(II) metal centre coordinated by two pyrazole nitrogen donors and two chloride anions (Figure II.11). The proximity of the adjacent bis-pyrazole unit sterically impedes the metalation of the adjacent chelating site allowing only 50% occupancy, as evidenced by SCXRD and SEM-EDX (Table II.2). The different bond lengths and angles are comparable to other similar examples, with exception of the Pd-N distance that is somewhat longer (2.26 Å vs 2.02-2.04 Å) (Table II.7).

Finally, by choosing a counter ion or co-ligand not able to bridge between two proximal metal centres, monomeric species can be isolated in UAM-1001. For instance, SCXRD analysis of UAM-1001 metalated with Cu(NO₃)₂ instead of CuCl₂ reveals the formation of a mononuclear complex, where the Cu(II) metal centre adopts an often encountered five coordinate square pyramidal geometry (Table II.8). In this species, the Cu(II) centre is coordinated by two pyrazole donors, two nitrate oxygen atoms and a water molecule (UAM-1001[Cu(NO₃)₂(H₂O)], Figure II.12). As in UAM-1001[PdCl₂], there is only 50% occupancy of the bis-pyrazole units as evidenced by SCXRD and SEM-EDX (Table II.2).

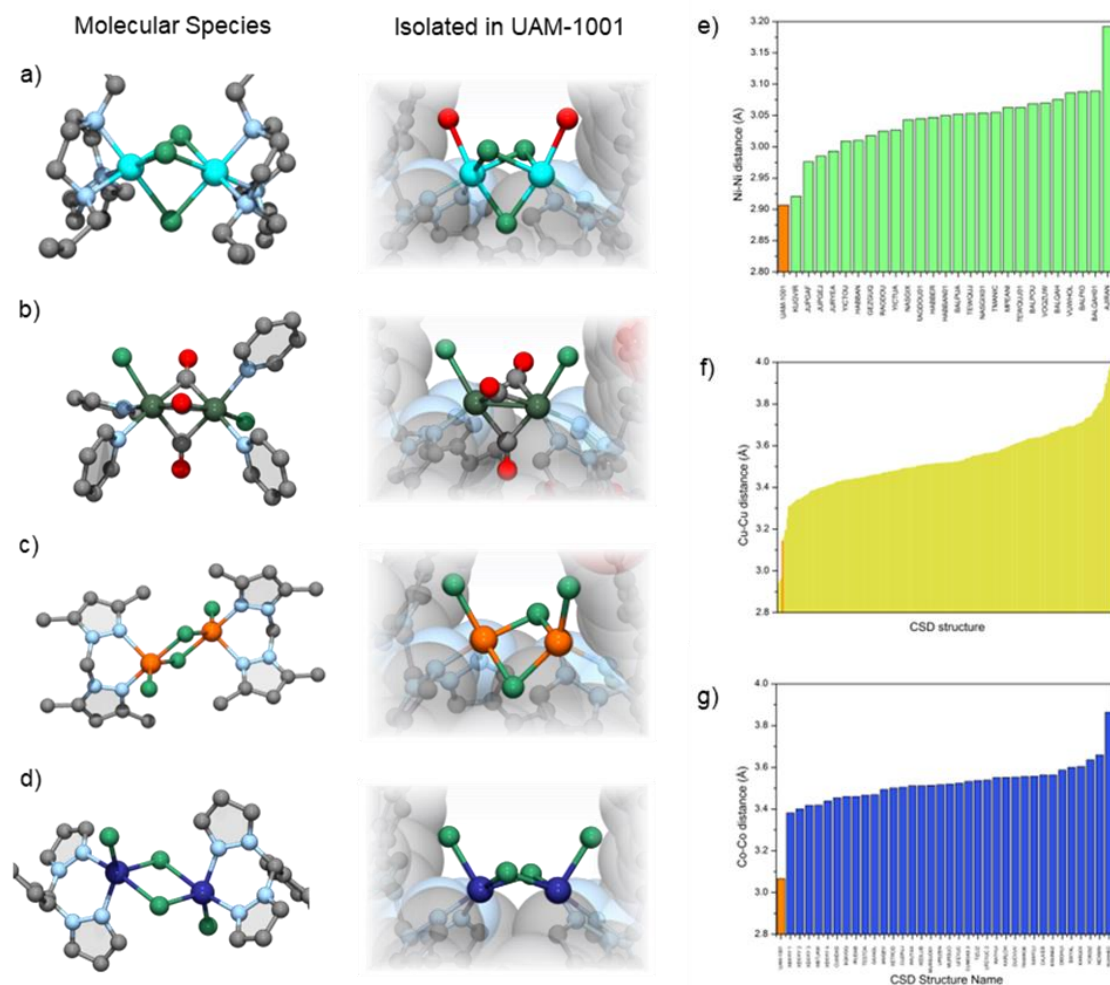


Figure 3.4. Structural representations of a) $[Ni_2Cl_3(tzcn)_2]PF_6$ (left) and UAM-1001 $[Ni_2Cl_3(H_2O)_2]Cl$ (right), b) $[Rh_2Py_4Cl_2(\mu-CO)_3]$ (left) and UAM-1001 $[Rh_2CO_3Cl_2]$, c) $[CuCl_2bpm]_2$ (left) and UAM-1001 $[Cu_2Cl_4]$ and d) $[CoCl_2bpm]_2$ (left) and UAM-1001 $[Co_2Cl_4]$ (right). (C, grey; N, light blue; O, red; Cl, green; Ni, bright light blue; Rh, dark green; Cu, orange; Co, dark blue). Graphic representation of the e) Ni-Ni, f) Cu-Cu and g) Co-Co distances of all the structures with a e) $[Ni_2\mu Cl_3]$, f) $[N_2CuCl(\mu Cl)]_2$ and g) $[N_2CoCl(\mu Cl)]_2$ moiety found in the Cambridge Crystallographic database (accessed 21/11/2022). The structures from this work are marked in orange. Larger figures are found in the SI.

3.4.4. UV-vis spectroscopic studies and reactivity

The significant distortion observed in some of the dimeric complexes isolated in UAM-1001, and their accessibility due to the large pores, implied these species may be reactive. To investigate this, we undertook solid-state UV-vis spectroscopy on all dinuclear complexes. As synthesised UAM-1001[Cu₂Cl₄] is yellow, consistent with the distorted trigonal bipyramidal geometry of the Cu centre in the dimer. During preparation of UAM-1001[Cu₂Cl₄] for spectroscopic measurements, an instant colour change from yellow to blue-green occurred when the sample was exposed to air (despite extensive efforts, a UV-vis spectrum of the intact UAM-1001[Cu₂Cl₄] species could not be obtained). The spectrum for UAM-1001[Cu₂Cl₄] (exposed to air) exhibited adsorption bands at both the blue and red regions of the spectrum (Figure 3.5), consistent with a 5-coordinated monomeric Cu(II) metal centre.⁴⁷ In fact, UAM-1001[Cu₂Cl₄] (exposed to air) displays an almost identical UV-vis spectrum to UAM-1001[Cu(NO₃)₂(H₂O)], which was determined to be a 5-coordinated monomeric complex through SCXRD analysis. When UAM-1001[Cu₂Cl₄] was not fully dried and retained a protective pore environment of dry solvent (toluene), a colour change was still observed (to green) with a band appearing at ca. 730 nm. A similar absorption was observed by Hurtado and coworkers during the hydrolysis of a [CuCl₂bpm]₂ dimer complex they synthesized, leading to the isolation of [Cu(bpm)₂Cl]Cl and free CuCl₂.⁴⁵ These findings suggest that for UAM-1001[Cu₂Cl₄] a stepwise conversion, perhaps to a mononuclear complex followed by hydrolysis occurs upon removal of the toluene solvent, and this highlights the reactivity of the Cu(II) complex due to the distorted conformation it adopts when isolated within the MOF. Unfortunately, these changes leads to a loss of long-range order. Additionally, when UAM-1001 is metalated with CuCl₂ in ethanol or exposed to wet solvent a similar blue-green complex is observed. We also looked at the UV-vis spectrum of UAM-1001[Co₂Cl₄], which also exhibited significant distortion of the dimer, but this was complicated by the presence of a broad absorption bands caused by the mixture of (trigonal bipyramidal and square pyramidal) dinuclear complexes present. The UV-vis spectra of the other metalated versions of UAM-1001 are reported in the SI (Figure II.13).

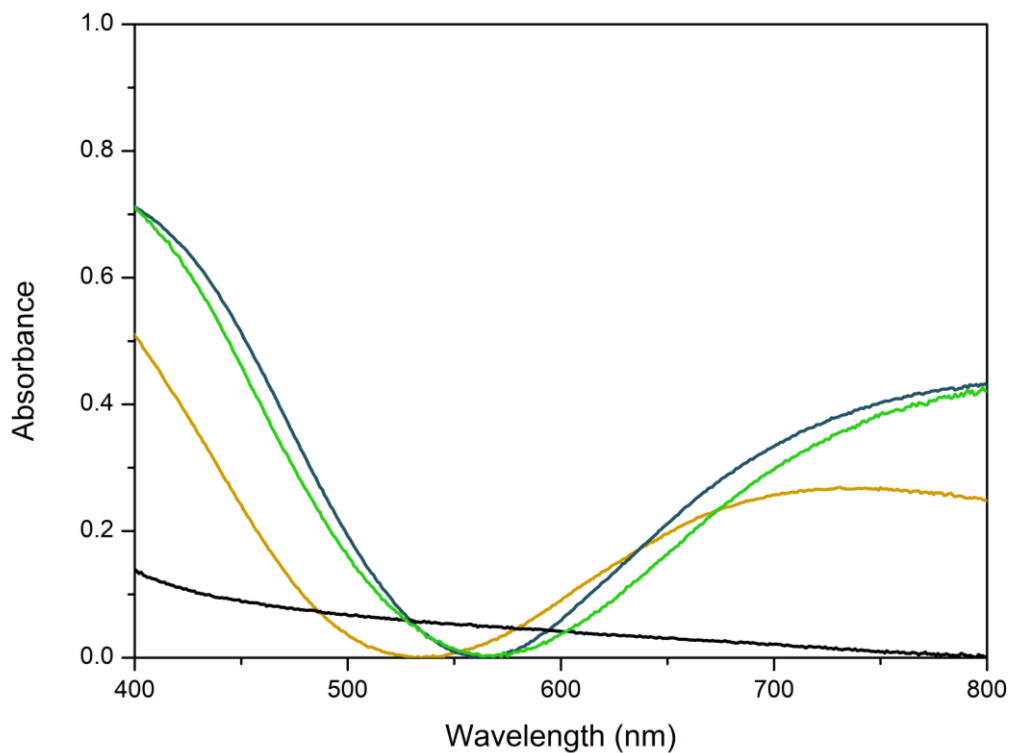


Figure 3.5. Solid state UV-vis spectrum of the non-metalated MOF, UAM-1001 (black), and the spectra for UAM-1001[Cu₂Cl₄] dried and exposed to air (light green), and UAM-1001[Cu(NO₃)₂(H₂O)] (dark green), suggesting formation of UAM-1001[CuCl₂(H₂O)] upon exposure to a humid environment. The solid UV-vis spectrum of UAM-1001[Cu₂Cl₄] solvated with toluene (yellow) is shown, which could be attributed to an intermediate species. Due to the manipulations required, the UV-vis spectrum of non-hydrolysed UAM-1001[Cu₂Cl₄] was unable to be isolated.

3.5. Conclusions

In summary, by using a bifunctional tetratopic linker (L1H₄) we have synthesized a new Zr-based MOF (UAM-1000) with a high density of free bis-pyrazole groups poised for PSMet. UAM-1000 exhibits excellent thermal and chemical stability, akin to other reported Zr-MOFs. PSM of UAM-1000 by inserting a secondary linker (BPDC) is necessary to form a more rigid framework (UAM-1001) and allow SCXRD characterisation of added metal complexes after PSMet. Using UAM-1001, we have isolated several dimeric species [Co₂Cl₄], [Cu₂Cl₄], [Ni₂Cl₃(H₂O)₂]Cl and [Rh₂(CO)₃Cl₂] and shown, with appropriate metal ions and co-ligands, the formation of two monomeric species [PdCl₂] and [Cu(NO₃)₂H₂O].

Comparison of the dimeric complexes isolated in UAM-1001 with similar dinuclear complexes crystalized from solution reveals that octahedral dimers [Ni₂Cl₃(H₂O)₂]Cl and [Rh₂(CO)₃Cl₂] experience little distortion when isolated in UAM-1001. In contrast, trigonal bipyramidal dimeric complexes like [Cu₂Cl₄] experience a greater distortion and in the case of [Co₂Cl₄] it even favours a square pyramidal geometry over the trigonal bipyramidal geometry seen for a solid-state dinuclear complex. This significant distortion enhances the reactivity of the complexes, as seen for UAM-1001[Cu₂Cl₄], which shows notable sensitivity to hydration leading to the hydrolysis of the dimer complex when exposed to air. Finally, due to the spacing between donors, the site isolation of square planar dinuclear complexes is not possible within UAM-1001 and instead, a monomeric complex is formed.

Here we have introduced design principles that allow for the controlled synthesis of dimeric complexes within a permanently porous MOF, UAM-1001. We anticipate that this system can be developed in the future to capitalise on the reactivity of novel multinuclear metal compounds that mimic the complex reactivity of species supported by biological architectures.

3.6. References

1. Li, G., Zhu, D., Wang, X., Su, Z. and Bryce, M. R. *Chem. Soc. Rev.*, **2020**, *49*, 765-838.
2. Tsuge, K., Chishina, Y., Hashiguchi, H., Sasaki, Y., Kato, M., Ishizaka, S. and Kitamura, N. *Coord. Chem. Rev.*, **2016**, *306*, 636-651.
3. Smirnov, B. M. and Yatsenko, A. S. *Phys.-Uspekhi*, **1996**, *166*, 225-245.
4. Cammack, R. *Nature*, **1999**, *397*, 214-215.
5. Lubitz, W., Ogata, H., Rüdiger, O. and Reijerse, E. *Chem. Rev.*, **2014**, *114*, 4081-4148.
6. Ghosh, A. C., Duboc, C. and Gennari, M. *Coord. Chem. Rev.*, **2021**, 428.
7. Schilter, D., Camara, J. M., Huynh, M. T., Hammes-Schiffer, S. and Rauchfuss, T. B. *Chem. Rev.*, **2016**, *116*, 8693-8749.
8. Powers, I. G. and Uyeda, C. *ACS Catal.*, **2016**, *7*, 936-958.
9. Fricke, C., Sperger, T., Mendel, M. and Schoenebeck, F. *Angew. Chem. Int. Ed.*, **2021**, *60*, 3355-3366.
10. Moonshiram, D., Jurss, J. W., Concepcion, J. J., Zakharova, T., Alperovich, I., Meyer, T. J. and Pushkar, Y. *J. Am. Chem. Soc.*, **2012**, *134*, 4625-4636.
11. Li, H., Eddaoudi, M., O'Keeffe, M. and Yaghi, O. M. *Nature*, **1999**, *402*, 276-279.
12. Yaghi, O. M., O'Keeffe, M., Ockwig, N. W., Chae, H. K., Eddaoudi, M. and Kim, J. *Nature*, **2003**, *423*, 705-714.
13. Furukawa, H., Cordova, K. E., O'Keeffe, M. and Yaghi, O. M. *Science*, **2013**, *341*, 1230444.
14. Evans, J. D., Sumbly, C. J. and Doonan, C. J. *Chem. Soc. Rev.*, **2014**, *43*, 5933-5951.
15. Bloch, W. M., Burgun, A., Doonan, C. J. and Sumbly, C. J. *Chem. Commun.*, **2015**, *51*, 5486-5489.
16. Young, R. J., Huxley, M. T., Pardo, E., Champness, N. R., Sumbly, C. J. and Doonan, C. J. *Chem. Sci.*, **2020**, *11*, 4031-4050.
17. Peralta, R. A., Huxley, M. T., Young, R. J., Linder-Patton, O. M., Evans, J. D., Doonan, C. J. and Sumbly, C. J. *Faraday Discuss.*, **2021**, *225*, 84-99.
18. Feng, D., Gu, Z. Y., Li, J. R., Jiang, H. L., Wei, Z. and Zhou, H. C. *Angew. Chem. Int. Ed.*, **2012**, *51*, 10307-10310.
19. Li, L., Tang, S., Wang, C., Lv, X., Jiang, M., Wu, H. and Zhao, X. *Chem. Commun.*, **2014**, *50*, 2304-2307.
20. Wei, Y. S., Zhang, M., Zou, R. and Xu, Q. *Chem. Rev.*, **2020**, *120*, 12089-12174.
21. Jiao, L. and Jiang, H. L. *Chem*, **2019**, *5*, 786-804.

22. Wasson, M. C., Buru, C. T., Chen, Z. J., Islamoglu, T. and Farha, O. K. *Appl. Catal. A: Gen.*, **2019**, 586, 117214.
23. Viciano-Chumillas, M., Mon, M., Ferrando-Soria, J., Corma, A., Leyva-Perez, A., Armentano, D. and Pardo, E. *Acc. Chem. Res.*, **2020**, 53, 520-531.
24. Fortea-Perez, F. R., Mon, M., Ferrando-Soria, J., Boronat, M., Leyva-Perez, A., Corma, A., Herrera, J. M., Osadchii, D., Gascon, J., Armentano, D. and Pardo, E. *Nat. Mater.*, **2017**, 16, 760-766.
25. Mon, M., Rivero-Crespo, M. A., Ferrando-Soria, J., Vidal-Moya, A., Boronat, M., Leyva-Perez, A., Corma, A., Hernandez-Garrido, J. C., Lopez-Haro, M., Calvino, J. J., Ragazzon, G., Credi, A., Armentano, D. and Pardo, E. *Angew. Chem. Int. Ed.*, **2018**, 57, 6186-6191.
26. Tiburcio, E., Zheng, Y., Mon, M., Martin, N., Ferrando Soria, J., Armentano, D., Leyva Perez, A. and Pardo, E. *Inorg. Chem.*, **2022**, 61, 11796-11802.
27. Dunning, S. G., Nandra, G., Conn, A. D., Chai, W. R., Sikma, R. E., Lee, J. S., Kunal, P., Reynolds, J. E., Chang, J. S., Steiner, A., Henkelman, G. and Humphrey, S. M. *Angew. Chem. Int. Ed.*, **2018**, 57, 9295-9299.
28. Sikma, R. E., Kunal, P., Dunning, S. G., Reynolds, J. E., 3rd, Lee, J. S., Chang, J. S. and Humphrey, S. M. *J. Am. Chem. Soc.*, **2018**, 140, 9806-9809.
29. Coghlan, C. J., Sumbly, C. J. and Doonan, C. J. *CrystEngComm*, **2014**, 16, 6364-6371.
30. Nudnova, E. A., Potapov, A. S., Khlebnikov, A. I. and Ogorodnikov, V. D. *Russ. J. Org. Chem.*, **2007**, 43, 1698-1702.
31. Kühne, T. D., Iannuzzi, M., Del Ben, M., Rybkin, V. V., Seewald, P., Stein, F., Laino, T., Khaliullin, R. Z., Schütt, O., Schiffmann, F., Golze, D., Wilhelm, J., Chulkov, S., Bani-Hashemian, M. H., Weber, V., Borštnik, U., Taillefumier, M., Jakobovits, A. S., Lazzaro, A., Pabst, H., Müller, T., Schade, R., Guidon, M., Andermatt, S., Holmberg, N., Schenter, G. K., Hehn, A., Bussy, A., Belleflamme, F., Tabacchi, G., Glöß, A., Lass, M., Bethune, I., Mundy, C. J., Plessl, C., Watkins, M., Vandevondele, J., Krack, M. and Hutter, J. *J. Chem. Phys.*, **2020**, 152, 194103.
32. Tao, J., Perdew, J. P., Tang, H. and Shahi, C. *J. Chem. Phys.*, **2018**, 148, 074110.
33. Grimme, S., Antony, J., Ehrlich, S. and Krieg, H. *J. Chem. Phys.*, **2010**, 132, 154104.
34. Goedecker, S., Teter, M. and Hutter, J. *Phys. Rev. B*, **1996**, 54, 1703-1710.
35. Willems, T. F., Rycroft, C., Kazi, M., Meza, J. C. and Haranczyk, M. *Microporous Mesoporous Mater.*, **2012**, 149, 134-141.

36. Ongari, D., Boyd, P. G., Barthel, S., Witman, M., Haranczyk, M. and Smit, B. *Langmuir*, **2017**, 33, 14529-14538.
37. Bloch, W. M., Burgun, A., Coghlan, C. J., Lee, R., Coote, M. L., Doonan, C. J. and Sumbly, C. J. *Nat. Chem.*, **2014**, 6, 906-912.
38. Gimeno-Fonquernie, P., Liang, W., Albalad, J., Kuznicki, A., Price, J. R., Bloch, E. D., Doonan, C. J. and Sumbly, C. J. *Chem. Commun.*, **2022**, 58, 957-960.
39. Schneider, C., Bodesheim, D., Keupp, J., Schmid, R. and Kieslich, G. *Nat. Commun.*, **2019**, 10, 4921.
40. Yuan, S., Chen, Y. P., Qin, J. S., Lu, W., Zou, L., Zhang, Q., Wang, X., Sun, X. and Zhou, H. C. *J. Am. Chem. Soc.*, **2016**, 138, 8912-8919.
41. Yuan, S., Zou, L., Li, H., Chen, Y. P., Qin, J., Zhang, Q., Lu, W., Hall, M. B. and Zhou, H. C. *Angew. Chem. Int. Ed.*, **2016**, 55, 10776-10780.
42. Baker, M. V., Brown, D. H., Skelton, B. W. and White, A. H. *Aust. J. Chem.*, **2002**, 55, 655-660.
43. Heaton, B. T., Jacob, C. and Sampanthar, J. T. *Dalton Trans.*, **1998**, 8, 1403-1410.
44. Dobos, S., Nunziantecesarrio, S. and Maltese, M. *Inorganica Chimica Acta*, **1986**, 113, 163-172.
45. Torres, J. F., Bello-Vieda, N. J., Macías, M. A., Muñoz-Castro, A., Rojas-Dotti, C., Martínez-Lillo, J. and Hurtado, J. *Eur. J. Inorg. Chem.*, **2018**, 2018, 3644-3651.
46. Mohr, F., Cerrada, E. and Laguna, M. *Dalton Trans.*, **2006**, 47, 5567-5573.
47. Massoud, S. S., Louka, F. R., David, R. N., Dartez, M. J., Nguyn, Q. L., Labry, N. J., Fischer, R. C. and Mautner, F. A. *Polyhedron*, **2015**, 90, 258-265.

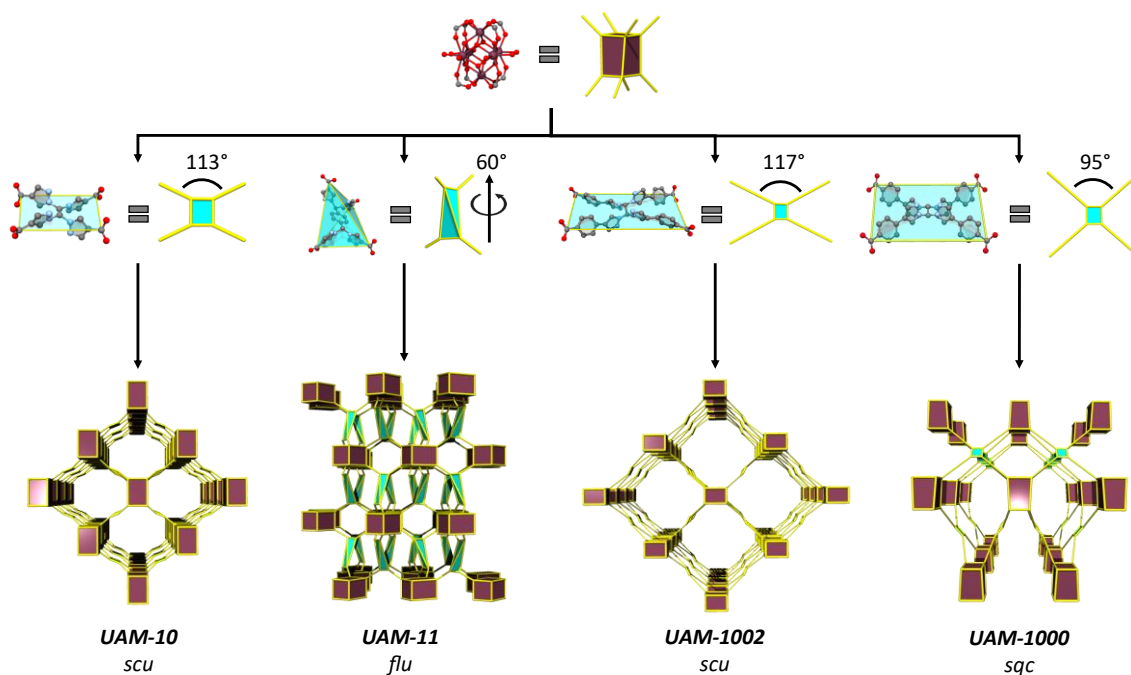
CHAPTER 4: Topological
control of post-synthetic
metalation sites in Zirconium-
based metal-organic
frameworks

Topological control of post-synthetic metalation sites in Zirconium-based metal-organic frameworks

Pol Gimeno-Fonquernie,^a Jorge Albalad,^a Jack D. Evans,^a Jason R. Price,^b Christian J. Doonan^{a*}
and Christopher J. Sumbly^{a*}

^a Centre for Advanced Nanomaterials and Department of Chemistry, The University of Adelaide, Adelaide, SA 5000, Australia.

^b ANSTO Melbourne, The Australian Synchrotron, 800 Blackburn Rd, Clayton, Vic 3168, Australia.



4.1. Statement of authorship

Statement of Authorship

Title of Paper	Ligand design strategies for topological control of Zirconium metal-organic frameworks for post synthetic organometallic installation		
Publication Status	<input type="checkbox"/> Published	<input type="checkbox"/> Accepted for Publication	
	<input type="checkbox"/> Submitted for Publication	<input checked="" type="checkbox"/> Unpublished and Unsubmitted work written in manuscript style	
Publication Details			

Principal Author

Name of Principal Author (Candidate)	Pol Gimeno I Fonquernie		
Contribution to the Paper	Design and development of the project. Preparation of samples and data collection. Analysis and interpretation of X-ray crystallography data and SEM-EDX data. Preparation, drafting and final version of manuscript.		
Overall percentage (%)	70%		
Certification:	This paper reports on original research I conducted during the period of my Higher Degree by Research candidature and is not subject to any obligations or contractual agreements with a third party that would constrain its inclusion in this thesis. I am the primary author of this paper.		
Signature		Date	13 - 07 - 2023

Co-Author Contributions

By signing the Statement of Authorship, each author certifies that:

- i. the candidate's stated contribution to the publication is accurate (as detailed above);
- ii. permission is granted for the candidate to include the publication in the thesis; and
- iii. the sum of all co-author contributions is equal to 100% less the candidate's stated contribution.

Name of Co-Author	Jorge Albalad		
Contribution to the Paper	Assisted with conception of the project and drafting of the manuscript.		
Signature		Date	17/7/2023

Name of Co-Author	Jack D. Evans		
Contribution to the Paper	Design and development of the computational studies.		
Signature		Date	28/7/23

Please cut and paste additional co-author panels here as required.

Name of Co-Author	Jason R. Price
Contribution to the Paper	Assisted with collection, analysis and interpretation of X-ray crystallography data.
Signature	<i>Signed on behalf of Jason R. Price</i> 15/8/2023

Name of Co-Author	Christian J. Doonan
Contribution to the Paper	Assisted with conception of the project, experiment design and drafting of the manuscript.
Signature	31/7/2023

Name of Co-Author	Christopher J. Sumby
Contribution to the Paper	Assisted with conception of the project experiment design, drafting of the manuscript and analysis of X-ray crystallography data.
Signature	26/7/2023

4.2. Introduction

The topology of a metal-organic framework (MOF) plays a crucial role in determining its stability, and its adsorption, separation, and catalytic properties.¹⁻³ Different topologies result in distinct pore shapes and sizes that can significantly impact guest adsorption and selectivity of the MOF toward particular adsorbates.⁴ Similarly, topology can determine substrate and product diffusion rates and thereby catalytic properties.^{5, 6} Despite extensive research on the reticulation of MOFs and the development of the secondary building block (SBU) approach⁶⁻⁸ to MOF design, with the exception of highly connected SBUs,⁹ predicting MOF structures remains a challenge as multiple net topologies exist for a given combination of metal node and link geometries.¹⁰⁻¹² Therefore, understanding topological control in MOFs is crucial to provide phase pure samples and ensure the topology with the most suitable performance characteristics is obtained.¹³

Zirconium (Zr) based MOFs have attracted increasing interest since their 2008 discovery due to the exceptional strength of the Zr-O bond, which enables the formation of highly stable and robust materials.¹⁴⁻¹⁶ The typical Zr cluster consists of six Zr atoms forming an octahedron that can coordinate up to 12 carboxylate groups, resulting in a wide variety of topologies with 4, 5, 6, 8, 10, and 12-connected clusters.¹¹ Several studies have provided understanding of the different connectivities of Zr clusters.¹⁷ For instance, the formation of the *ftw* topology, formed by the combination of a 12-connected cluster and a square linker, is only possible with square linkers where the oxygen atoms of the carboxylate groups are in plane with the core of the linker.¹⁸ The use of a rectangular linkers, substituents or bulky ligands to induce an out-of-plane arrangement of the carboxylate groups leads to the formation of an 8-connected cluster.¹⁹ In some of these cases, different topologies can be possible from the same metal cluster and linker connectivity, and control of Zr MOF topology becomes more challenging. An illustrative example is the reaction of the cubic 8-connected Zr-cluster with a tetratopic linker, which can lead to the formation of four different topologies: *flu* when the linker adopts a tetrahedral arrangement of the donors and *csq*, *scu*, and *sqc* when the linker adopts a planar conformation (Figure 4.1). Several studies have probed the factors, such as the presence of bulky substituents in the organic linker,^{20, 21} synthetic conditions,^{22, 23} modulator rigidity and co-modulator acidity,²⁴ that can influence the formation of different topologies. Furthermore, in certain cases, the addition of a seed of a phase pure MOF has been shown to be required for the synthesis of a particular MOF, while the absence often leads to the formation of a mixture of phases.²⁵

Despite the existence of four possible topologies from reacting a cubic 8-connected Zr-cluster with a tetratopic linker, previous studies have mainly focused on differentiating between

the formation of the *flu*, *scu* and *csq* topologies.²⁰⁻²³ This is primarily due to the rarity of MOFs with the *sqc* topology, with only two reported examples to date.^{26, 27} Notably, our group recently reported the synthesis of a MOF with the *sqc* topology (UAM-1000).²⁷ In this MOF and braced analogues (UAM-1001), a flexible linker containing free bis-pyrazole groups allows for post-synthetic metalation (PSMet) with dinuclear complexes. PSMet is a widely applied technique that allows the functionalization of MOFs with secondary, often non-structural metal centres, conferring MOFs with novel physical, optical, sorption and catalytic properties. Given that Zr-MOFs based on tetratopic carboxylate linkers can access different topologies, control over MOF topology can therefore be used to dictate the outcome of PSMet as the spatial disposition of the metalation sites can lead to the isolation of different metalation products.

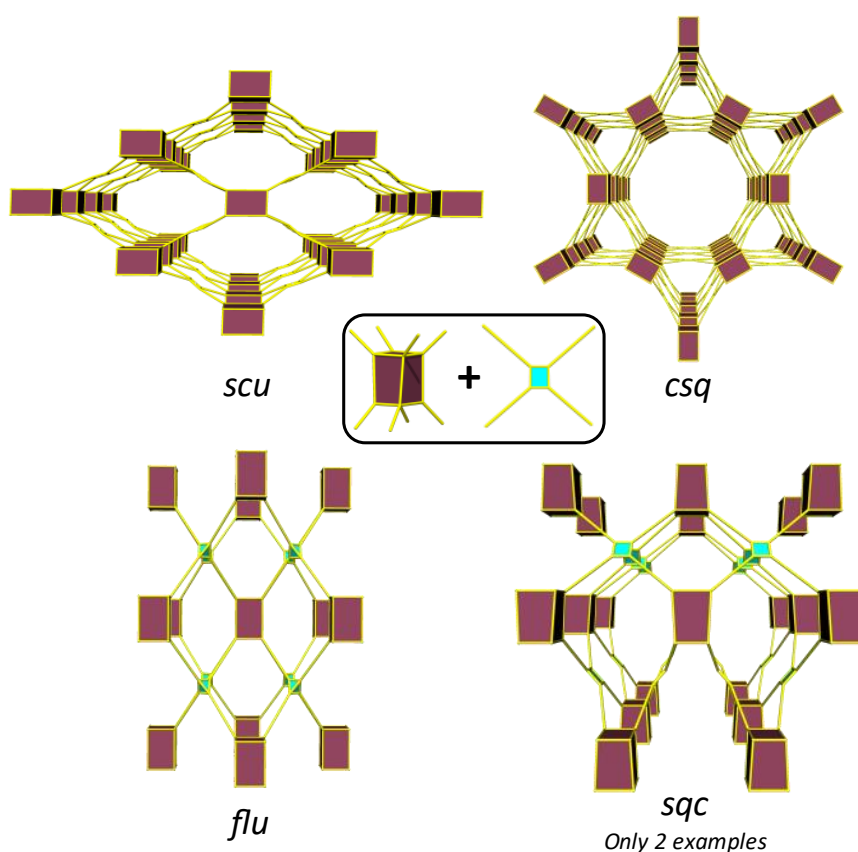


Figure 4.1. Representations of the four different topologies that can be formed from a cubic 8-connected cluster and a tetratopic linker. The maroon polyhedron represents the cluster and the blue shaded rectangle with yellow lines represents the organic linker.

To enhance our understanding of the synthesis of Zr-MOFs for PSMet, and provide insights into the formation of the *sqc* topology in UAM-1000, this study investigates the effect of flexible tetrapyrazole carboxylate linker metrics on MOF topology. Starting from the linker 1,1,2,2-tetrakis[4-(4-carboxyphenyl)-1H-pyrazol-1-yl]ethane (TCPE), which was used to form UAM-1000, we modified the length and width of the linker, resulting in two new linkers: 1,1'-methylenebis(1H-

pyrazole-4-carboxylic acid) (L1H₄) and 1,4-bis(bis(4-carboxy-1H-pyrazol-1-yl)methyl)benzene (L2H₄). Each linker, including TCPE, was reacted with ZrCl₄ under different conditions to evaluate the formation of different topologies, allowing an assessment of the characteristics needed to form the different MOFs and the effect of MOF topology on PSMet outcome. Overall, the study reports the synthesis and characterization of three new Zr-MOFs (UAM-10, UAM-11, and UAM-1002), each containing non-coordinated bis-pyrazole units, and investigates their potential for PSMet, showing the ability to form metalation sites for discrete mononuclear and dinuclear complexes.

4.3. Experimental Section

4.3.1. Materials and methods

Unless otherwise stated, all chemicals were obtained from commercial sources and used as received. 1,1,2,2-Tetrakis[4-(4-carboxyphenyl)-1H-pyrazol-1-yl]ethane^{28, 29} and 1,4-bis(dibromomethyl)benzene³⁰ were synthesized following an already reported procedure. Acetonitrile (MeCN) was dried from CaH₂ under N₂ and degassed with Ar prior to use.

Powder X-ray Diffraction (PXRD) data were collected on a Bruker Advanced D8 diffractometer (capillary stage) using Cu K α radiation (λ = 1.5456 Å, 40 kW/40 mA, 2θ = 2–52.94°, ϕ rotation= 20 rotations/min, at 1 s exposure per step with 5001 steps, and using 0.5 mm glass capillaries). Fourier Transform Infrared Spectroscopy (FTIR) spectra were collected on a Shimadzu IR spirit using ATR mode (Spectral range: 7800 – 350 cm⁻¹). Nuclear Magnetic Resonance (NMR) spectra were collected at 25 °C in deuterated solvents on an Agilent DD2 500 MHz NMR with a 5 mm OneNMR probe, using tetramethylsilane (TMS) signals as the internal reference standard.

Scanning Electron Microscopy (SEM) images were collected, and Energy Dispersive X-ray (EDX) analysis performed on a FEI Quanta 450 field-emission scanning electron microscope, operating at 10.0 – 20.0 kV and under ultra-high vacuum (10⁻⁷ – 10⁻¹² hPa) conditions.

Gas adsorption measurements were performed on a Micromeritics 3-Flex surface area and pore size analyser. Activation conditions for each sample is stated in figure captions (Figure III.10, Figure III.15, Figure III.21, Figure III.30 – III.32).

Thermogravimetric analysis data was collected on an STA 449 F3 Jupiter analyser from 45 °C – 700 °C at 5 °C/min under 21% O₂, 79% N₂.

4.3.2. Molecular simulations

The ligands L1, L2 and L3 were considered as the corresponding acid and the conformational landscape was assessed using the Conformer-Rotamer Ensemble Sampling Tool (CREST)³¹ with an energy window of 30 kJ/mol and energies computed using GFN2-xTB³² with implicit solvation of DMF considered by the analytical linearized Poisson-Boltzmann approach.³³

Framework models were produced using the weaver code³⁴ and resulting frameworks first optimised using the UFF³⁵ as implemented by the lammps-interface³⁶ using the lammps simulation engine.³⁷ Subsequently, the geometry and cell parameters for these frameworks were optimised using density functional theory (DFT). These calculations used the PBE functional³⁸, Goedecker-Teter-Hutter pseudopotential³⁹ and D3 London dispersion corrections,⁴⁰ together with a double-zeta valence (DZVP) basis set. A grid cutoff of 800 Ry was employed and a relative cutoff of 70 Ry. The DFT approach used the QUICKSTEP⁴¹ module of the CP2K program package.⁴² Pore metrics of these frameworks were computed using the Zeo++ software package.⁴³ Frameworks based on different anti-anti or syn-syn ligand conformations were considered at the classical level of theory (UFF) and the framework was constructed based on the lowest energy conformer observed with anti-anti or syn-syn arrangement.

4.3.3. Single Crystal X-ray Diffraction

Single crystals were mounted in Paratone-N oil on a MiTeGen micromount. Single-crystal X-ray data of UAM-10, UAM-11 and UAM-1002 were collected at 100 K on the MX1 or MX2 beamlines of the Australian Synchrotron using the Blue-ice software interface,⁴⁴ $\lambda = 0.71073 \text{ \AA}$ and absorption corrections were applied using multiscan methods using XDS.^{45, 46} UAM-1002[PdCl₂] was collected at 100 K on a Rigaku XtaLAB Synergy-s diffractometer equipped with a HyPix-6000HE detector. The structures were solved using SHELXS or SHELXT,^{47, 48} and refined by full-matrix least squares on F^2 by SHELXL,⁴⁹ interfaced through the program X-Seed or OLEX.^{50, 51} In general, all atoms were refined anisotropically and hydrogens atoms were included as invariants at geometrically estimated positions, unless specified otherwise in additional details in supporting information. Where noted, the data was treated with the SQUEEZE routine available in Platon⁵² or using the solvent masking feature of Olex. Figures were produced using the software Diamond Version 4.6.8. X-ray experimental data is given in Table III.4. CIF data have been deposited with the Cambridge Crystallographic Data Centre, CCDC reference numbers CCDC 2288076-2288079 (2288076 = UAM-10; 2288077 = UAM-11; 2288079 = UAM-1002; 2288078 = UAM-1002[PdCl₂]).

4.3.4. Synthetic protocols

4.3.4.1. Synthesis of 1,1'-methylenebis(1H-pyrazole-4-carboxylic acid) (L1H₄)

Ethyl 1*H*-pyrazole-4-carboxylate (5.1 g, 0.036 mmol) and potassium carbonate (2.0 g, 0.036 mmol) were dissolved in 10 mL of DMSO, and the resulting solution was stirred for 1 h at 80 °C. After that, a solution of 1,1,2,2-tetrabromoethane (1.16 mL, 0.010 mmol) in 15 mL of DMSO was added dropwise before being left to stir overnight at 80 °C. The mixture was cooled to room temperature and poured into water (250 mL) to precipitate a white solid. The solid was collected, washed with water and 3:7 ethanol/water, and dried in air to give the ester-protected compound. Deprotection was achieved by boiling the white solid in 1 M NaOH overnight. The resulting solution was acidified with 4 M HCl to pH 2 to precipitate H₄L1 as a white solid, which was subsequently collected, washed with water and acetone, and dried under vacuum overnight. Yield: 1.8 g (40%). ¹H NMR (500 MHz, DMSO-*d*₆): 12.62 (s, 4H, COOH), 8.69 (s, 4H, CH₂ pyrazole), 8.52 (s, 2H, N-CH-N), 7.84 (s, 4H, CH₂ pyrazole). ¹³C-NMR spectrum (500 MHz, DMSO-*d*₆): 162.98 (COOH), 141.86 (C pyr), 134.76 (C pyr), 116.03 (C py), 71.98 (C-sp³). MS (ESI): calcd for C₁₈H₁₃N₈O₈⁺ [M]⁺ 469.08, found 469.08.

4.3.4.2. Synthesis of 1,4-bis(bis(4-carboxy-1H-pyrazol-1-yl)methyl)benzene (L2H₄)

Ethyl 1*H*-pyrazole-4-carboxylate (5.1 g, 0.036 mmol) and potassium carbonate (2.0 g, 0.036 mmol) were dissolved in 10 mL of DMSO, and the resulting solution was stirred for 1 h at 80 °C. After that, a solution of 1,4-bis(dibromomethyl)benzene (4.21 g, 0.010 mmol) in 15 mL of DMSO was added dropwise before being left to stir overnight at 80 °C. The mixture was cooled to room temperature and poured into water (250 mL) to precipitate a white solid. The solid was collected, washed with water and 3:7 ethanol/water, and dried in air to give the ester-protected compound. Deprotection was achieved by boiling the white solid in 1 M NaOH overnight. The resulting solution was acidified with 4 M HCl to pH 2 to precipitate H₄L2 as a yellow solid, which was subsequently collected, washed with water and acetone, and dried under vacuum overnight. Yield: 1.08 g (22%). ¹H NMR (500 MHz, DMSO-*d*₆): 12.62 (s, 4H, COOH), 8.37 (s, 4H, CH₂ pyrazole), 8.25 (s, 2H, N-CH-N), 7.98 (s, 4H, CH₂ pyrazole), 7.25 (s, 4H, CH phenyl). ¹³C-NMR spectrum (500 MHz, DMSO-*d*₆): 163.22 (COOH), 141.80 (COOH), 136.21 (C pyr), 134.04 (C pyr), 127.72 (C phey), 116.09 (s, 4H, C pyr), 75.93 (C-sp³). MS (ESI): calcd for C₂₄H₁₇N₈O₈⁺ [M]⁺ 545.12, found 545.12.

4.3.4.3. Synthesis of UAM-10

ZrCl₄ (12 mg, 0.05 mmol) and L1H₄ (10 mg, 0.02 mmol) were dissolved in 0.5 mL of DMF by sonicating the initial suspension (2 min). Acetic acid (0.8 mL, 14 mmol, 280 mol. eq.) was then added to the solution, and the resulting mixture was transferred to a solvothermal scintillation vial, capped tightly, and heated at 120 °C for 24 h. Colourless needle shaped crystals of UAM-10 were collected by filtration and washed with DMF (4 x 5 mL), acetone (3 x 5 mL) and dried under vacuum for 24 h.

4.3.4.4. Synthesis of UAM-11

ZrCl₄ (12 mg, 0.05 mmol) and L2H₄ (10 mg, 0.018 mmol) were dissolved in 0.5 mL of DMF by sonicating the initial suspension (2 min). Acetic acid (0.5 mL, 8.74 mmol, 175 mol. eq.) was then added to the solution, and the resulting mixture was transferred to a solvothermal scintillation vial, capped tightly, and heated at 120 °C for 72 h. Yellow clumped block shaped crystals of UAM-11 were collected by filtration and washed with DMF (4 x 5 mL), acetone (3 x 5 mL) and dried under vacuum for 24 h.

4.3.4.5. Synthesis of UAM-1000

UAM-1000 was synthesized by modifying an already reported procedure.²⁷ Briefly, ZrCl₄ (12 mg, 0.05 mmol) and TCPE (10 mg, 0.018 mmol) were dissolved in 2 mL of DMF by sonicating the initial suspension (2 min). Acetic acid (0.5 mL, 8.74 mmol, 175 mol. eq.) was then added to the solution, and the resulting mixture was transferred to a solvothermal scintillation vial, capped tightly, and heated at 120 °C for 72 h. Colourless octahedral crystals of UAM-1000 were collected by filtration and washed with DMF (4 x 5 mL), acetone (3 x 5 mL) and dried under vacuum for 24 h. Alternatively, UAM-1000 can be synthesized by replacing acetic acid for trifluoroacetic acid (0.3 mL, 3.92 mmol, 78 mol. eq.) or benzoic acid (300 mg, 2.46 mmol, 49 mol. eq.).

4.3.4.6. Synthesis of UAM-1002

ZrCl₄ (12 mg, 0.05 mmol) and formic acid (0.5 mL, 8.74 mmol, 175 mol. eq.) were dissolved in 1 mL of DEF by sonicating the initial suspension (2 min) and the solution was heated to 100 °C for 1 h. A solution of TCPE (10 mg, 0.018 mmol) in DEF (1 mL) was then added, and the resulting mixture was transferred to a solvothermal scintillation vial, capped tightly, and heated at 120 °C for 72 h. Colourless needle shaped crystals of UAM-1002 were collected by filtration and washed with DEF (4 x 5 mL), acetone (3 x 5 mL) and dried under vacuum for 24 h.

4.3.4.7. Synthesis of UAM-1002[PdCl₂]

UAM-1002 crystals (two batches, ca. 50 mg, 0.028 mmol) were soaked in 3 mL of dry acetonitrile. An excess of PdCl₂ (~5 mg) was added, and the solution was heated to 80 °C for 16 h. The sample was then washed by decantation with dry acetonitrile (4 x 4 mL) and with dry toluene (4 x 4 mL). The orange crystals (54 mg, quantitative) were left in solution for characterization by SCXRD. SEM-EDX molar ratio 3.0(Zr):2.0(Pd):4(Cl).

4.4. Results and discussion

4.4.1. Linker synthesis and preferred conformation

The new flexible tetrapyrazole carboxylate linkers, 1,1'-methylenebis(1H-pyrazole-4-carboxylic acid) (L1H₄) and 1,4-bis(bis(4-carboxy-1H-pyrazol-1-yl)methyl)benzene (L2H₄), were synthesized using a similar two-step synthesis procedure, where ethyl 4-carboxypyrazole was coupled to 1,1,2,2-tetrabromoethane or 1,4-bis(dibromomethyl)benzene, followed by deprotection of the ester groups. The synthesis of both linkers was confirmed by ¹H-NMR (Figure III.1-III.2), ¹³C-NMR (Figure III.3-III.4).

Given that at least three topologies are accessible for a cubic 8-connected cluster and a flexible rectangular tetratopic linker, simulations were employed to explore the conformational flexibility of TCPE and these new ligands, thereby unveiling their preferred conformation (Figure 4.1). A series of possible and unique conformers in a relative energy window of 30 kJ/mol were computed. The different dihedral angles of the resulting ensembles of conformers were analysed to consider the arrangement of framework forming bonds. Specifically, two sets of NNNN dihedrals were measured, which dictate the syn or anti conformation for each set of pyrazole units, and the HCCH angle that describe the relative positions of the carboxylate groups (planar or tetrahedral) was determined (Figure 4.1). Analysis of the NNNN dihedral angle for each of the ligands reveals that L1H₄ and TCPE access similar conformational space (Figure 4.1a, 4.1c) showing the anti-anti conformation of the bis-pyrazole units is the lowest in energy (NNNN ~+-180°). The longer arm length (width) of TCPE seems to facilitate the transition from anti-anti to syn-syn conformation as it shows intermediate conformers lower in energy, which suggest an easier transition. A different outcome was observed for L2H₄. Analysis of the NNNN dihedral angles for L2H₄ reveals a greater range of conformations with low energy but the perfect syn-syn and anti-anti conformations (NNNN ~+-180°) are not accessible owing to steric hinderance of the central phenyl ring. Conformations closed to anti-anti conformations (NNNN ~+-180°) have the lowest energy. In all cases, we observe the same trends in energy for syn and anti conformations

of the pyrazole units as previously reported for a similar bis-pyrazole carboxylate ligand,⁵³ with an energy difference disfavoured the syn-conformations on the order of 5-10 kJ/mol.

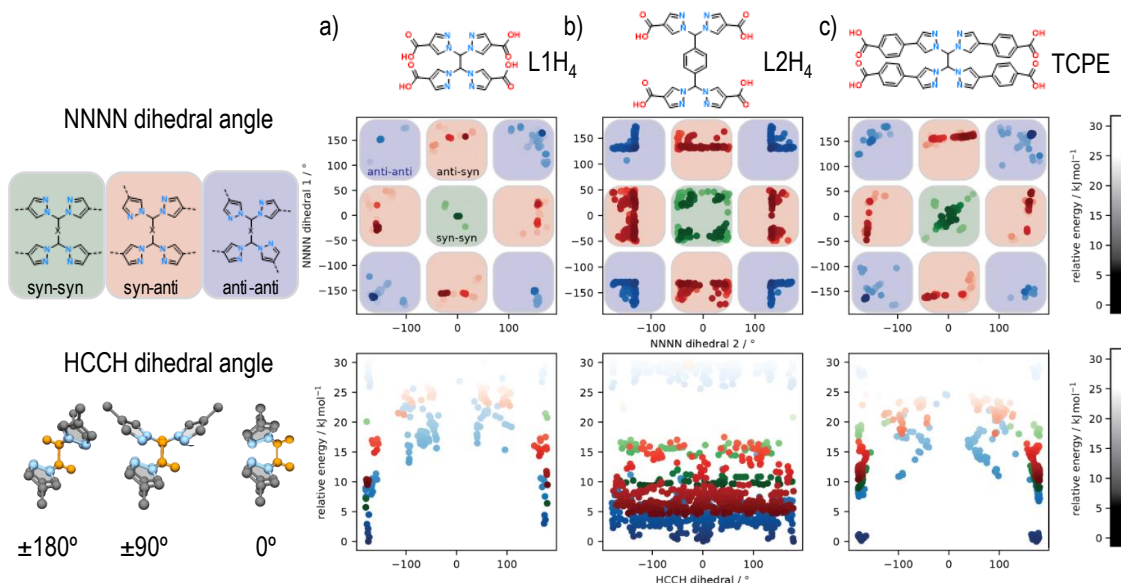


Figure 4.2. Plots of the simulation output showing the relative energy of different conformations of L1H₄, L2H₄ and TCPE upon changing the NNNN dihedral angle of the bis-pyrazole groups (top row) and the HCCH dihedral angle of the ethylene bridge (bottom row). Colour intensity is indicative of the relative energy, with darker colours being lower in energy and lighter colours higher in energy. On the left of the plots there are representations of the representative conformations upon changing each of the respective dihedral angles. In the representation of the HCCH dihedral angle (bottom-left), the H and C atoms are highlighted in orange.

Analysis of the HCCH angle, reveals the effect of the phenyl unit on L2H₄, where the HCCH dihedral of the central methyl groups, which in turn dictates positions of carboxylates (planar or tetrahedral), can rotate almost without restriction. In comparison, L1H₄ and TCPE are restricted to approximately coplanar and anti HCCH conformations. Overall, these simulations demonstrate that a range of different conformations are possible for these flexible tetrapyrazole carboxylate linkers, but the individual bis-pyrazole units typically prefer one of two possible arrangements (anti preferred over syn). In terms of the overall linker geometry, L1H₄ and TCPE are restricted to broadly anti HCCH conformations but the phenyl spacer of L2H₄ provides even greater conformational flexibility. Based on the restricted flexibility seen in the conformational modelling, it is anticipated that certain MOF topologies should be favoured by the three ligands, with the *flu* topology likely to be accessible for L2H₄, but L1H₄ and TCPE likely restricted to the *csq*, *scu*, and *sqc* topologies (e.g., UAM-1000, based on TCPE, adopts the *sqc* topology).

4.4.2. MOF synthesis and structures

With this information in hand, we investigated the synthesis of MOFs with the two new linkers. Reaction of L1H₄ with ZrCl₄ using an acetic acid (AcH) modulator in dimethylformamide (DMF) yielded colourless needle-shaped crystals corresponding to a MOF with a chemical formula of [Zr₆(μ₃-OH)₈(μ₂-CH₃COO)₄(L1)₂] (UAM-10) (Figure III.5). SCXRD revealed the MOF to have a 3D structure that consists of an 8-connected octahedral Zr₆ cluster forming the common cubic SBU (Figure 4.2). L1 adopts a rectangular geometry where all four carboxylate groups sit in a plane, as suggested by calculations, connecting four Zr-SBUs. The 3D structure has an *scu* topology with 17.0 by 15.8 Å rhombic channels that are accessible along the *c* axis (Figure 4.2, Figure III.6). The proximity of the Zr-clusters in the *c*-axis leads to these being bridged by acetate groups (Figure III.7). PXRD analysis of a bulk sample of UAM-10 confirmed phase purity (Figure III.8). Thermogravimetric analysis (TGA), after activation under vacuum at room temperature, reveals thermal stability up to 350 °C (Figure III.9) typical of Zr-MOFs. A 77K N₂ adsorption isotherm of UAM-10 after activation shows the material to be porous to nitrogen with a type I isotherm, a Brunauer–Emmett–Teller (BET) surface area of 864 m²g⁻¹ (Figure III.10) and a total pore volume of 0.28 cm³g⁻¹.

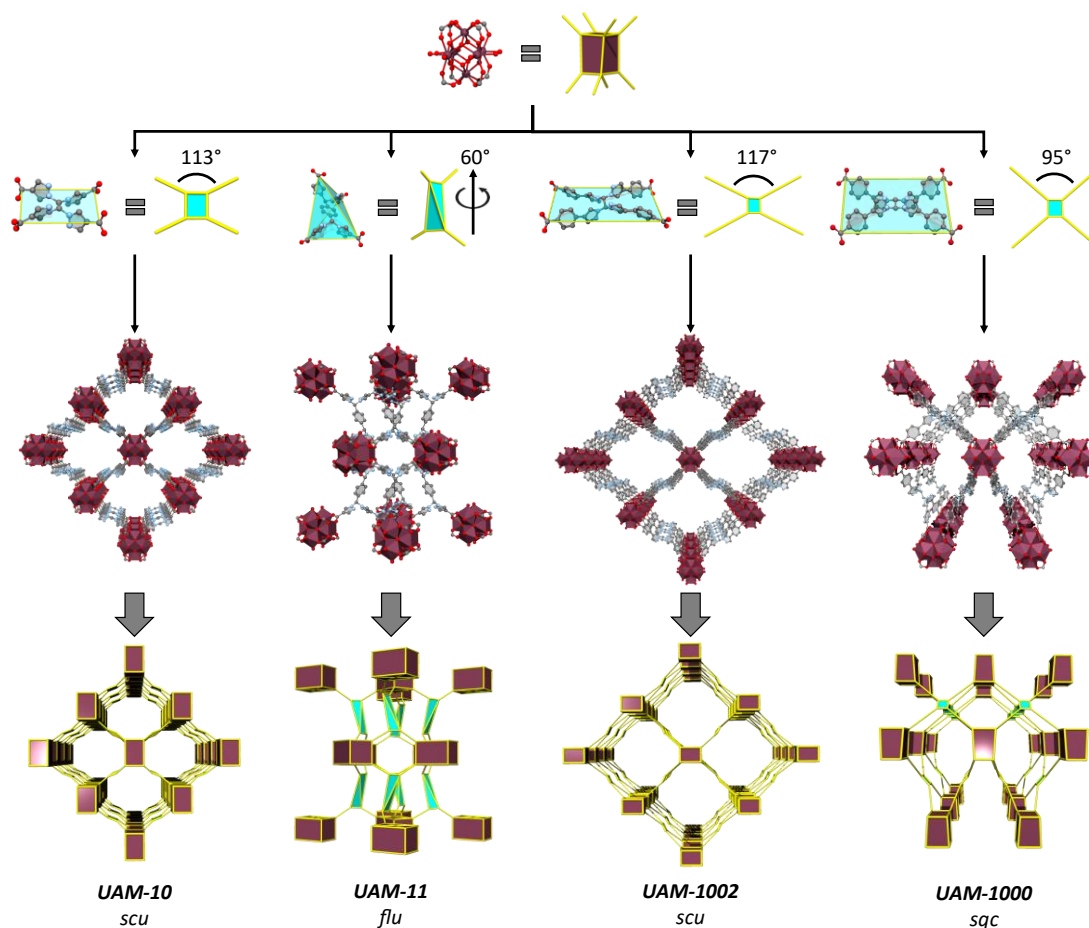


Figure 4.3. A summary of the synthesis, structure and topologies of UAM-10, UAM-11, UAM-1002 and UAM-1000. All four MOFs are formed from the same 8-connected cubic Zr-cluster but different linkers and linker conformations lead to the formation of different MOF topologies, in part governed by the restrictions on linker flexibility. The maroon polyhedron represents the cluster and the blue shaded rectangle/polyhedron with yellow lines represents the organic linker.

Reaction of L2H₄, which possesses the phenyl spacer that leads to decoupling of the bis-pyrazole units, with ZrCl₄ and an AcH modulator in DMF yielded pale yellow crystals corresponding to a MOF with a chemical formula of [Zr₆(μ₃-OH)₈(μ₂-CH₃COO)₄(L2)₂] (UAM-11) (Figure III.11). UAM-11 also has the cubic 8-connected SBUs with each L2 connecting four Zr SBUs. However, in this case, L2 adopts a tetrahedral geometry to form a *flu* topology (Figure 4.2, Figure III.12) as might be anticipated from the analysis of preferred conformations. Phase purity of the sample was confirmed by PXRD (Figure III.13) and TGA also reveals thermal stability up to 350 °C (Figure III.14). A 77K N₂ adsorption isotherm of UAM-10 after activation shows the material to be porous to nitrogen with a type I isotherm, a BET surface area of 844 m²g⁻¹ (Figure III.15) and a total pore volume of 0.27 cm³g⁻¹. Despite the ligand length being increased from L1 to L2, the greater flexibility of L2 facilitates access to the more dense *flu* topology and thereby a similar BET surface area and total pore volume.

The formation of UAM-1000 as the product of the reaction of TCPE with $ZrCl_4$ using trifluoroacetic acid (TFA) as modulator in DMF was recently reported by our group.²⁷ The synthesis was reported using TFA as modulator. As the use of different solvents and modulators could lead to different topologies, we reinvestigated the synthesized UAM-1000. Using AcH as the modulator, UAM-1000AA (acetic acid) was formed and PXRD analysis confirmed the formation of UAM-1000 as the sole product (Figure III.16). Briefly, UAM-1000 consists of the cubic Zr-SBU with each linker connecting four Zr-SBUs to form a MOF with *sqc* topology (Figure 4.2, 2nd example reported).^{7, 26} UAM-1000 can also be synthesized in DMF in using benzoic acid (BA) (UAM-1000BA) and TFA (UAM-1000TFA) as confirmed by PXRD (Figure III.16). However, a different structure and topology is formed when using both DEF as the solvent and formic acid (FA) as the modulator; using FA in DMF only gives amorphous material. Using the other modulators (AA, BA, and TFA) in DEF also gives amorphous material except in the case of BA which leads to the formation of the *sqc* topology (UAM-1000). Reaction of TCPE with $ZrCl_4$ in the presence of DEF using FA as modulator provides UAM-1002, which forms as large colourless needle-shaped crystals that could be characterized by SCXRD (Figure III.17). Structure solution and refinement by SCXRD revealed the formation of a MOF with an *scu* topology, like UAM-10, but where the Zr clusters are not bridged by the carboxylate group of the modulator (Figure 4.2, Figure III.18). PXRD analysis of bulk UAM-1002 confirmed phase purity of the samples (Figure III.19). Thermogravimetric analysis (TGA) analysis, after activation under vacuum at room temperature, reveals thermal stability up to 475 °C (Figure III.20). A 77K N_2 adsorption isotherm of UAM-1002 after thermal activation shows a BET surface area of 138 m^2g^{-1} (Figure III.21) and a total pore volume of 0.04 cm^3g^{-1} . These values are considerably lower than expected based on calculations conducted on the crystal structure (3400 m^2g^{-1} and 1.14 cm^3g^{-1}). Activation under supercritical CO_2 showed a slight increase in porosity with a BET of 567 m^2g^{-1} (Figure III.21) and a total pore volume of 0.18 cm^3g^{-1} . However, this remained much lower than the calculated values. We hypothesize that the larger pore volume and anticipated flexibility of UAM-1002 is allowing partial collapse of the structure upon activation. PXRD data (Figure III.22) for activated UAM-1002 (UAM-1002·activated) shows peaks associated with hkl planes (0,2,0), (0,0,1) and (2,0,0) shift compared to those in as-synthesised UAM-1002. While the activated structure was not able to be determined by SCXRD, the PXRD changes and the loss of accessible pore volume is consistent with a transition to a closed phase, as is observed with other similar MOFs (e.g. MIL-53 type MOFs, CuMOF-1...).⁵⁴⁻⁵⁶

4.4.3. Topologies of UAM-10, UAM-11, UAM-1002 and UAM-1000

Zr clusters with 4, 5, 6, 8, 10, and 12-connected SBUs have been reported, but the 8 and 12-connected examples are the most common. Thus, we will focus on possible topologies with the 8-connected Zr-SBU (cubic) and the 12-connected SBU (cuboctahedra), and considering that all linkers used are tetratopic linkers, only six topologies are possible. Among the six topologies, *ftw* is only accessed with a planar linker and a cuboctahedral SBU, *ith* is the only combination for a tetrahedral linker and a cuboctahedral SBU, and *flu* is the only possibility of a tetrahedral linker and the cubic SBU. Finally, three possible topologies can be formed with a cubic SBU and a planar linker: *csq*, *scu*, and the less common *sqc*.

To understand the linker preferences for different topologies we produced hypothetical models for each framework. We used single conformation of each ligand (based on the lowest energy conformer discovered above) and arranged these to produce likely framework structures for each of the six possible topologies. There are an immense number of combinations of inorganic node and ligand orientations⁵⁷ but here only a single representative framework was produced to provide a reasonable model for each topology and ligand. We note, the production of framework models of complex topologies, where there are many possible linker orientations and conformations, are challenging and require exhaustive search approaches.³⁴ In this study a single arrangement of the ligands with a single conformation were considered. As a result, these hypothetical frameworks serve as a simple guide of the energy landscape for these topologies.

The *ftw* topology is edge-transitive and, as noted, based on a cuboctahedral SBU and a square linker. It is the most common topology, when possible, as the Zr_6 cluster is fully saturated with the maximum number of carboxylates it can accommodate. However, studies have shown that for this to be possible, the torsion angle between the carboxylates with the backbone (core) of the linker needs to be close to 0° .¹⁸ As the linkers used in this work have two sp^3 carbons, the pyrazole and phenyl rings are out of the plane formed by the carbon of the carboxylic groups. As the carboxylates are conjugated with the aromatic rings they are attached to, they are going to be out of that plane too, making the *ftw* topology very unlikely. This is evidenced by analysis of the MOF structures reported in this work; none of the structures have the carboxylates in plane with the core of the linker, and thus ruling out the *ftw* topology (Figure III.23). The hypothetical structure for the ligands arranged in the *ftw* topology also shows significant strain based on observation of the framework structure. This strain may be partially offset by the fully saturated cluster, but this does not represent a likely framework product. If the linkers adopted a tetrahedral geometry, *ith* could also be possible. However, this topology is rare, as it is challenging to form a

cuboctahedra SBU with a tetrahedral linker; the single example reported was obtained as a byproduct and could not be obtained phase pure.⁵⁸

Since the *ftw* and *ith* topologies are unlikely products, we turned our attention to evaluating the topologies that can be formed with a tetratopic linker and the 8-connected (cubic) Zr-SBU. The combination of a tetratopic linker and a cubic SBU can lead to four different topologies: *csq*, *scu*, *sqc* and *flu*. The energetics of the framework formation for all different linkers in the possible topologies suggest the *csq* topology is lowest in energy for L1 and TCPE and the *scu* topology for L2 (Table III.1). However, there does not appear to be a large difference in the relative energies for each of the topologies and this suggests all are likely for the three linkers. Notably we find the spread of energies becomes significantly lower in TCPE (~0.005 eV/atom) compared to L1 (~0.1 eV/atom) demonstrating that larger more flexible ligands can provide access to a greater range of topologies than smaller, more rigid, ligands.

As noted, all three linkers contain two sp³ carbons, and they can adopt either a tetrahedral or square planar conformation. In the case where the linker adopts a tetrahedral conformation, only one topology is expected: *flu*. This is observed in UAM-11 due to the conformational flexibility of the central phenyl group, allowing L2 to adopt a "tetrahedral-like" conformation with a torsion angle of 60° between all four carboxylates forming a distorted *flu* topology. It is not clear why L2 prefers to adopt a tetrahedral conformation over a square planar conformation but one hypothesis is that the small energy difference between the different HCCH dihedral angles observed in the study of the free ligand means that it does not favour any specific angle within the MOF that is formed. Consequently, we hypothesize that *flu* could be favoured because out of the four possible topologies *flu* is the only topology that does not form channels, and rather it forms a more rigid and stable structure with large pores accessible only through smaller pore apertures. While other topologies for L2 based MOFs might be accessible based on the simulation data, attempts to induce the formation these by altering the synthetic conditions were unsuccessful, resulting in the production of either amorphous powders or the same *flu* topology.

When the linker adopts a square/rectangular planar geometry, instead of a tetrahedral geometry, this can lead to the formation of three possible topologies: *csq*, *scu*, and *sqc*, as documented in literature.⁷ Normally, the *csq* topology is more commonly observed compared to *scu* and *sqc*. Surprisingly, none of the MOFs formed in our study had the *csq* topology despite this being predicted to be energetically possible (further discussion below); however, our

simulation approach did not consider the possibility of coordinating molecules that may act to bridge proximal Zr nodes which is observed in the *scu* topology, particularly for L1 (Figure III.7).

Ligand L1 is observed to form UAM-10, where the framework adopts an *scu* topology, while TCPE provides MOFs UAM-1000 and UAM-1002, which adopt *sqc* and *scu* topologies, respectively. Analysis of structures shows that the adoption of an anti-conformation and thereby a more rectangular linker results in an *scu* topology, whereas a syn conformation (and more square linker) leads to the *sqc* topology. This small difference in linker conformation looks to be important, as the *scu* topology normally forms with rectangular ligands while for the *sqc* topology appears to prefer a more square arrangement, albeit the latter is based on only two reported examples. Comparing UAM-1000 and UAM-1002 shows that the orientation of the metal clusters and the carboxylates of the ligand are the same in both UAM-1002 and UAM-1000 with the only difference being that in UAM-1000 the ligand has squarer dimensions and in UAM-1002 more rectangular (Figure 4.4). Simulations of hypothetical frameworks based on different ligand conformations of L1 and TCPE support these observations (Table III.2).

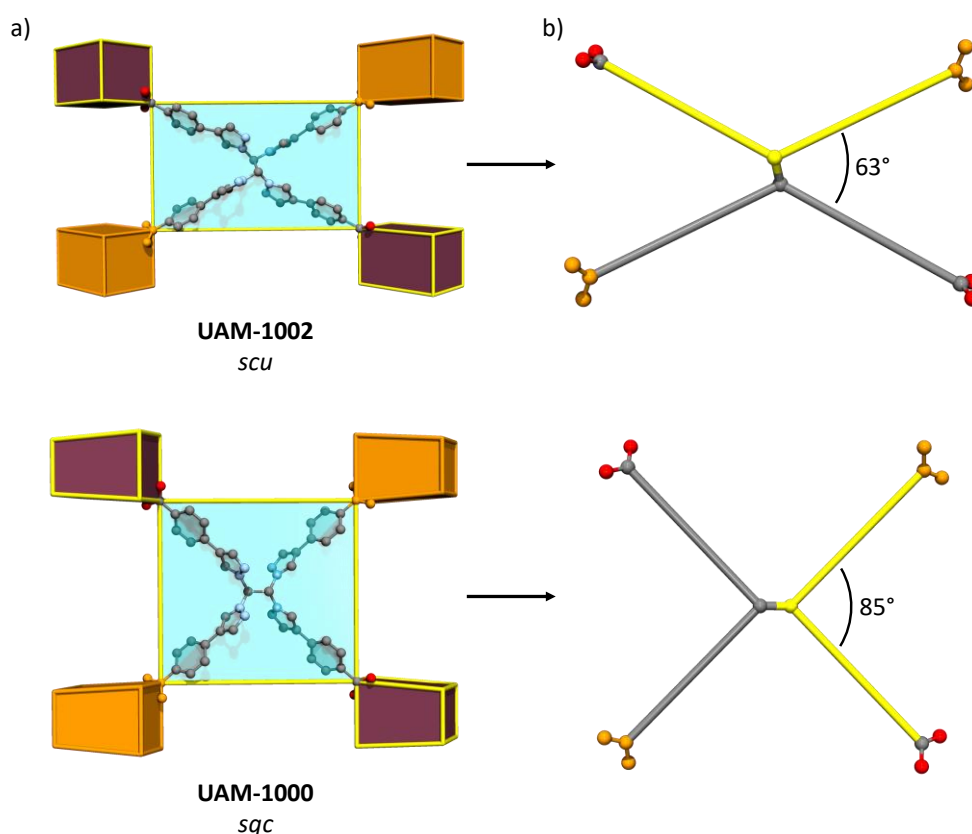


Figure 4.4. a) Representations of the *scu* (top) and *sqc* (bottom) MOF topologies showing the linker orientation and disposition that allows it to be connected to four cubic clusters that are in the same orientation. b) Schematic representation of the linkers highlighting in the same colour the two arms that are attached to the same carbon of the central ethylene group.

Finally, as noted, we have observed that the *csq* topology (e.g., NU-1000 type materials) cannot be obtained with any of the linkers studied. In general, the *csq* topology tends to be favoured more with square linkers, while *scu* topology is favoured with more rectangular linkers, which is consistent with our observations in UAM-10 and UAM-1002. We hypothesize that while the linkers L1 and TCPE can adopt a squarer arrangement (seen for the latter in UAM-1000) they may be too flexible to form a *csq* topology with such large pores, consistent with its absence in this work.

4.4.4. Post-synthetic metalation of the MOFs

To evaluate the ability of the bis-pyrazole units in UAM-10, UAM-11, UAM-1000, and UAM-1002 undergo PSMet, we examined reactions conducted with a relatively inert metal (minimal leaching) that could induce an easily detectable colour change in the crystals. PdCl₂ was chosen for this purpose. Metalation of UAM-1000 with PdCl₂ was recently investigated by us.²⁷ Partial metalation (ca. 50% PSMet) was achievable at the bis-pyrazole units due to the proximity of the adjacent bis-pyrazole unit, which hindered full metalation for steric reasons. The flexibility of the linker TCPE also posed challenges for determining the structure by SCXRD, but this could be overcome by incorporating a secondary linker to create UAM-1001, where the material was effectively locked.

Considering that UAM-10 and UAM-11 have shorter ligands compared to UAM-1000, we anticipated that these compounds would be easier to metalate in a single crystal-to-single crystal manner and characterise the outcome by SCXRD. However, attempts to PSMet UAM-10 and UAM-11 with PdCl₂ was unsuccessful. SEM-EDX analysis revealed some Pd present (Table III.3); however, the metalation was inconsistent across the sample and between samples, and SCXRD analysis revealed the pyrazoles to still be in an anti-conformation. Given that UAM-10 and UAM-11 have linkers with the pyrazoles directly attached to carboxylate groups and exhibit an anti-conformation of the bis-pyrazole units in the as-synthesised form of the MOF, these results suggest there is a significant barrier to convert from anti to syn within the MOF. This is likely due to this anti to syn change requiring a significant geometric and structure metric change in the linker that cannot be tolerated by the MOF topology.

In contrast, heating crystals of UAM-1002 in an acetonitrile solution of PdCl₂ resulted in a colour change of the crystals to the typical orange colour of bis-pyrazole coordinated Pd(II) (Figure III.25). SEM-EDX analysis confirmed the presence of Pd(II) in the MOF, with a Zr:Pd ratio of 3:2 for UAM-1002 (Table III.3), consistent with full metalation of the bis-pyrazole sites. This is a notable contrast to UAM-1000, which due to the short 5.3 Å separation between two the two bis-pyrazole groups, only allows 50% metalation with PdCl₂ under similar conditions. As UAM-1002 has shown significant structural flexibility (PXRD and gas adsorption data) we also expected the crystals to diffract poorly. To our surprise, the toluene-solvated crystals (formed by solvent exchange) diffracted very well and SCXRD analysis of a crystal of UAM-1002[PdCl₂] confirmed that the Pd(II) metal centre was bound to the bis-pyrazole units in a typical square planar geometry, with two chlorides completing the coordination sphere (Figure 4.5b). Interestingly, compared to as-synthesised UAM-1002, the Zr-clusters were now significantly closer in the c-axis and bridged by formate anions (Figure 4.5a). We hypothesize that when chelating the Pd(II) centre, the pyrazoles switch from anti to syn (facilitated by the phenyl spacer in the ligand arms decoupling this motion from the carboxylates, compare with UAM-10 and UAM-11) and the overall ligand changes its donor disposition to a more anisotropic shape, which forces the Zr nodes closer. The proximity of the nodes allow the formates to change from chelating the Zr-clusters to bridging them, in turn providing more rigidity to the structure and allowing a better quality diffraction.

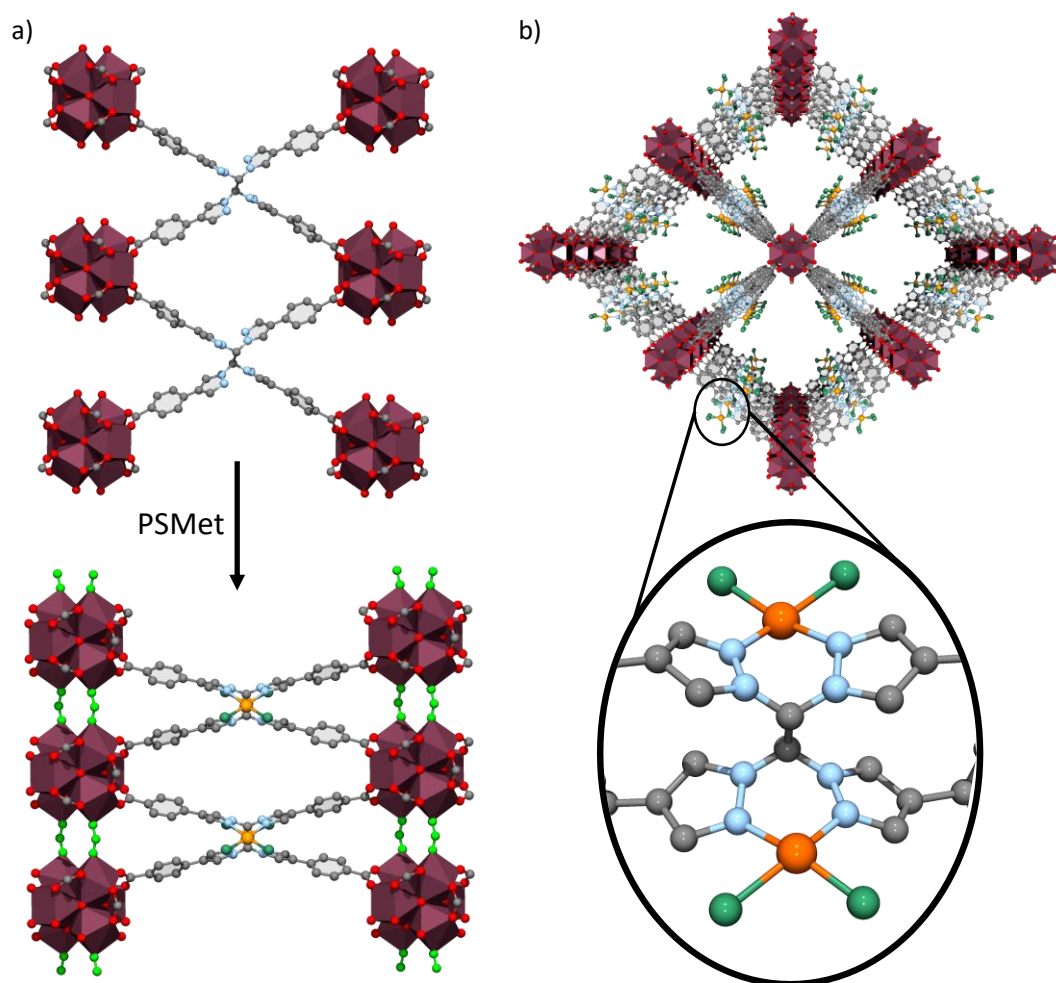


Figure 4.5. a) Representations of ligands bound to the Zr clusters in UAM-1002 (top) and UAM-1002[PdCl₂] (bottom). The transition from anti- (top) to syn-conformation (bottom) brings the Zr-clusters close enough that they end up being bridged by formate anions (represented in light green). b) Representation of the structure of UAM-1002[PdCl₂] along the c axis, with the enlargement showing the PdCl₂ complex bound to the bis-pyrazole groups with a square planar geometry.

4.5. Conclusions

In summary, we have reported a study into the formation of Zr-MOFs formed from flexible tetratopic pyrazole carboxylate linkers. Two new linkers have been reported (L1H₄ and L2H₄) and the formation of three new Zr-MOFs (UAM-10, UAM-11 and UAM-1002) observed. The combination of our experimental observations and simulations reveals that when using flexible pyrazole carboxylate linkers in the synthesis of Zr-MOFs the overall linker length and width (phenyl spacers within the arms) affects the accessible conformations of the linker, thereby limiting or allowing the synthesis of particular MOF topologies. Narrower linkers like L1H₄ are more conformationally restricted, allowing access to a single topology while wider linkers like TCPE allow synthesis of different topologies by fine tuning of the synthetic conditions. For example, the reaction of TCPE and ZrCl₄ in DMF and TFA form an *sqc* topology while the reaction in DEF and formic acid forms the *scu* topology. Interestingly, when TCPE adopts a syn-conformation the *sqc* topology appears to be preferred and when it adopts an anti-conformation it forms the *scu* topology. L2H₄ is somewhat unique in that it has significant conformational freedom yet still forms only one MOF structure preferentially. We hypothesize the formation of the uncommon *sqc* topology, rather than the *scu* and *csq*, is favoured for flexible tetracarboxylate linkers that have a square arrangement of the donors. Alternative topologies, such as *csq*, may represent unstable frameworks considering the size of the channels in this topology.

The length and width of the linker not only affects the topologies that can be formed but also the ability of the bis-pyrazole groups to transition from an anti- to a syn-conformation. Shorter and rigid linkers disfavour the transition preventing PSMet, as observed with UAM-10 and UAM-11. Wider linkers like TCPE allow easier transition from an anti to a syn-conformation as the carboxylate and pyrazole core of the ligand is decoupled, allowing PSMet. Consequently, UAM-1002 possesses the right flexibility to allow structural changes upon PSMet and the elucidation of the inserted organometallic complex. These properties, combined with large unidirectional channels make UAM-1002 a great platform that could be exploited as a crystalline sponge for the study of the chemistry that occurs at the anchored organometallic complexes.

4.6. References

1. Bhatt, P. M., Guillerme, V., Datta, S. J., Shkurenko, A. and Eddaoudi, M. *Chem*, **2020**, *6*, 1613-1633.
2. Deria, P., Gómez-Gualdrón, D. A., Hod, I., Snurr, R. Q., Hupp, J. T. and Farha, O. K. *J. Am. Chem. Soc.*, **2016**, *138*, 14449-14457.
3. Li, Z.-J., Ju, Y., Wu, X.-L., Li, X., Qiu, J., Li, Y., Zhang, Z.-H., He, M.-Y., Zhang, L., Wang, J.-Q. and Lin, J. *Inorg. Chem. Front.*, **2023**, *10*, 1721-1730.
4. Kurzydym, I. and Czekaj, I. *Technical Transactions*, **2020**, *117*, e2020012.
5. Wasson, M. C., Buru, C. T., Chen, Z. J., Islamoglu, T. and Farha, O. K. *Appl. Catal. A: Gen.*, **2019**, *586*, 117214.
6. Chen, Z., Kirlikovali, K. O., Li, P. and Farha, O. K. *Acc. Chem. Res.*, **2022**, *55*, 579-591.
7. Jiang, H., Alezi, D. and Eddaoudi, M. *Nat. Rev. Mater.*, **2021**, *6*, 466-487.
8. Yaghi, O. M., O'Keeffe, M., Ockwig, N. W., Chae, H. K., Eddaoudi, M. and Kim, J. *Nature*, **2003**, *423*, 705-714.
9. Chen, Z., Weseliński, Ł. J., Adil, K., Belmabkhout, Y., Shkurenko, A., Jiang, H., Bhatt, P. M., Guillerme, V., Dauzon, E., Xue, D.-X., O'Keeffe, M. and Eddaoudi, M. *J. Am. Chem. Soc.*, **2017**, *139*, 3265-3274.
10. Sun, D., Ma, S., Simmons, J. M., Li, J. R., Yuan, D. and Zhou, H. C. *Chem. Commun.*, **2010**, *46*, 1329-1331.
11. Chen, Z., Hanna, S. L., Redfern, L. R., Alezi, D., Islamoglu, T. and Farha, O. K. *Coord. Chem. Rev.*, **2019**, *386*, 32-49.
12. Kalmutzki, M. J., Hanikel, N. and Yaghi, O. M. *Sci. Adv.*, **2018**, *4*, eaat9180.
13. Biemmi, E., Christian, S., Stock, N. and Bein, T. *Microporous Mesoporous Mater.*, **2009**, *117*, 111-117.
14. Qiao, G.-Y., Yuan, S., Pang, J., Rao, H., Lollar, C. T., Dang, D., Qin, J.-S., Zhou, H.-C. and Yu, J. *Angew. Chem. Int. Ed.*, **2020**, *59*, 18224-18228.
15. Feng, D., Gu, Z. Y., Li, J. R., Jiang, H. L., Wei, Z. and Zhou, H. C. *Angew. Chem. Int. Ed.*, **2012**, *51*, 10307-10310.
16. Cavka, J. H., Jakobsen, S., Olsbye, U., Guillou, N., Lamberti, C., Bordiga, S. and Lillerud, K. P. *J. Am. Chem. Soc.*, **2008**, *130*, 13850-13851.
17. Koschnick, C., Terban, M. W., Frison, R., Etter, M., Böhm, F. A., Proserpio, D. M., Krause, S., Dinnebier, R. E., Canossa, S. and Lotsch, B. V. *J. Am. Chem. Soc.*, **2023**, *145*, 10051-10060.

18. Luebke, R., Belmabkhout, Y., Weseliński, Ł. J., Cairns, A. J., Alkordi, M., Norton, G., Wojtas, Ł., Adil, K. and Eddaoudi, M. *Chem. Sci.*, **2015**, *6*, 4095-4102.
19. Ma, J., Tran, L. D. and Matzger, A. J. *Cryst. Growth Des.*, **2016**, *16*, 4148-4153.
20. Pang, J., Yuan, S., Qin, J., Liu, C., Lollar, C., Wu, M., Yuan, D., Zhou, H.-C. and Hong, M. *J. Am. Chem. Soc.*, **2017**, *139*, 16939-16945.
21. Lyu, J., Zhang, X., Otake, K.-I., Wang, X., Li, P., Li, Z., Chen, Z., Zhang, Y., Wasson, M. C., Yang, Y., Bai, P., Guo, X., Islamoglu, T. and Farha, O. K. *Chem. Sci.*, **2019**, *10*, 1186-1192.
22. Chen, Y., Zhang, X., Mian, M. R., Son, F. A., Zhang, K., Cao, R., Chen, Z., Lee, S.-J., Idrees, K. B., Goetjen, T. A., Lyu, J., Li, P., Xia, Q., Li, Z., Hupp, J. T., Islamoglu, T., Napolitano, A., Peterson, G. W. and Farha, O. K. *J. Am. Chem. Soc.*, **2020**, *142*, 21428-21438.
23. Xia, H.-L., Zhou, K., Yu, L., Wang, H., Liu, X.-Y., Proserpio, D. M. and Li, J. *Inorg. Chem.*, **2022**, *61*, 7980-7988.
24. Islamoglu, T., Otake, K.-I., Li, P., Buru, C. T., Peters, A. W., Akpınar, I., Garibay, S. J. and Farha, O. K. *CrystEngComm*, **2018**, *20*, 5913-5918.
25. Xu, H.-Q., Wang, K., Ding, M., Feng, D., Jiang, H.-L. and Zhou, H.-C. *J. Am. Chem. Soc.*, **2016**, *138*, 5316-5320.
26. Jiang, H.-L., Feng, D., Wang, K., Gu, Z.-Y., Wei, Z., Chen, Y.-P. and Zhou, H.-C. *J. Am. Chem. Soc.*, **2013**, *135*, 13934-13938.
27. Gimeno-Fonquernie, P., Albalad, J., Evans, J. D., Price, J. R., Doonan, C. J. and Sumbly, C. J. *Submitted* **2023**, (Chapter 3).
28. Coghlan, C. J., Sumbly, C. J. and Doonan, C. J. *CrystEngComm*, **2014**, *16*, 6364-6371.
29. Nudnova, E. A., Potapov, A. S., Khlebnikov, A. I. and Ogorodnikov, V. D. *Russ. J. Org. Chem.*, **2007**, *43*, 1698-1702.
30. Cao, H., Liu, Z. and Wang, Q. *Polym. Chem.*, **2017**, *8*, 3810-3814.
31. Pracht, P., Bohle, F. and Grimme, S. *Physical Chemistry Chemical Physics*, **2020**, *22*, 7169-7192.
32. Bannwarth, C., Ehlert, S. and Grimme, S. *J. Chem. Theory Comput.*, **2019**, *15*, 1652-1671.
33. Ehlert, S., Stahn, M., Spicher, S. and Grimme, S. *J. Chem. Theory Comput.*, **2021**, *17*, 4250-4261.
34. Keupp, J. and Schmid, R. *Faraday Discuss.*, **2018**, *211*, 79-101.

35. Rappe, A. K., Casewit, C. J., Colwell, K. S., Goddard, W. A. and Skiff, W. M. *J. Am. Chem. Soc.*, **1992**, *114*, 10024-10035.
36. Boyd, P. G., Moosavi, S. M., Witman, M. and Smit, B. *J. Phys. Chem. Lett.*, **2017**, *8*, 357-363.
37. Thompson, A. P., Aktulga, H. M., Berger, R., Bolintineanu, D. S., Brown, W. M., Crozier, P. S., in 't Veld, P. J., Kohlmeyer, A., Moore, S. G., Nguyen, T. D., Shan, R., Stevens, M. J., Tranchida, J., Trott, C. and Plimpton, S. J. *Comput. Phys. Commun.*, **2022**, *271*, 108171.
38. Perdew, J. P., Burke, K. and Ernzerhof, M. *Phys. Rev. Lett.*, **1996**, *77*, 3865-3868.
39. Goedecker, S., Teter, M. and Hutter, J. *Phys. Rev. B*, **1996**, *54*, 1703-1710.
40. Grimme, S., Antony, J., Ehrlich, S. and Krieg, H. *J. Chem. Phys.*, **2010**, *132*, 154104.
41. Vandevondele, J., Krack, M., Mohamed, F., Parrinello, M., Chassaing, T. and Hutter, J. *Comput. Phys. Commun.*, **2005**, *167*, 103-128.
42. Kühne, T. D., Iannuzzi, M., Del Ben, M., Rybkin, V. V., Seewald, P., Stein, F., Laino, T., Khaliullin, R. Z., Schütt, O., Schiffmann, F., Golze, D., Wilhelm, J., Chulkov, S., Bani-Hashemian, M. H., Weber, V., Borštnik, U., Taillefumier, M., Jakobovits, A. S., Lazzaro, A., Pabst, H., Müller, T., Schade, R., Guidon, M., Andermatt, S., Holmberg, N., Schenter, G. K., Hehn, A., Bussy, A., Belleflamme, F., Tabacchi, G., Glöß, A., Lass, M., Bethune, I., Mundy, C. J., Plessl, C., Watkins, M., Vandevondele, J., Krack, M. and Hutter, J. *J. Chem. Phys.*, **2020**, *152*, 194103.
43. Willems, T. F., Rycroft, C., Kazi, M., Meza, J. C. and Haranczyk, M. *Microporous Mesoporous Mater.*, **2012**, *149*, 134-141.
44. McPhillips, T. M., McPhillips, S. E., Chiu, H. J., Cohen, A. E., Deacon, A. M., Ellis, P. J., Garman, E., Gonzalez, A., Sauter, N. K., Phizackerley, R. P., Soltis, S. M. and Kuhn, P. *J. Synchrotron Radiat.*, **2002**, *9*, 401-406.
45. Cowieson, N. P., Aragao, D., Clift, M., Ericsson, D. J., Gee, C., Harrop, S. J., Mudie, N., Panjikar, S., Price, J. R., Riboldi-Tunncliffe, A., Williamson, R. and Caradoc-Davies, T. *J. Synchrotron Radiat.*, **2015**, *22*, 187-190.
46. Aragao, D., Aishima, J., Cherukuvada, H., Clarken, R., Clift, M., Cowieson, N. P., Ericsson, D. J., Gee, C. L., Macedo, S., Mudie, N., Panjikar, S., Price, J. R., Riboldi-Tunncliffe, A., Rostan, R., Williamson, R. and Caradoc-Davies, T. *J. Synchrotron Radiat.*, **2018**, *25*, 885-891.
47. Sheldrick, G. M. *Acta Crystallogr. Sect. A: Found. Crystallogr.*, **2008**, *64*, 112-122.
48. Sheldrick, G. M. *Acta Crystallogr. Sect. A: Found. Crystallogr.*, **2015**, *71*, 3-8.
49. Sheldrick, G. M. *Acta Crystallogr. Sect. C: Cryst. Struct. Commun.*, **2015**, *71*, 3-8.

-
50. Barbour, L. J. *Supramol. Chem.*, **2001**, *1*, 189-191.
 51. Dolomanov, O. V., Bourhis, L. J., Gildea, R. J., Howard, J. A. K. and Puschmann, H. *J. Appl. Crystallogr.*, **2009**, *42*, 339-341.
 52. Spek, A. L. *Acta. Crystallogr. C*, **2015**, *71*, 9-18.
 53. Peralta, R. A., Huxley, M. T., Young, R. J., Linder-Patton, O. M., Evans, J. D., Doonan, C. J. and Sumbly, C. J. *Faraday Discuss.*, **2021**, *225*, 84-99.
 54. Liu, Y., Her, J. H., Dailly, A., Ramirez-Cuesta, A. J., Neumann, D. A. and Brown, C. M. *J. Am. Chem. Soc.*, **2008**, *130*, 11813-11818.
 55. Bloch, W. M., Doonan, C. J. and Sumbly, C. J. *CrystEngComm*, **2013**, *15*, 9663.
 56. Chen, L., Mowat, J. P. S., Fairen-Jimenez, D., Morrison, C. A., Thompson, S. P., Wright, P. A. and Düren, T. *J. Am. Chem. Soc.*, **2013**, *135*, 15763-15773.
 57. Amirjalayer, S. and Schmid, R. *J. Phys. Chem. C*, **2008**, *112*, 14980-14987.
 58. Furukawa, H., Gándara, F., Zhang, Y.-B., Jiang, J., Queen, W. L., Hudson, M. R. and Yaghi, O. M. *J. Am. Chem. Soc.*, **2014**, *136*, 4369-4381.

CHAPTER 5: Effect of linker “geometry mismatch” on MOF topology

5.1. Introduction

The geometry of the organic linkers used play a crucial role in determining the topology and dimensionality of the resulting Metal-organic Framework (MOF) structures. In 2019, Maspoch and coworkers introduced the concept of 'geometry mismatch', in a review wherein seemingly incompatible building blocks are combined to generate non-default structures.¹ By using ligands with non-linear structures, so-called zigzag ligands, and other elements, like the twisting of the carboxylate groups, they highlight how MOF structures can be built through geometry mismatch. Similarly, other studies have explored the influence of breaking the symmetry of planar ditopic linkers, using angular linkers to change structure dimensionality or MOF topology. For instance, the reaction of 1,3-bis(4-carboxyphenyl)imidazolium chloride with $Zn(NO_3)_2$ and $Cu(CH_3CN)_4PF_6$ salts leads to the formation of a 3D-MOF.² However, reaction under the same conditions but using 1,3-bis(3-carboxyphenyl)imidazolium bromide leads to the formation of a 1D-chain coordination polymer.³ In a research contribution, Maspoch and coworkers reported the topological influence of zigzag ligands in the assembly of Zr(IV) MOFs. Through a linker design strategy that includes an off-set of the donors, they were able to synthesize a family of isorecticular Zr(IV)-based MOFs exhibiting the *bcu* topology, rather than the *fcu* topology that is normally observed for straight ditopic ligands.⁴ For tetratopic linkers, as described in chapter 4, the twisting of the carboxylates and the addition of functional groups can also induce the formation of different topologies.^{5, 6} However, to the best of our knowledge, there are no reported examples of MOFs formed with a tetratopic linker where the carboxylate group is in the meta-position of the phenyl ring. This appendix reports an investigation into the synthesis of Zr-based MOFs formed from a ligand showing this geometry mismatch.

In chapters 3 and 4, we showed that the formation of different MOF topologies from the same linker can change the spatial distribution of the bis-pyrazole groups. These alterations to the site for post-synthetic metalation (PSMet) allowed the isolation of different metal complexes. For instance, UAM-1002 formed a MOF with an *scu* topology where the bis-pyrazole groups were well distributed, allowing only the isolation of mononuclear complexes by PSMet. On the other hand, when UAM-1001 was synthesized with the same linker a MOF with a different topology (*sqc*) was formed. In this case, the close arrangement of bis-pyrazole groups facilitated the isolation of dinuclear complexes when appropriate bridging co-ligands or anions were used. Additionally, in UAM-1001, the positioning of the bis-pyrazole groups influenced the type of dinuclear complexes that could be isolated. Specifically, the positioning (distance and angle between coordination sites) of the adjacent bis-pyrazole groups in UAM-1001 was well-suited for

the isolation of octahedral dinuclear complexes, as demonstrated by examples like UAM-1001[$\text{Ni}_2\text{Cl}_3(\text{H}_2\text{O})_2$] and UAM-1001[$\text{Rh}_2(\text{CO})_3\text{Cl}_2$]. It was also possible to isolate dinuclear complexes with 5-coordinate metal centres, with greater distortion, as observed with UAM-1001[Cu_2Cl_4] and UAM-1001[Co_2Cl_4]. However, attempting to PSMet UAM-1001 with metals that typically adopt a square planar geometry resulted in the formation of monomeric complexes due to the arrangement of the bis-pyrazole groups.

Based on these results and precedent in the literature for modifying the positioning of the donors within a linker, we decided to explore the possibility of altering the spatial distribution of the bis-pyrazole groups by modifying the substitution pattern of the linker and potentially introducing geometry mismatch. Consequently, we chose to synthesize 1,1,2,2-tetrakis[4-(3-carboxyphenyl)-1H-pyrazol-1-yl]ethane (L3H_4) (Figure 5.1), which represents a slight modification of TCPE by changing the position of the carboxylate group in the phenyl ring from the para to the meta carbon. The goal was to investigate whether this alteration could affect the topologies of the MOFs that were formed with Zr nodes, and more specifically whether this would change positioning of the bis-pyrazole groups relative to each other and thereby enable PSMet with different dinuclear complexes (or indeed mononuclear complexes). The results presented herein are preliminary but have been included to provide some context to the other results, and to retain the ideas and the data.

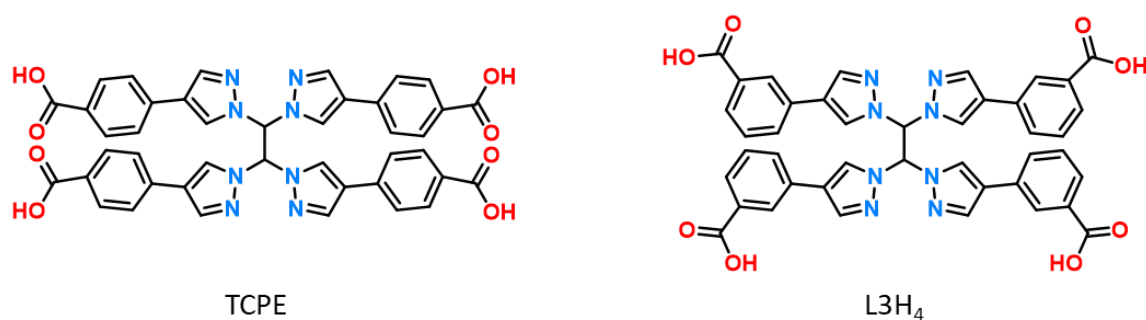


Figure 5.1. The structures of TCPE (left) and L3H_4 (right).

5.2. Experimental Section

5.2.1. Materials and methods

Unless otherwise stated, all chemicals were obtained from commercial sources and used as received. 1,1,2,2-Tetrakis[4-iodo-1H-pyrazol-1-yl]ethane was synthesized following an already reported procedure.⁷

5.2.2. Synthetic protocols

5.2.2.1. Synthesis of 1,1,2,2-tetrakis[4-(3-carboxyphenyl)-1H-pyrazol-1-yl]ethane

1,1,2,2-Tetrakis(4-iodo-1H-pyrazol-1-yl)ethane (1.00 g, 1.25 mmol), 3-carboxyphenylboronic acid (1.25 g, 7.52 mmol) and aqueous K₂CO₃ (6.93 g in 40 mL of water) were combined in DMF (100 mL). After degassing with Ar for 30 mins, Pd(PPh₃)₄ (0.171 g, 0.15 mmol) was added, the mixture degassed for a further 30 mins and heated to 90 °C for 24 hours. After cooling, the mixture was filtered, diluted with water (50 mL) and washed with dichloromethane (5 × 50 mL). Acidifying the aqueous layer with 20% HCl (pH = 3) afforded a white solid which was isolated under reduced pressure, washed with ethanol, and dried. Yield 763 mg (79%). ¹H NMR (600 MHz/DMSO); δ 8.83 (s, 4H, PyrH), 8.40 (s, 2H, CH), 8.05 (s, 4H, ArH), 8.04 (s, 4H, PyrH), 7.76 (d, 8H, ArH), 7.45 (t, 4H, ArH).

5.2.2.2. Synthesis of UAM-1006

ZrCl₄ (15 mg, 0.064 mmol) and trifluoroacetic acid (0.2 mL, 2.61 mmol, 41 mol. eq.) were dissolved in 0.5 mL of DMF and sonicated for 30 min. L1H₄ (10 mg, 0.013 mmol) was added to the reaction mixture and sonicated for 10 min. The resulting mixture was transferred to a solvothermal scintillation vial and heated at 120 °C for 6 days. The few colourless crystals of UAM-1006 that were obtained were solvent exchanged with fresh DMF (4 x 5 mL).

5.2.3. Single-crystal X-ray crystallography

5.2.3.1. General Procedure

Single crystals were mounted in Paratone-N oil on a MiTeGen micromount. Single-crystal X-ray data were collected at 100 K on the Rigaku-Oxford XtaLAB Synergy-S diffractometer and the structure solved using SHELXS,⁸ and refined by full-matrix least squares on F² by SHELXL,⁹ interfaced through the program OLEX.¹⁰ All atoms were refined anisotropically and hydrogens atoms were included as invariants at geometrically estimated positions, unless specified otherwise in additional details in supporting information. The data was treated with the SQUEEZE routine available in Platon¹¹ or using the solvent masking feature of OLEX. Figures

were produced using the software Diamond Version 4.6.8. X-ray experimental data is given in Table 5.1.

5.2.3.2. Specific Data and Refinement Details

UAM-1006. Crystals of UAM-1006 were very small an extended data collection that caused issues with icing. As a result, the data is of low quality (high R_{int}) and there are abnormally high residual electron densities within the metal node (possibly related to issues with the adsorption correction). Attempts to collect data at the Australian Synchrotron has thus far been unsuccessful as suitable conditions for sample preparation and shipping has not been determined. Some of the phenyl rings and pyrazoles did not refine satisfactorily and, in some cases, AFIX, SIMU and RIGU restraints were applied in the refinement. Some bond distances were fixed too.

5.3. Results and discussion

We synthesized 1,1,2,2-tetrakis[4-(3-carboxyphenyl)-1H-pyrazol-1-yl]ethane (L3H₄) using a procedure similar to that employed for the synthesis of 1,1,2,2-tetrakis[4-(4-carboxyphenyl)-1H-pyrazol-1-yl]ethane (TCPE). The synthesis consisted of three steps, with the first step involved the coupling of four pyrazoles to 1,1,2,2-tetrabromoethane, followed by iodination of the pyrazole rings at the 3-position. With this common starting material to hand, the last step was a Suzuki coupling with 3-carboxyphenyl boronic acid giving L3H₄ in 79% yield. The synthesis of L3H₄ was confirmed by ¹H (Figure 5.2) and ¹³C NMR, and electrospray ionisation mass spectrometry.

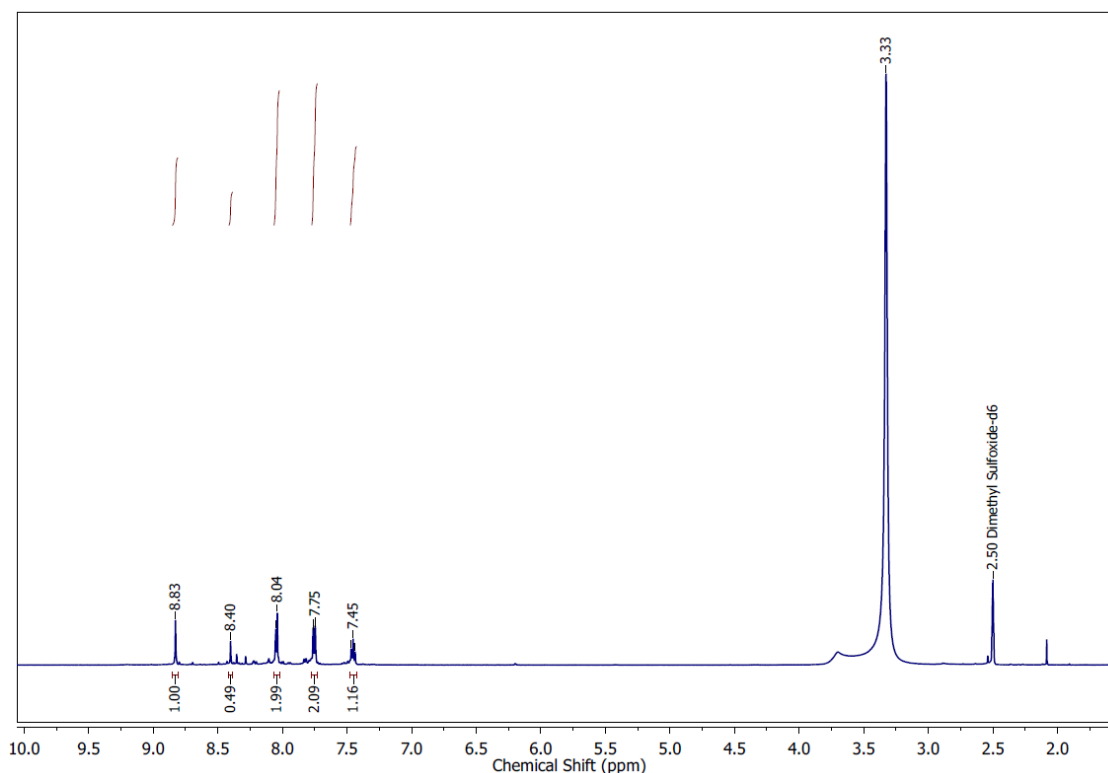


Figure 5.2. $^1\text{H-NMR}$ spectrum of L3H_4 (600 MHz/DMSO); δ 8.83 (s, 4H, PyrH), 8.40 (s, 2H, CH), 8.05 (s, 4H, ArH), 8.04 (s, 4H, PyrH), 7.76 (d, 8H, ArH), 7.45 (t, 4H, ArH). There is a small amount of some of the possible byproducts stemming from partial substitution of the iodo-substituted starting material which is difficult to separate.

With L3H_4 in hand, we investigated the synthesis of a Zr-MOF by reacting it with a Zr salt under procedures established in the earlier chapters. Reaction of L3H_4 with ZrCl_4 , using trifluoroacetic acid (TFA) as a modulator in dimethylformamide (DMF) for 6 days, yielded a few colourless needle crystals corresponding to a MOF with a chemical formula of $[\text{Zr}_6(\mu_3\text{-OH})_8(\mu_2\text{-CH}_3\text{COO})_4(\text{L3})_2]$ (UAM-1006) (Figure 5.3b, Figure 5.3d). The very small, needle shaped crystals required a long SCXRD experiment that resulted in significant icing and a less than ideal quality dataset; this has provided a preliminary structure, but further work needs to be done to get a better quality structure. These needle-shaped crystals were typical of Zr-MOFs with an *scu* topology (e.g. UAM-1002) and SCXRD analysis confirmed the formation of a Zr-MOF with a *scu* topology, composed of 8-connected (cubic) Zr-clusters, with each organic linker connecting four Zr-clusters (Figure 5.3a, Figure 5.3c).

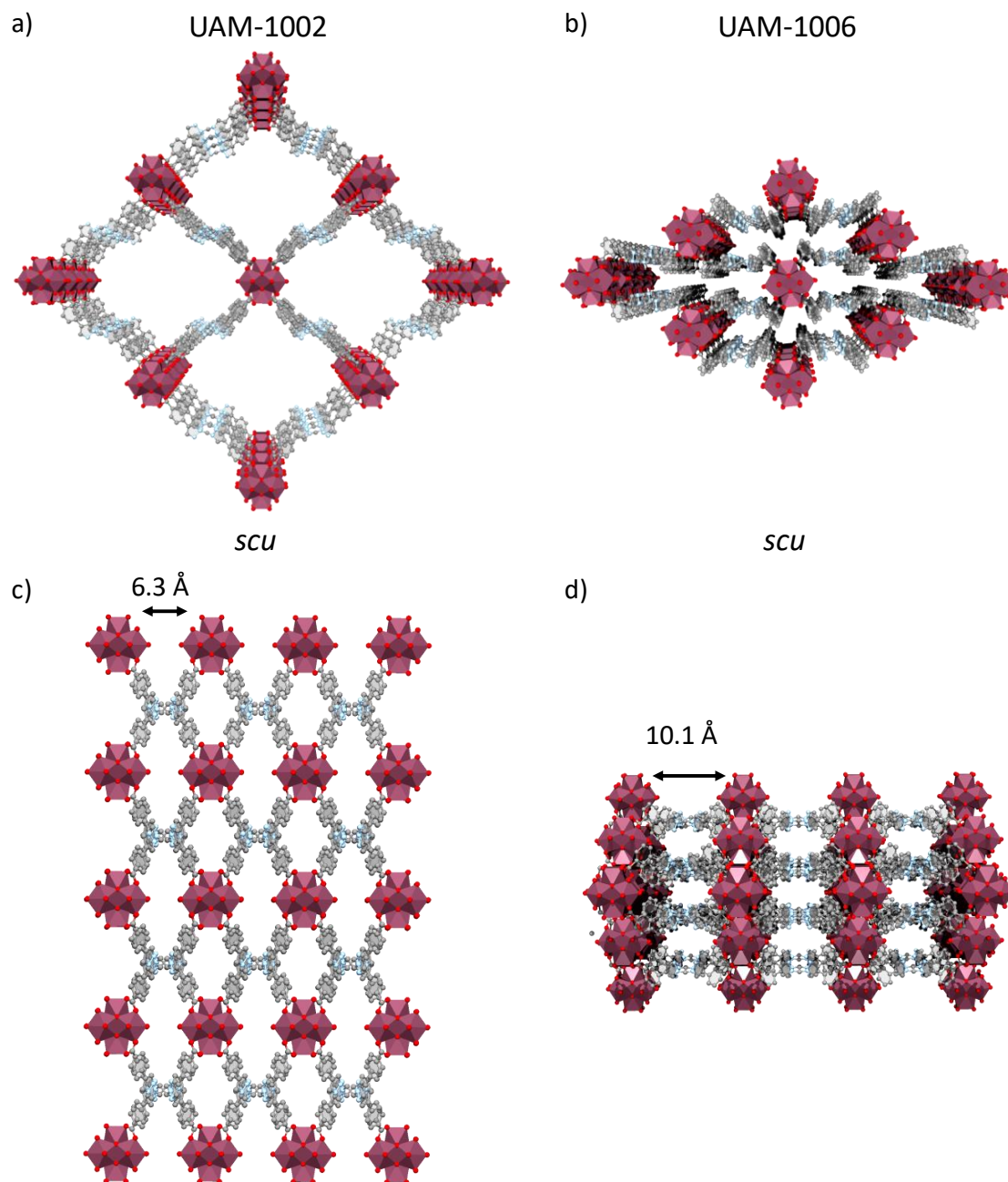


Figure 5.3. Representations of the structure of UAM-1002 (a) and UAM-1006 (b) when viewed along the *c* axis and UAM-1002 (c) and UAM-1006 (d) along the *b* axis. The black double headed arrow highlights the shorter distance between the Zr-clusters in UAM-1002 compared to UAM-1006. Colour scheme C, grey; N, light blue; O, red; Zr, cyan. Hydrogens have been omitted for clarity.

Despite sharing the same topology as UAM-1002, UAM-1006 exhibits significant structural differences. Visualizing the structure along the *c*-axis reveals UAM-1006 as a "closed phase" of UAM-1002. The prominent channels observed in UAM-1002 are now closed due to the more angular shape of L3 (Figure 5.3a, Figure 5.3b). Further differences can also be observed when observing the structure along the *a* or *b* axis, where UAM-1006 shows a longer distance

between Zr-clusters compared to UAM-1002, increasing from 6.3 Å in UAM-1002 to 10.1 Å in UAM-1006 (Figure 5.3c, Figure 5.3d). Interestingly, this “closed phase” seen in UAM-1006 brings the bis-pyrazole groups significantly closer to each other than in UAM-1002; these are now only 5.5 Å apart versus effectively being discrete donor sites in UAM-1002. This distance is similar to the distance between bis-pyrazole groups in UAM-1001 (5.7 Å), despite UAM-1001 having a different topology (sqc). However, compared to UAM-1001, the lone pair donor orientation pyrazolyl nitrogen atoms in UAM-1006 are now closer to the plane formed by the nitrogen atoms (Figure 5.4). This different orientation of the bis-pyrazole groups relative to each other could potentially favour the isolation of different dinuclear complexes, like square planar dimers, that were not possible to form in UAM-1001. The arrangement of the four donors in UA-1006 is almost dome-porphyrin¹² or calixpyrrole-like in shape and potentially could be viewed as a tetradentate donor for a single 4d or 5d transition metal.

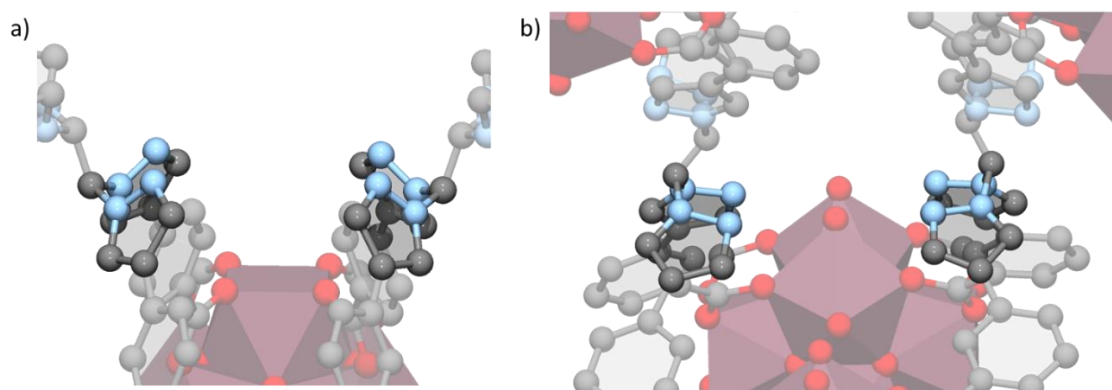


Figure 5.4. Portion of the structures of UAM-1001 (a) and UAM-1006 (b) highlighting the arrangement of the proximal bis-pyrazole groups. Colour scheme C, grey; N, light blue; O, red; Zr, cyan. Hydrogens have been omitted for clarity.

Despite the potentially promising structural features of UAM-1006, we were unable to conduct further studies due to the low yield of the MOF synthesis step. Only a very small number of tiny crystals appeared at the bottom of the vials and attempts to scale up the synthesis or modify the synthetic conditions to increase the yield of MOF were unsuccessful. Comparing TCPE with L3 for the synthesis of MOFs, we suspect that L3 can access a larger number of more distinct conformations (i.e., the syn-syn, syn-anti and anti-anti are different plus the ability for the four carboxylates to rotate relative to the pyrazole rings) and this could be responsible of making crystallization more difficult. Standard characterization techniques for MOFs, such as PXRD, TGA, or adsorption experiments, were not possible for UAM-1006 due to the extremely low yield.

5.4. Conclusions

In summary, we have demonstrated how modifying the linker geometry can alter the arrangement of bis-pyrazole groups within the MOF structure. Changing the substitution of the carboxylate donors on the phenyl spacers to give L3H₄ (as opposed to TCPE) allowed the synthesis of a new Zr-MOF, UAM-1006. The different geometry of L3H₄ compared to TCPE allows to change the spatial distribution of the bis-pyrazole groups. In this short study, we have observed that two MOFs of the same topology but synthesized with two linkers with different substitution patterns can alter the separation and arrangement of the bis-pyrazole groups relative to each other. In UAM-1002, these bis-pyrazole groups were isolated, allowing only the isolation of mononuclear complexes, while in UAM-1006, they were much closer together (5.5 Å), suggesting the potential for the isolation of dinuclear complexes as observed in UAM-1001. However, the low yield for UAM-1006 hindered comprehensive characterization, and limited further exploration. Further research is needed to optimize the synthetic conditions of UAM-1006.

5.5. Supplementary information

5.5.1. Thermal ellipsoid plot for UAM-1006 at the 50% probability level

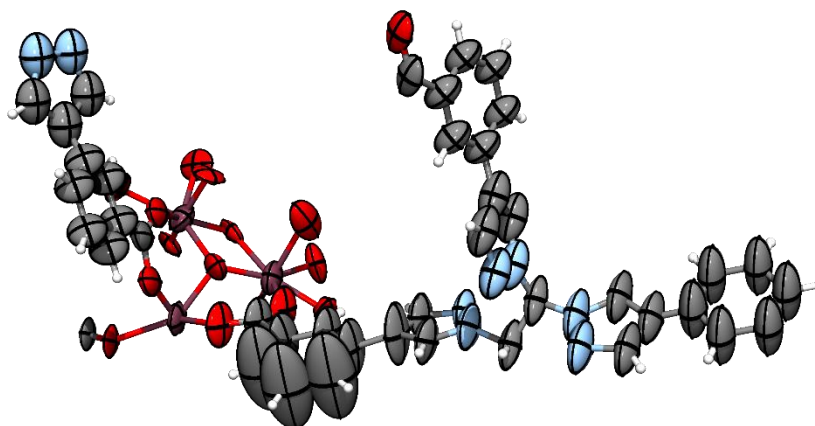


Figure 5.5. Asymmetric unit of **UAM-1006**, with all non-hydrogen atoms represented by ellipsoids at the 50% probability level (C, grey; H, white; N, light blue; O, red; Zr, dark red).

5.5.1. Alternative images of the structure of UAM-1006

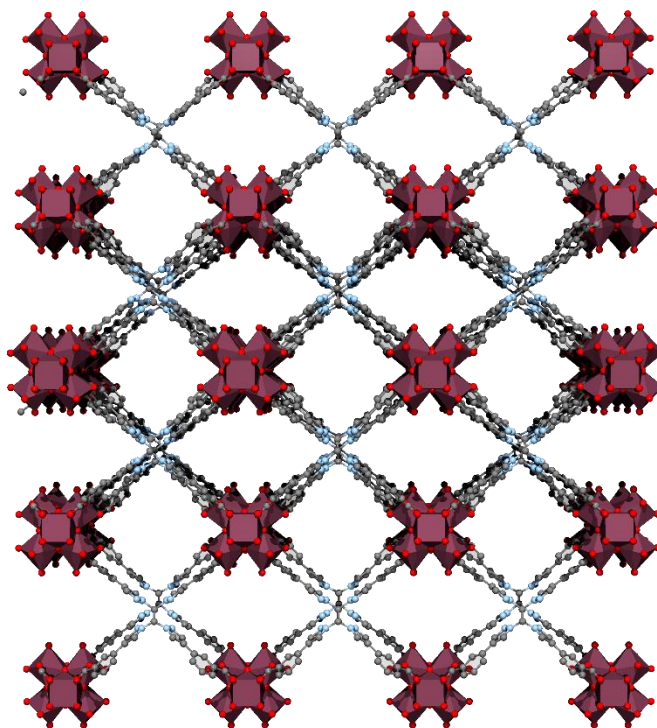


Figure 5.6. Representation of **UAM-1006** viewed along the *b* axis. Colour scheme C, grey; N, light blue; O, red; Zr, cyan. Hydrogens have been omitted for clarity.

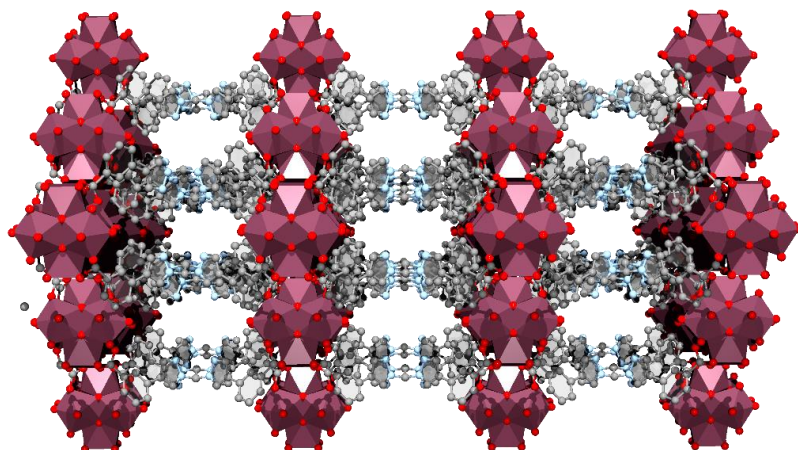


Figure 5.7. Representation of **UAM-1006** viewed along the *a* axis. Colour scheme C, grey; N, light blue; O, red; Zr, cyan. Hydrogens have been omitted for clarity.

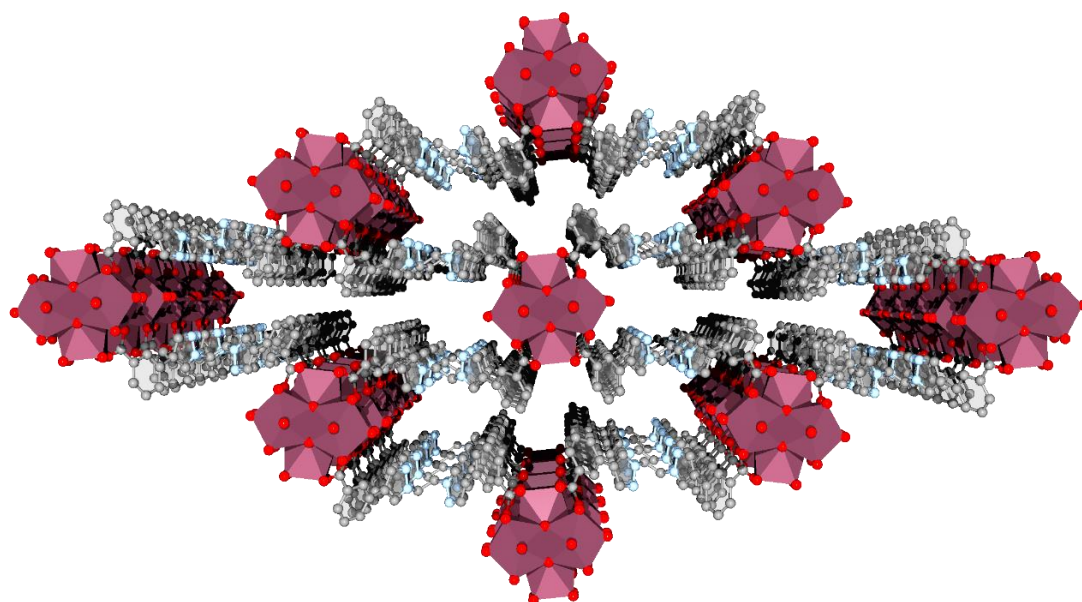


Figure 5.8. Representation of **UAM-1006** viewed along the *c* axis. Colour scheme C, grey; N, light blue; O, red; Zr, cyan. Hydrogens have been omitted for clarity.

5.5.2. Table of X-ray crystallography data collection and refinement parameters

Table 5.1. Crystallographic data collection and refinement parameters for **UAM-1006**.

Sample	UAM-1006
Crystallographic Parameter	
Formula	C ₄₂ H ₂₆ N ₈ O ₁₆ Zr ₃
FW	2705.2
T, K	99.98(10)
Crystal system	orthorhombic
Crystal system, space group	Pba2
a, Å	15.4117(14)
b, Å	31.028(2)
c, Å	17.9482(12)
α, °	90
β, °	90
γ, °	90
V, Å ³	8582.7(11)
Z	4
d _{calc.} , g/cm ³	2.094
Absorption coefficient, mm ⁻¹	6.73
F(000)	5424
Crystal size, mm ³	0.023 × 0.043 × 0.092
Radiation	Cu Kα (λ = 1.54184)
2θ range for data collection	5.696 to 163.86
Index range	-19 ≤ h ≤ 18, -18 ≤ k ≤ 37, -18 ≤ l ≤ 21
Reflections collected	30348
Independent reflections	12804 [R _{int} = 0.2065, R _{sigma} = 0.1240]
Data/restraints/parameters	12804/4/271
GOF on F ²	1.9
Largest diff. peak and hole, eÅ ⁻³	10.86/-3.58
R ₁ , [I > 2σ(I)]	0.2669
wR ₂ , all data	0.6302
CCDC Number	

5.6. References

1. Guillerm, V. and MasPOCH, D. *J. Am. Chem. Soc.*, **2019**, *141*, 16517-16538.
2. Burgun, A., Crees, R. S., Cole, M. L., Doonan, C. J. and Sumbly, C. J. *Chem. Commun.*, **2014**, *50*, 11760-11763.
3. Capon, P. K., Burgun, A., Coghlan, C. J., Crees, R. S., Doonan, C. J. and Sumbly, C. J. *CrystEngComm*, **2016**, *18*, 7003-7010.
4. Guillerm, V., Grancha, T., Imaz, I., Juanhuix, J. and MasPOCH, D. *J. Am. Chem. Soc.*, **2018**, *140*, 10153-10157.
5. Dau, P. V., Tanabe, K. K. and Cohen, S. M. *Chem. Commun.*, **2012**, *48*, 9370.
6. Lyu, J., Zhang, X., Otake, K.-I., Wang, X., Li, P., Li, Z., Chen, Z., Zhang, Y., Wasson, M. C., Yang, Y., Bai, P., Guo, X., Islamoglu, T. and Farha, O. K. *Chem. Sci.*, **2019**, *10*, 1186-1192.
7. Nudnova, E. A., Potapov, A. S., Khlebnikov, A. I. and Ogorodnikov, V. D. *Russ. J. Org. Chem.*, **2007**, *43*, 1698-1702.
8. Sheldrick, G. M. *Acta Crystallogr. Sect. A: Found. Crystallogr.*, **2008**, *64*, 112-122.
9. Sheldrick, G. M. *Acta Crystallogr. Sect. C: Cryst. Struct. Commun.*, **2015**, *71*, 3-8.
10. Dolomanov, O. V., Bourhis, L. J., Gildea, R. J., Howard, J. A. K. and Puschmann, H. *J. Appl. Crystallogr.*, **2009**, *42*, 339-341.
11. Spek, A. L. *Acta Crystallogr. Sect. C: Cryst. Struct. Commun.*, **2015**, *71*, 9-18.
12. Kingsbury, C. J. and Senge, M. O. *Coord. Chem. Rev.*, **2021**, *431*, 213760.

CHAPTER 6: Conclusions and Future Directions

In summary, this thesis has focused on the synthesis of robust and highly porous crystalline sponges for site-isolating and investigating the structures and chemistry occurring at transition metal complexes anchored within the pores. These crystalline sponges are new Zr-MOFs bearing different arrangements of vacant bis-pyrazole groups. The findings highlight the challenges of synthesising new MOFs to act as crystalline sponges, which it has been shown, requires multiple factors to align harmoniously. The individual results have been summarised and concluded in each chapter but here some overall learnings are identified that reflect the main aim of the thesis.

Firstly, it is unlikely for 2D layered MOFs to be able to function as crystalline sponges due to a lack of control over the packing of the layered structures and a preference for more densely packed materials. Chapter 2 also demonstrates that for the short bis-pyrazole ligands (i.e. those lacking a phenyl spacer between the pyrazole and carboxylate donor), if the chelating site is not pre-oriented to accommodate a metal centre, it becomes impossible to rearrange the chelating group without disrupting the structure and the efficient packing of the crystal, thereby making PSMet unachievable. In cases where delamination of a layered MOF is possible, PSMet can be successful. However, delamination also results in a loss of long-range order, making it impossible to characterize the resulting material by SCXRD. This was observed during the chemical delamination of UAM-2 to UAM-2ns, as presented in Chapter 2. Although UAM-2ns with free bis-pyrazole groups can be metalated with different metal complexes, the efficient delamination also leads to a loss of the 3D structure, making its characterization by SCXRD impossible. It is worth noting that these materials exhibit a diffraction pattern under transmission electron microscopy (TEM), but this only reflects long range order in two dimensions.

On the other hand, the formation of 3D MOFs provides one of the pre-conditions for allowing the preservation of crystallinity during PSMet, as demonstrated in Chapters 3 and 4, and appendix 1. Employing linkers with higher connectivity promotes the formation of 3D MOFs over 2D MOFs. The angular shape of di-topic linkers, facilitated by the methylene bridge in the bis-pyrazole group, along with the shape and connectivity of the Zr-nodes, favours the formation of corrugated layers, as seen in UAM-1. The results from Chapters 3 and 4, and appendix 1 consistently indicate that the exclusive use of tetratopic linkers formed by combining two of these bis-pyrazole groups, leads to the formation of 3D MOFs based these corrugated layer motifs, that maintain their crystallinity during attempted PSMet.

The use of pyrazole groups with reduced rotational freedom, in comparison to other commonly employed functional groups like 2,2'-bipyridines (facile rotation around the axial biaryl

bonds), appears to result in less crystallographic disorder and enables more accurate characterization by SCXRD. However, this diminished rotational freedom can occasionally impede PSMet, as observed in UAM-10 and UAM-11, synthesized with 1,4-bis(bis(4-carboxy-1H-pyrazol-1-yl)methyl)benzene and 1,4-bis(bis(4(4-carboxyphenyl)-1H-pyrazol-1-yl)methyl)benzene organic linkers, respectively. In both cases, PSMet was unachievable, even at moderate to high temperatures. As for UAM-1, the presence of carboxylic groups directly attached to the pyrazoles increases the energetic barrier for transitioning from an anti-conformation to a syn-conformation. Consequently, the linker is unable to adopt the necessary strained conformation to maintain the same directionality and coordination with the metal clusters, rendering PSMet of the bis-pyrazole groups impossible at moderate temperatures. These observations are supported by the DFT calculations presented in Chapter 4.

To address this challenge, decoupling the pyrazole and carboxylate groups by introducing a phenyl ring to the linker enhances flexibility, facilitating an easier transition from an anti-conformation to a syn-conformation and enabling PSMet in the bis-pyrazole groups. This approach was successfully demonstrated in the synthesis of MOFs with TCPE, where the carboxylates and pyrazoles are separated by a phenyl spacer (UAM-1000 and UAM-1002), as detailed in Chapters 3 and 4. While UAM-1000 and UAM-1002 could be PSMet at their bis-pyrazole units with various metal complexes, their higher flexibility posed challenges for characterization by SCXRD. The increased flexibility allows greater mobility of the linkers, resulting in a decrease in data resolution for the SCXRD experiment. The diffraction pattern of the crystals of UAM-1000 and UAM-1002 lacks the high-angle diffraction seen in parent crystals of the same sample. Upon PSMet, the lower resolution of the data complicates the characterization of the metal environment or, in some cases, leads to an inability to satisfactorily model the MOF support, let alone the metal site added by PSMet. In extreme cases, loss of crystallinity makes it impossible to characterize the MOF by SCXRD, and this was commonly observed in the case of PSMet of UAM-1000 and UAM-1002. These findings highlight that large and flexible linkers like TCPE can form MOFs that, although capable of being metalated, cannot be effectively utilized as crystalline sponges. The significant flexibility of the linker in these highly porous MOF topologies hampers the detailed SCXRD characterization of the PSMet metal centre.

Therefore, it appears to be crucial to strike a balance between the rigidity and flexibility of materials intended for use as crystalline sponges. To improve the reproducibility of SCXRD characterization, the flexibility UAM-1000 and UAM-1002 can be slightly reduced by increasing their connectivity. Chapter 3 demonstrates how the introduction of a secondary linker into UAM-

1000, forming UAM-1001, increases the framework's connectivity and limits its flexibility, resulting in improved SCXRD data. In cases where linker insertion is not possible, the pore solvent can induce better ordering to improve SCXRD data. Chapter 4 shows how PSMet of UAM-1002 forces a change of conformation of the linker that brings the clusters very close in space. This also causes a rearrangement of the formates that are capping the Zr cluster into a bridging coordination mode to link two separate clusters, increasing the connectivity. However, in the case of UAM-1002, the increase in connectivity is not enough to lock the structure sufficiently to obtain good SCXRD. Solvent-exchanging metalated UAM-1002 to toluene orders the structure, dramatically improving the resolution of the SCXRD data. In both cases, the SCXRD analysis of the metalated UAM-1001 and UAM-1002 allows for detailed structural elucidation of the metal complexes anchored in the bis-pyrazole groups.

The different topologies for UAM-1001 and UAM-1002 highlights two important factors to consider in the design of crystalline sponges. The *sqc* topology, observed in UAM-1001, exhibits no linker disorder, while the *scu* topology, observed in UAM-1002, after PSMet displays linker disorder over two crystallographic positions. This distinction makes UAM-1001 a superior crystalline sponge, ensuring that the metal complexes are not disordered and all atoms have full occupancy, thus facilitating SCXRD analysis. Additionally, this difference in topology not only affects crystallographic elucidation but also influences the types of metal complexes that can be isolated within the MOFs. In UAM-1002, the bis-pyrazole groups are well separated, allowing for the isolation of monomeric complexes. In contrast, in UAM-1001, the adjacency of bis-pyrazole groups permits the formation of dimeric complexes. Additionally, the arrangement of the bis-pyrazole units determines the types of dimeric complexes that can be isolated. The slight upward inclination of the bis-pyrazole units in UAM-1001 enables the isolation of octahedral complexes without any crystallographic disorder, a remarkable result demonstrating 100% crystallographic occupancy and absence of disorder. However, the isolation of metal complexes with other geometries in UAM-1001 is less favoured and leads to crystallographic disorder, as observed with the metalation of UAM-1001 using CuCl_2 and CoCl_2 . Despite the disorder, these metal complexes could still be modelled and exhibited notably short metal-metal distances. The significant distortion of these dimeric complexes suggests the complexes may be quite reactive, and indeed the CuCl_2 dimer reported in Chapter 3 is rapidly hydrolysed, as evidenced by the UV-vis studies of the complex. This result underscores how MOFs not only serve as crystalline sponges but also enable the isolation of unconventional metal complexes that are challenging to obtain in solution.

Despite being useful for isolating dinuclear complexes, UAM-1001 is less effective as a crystalline sponge when the formation of dimeric complexes is not possible. In such cases, mononuclear complexes can be isolated in UAM-1001, but only 50% of the bis-pyrazole units undergo metalation. This leads to crystallographic disorder, as the metal complexes can occupy either of the adjacent bis-pyrazole units. While modelling is feasible for simple metal complexes, as demonstrated in this thesis, it is anticipated that modelling will become more challenging with more complicated metal complexes (e.g., those with non-identical equatorial or axial ligands; if the N-N chelating site is considered to be part of the equatorial plane).

Overall, the use of MOFs as crystalline sponges offers several advantages over “in crystallo” characterisation for molecular systems. Their high porosity enables a wider range of reagents to diffuse and access the metal centres, allowing for the exploration of diverse reactions. The quasi-rigid structure of MOFs enables the isolation of metal complexes without the need for bulky ligands to achieve site isolation of the metal centres. Additionally, the ample space within the pores allows for significant structural changes without the loss of crystallinity.

However, the high porosity of MOFs also poses some limitations. Metal complexes site isolated within a MOF are in contact with the solvent, which can lead to undesired reactivity, especially when reactive metal centres are involved. Additionally, labile metal ions, such as first transition metals, are prone to leaching, particularly when reactive complexes are formed. While the use of non-polar organic solvents can mitigate leaching in some cases, it does not guarantee this, as evidenced by the results reported within this thesis. In contrast, molecular systems, as synthesized by Powers and Weller, have a confined space where solvent molecules are largely absent. Although molecular systems have limitations in terms of the ability to admit reagents and the inability to tolerate significant structural changes without loss of crystallinity, the reactive species is better protected from leaching or unwanted reaction. Moreover, crystals of molecular systems, which are typically more dense, are generally more straightforward to prepare compared to MOFs. This thesis highlights that a multitude of factors require careful consideration to allow formation of an effective crystalline sponge MOF, necessitating a delicate balance between flexibility and rigidity, as well as precise tuning of topology.

Further advancements in the development of MOFs as crystalline sponges could focus on enhancing the interaction between the inserted metal and the ligand to prevent leaching. This can be achieved by incorporating functional groups into MOFs that exhibit stronger binding to low-valent metals, which are typically soft. Examples of such functional groups include phosphine or thiolate groups. However, these groups present challenges due to their susceptibility to

oxidation. Despite these challenges, a few examples reported in the literature demonstrate that it is possible to successfully incorporate these functional groups into MOFs by carefully controlling the synthetic conditions. Additionally, the use of post-synthetic modification (PSM) techniques could potentially simplify the incorporation of these functional groups. PSM methods require milder conditions compared to MOF synthesis and allow the ligands to be pre-metallated as metallolinkers. MOFs like UAM-1000/1001 have the potential to incorporate secondary linkers with softer groups to accommodate the desired functional groups (via the biphenyldicarboxylate brace). However, there are still challenges to overcome. Firstly, the secondary linkers should not contain these functional groups as pendant groups (donors appended to the rigid core by a flexible spacer), as pendant groups exhibit high thermal motion and can lead to crystallographic disorder. Moreover, the linkers should not possess excessively low symmetry, as this would also result in crystallographic disorder. Similarly, the use of charged linkers that enable both coordinative bonding and ionic interactions with the metal centre could also help prevent leaching. While these groups do not exhibit the same chemical instability as phosphines or thiolates, the synthesis of linkers containing such functional groups still presents challenges in terms of feasible synthetic routes, achieving the required symmetry for the site (e.g., in UAM-1000/1001 we anticipate di- or tetra- substituted ligands are required to minimise/avoid disorder) with restricted rotational freedom.

Another promising area of development is the utilization of MOFs to generate unconventional metal complexes that possess unique properties. This thesis has underscored that the confined space within MOFs can facilitate the formation of metal complexes with distorted metal ion geometries, shorter metal-metal distances than normally encountered and species that are not readily able to be made in solution. Building upon this, further investigation in the case of UAM-1001 could focus on isolating additional dimeric metal complexes and examining their distortions. This exploration could shed light on potential new reactivities that may prove fundamentally interesting or valuable for catalytic applications. By studying the distortions and reactivity of these metal complexes, new insights and opportunities for metal-based reactivity could emerge.

Appendixes

I. Appendix 1: Supplementary Information for Chapter 2

I.I. Main text supporting characterization

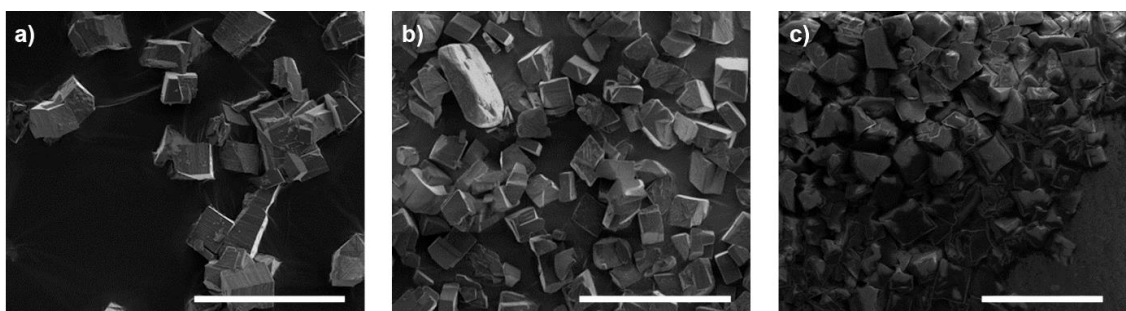


Figure I.1. a) SEM images of (a) UAM-1 as made, (b) UAM-1 after 2 h under sonication, and (c) UAM-1·HCl. (Scale bar= 50 μm).

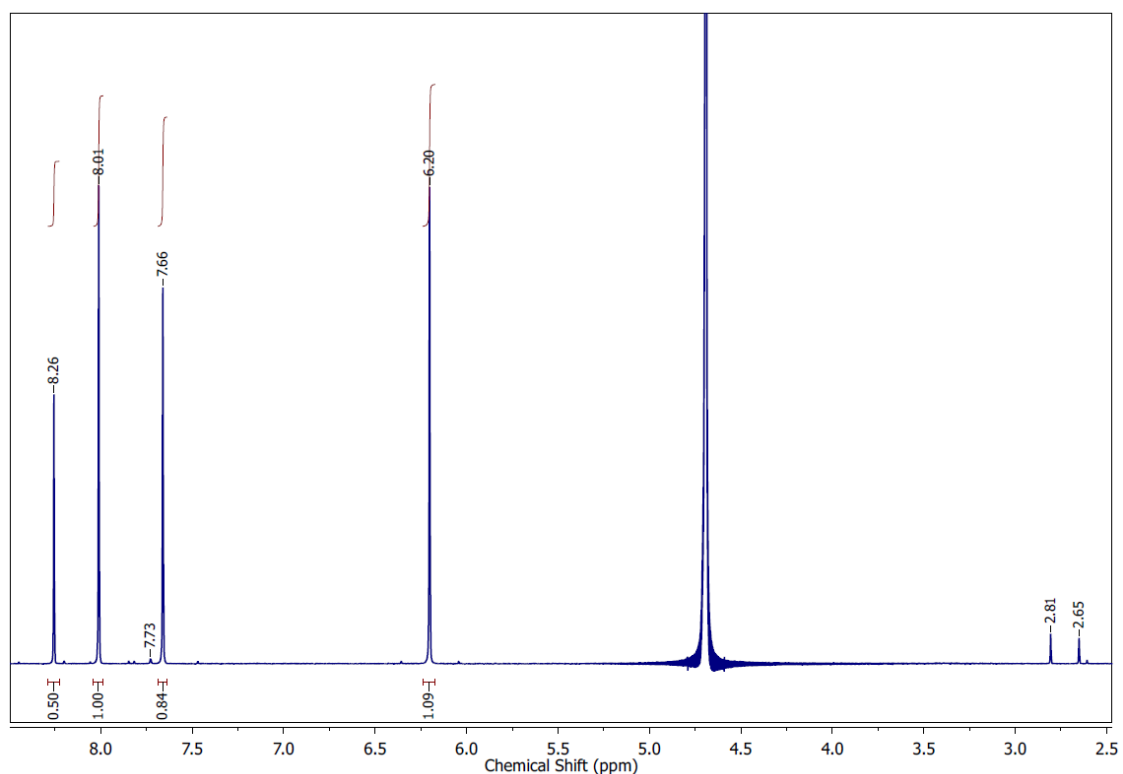


Figure I.2. ¹H-NMR spectrum of digested UAM-1. Digestion conditions: 50 μL NaOD in 500 μL of D_2O , heated at 80 $^\circ\text{C}$ for 1 h. Sample preparation: UAM-1 was washed with DMF (4 x 5 mL), acetone (3 x 5 mL) and dried under vacuum for 24 h. Digestion conditions: 50 μL NaOD in 500 μL of D_2O , heated at 80 $^\circ\text{C}$ for 1 h. Peak at 8.26 ppm corresponds to the formate anion. Its relative integration compared with the L peaks show a molar ratio L:formate 1:1 which is consistent with four L and four formate anions linked to each Zr cluster. Peaks at 7.73, 2.81 and 2.65 show the presence of some DMF trapped in the structure.

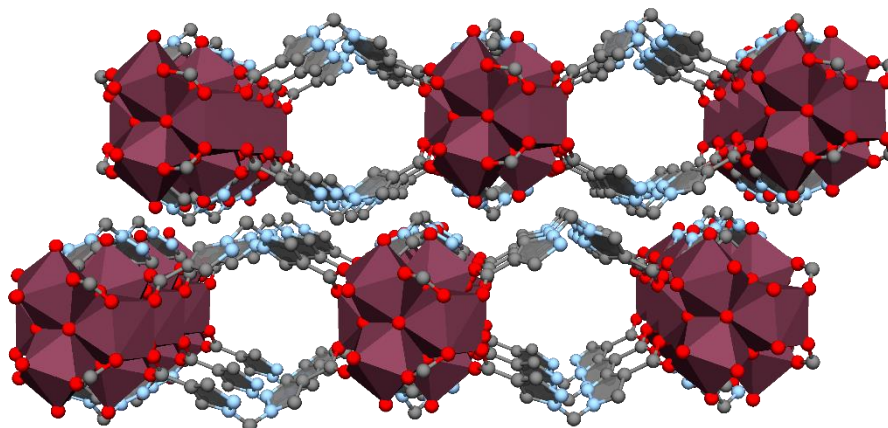


Figure I.3. Representation of the interlayer packing in UAM-1.

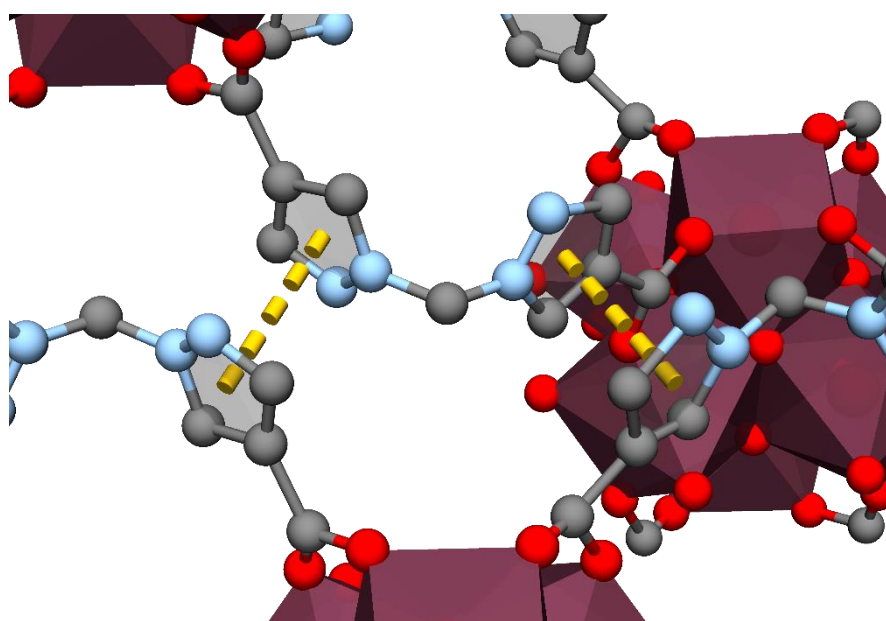


Figure I.4. A close-up of the π - π interactions between vicinal pyrazoles of two UAM-1 layers.

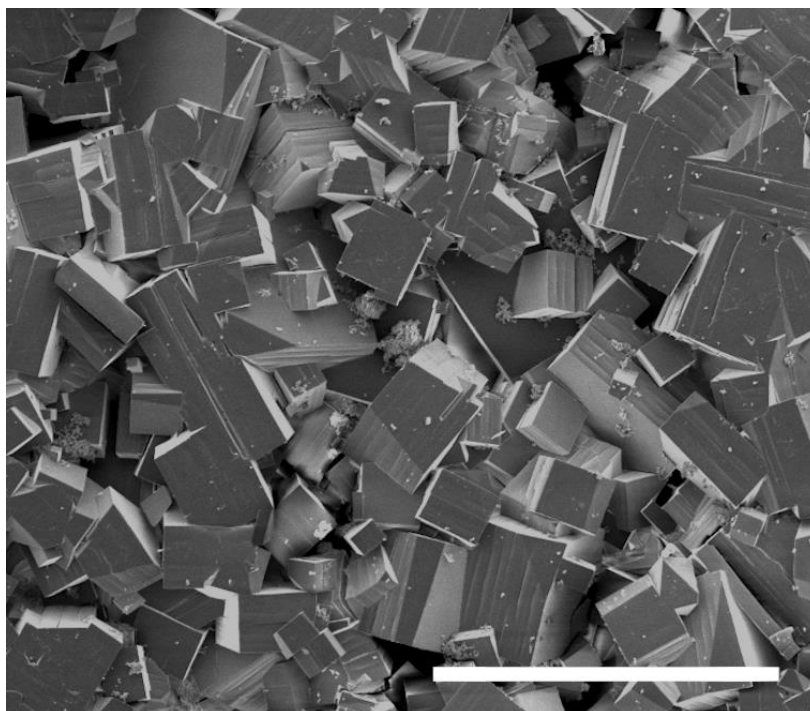


Figure I.5. SEM image of UAM-2 as made (scale bar= 50 μm).

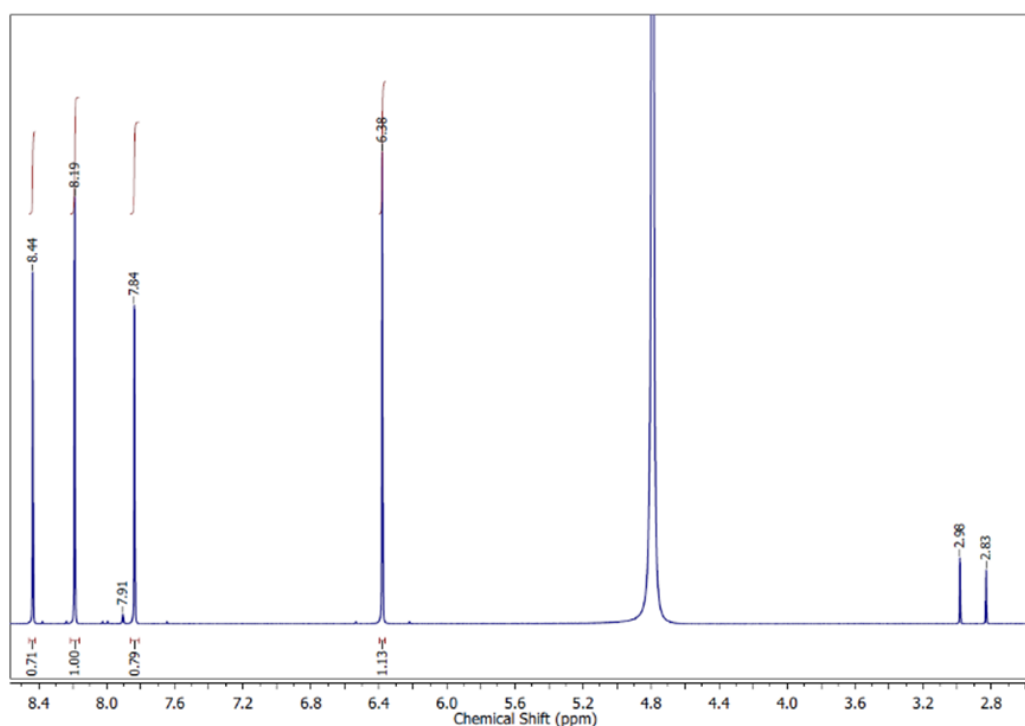


Figure I.6. $^1\text{H-NMR}$ spectrum of digested **UAM-2**. Sample preparation: UAM-2 was washed with DMF (4 x 5 mL), acetone (3 x 5 mL) and dried under vacuum for 24 h. Digestion conditions: 50 μL NaOD in 500 μL of D_2O , heated at 80 $^\circ\text{C}$ for 1 h. The peak at 8.31 ppm corresponds to the formate anion. Its relative integration compared with the L peaks show a molar ratio L:formate 1:1.4 which is consistent with the presence of 5.5 formate anions per Zr cluster suggesting that some of the formate anions are monodentate. Peaks at 7.91, 2.98 and 2.83 ppm show the presence of DMF molecules trapped in the structure.

Table I.1. Energy-dispersive X-ray (EDX) data for Cu, I, and Cl after acid and base exfoliation treatments of UAM-2. Quantification of % occupancy on the bis(pyrazolyl)methane coordinating sites was determined by measuring Zr:Cu, Cu:I and Zr:Cl ratios.

Sample	Cu (% occupancy) ^{a,b}	I (% occupancy) ^{a,b}	Cl (% occupancy) ^{a,b}
UAM-2	100 ± 5	98 ± 4	6 ± 1
UAM-2-HCl	No detectable Cu	No detectable I	108 ± 5
UAM-2·ns	No detectable Cu	No detectable I	No detectable Cl

^aAverage atomic% obtained from three areas of three different crystals.

^bRelative to full occupancy of the bis(pyrazolyl)methane sites in **UAM-2** (Zr:Cu:I = 3:2:2) and **UAM-2·ns** (Zr:Cl = 3:2).

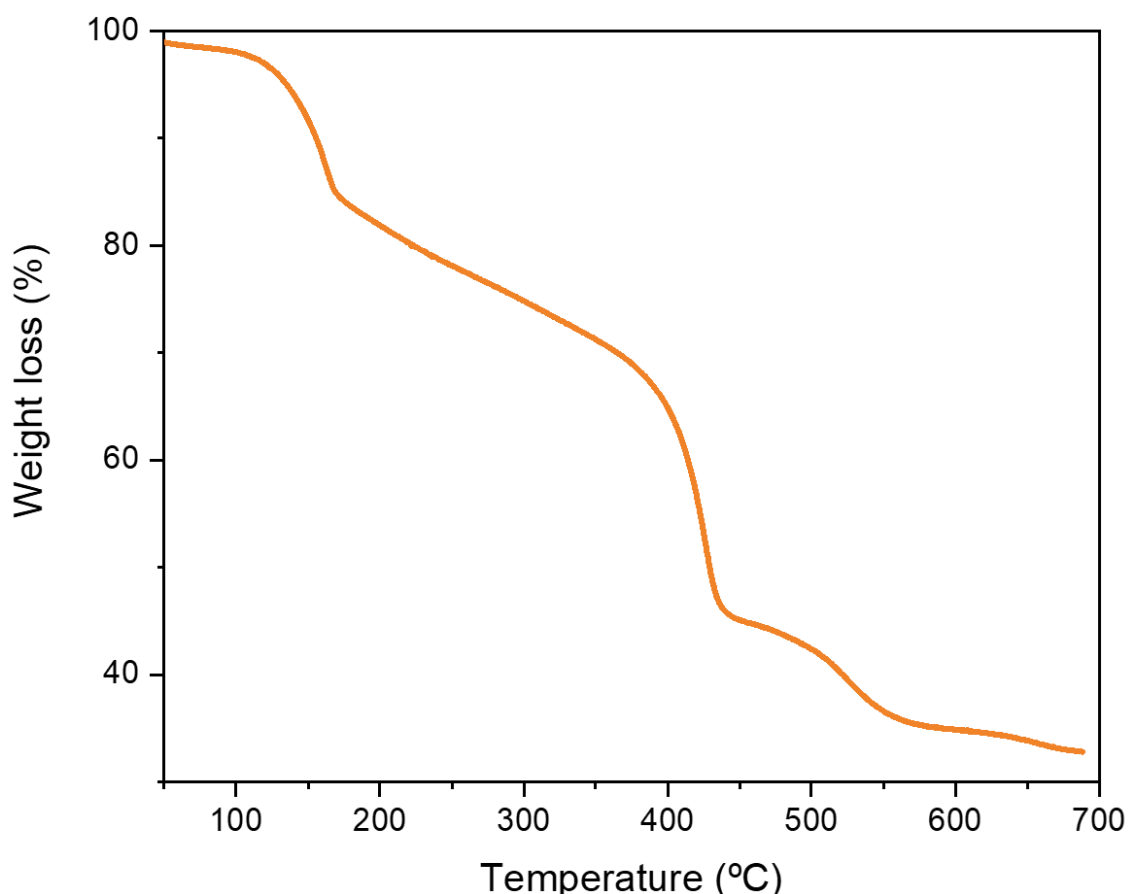


Figure I.7. Thermogravimetric analysis spectrum (orange) of UAM-1. Analysis conditions: 50 °C – 700 °C at 5 °C/min, under an oxidising (air) atmosphere.

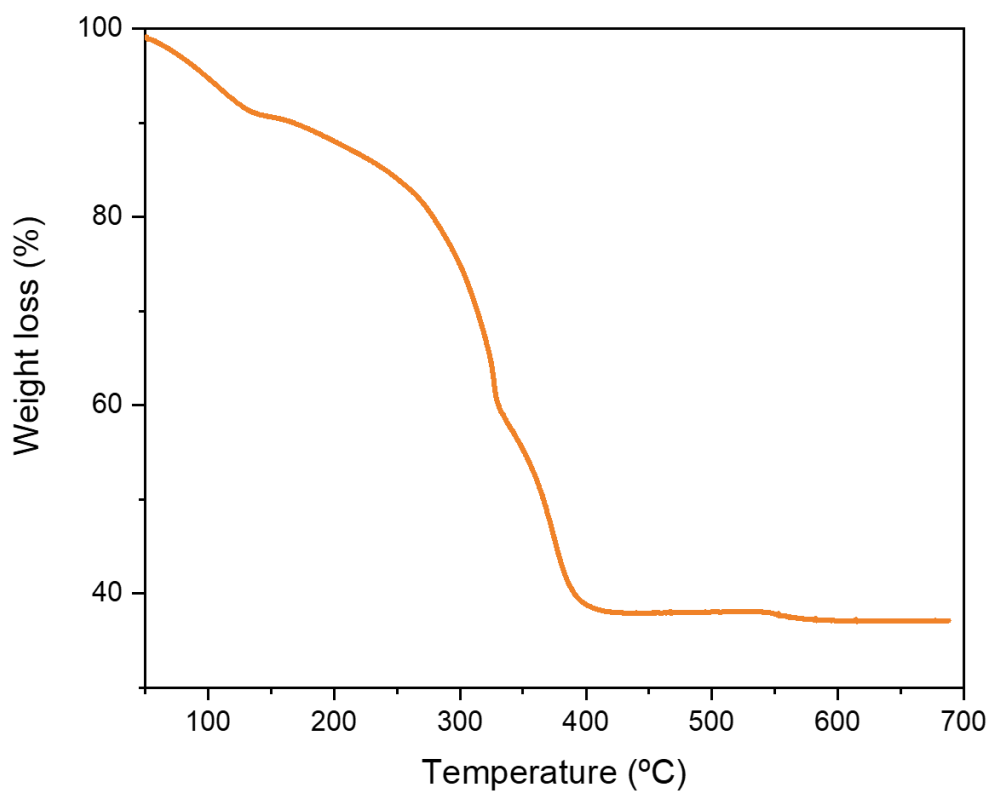


Figure I.8. Thermogravimetric analysis spectrum (orange) of UAM-2. Analysis conditions: 50 °C – 700 °C at 5 °C/min, under an oxidising (air) atmosphere.

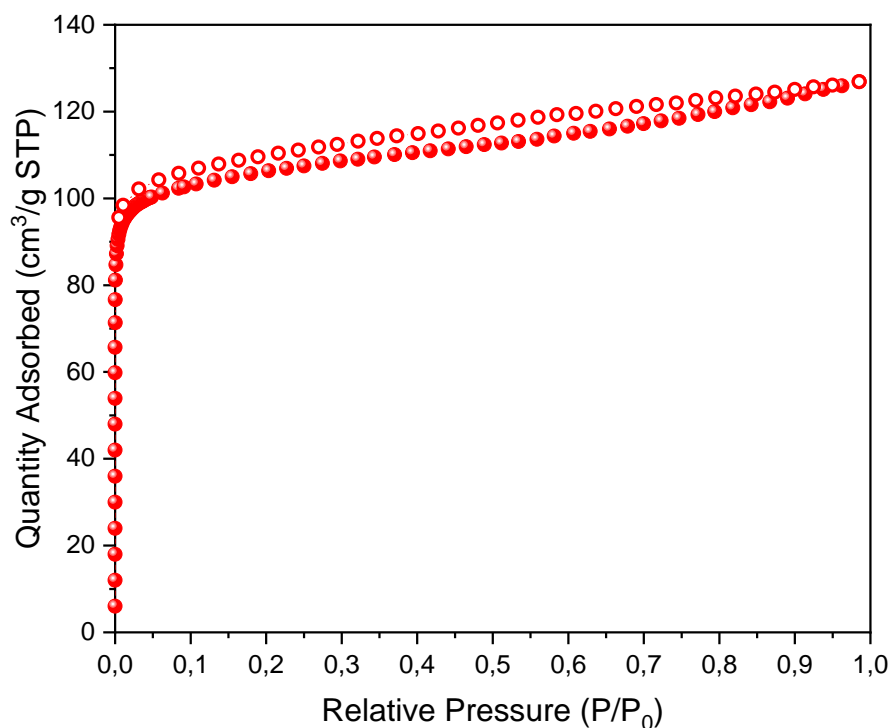


Figure I.9. 77 K N₂ isotherm data of UAM-1, after activation from methanol at 120 °C for 3 h. Coloured circles represent adsorption, open circles represent desorption.

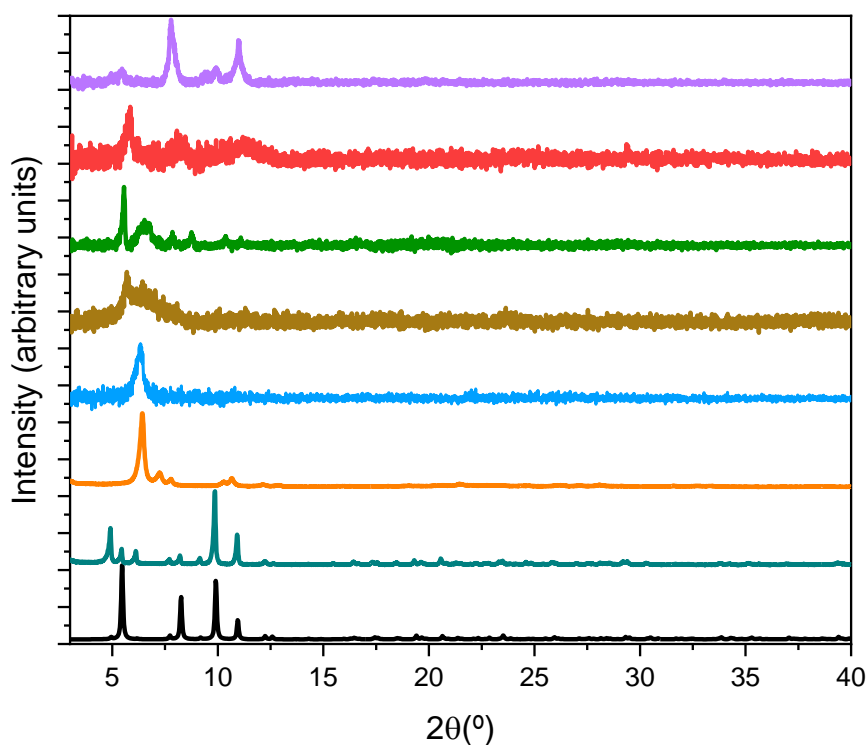


Figure I.10. Experimental PXRD plots for UAM-2 as made (green), UAM-2·HCl (orange), UAM-2·ns (blue), UAM-2·CoCl₂ (gold), and UAM-2 after BET analysis (purple) versus simulated UAM-2 (black). Like other related materials with flexible linkers, the flexibility of the framework appears to cause slight shifts in the PXRD peak positions upon changes in the solvent and loss of solvent during sample preparation for PXRD.

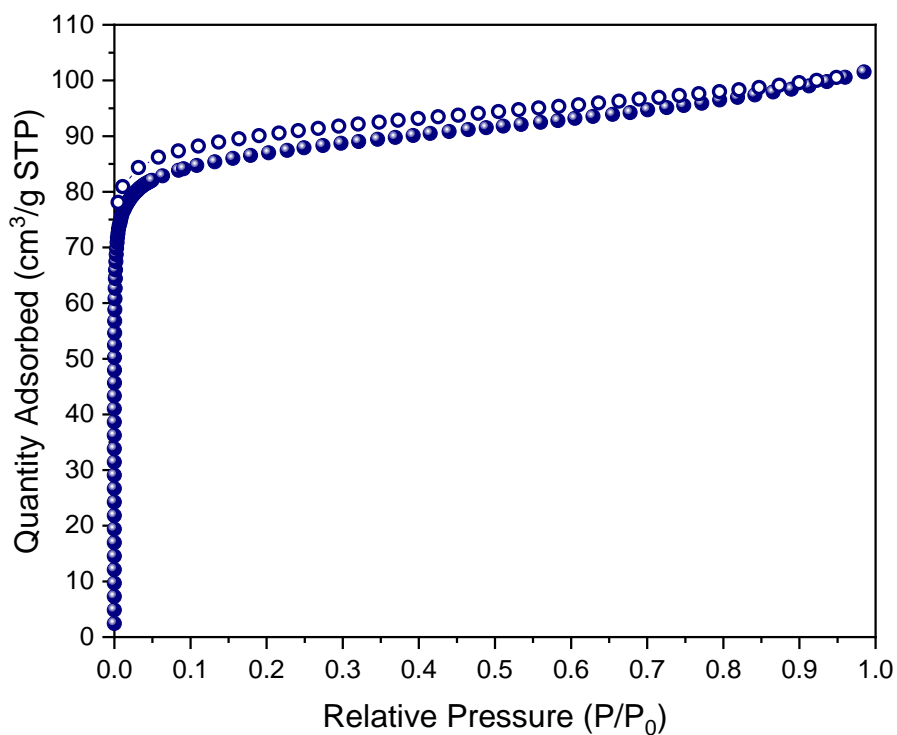


Figure I.11. 77 K N₂ isotherm data of UAM-2, after activation from methanol at 120 °C for 3 h. Coloured circles represent adsorption, open circles represent desorption.

Table I.2. Energy-dispersive X-ray (EDX) data for Co and Cl after metalation of UAM-1 at different times. Quantification of % occupancy on the bis(pyrazolyl)methane coordinating sites was determined by measuring Zr:Co and Zr:Cl ratios.

Sample	Co (% occupancy) ^{a,b}	Cl (% occupancy) ^{a,b}
UAM-1	No detectable Co	No detectable Cl
UAM-1·CoCl ₂ 2 h	4 ± 3	8 ± 4
UAM-1·CoCl ₂ 5 h	3 ± 3	7 ± 5
UAM-1·CoCl ₂ 24 h	4 ± 3	8 ± 4

^aAverage atomic% obtained from three areas of five different crystals.

^bRelative to full occupancy of the bis(pyrazole)methane coordinating sites in UAM-1 (Zr:Co = 3:2).

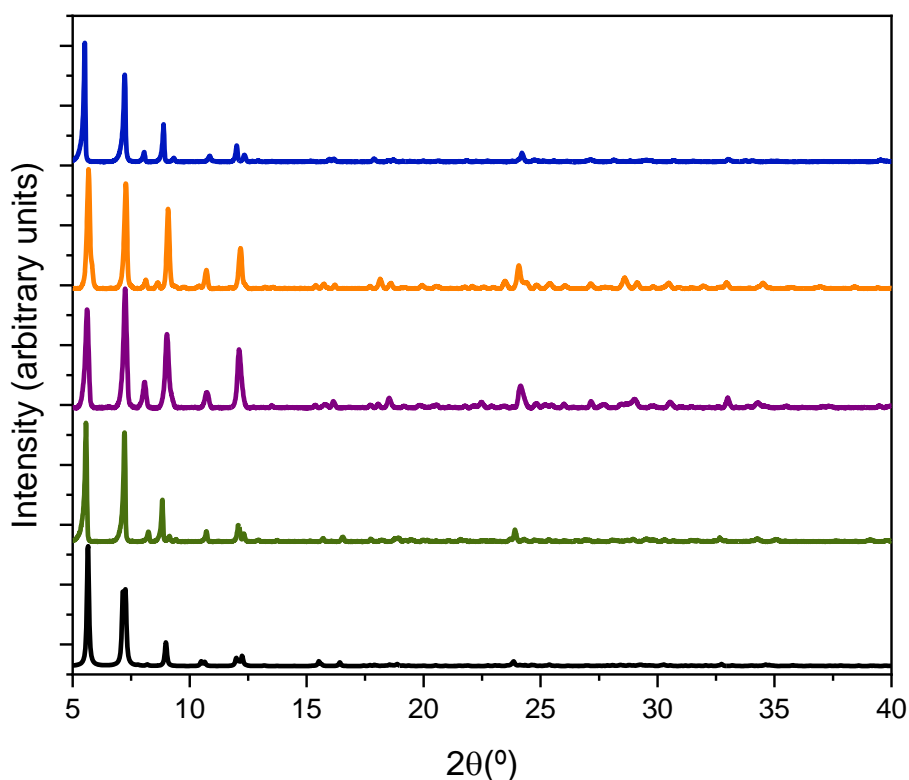


Figure I.12. Experimental PXRD plots for UAM-1 as made (green), UAM-1 sonicated (purple), UAM-1 after acid-base treatment (orange) and UAM-1·CoCl₂ (blue), versus simulated UAM-1 (black). Like other related materials with flexible linkers, the flexibility of the framework appears to cause slight shifts in the PXRD peak positions upon changes in the solvent and loss of solvent during sample preparation for PXRD.

Table I.3. Energy-dispersive X-ray (EDX) data for Co and Cl after metalation of “delaminated” UAM-1 at different times. Quantification of % occupancy on the bis(pyrazolyl)methane coordinating sites was determined by measuring Zr:Co and Zr:Cl ratios.

Sample	Co, (% occupancy) ^{a,b}	Cl, (% occupancy) ^{a,b}
UAM-1	No detectable Co	No detectable Cl
UAM-1·HCl	No detectable Co	104 ± 3
UAM-1·abt	No detectable Co	No detectable Cl
UAM-1·abt·CoCl ₂ 2 h	3 ± 3	7 ± 3
UAM-1·abt·CoCl ₂ 5 h	3 ± 4	6 ± 5
UAM-1·abt·CoCl ₂ 24 h	3 ± 3	6 ± 4

^aAverage atomic% obtained from three areas of three different crystals.

^bRelative to full occupancy of the bis(pyrazole)methane coordinating sites in UAM-1 (Zr:Co = 3:2).

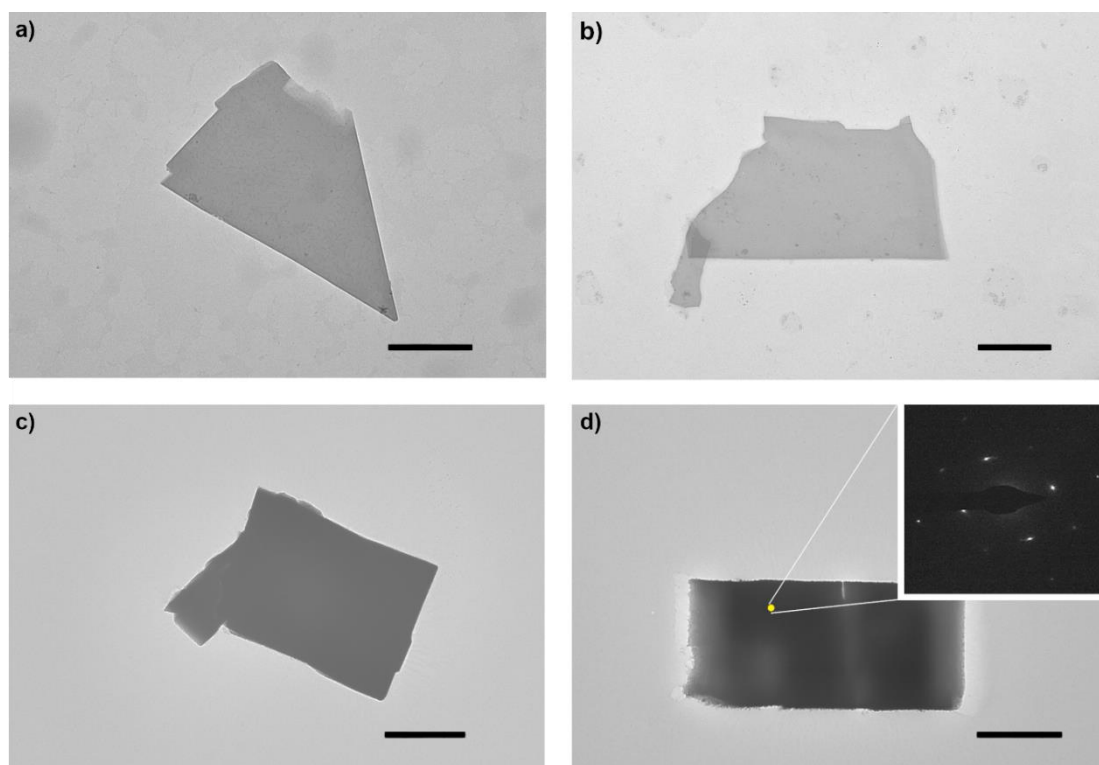


Figure I.13. TEM images of UAM-2·HCl (a, b) and UAM-2·ns (c,d). Scale bar= 1 μ m.

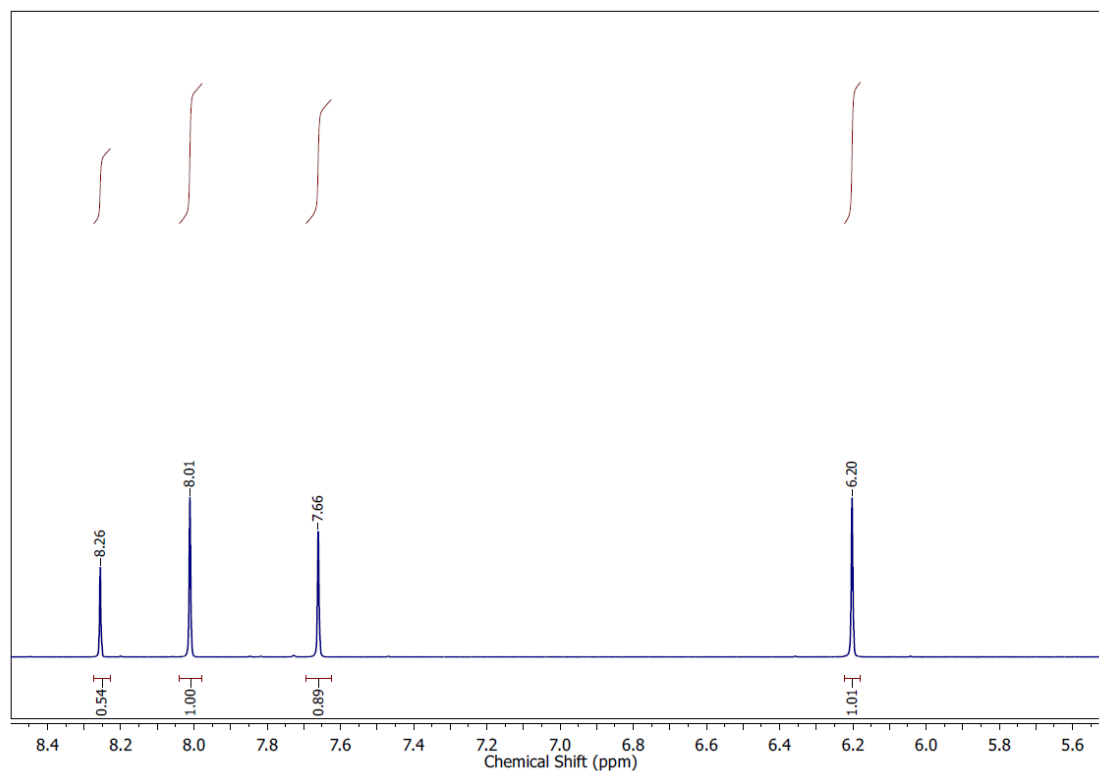


Figure I.14. ^1H -NMR spectrum of $\text{UAM-2}\cdot\text{HCl}$ after $\text{NaOD}/\text{D}_2\text{O}$ digestion. Digestion conditions: $50\ \mu\text{L}$ NaOD in $500\ \mu\text{L}$ of D_2O heated at $80\ ^\circ\text{C}$ for 1 h. Peak at 8.26 ppm corresponds to the formate anion. Its relative integration compared with the L peaks show a decrease of formate anions compared to UAM-2 with molar ratio L:formate 1:1 which is consistent with the presence of four formate anions per Zr cluster suggesting that all formates are now bidentate.

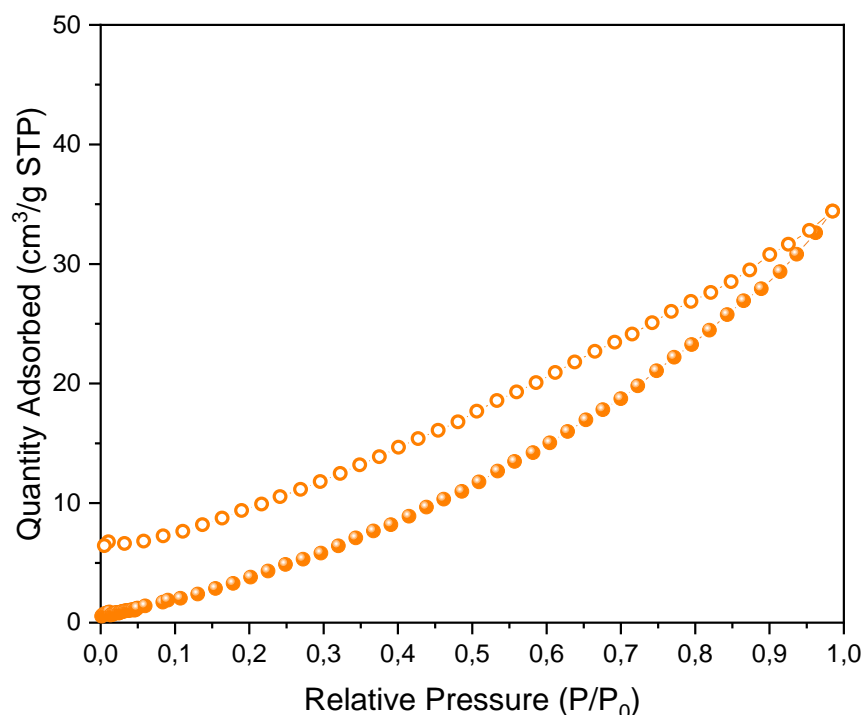


Figure I.15. 77 K N_2 isotherm data of UAM-2·ns, after activation from methanol at 120 °C for 3 h (identical conditions to the non-delaminated material). Coloured circles represent adsorption, open circles represent desorption.

Table I.4. Energy-dispersive X-ray (EDX) data for the metalation of UAM-2 at different interval times. Quantification of % occupancy on the bis(pyrazolyl)methane coordinating sites was determined by measuring Zr:Co, Zr:Cu, Zr:Pd and Zr:Cl ratios.

Sample	Co (% occupancy) ^{a,b}	Cu (% occupancy) ^{a,b}	Pd (% occupancy) ^{a,b}	Cl (% occupancy) ^{a,b}
UAM-2·CoCl ₂ 2 h	99 ± 6	No detectable	No detectable	212 ± 1
UAM-2·CoCl ₂ 5 h	99 ± 5	No detectable	No detectable	213 ± 2
UAM-2·CoCl ₂ 24 h	97 ± 3	No detectable	No detectable	205 ± 2
UAM-2·CuCl ₂ 2 h	No detectable	98 ± 4	No detectable	200 ± 2
UAM-2·CuCl ₂ 5 h	No detectable	99 ± 4	No detectable	205 ± 4
UAM-2·CuCl ₂ 24 h	No detectable	103 ± 5	No detectable	201 ± 4
UAM-2·PdCl ₂ 2 h	No detectable	No detectable	93 ± 3	186 ± 3
UAM-2·PdCl ₂ 5 h	No detectable	No detectable	99 ± 5	201 ± 3
UAM-2·PdCl ₂ 24 h	No detectable	No detectable	101 ± 4	201 ± 4

^aAverage atomic% obtained from three areas of three different crystals.

^bRelative to full occupancy of the bis(pyrazole)methane coordinating sites in UAM-2·ns (Zr:Co:Cl = 3:2:4; Zr:Cu:Cl = 3:2:4; Zr:Pd:Cl = 3:2:4).

I.II. Fourier Transform Infrared Spectroscopy (FTIR) spectra

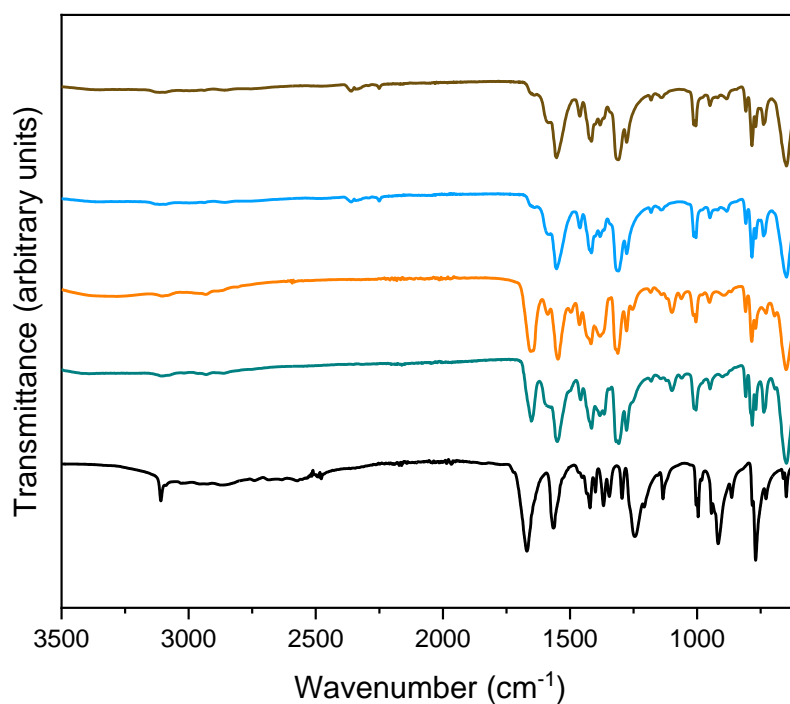


Figure I.16. FTIR spectra of H₂L (black), UAM-1 as made (green), UAM-1·HCl (orange), UAM-1 after base (blue) and UAM-1·CoCl₂ after sonication (brown).

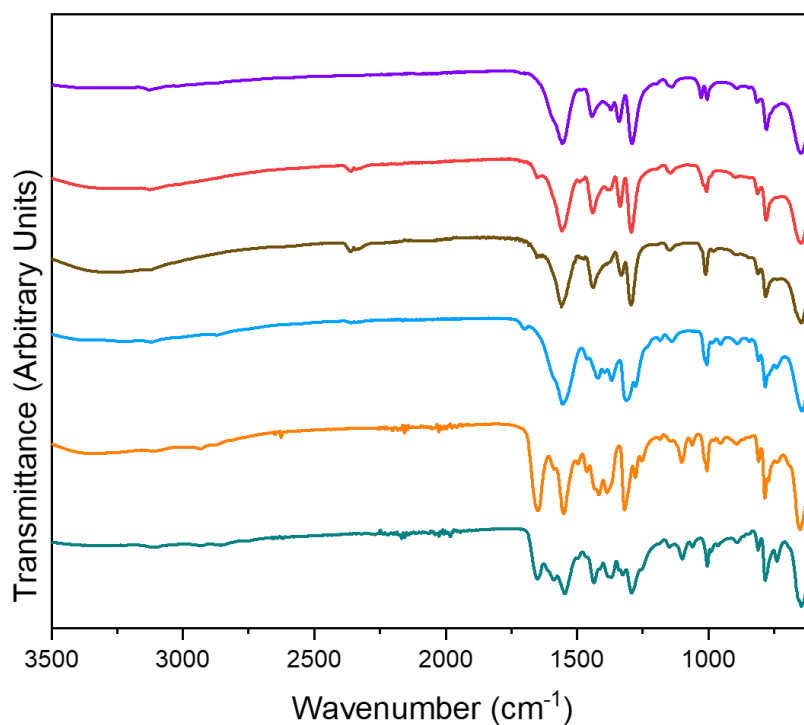


Figure I.17. FTIR spectra of UAM-2·CuI (green), UAM-2·HCl (orange), UAM-2 (blue), UAM-2·CoCl₂ (brown), UAM-2·CuCl₂ (red) and UAM-2·PdCl₂ (purple).

I.III. Nuclear Magnetic Resonance (NMR) data

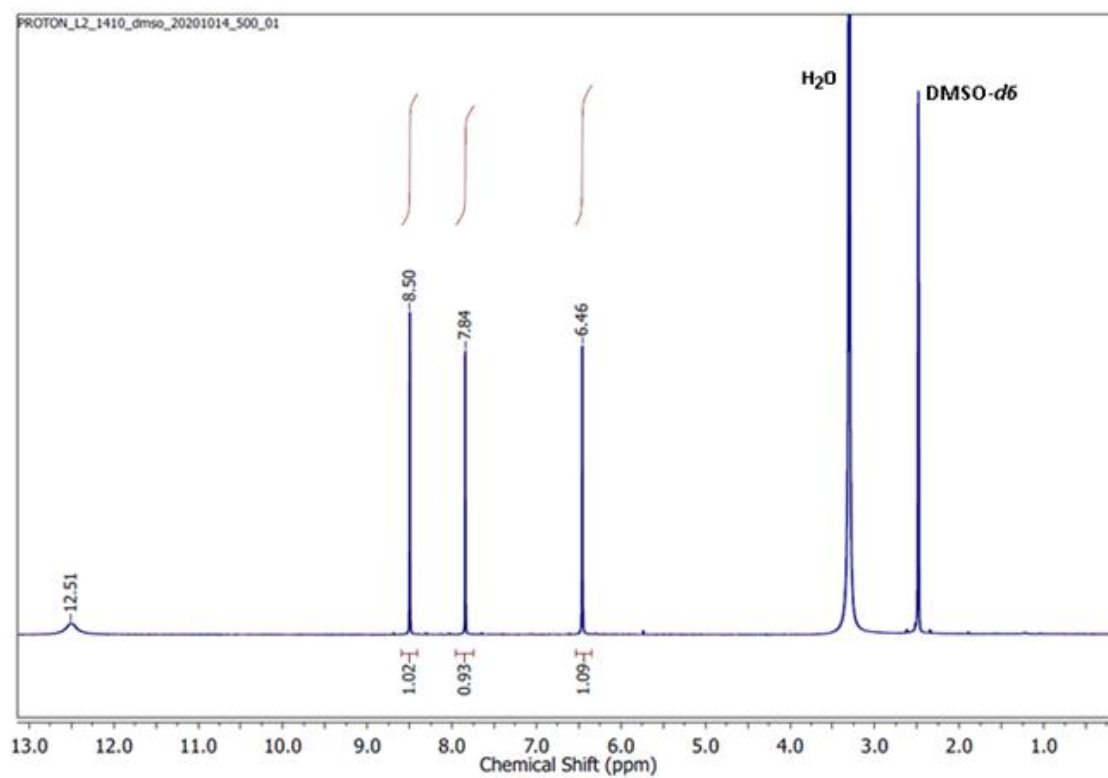


Figure I.18. ^1H -NMR spectrum of H_2L .

I.IV. Single crystal X-ray crystallography

I.IV.I. Thermal ellipsoid plots for all structures at the 50% probability level

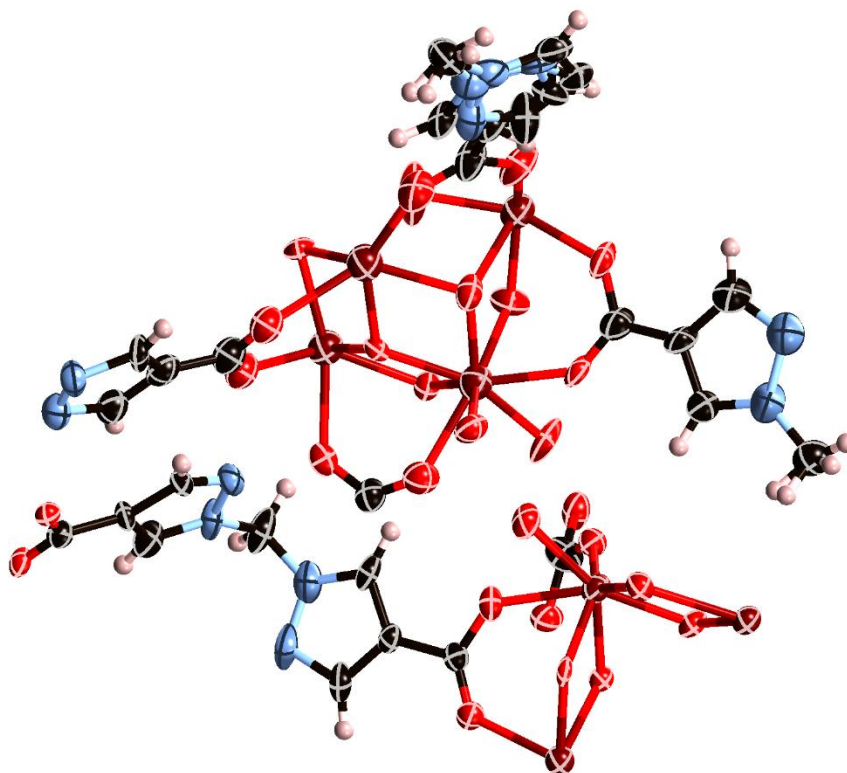


Figure I.19. Asymmetric unit of UAM-1, with all non-hydrogen atoms represented by ellipsoids at the 50% probability level (C, black; H, pink; N, light blue; O, red; Cu, dark blue; Zr, dark red; I, purple).

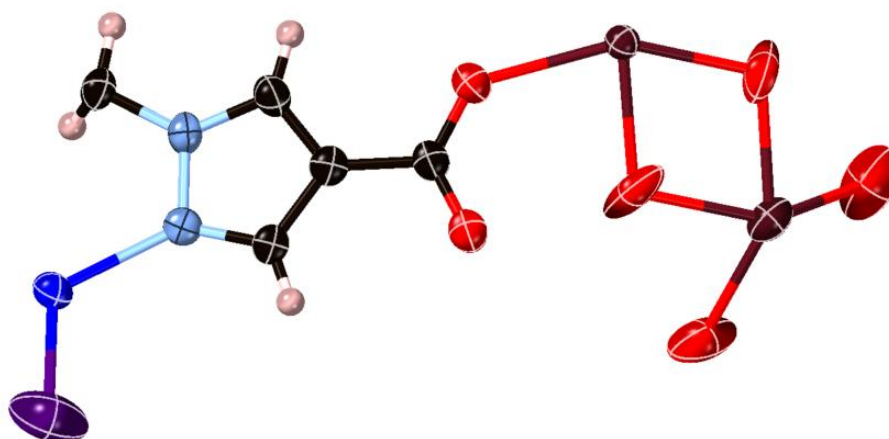


Figure I.20. Asymmetric unit of UAM-2, with all non-hydrogen atoms represented by ellipsoids at the 50% probability level (C, black; H, pink; N, light blue; O, red; Cu, dark blue; Zr, dark red; I, purple).

I.IV.II. Crystallographic representations

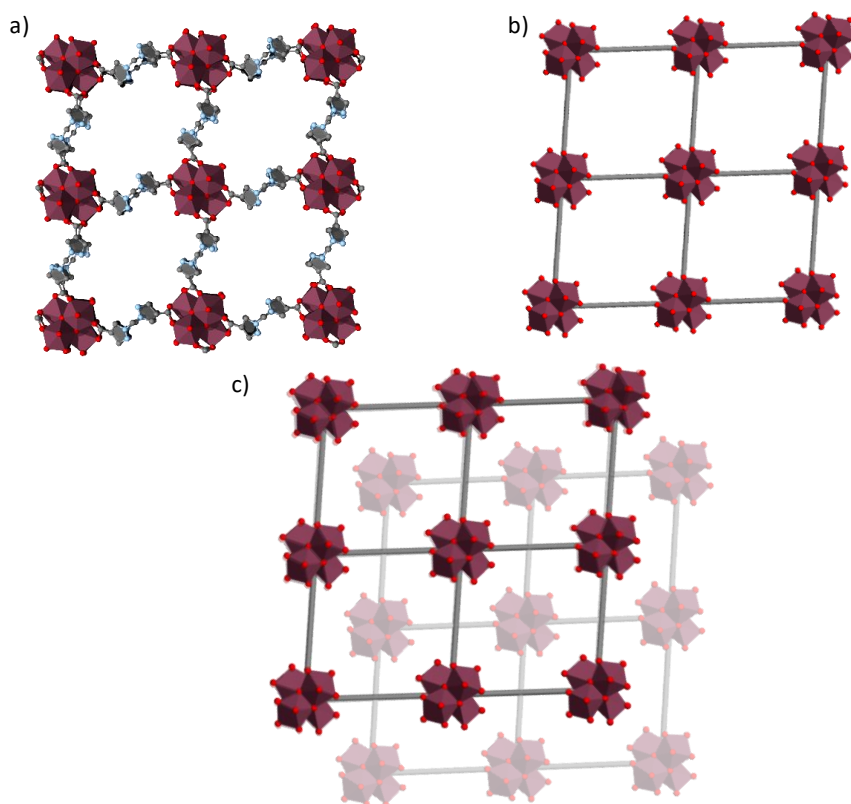
UAM-1

Figure I.21. a) Top view crystallographic representation of a single layer of UAM-1. b) Top view of a simplified representation of a single layer of UAM-1. c) Top view of a simplified representation of the two different positions of the disordered layer of UAM-1. (C, grey; N, light blue; O, red; Zr, dark red). Hydrogens have been hidden for clarity.

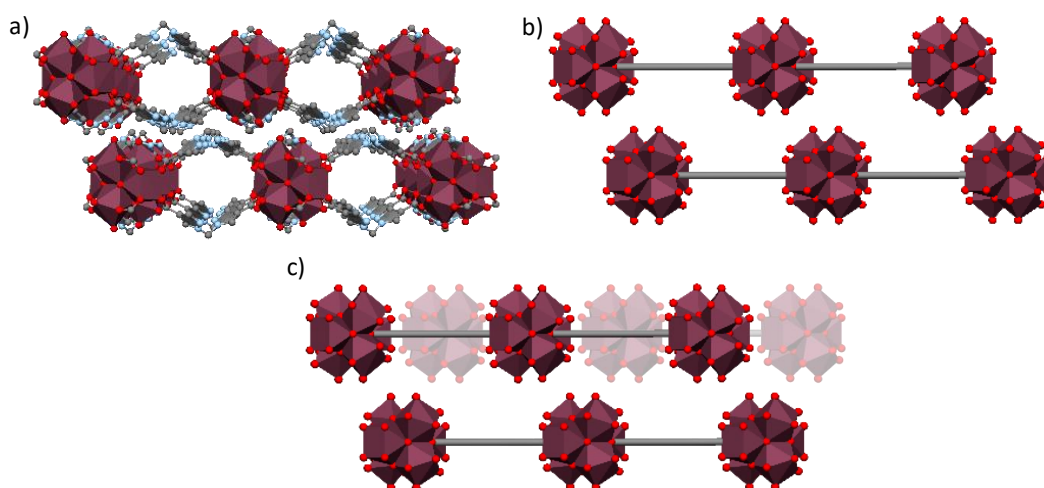


Figure I.22. a) Side view crystallographic representation of two layers of UAM-1. b) Side view schematic representation of two layers of UAM-1. c) Side view schematic representation of two layers of UAM-1. The top layer can occupy two different positions. One of the layer positions is shaded for clarity. (C, grey; N, light blue; O, red; Zr, dark red). Hydrogens have been hidden for clarity.

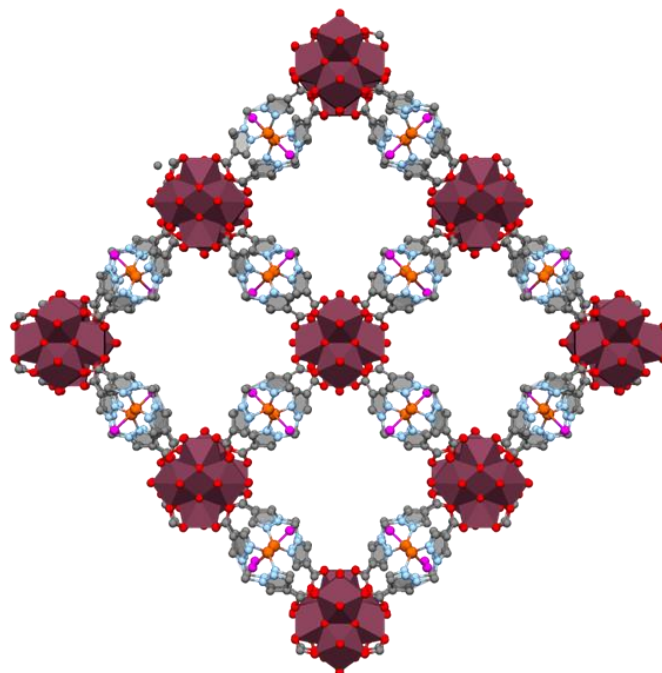
UAM-2

Figure I.23. *ab* plane crystallographic representation of UAM-2 (C, grey; N, light blue; O, red; Cu, orange; Zr, dark red; I, pink). Hydrogens have been hidden for clarity.

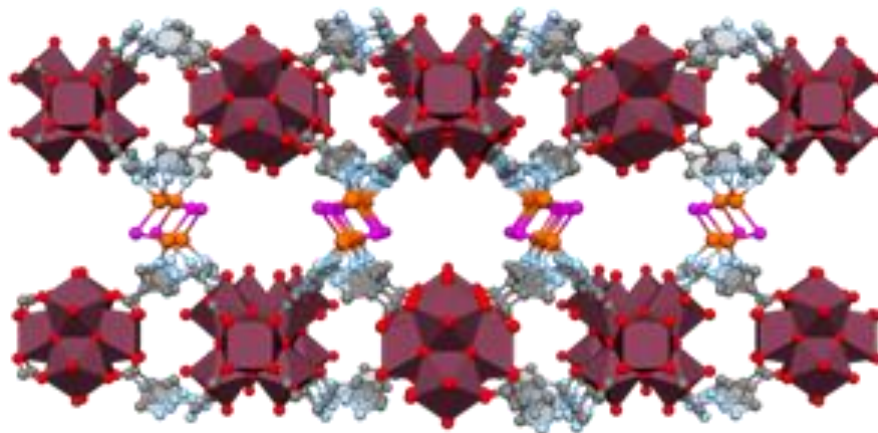


Figure I.24. *ac* plane crystallographic representation of UAM-2 (C, grey; N, light blue; O, red; Cu, orange; Zr, dark red; I, pink). Hydrogens have been hidden for clarity.

I.IV.III. Tables of X-ray crystallography data collection and refinement parameters**Table 1.5.** Crystallographic data collection and refinement parameters for UAM-1 and UAM-2.

Sample	UAM-1	UAM-2
Crystallographic Parameter		
Formula	$C_{20.5}H_{15.5}N_{8.5}O_{16.5}Zr_3$	$C_{18}H_{12}Cu_2I_2N_8O_{16}Zr_3$
FW	1027.59	1250.90
T, K	100(2)	100
Wavelength, Å	Synchrotron ($\lambda = 0.6888$)	Synchrotron ($\lambda = 0.71073$)
Crystal system, space group	Orthorhombic, Amm2	Tetragonal, I4/mmm
Z	8	8
a, Å	19.017(4)	22.738(3)
b, Å	23.361(5)	22.738(3)
c, Å	21.208(4)	28.593(6)
α°	90	90
β°	90	90
γ°	90	90
V, Å ³	9422(3)	14783(5)
dcalc, g/cm ³	1.449	1.124
Absorption coefficient, mm ⁻¹	3.828	1.846
F(000)	4040.0	4704.0
Crystal size, mm ³	0.02 × 0.02 × 0.02	0.03 × 0.03 × 0.03
2 θ range for data collection	2.076 to 58.346	2.288 to 58.152
Index range	-23 ≤ h ≤ 23, -28 ≤ k ≤ 30, -28 ≤ l ≤ 29	-30 ≤ h ≤ 30, -31 ≤ k ≤ 30, -38 ≤ l ≤ 39
Reflections collected	106441	95189
Independent reflections	12746 [Rint = 0.0619, Rsigma = 0.0418]	4771 [Rint = 0.0280, Rsigma = 0.0080]
Data/restraints/parameters	12746/442/601	4771/0/125
GOF on F ²	1.183	1.079
Largest diff. peak and hole, eÅ ⁻³	1.34/-1.30	1.35/-2.37
R ₁ , [I > 2 σ (I)]	0.0855	0.0740
wR ₂ , all data	0.2837	0.2306
CCDC Number	2119441	2119442

I.V. References

1. McPhillips, T. M., McPhillips, S. E., Chiu, H. J., Cohen, A. E., Deacon, A. M., Ellis, P. J., Garman, E., Gonzalez, A., Sauter, N. K., Phizackerley, R. P., Soltis, S. M. and Kuhn, P. J. *Synchrotron Radiat.*, **2002**, 9, 401-406.
2. Aragao, D., Aishima, J., Cherukuvada, H., Clarken, R., Clift, M., Cowieson, N. P., Ericsson, D. J., Gee, C. L., Macedo, S., Mudie, N., Panjikar, S., Price, J. R., Riboldi-Tunncliffe, A., Rostan, R., Williamson, R. and Caradoc-Davies, T. T. *J. Synchrotron Radiat.*, **2018**, 25, 885-891.
3. Cowieson, N. P., Aragao, D., Clift, M., Ericsson, D. J., Gee, C., Harrop, S. J., Mudie, N., Panjikar, S., Price, J. R., Riboldi-Tunncliffe, A., Williamson, R. and Caradoc-Davies, T. *J. Synchrotron Radiat.*, **2015**, 22, 187-190.
4. Sheldrick, G. M. *Acta Crystallogr. Sect. A: Found. Crystallogr.*, **2015**, 71, 3-8.
5. Sheldrick, G. M. *Acta Crystallogr. Sect. A: Found. Crystallogr.*, **2008**, 64, 112-122.
6. Sheldrick, G. M. *Acta Crystallogr. Sect. C: Cryst. Struct. Commun.*, **2015**, 71, 3-8.
7. Barbour, L. J. *Supramol. Chem.*, **2001**, 1, 189-191.
8. Dolomanov, O. V., Bourhis, L. J., Gildea, R. J., Howard, J. A. K. and Puschmann, H. J. *Appl. Crystallogr.*, **2009**, 42, 339-341.
9. Spek, A. L. *Acta Crystallogr. Sect. C: Cryst. Struct. Commun.*, **2015**, 71, 9-18.

II. Appendix 2: Supplementary Information for Chapter 3

II.I. Main Text Supporting Characterisation

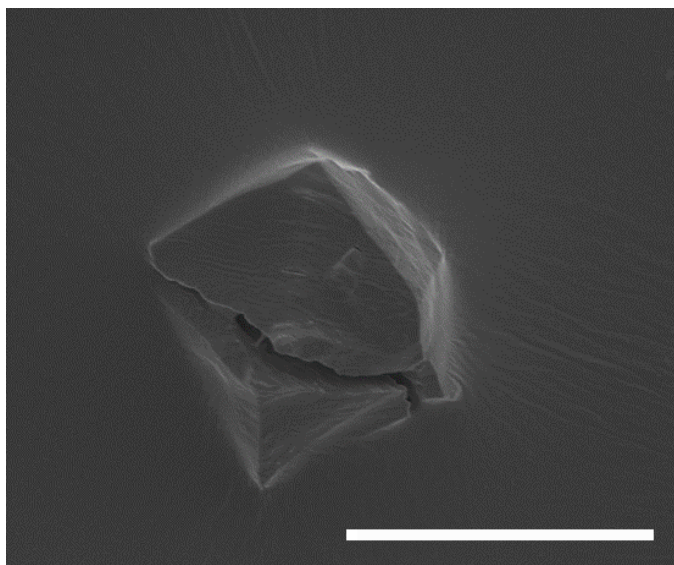


Figure II.1. SEM image of a UAM-1000 crystal. Scale bar 50 μm .

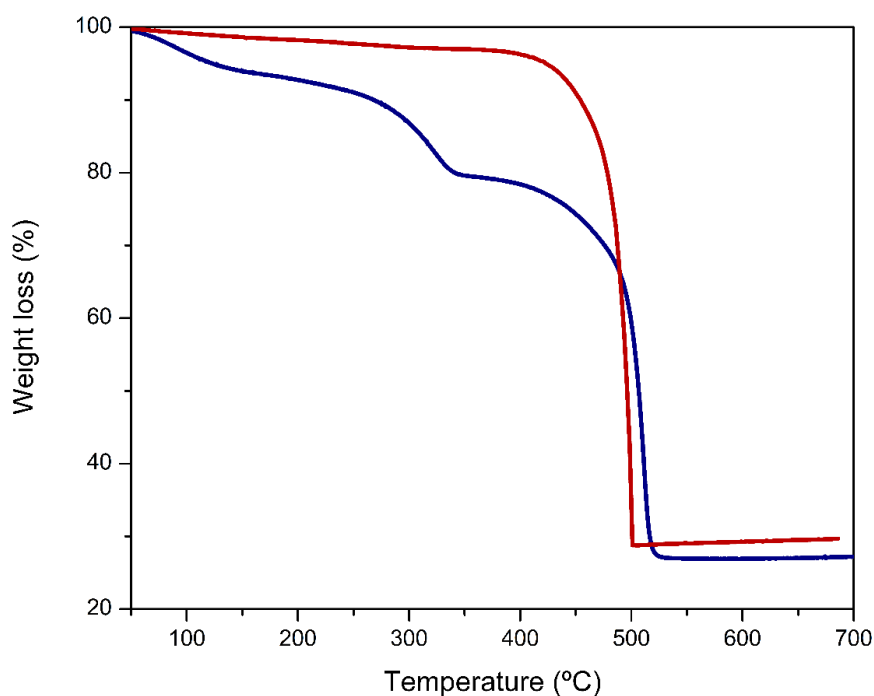


Figure II.2. Thermogravimetric analysis plot for UAM-1000 (blue) and UAM-1001 (red). Analysis conditions: 50 $^{\circ}\text{C}$ – 700 $^{\circ}\text{C}$ at 5 $^{\circ}\text{C}/\text{min}$, under an oxidising (air) atmosphere. The first step loss in UAM-1000 represents 14% of weight loss that can be attributed to the loss of the DMF and OH groups coordinated to the Zr cluster.

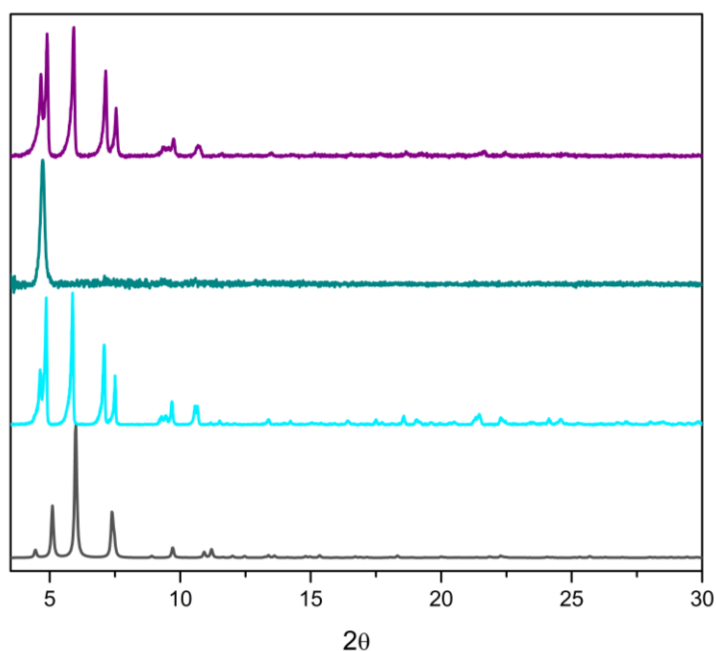


Figure II.3. Experimental PXRD plots for UAM-1000 as made (blue), UAM-1000·act (green), UAM-1000 resolvated (purple) versus simulated UAM-1000 (black).

Table II.1. Energy-dispersive X-ray (EDX) data for Cu, Pd and Cl before and after metalation of UAM-1000. Quantification of % occupancy in the bis(pyrazolyl)methane coordinating sites was determined by measuring Zr:Cu, Zr:Pd and Pd:Cl ratios.

Sample	M (% occupancy) ^{a,b}	Cl (% occupancy) ^{a,b}
UAM-1000	No detectable	6 ± 3
UAM-1000·Cu(NO ₃) ₂	47.8 ± 4	No detectable
UAM-1000·PdCl ₂	52.8 ± 3	101.2 ± 3

^a Average atomic% obtained from three areas of three different crystals.

^b Relative to full occupancy of the bis(pyrazolyl)methane sites in UAM-1000 (Zr:M = 3:2).

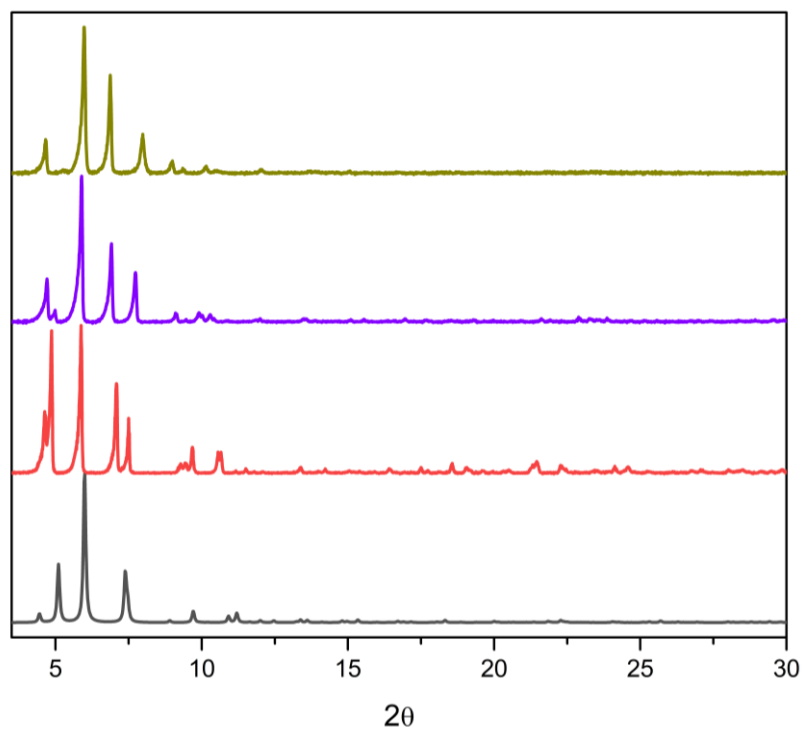


Figure II.4. Experimental PXRD plots for UAM-1000 as made (red), UAM-1000·Cu(NO₃)₂ (purple) and UAM-1000·PdCl₂ (olive) versus simulated UAM-1000 (black).

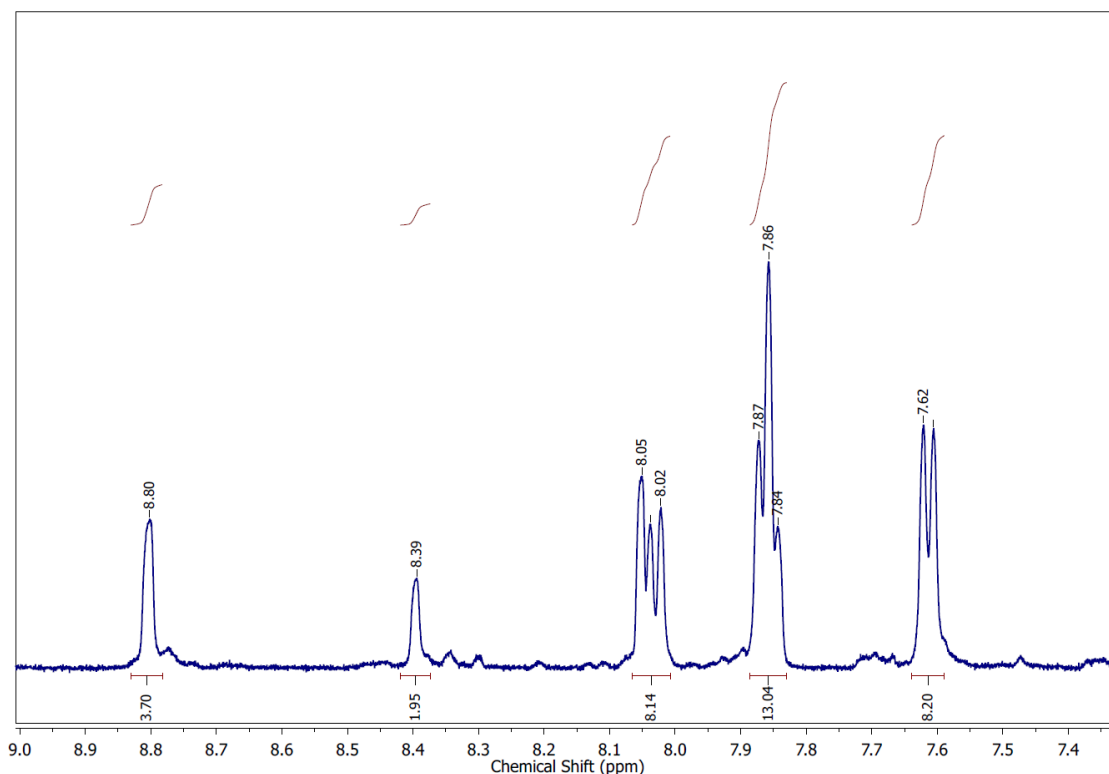


Figure II.5. NMR digestion of UAM-1001. BPDC doublets are overlapped with L1 peaks. Taking as a reference the 8.39 ppm singlet that corresponds with CH (methylene hinge) we can calculate the integration peaks of L1. The peak at 8.05 ppm corresponds to one of the CH-pyrazole that should integrate 4H. The doublet right next to it and partially overlapped at 8.01 ppm corresponds to CH-BPDC. If the singlet and doublet together integrate 8H and we know that the CH-pyrazole peak integrates 4H that means the BPDC doublet integrates 4H. This means that for each L1 molecule we have one BPDC molecule giving a molar ratio of 1:1.

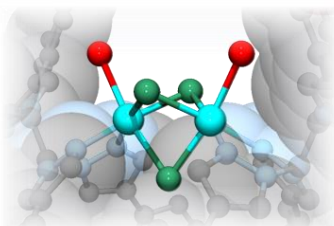
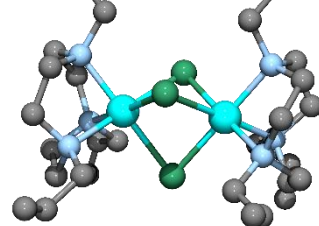
Table II.2. Energy-dispersive X-ray (EDX) data for Cu, Pd, Rh, Ni, Co and Cl before and after metalation of UAM-1001. Quantification of % occupancy of the bis(pyrazolyl)methane coordinating sites was determined by measuring Zr:Cu, Zr:Pd, Zr:Rh, Zr:Ni, Zr:Co and Zr:Cl ratios.

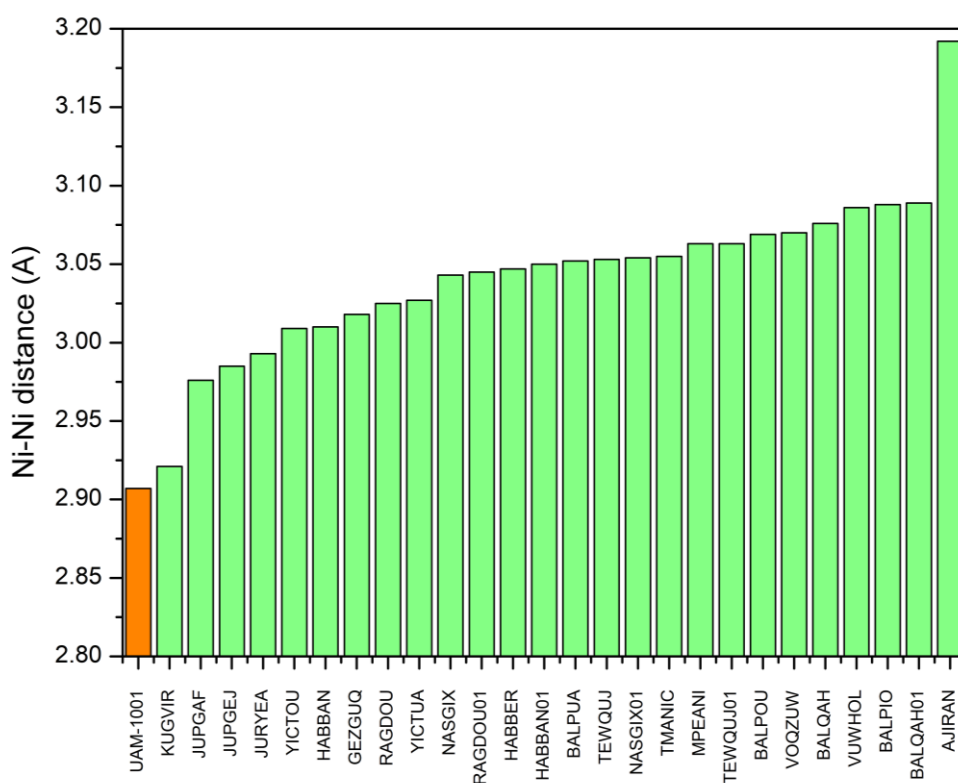
Sample	M (% occupancy) ^{a,b}	Cl (% occupancy) ^{a,b}
UAM-1001	No detectable	No detectable
UAM-1001[Cu(NO ₃) ₂ H ₂ O]	45.8 ± 3	No detectable
UAM-1001[PdCl ₂]	50.5 ± 1	102.5 ± 2
UAM-1001[Rh ₂ (CO) ₃ Cl ₂]	92.7 ± 3	96.3 ± 3
UAM-1001[Cu ₂ Cl ₄]	92.3 ± 3	194.4 ± 2
UAM-1001[Ni ₂ Cl ₃ (H ₂ O) ₂ Cl]	95.4 ± 2	197.2 ± 2
UAM-1001[Co ₂ Cl ₄]	75.5 ± 3	160.1 ± 2

^a Average atomic% obtained from three areas of three different crystals.

^b Relative to full occupancy of the bis(pyrazolyl)methane sites in **UAM-1001** (Zr:M = 3:2).

Table II.3. Comparison of the MOF-isolated dinuclear complex and a closely related dimer from the literature.

	UAM-1001[Ni ₂ Cl ₃ (H ₂ O) ₂]Cl	[Ni ₂ Cl ₃ (tzcn) ₂]PF ₆ ¹
Crystal Colour	Green	Blue-green
Geometry	Octahedral	Octahedral
Ni-N(1) (Å)	2.094	2.110
Ni-N(2) (Å)	2.094	2.111
Ni-μCl(1) (Å)	2.383	2.451
Ni-μCl(2) (Å)	2.378	2.445
N(1)-Ni- μCl(1) (°)	174.86	178.04
N(1)-Ni-N(2) (°)	89.15	84.49
μCl(1)-Ni-μCl(2) (°)	88.14	84.67
Ni-Ni (Å)	2.907	3.088
CCDC Number	This work	182700
Representation		

**Figure II.6.** Graphic representation of the Ni-Ni distance of all the structures with a [Ni₂μCl₃] moiety found in the Cambridge Crystallographic database (accessed 21/11/2022). The structure from this work is in orange.

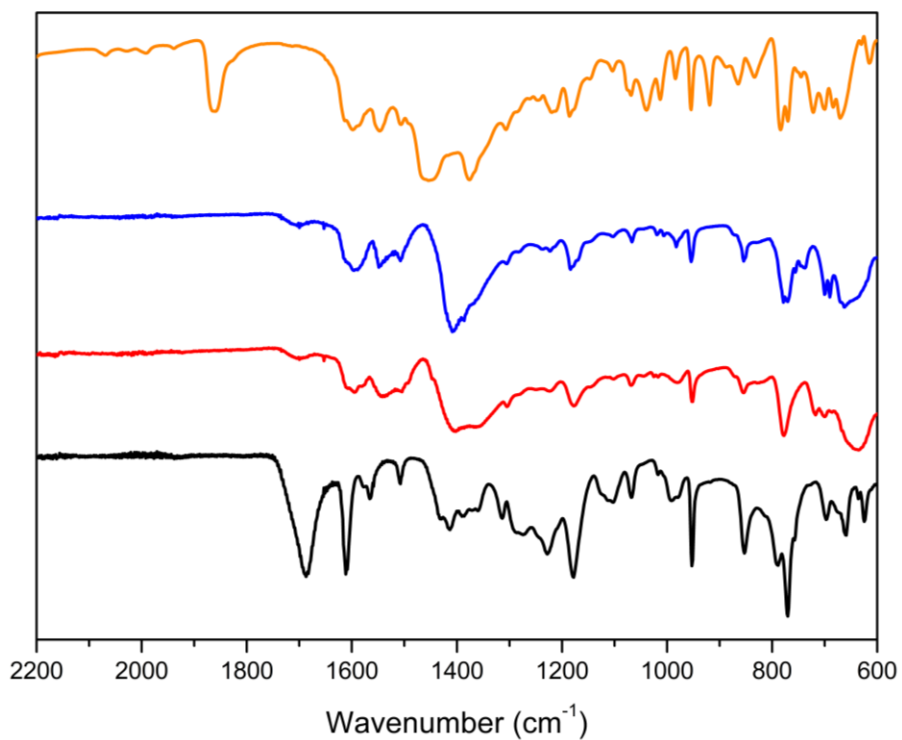


Figure II.7. Fourier-transform infrared spectra of L1H₄ (black), UAM-1000 (red), UAM-1001 (blue) and UAM-1001[Rh₂(CO)₃Cl₂] (orange).

Table II.4. Comparison of the MOF-isolated dinuclear complex and a closely related dimer from the literature.

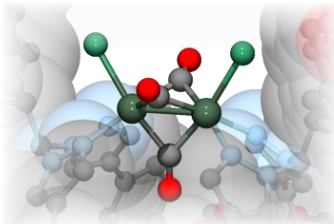
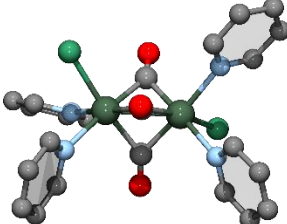
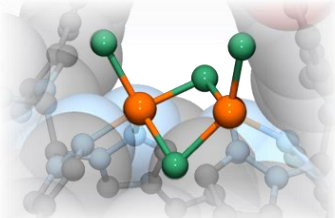
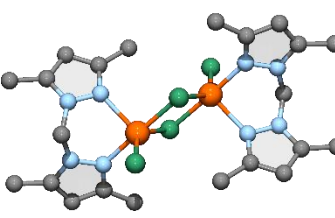
	UAM-1001[Rh ₂ (CO) ₃ Cl ₂]	Rh ₂ (CO) ₃ Py ₄ Cl ₂ ²
Crystal Colour	Yellow	Yellow
Geometry	Octahedral	Octahedral
Rh-N(1) (Å)	2.224	2.223
Rh-N(2) (Å)	2.224	2.188
Rh-μCO(1) (Å)	2.007	2.010
Rh-μCO(2) (Å)	2.007	2.010
Rh-Cl (Å)	2.458	2.472
N(1)-Rh- μCO(1) (°)	174.31	177.77
N(1)-Rh-N(2) (°)	84.99	91.19
μCO(1)-Rh- μCO(2) (°)	83.19	83.57
Rh-Rh (Å)	2.584	2.566
CCDC Number	This work	1222228
Representation		

Table II.5. Comparison of the MOF-isolated dinuclear complex and a closely related dimer from the literature.

	UAM-1001[Cu ₂ Cl ₄]	[CuCl ₂ bpm] ₂ ³
Crystal Colour	Yellow	Yellow
Geometry	Distorted trigonal Bipyram.	Distorted trigonal Bipyram.
Cu-N(1) (Å)	2.082	2.033
Cu-N(2) (Å)	2.082	2.196
Cu-μCl(1) (Å)	2.261	2.372
Cu-μCl(2) (Å)	2.161	2.322
Cu-Cl (Å)	2.319	2.301
N(1)-Cu-μCl(1) (°)	165.37	178.19
N(1)-Cu-N(2) (°)	90.36	85.82
Cl-Cu-μCl(2) (°)	141.48	139.98
Cu-Cu (Å)	3.143	3.518
CCDC Number	This work	1822681
Representation		

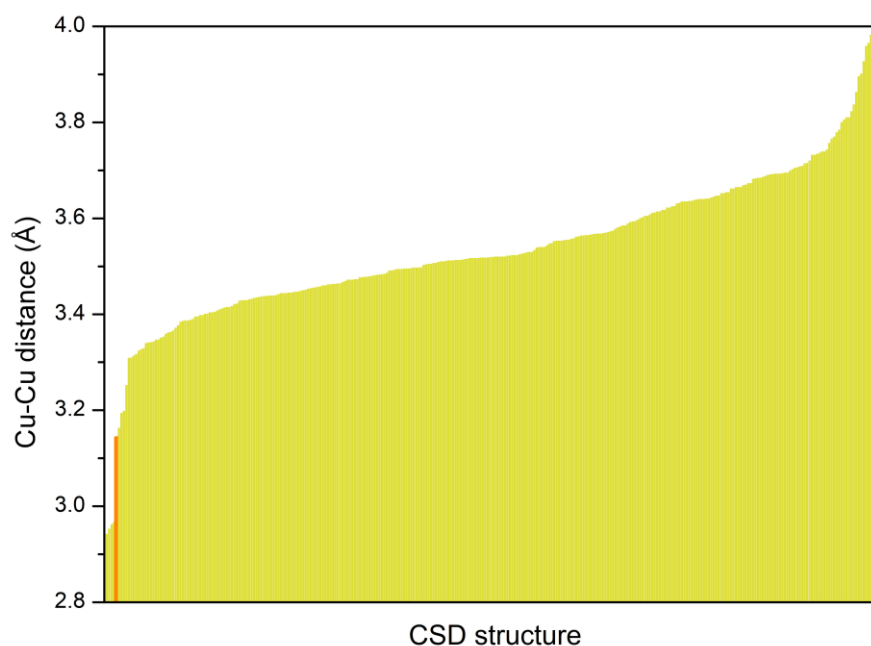


Figure II.8. Graphic representation of the Cu-Cu distance of all the structures with a $[N_2CuCl(\mu Cl)]_2$ moiety found in the Cambridge Crystallographic database (accessed 21/11/2022). UAM-1001[Cu₂Cl₄] is marked in orange. Only four structures have a shorter Cu-Cu distance than UAM-1001[Cu₂Cl₄]; however, in those cases the N-donor bridging ligand that is bridging both Cu atoms rather chelating the individual Cu(II) centres. For clarity, the X axis has not been labelled given the number of results plotted in the graph.

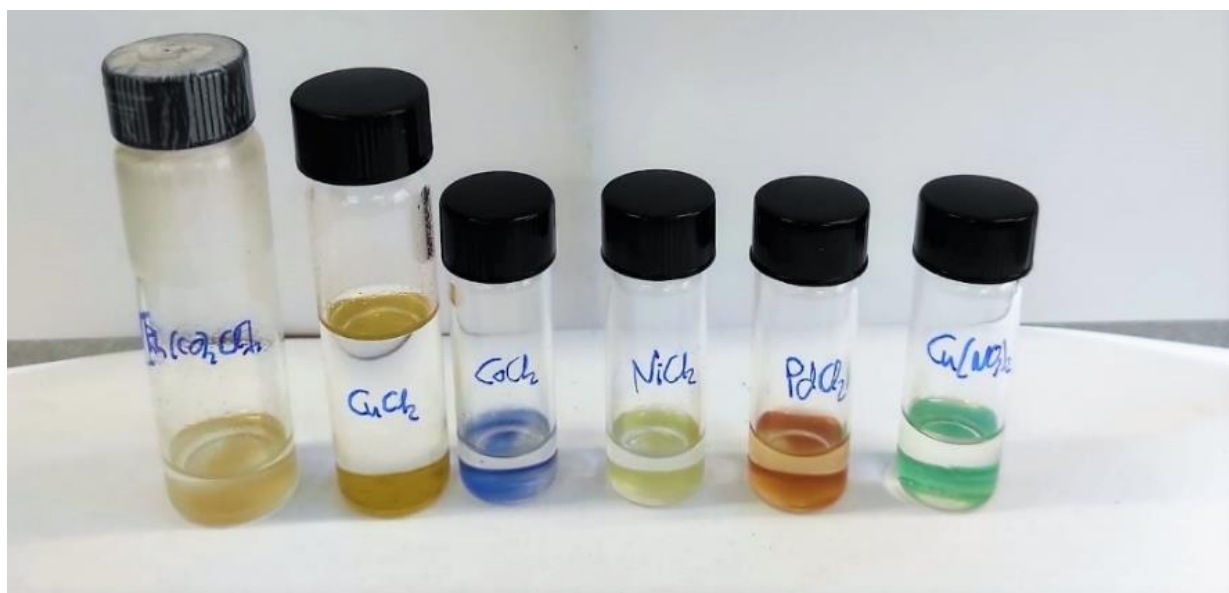
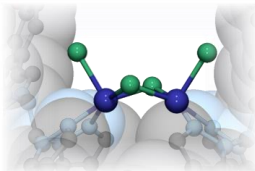
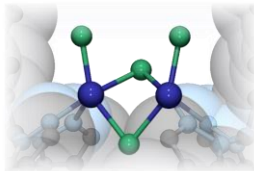
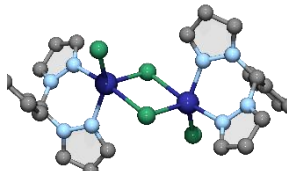
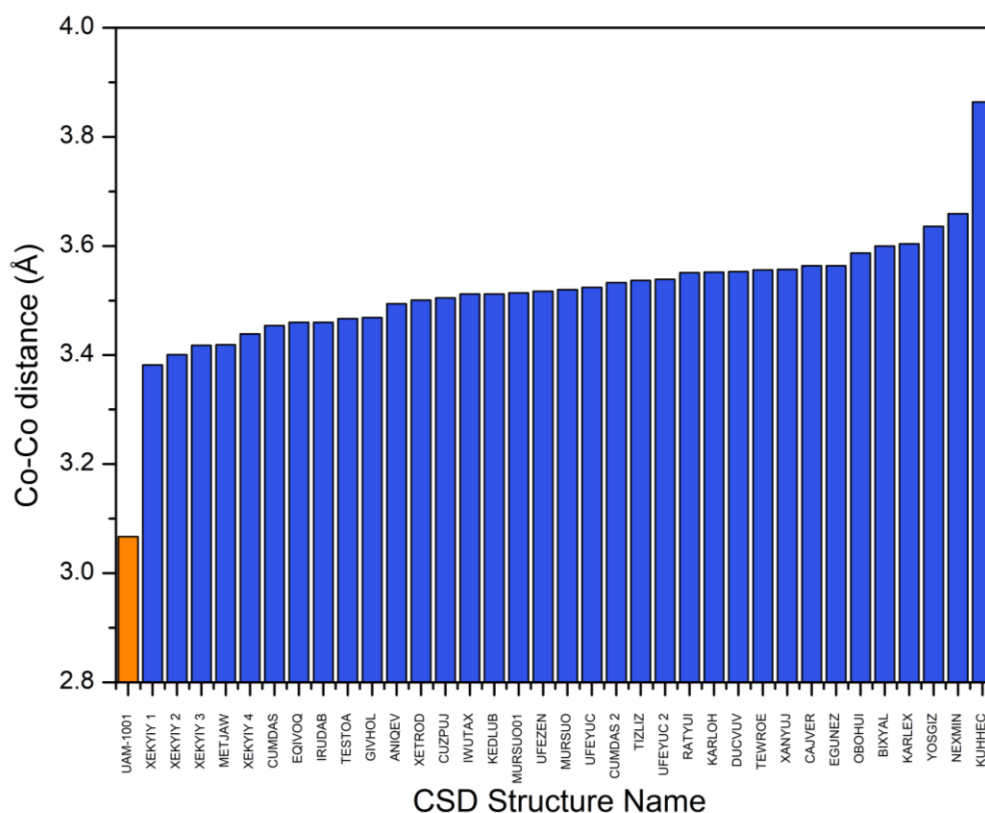


Figure II.9. From left to right, an image showing UAM-1001[Rh₂(CO)₃Cl₂], UAM-1001[Cu₂Cl₄], UAM-1001[Co₂Cl₄], UAM-1001[Ni₂Cl₃(H₂O)₂]Cl, UAM-1001[PdCl₂] and UAM-1001[Cu(NO₃)₂H₂O].

Table II.6. Comparison of the MOF-isolated dinuclear complex and a closely related dimer from the literature.

	<i>sqpy</i> -UAM-1001 [Co ₂ Cl ₄]	<i>trbipy</i> -UAM-1001 [Co ₂ Cl ₄]	[CoCl ₂ bpm] ₂ ⁴
Crystal Colour	Blue	Blue	Bright blue
Geometry	Square pyramidal	Trigonal bipyramidal	Trigonal bipyramidal
Co-N(1) (Å)	2.167	2.167	2.037
Co-N(2) (Å)	2.167	2.167	2.124
Co-μCl(1) (Å)	2.329	2.329	2.634
Co-μCl(2) (Å)	2.329	2.329	2.330
Co-Cl (Å)	2.372	2.372	2.268
Cl-Co-μCl(2) (°)	97.34	150.72	113.78
N(1)-Co-μCl(1) (°)	164.60	171.44	171.42
N(1)-Co-N(2) (°)	85.59	85.59	87.65
μCl(1)-Co-μCl(2) (°)	89.33	84.72	85.25
Co-Co (Å)	3.067	3.067	3.659
CCDC Number	This work	This work	620814
Representation			

**Figure II.10.** Graphic representation of the Co-Co distance of all the structures with a [N₂CoCl(μCl)]₂ moiety found in the Cambridge Crystallographic Database (CSD) (accessed 21/11/2022). UAM-1001[Co₂Cl₄] is marked in orange.

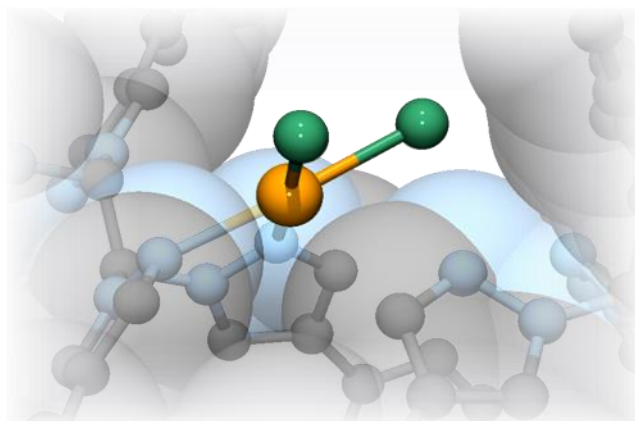


Figure II.11. Representation of the structure of UAM-1001[PdCl₂]. Colour legend: O (red), N (blue) and C (black), Pd (orange), Cl (green) and the Zr centres are shown as green polygons. DMF molecules and hydrogen atoms have been omitted for clarity.

Table II.7. Comparison of the MOF-isolated monomeric complex and two closely related mononuclear complexes from the literature.

	UAM-1001[PdCl ₂]	[bppmPdCl ₂] ⁵	[bmpmPdCl ₂] ⁶
Crystal Colour	Orange	Orange	Orange
Geometry	Square-planar	Square-planar	Square-planar
Pd-N(1) (Å)	2.262	2.036	2.035
Pd-N(2) (Å)	2.262	2.019	2.022
Pd-Cl(1) (Å)	2.371	2.287	2.291
Pd-Cl(2) (Å)	2.371	2.282	2.286
N(1)-Pd-Cl(1) (°)	177.15	176.09	177.17
N(1)-Pd-N(2) (°)	85.26	85.57	85.74
Cl(1)-Pd-Cl(2) (°)	87.01	91.26	90.56
CCDC Number	This work	773025	686189
Representation			

Table II.8. Comparison of the MOF-isolated monomeric complex and two closely related mononuclear complexes from the literature.

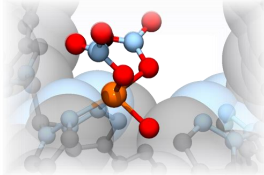
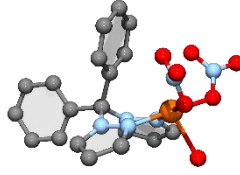
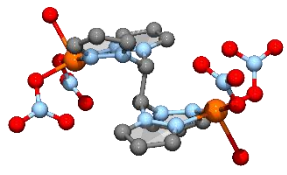
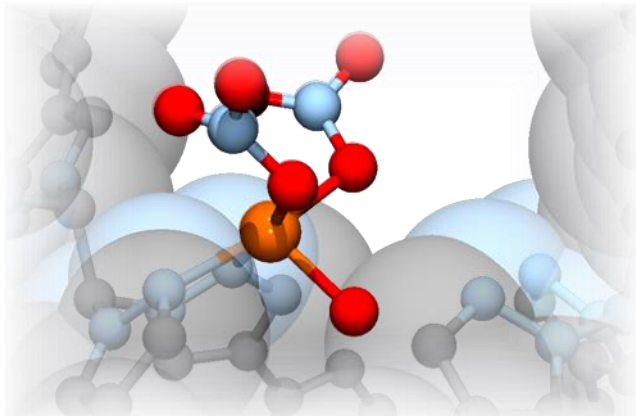
	UAM-1001 [Cu(NO ₃) ₂ H ₂ O]	[Pz ₂ CPh ₂ Cu(NO ₃) ₂ H ₂ O] ⁷	[bpe ₂ Cu(NO ₃) ₂ H ₂ O] ⁸
Crystal Colour	green	Blue	Blue
Geometry	Square pyramidal	Square pyramidal	Square pyramidal
Cu-N(1) (Å)	2.130	1.985	1.983
Cu-N(2) (Å)	2.130	1.986	1.999
Cu-ONO ₂ (1) (Å)	1.939	1.971	1.985
Cu-ONO ₂ (2) (Å)	1.939	1.975	1.980
Cu-OH ₂ (Å)	1.967	2.257	2.187
N(1)-Cu-ONO ₂ (1) (°)	171.44	176.84	178.27
N(1)-Cu-N(2) (°)	88.60	87.59	89.91
NO ₃ (1)-Cu-ONO ₂ (2) (°)	90.43	93.52	90.34
CCDC Number	This work	216894	1033091
Representation			
			

Figure II.12. Representation of the structure of UAM-1001[Cu(NO₃)₂H₂O]. Colour legend: O (red), N (blue) and C (black), Cu (orange) and the Zr centres are shown as green polygons. DMF molecules and hydrogen atoms have been omitted for clarity.

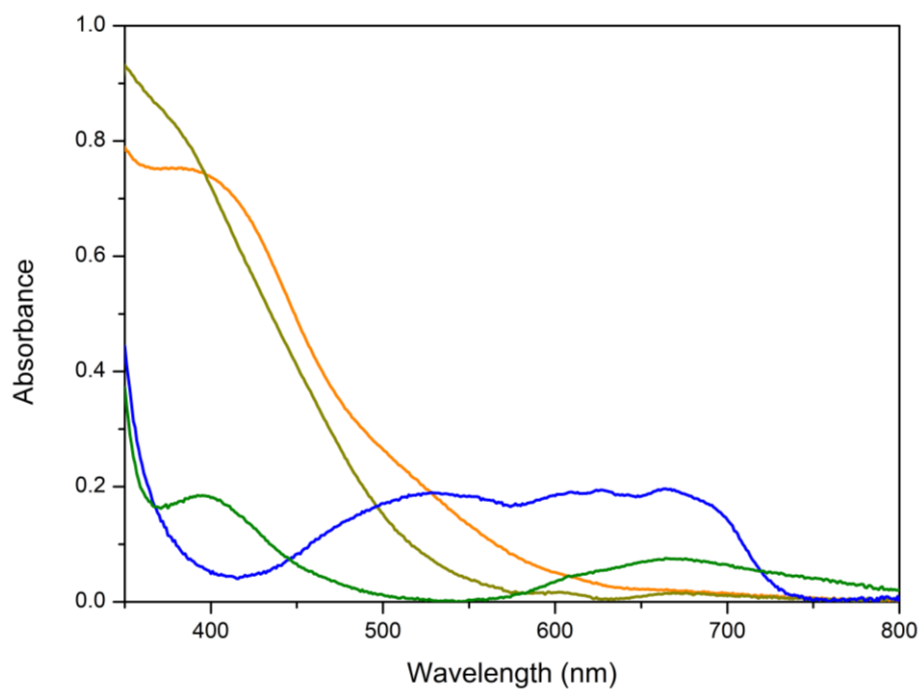


Figure II.13. Solid state UV-vis spectra of UAM-1001[Co₂Cl₄] (blue), UAM-1001[Rh₂CO₃Cl₂] (gold), UAM-1001[Ni₂Cl₃(H₂O)₂]Cl (green) and UAM-1001[PdCl₂] (orange).

II.II. Other Supplementary Information

II.II.I. Adsorption Experiments

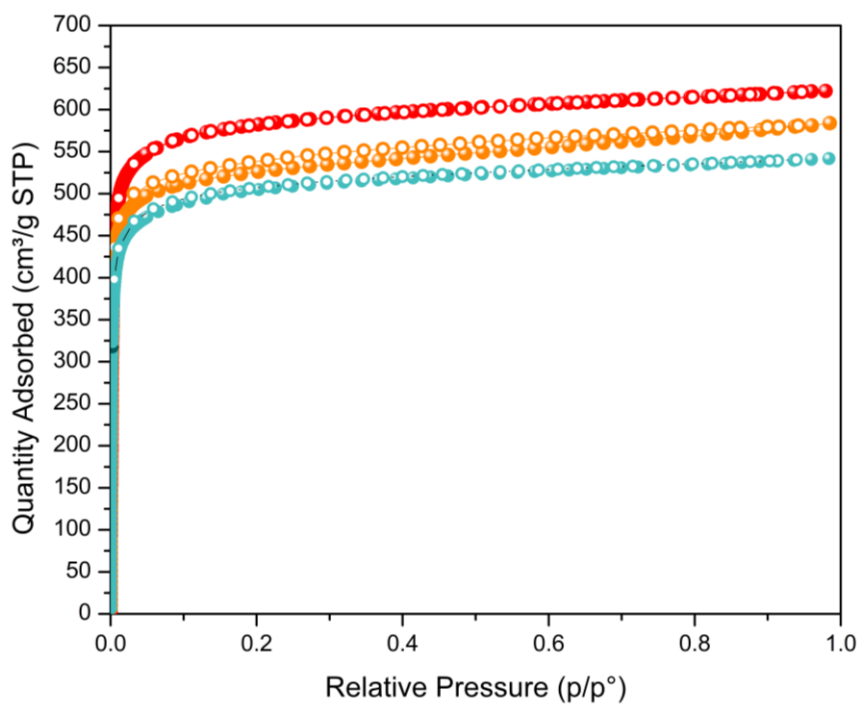


Figure II.14. 77 K N₂ isotherm data of UAM-1001 (red), UAM-1001[PdCl₂] (orange) and UAM-1001[Rh₂(CO)₃Cl₂] (blue) after activation from acetone at 120 °C for 3 h. Filled circles represent adsorption, open circles represent desorption.

II.II.II. Powder X-Ray Diffraction (PXRD) Data

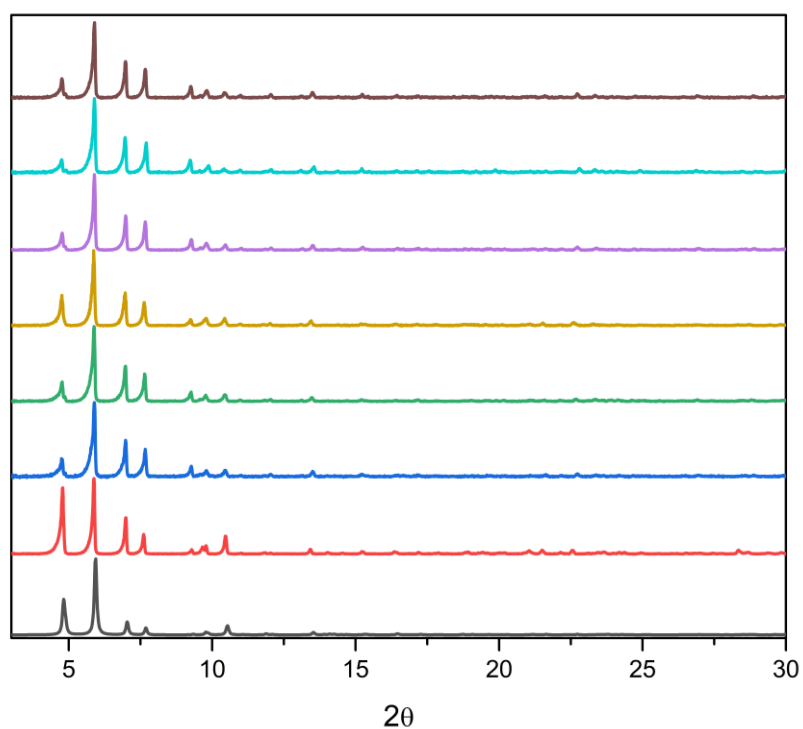


Figure II.15. Experimental PXRD plots for UAM-1001 as made (red), UAM-1001[PdCl₂] (blue), UAM-1001[Cu(NO₃)₂H₂O] (green), UAM-1001[Rh₂(CO)₃Cl₂] (gold), UAM-1001[Cu₂Cl₄] (purple), UAM-1001[Ni₂Cl₃(H₂O)₂]Cl (light blue) and UAM-1001[Co₂Cl₄] (brown) versus simulated UAM-1001 (black).

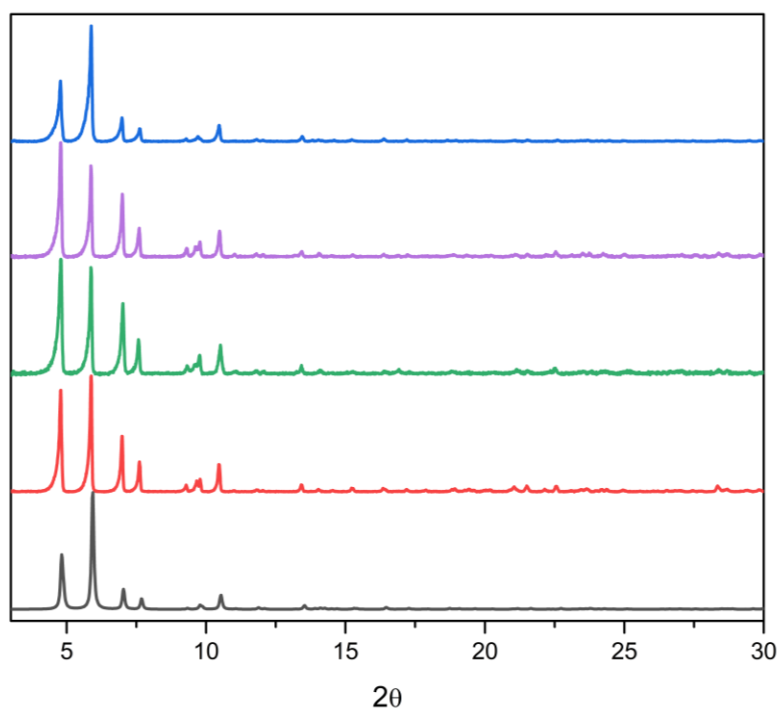


Figure II.16. Experimental PXRD plots for UAM-1001 as made (red), UAM-1001 after being at pH 1 for 72 h (green), UAM-1001 after being at pH 11 for 72 h (purple), UAM-1001·act (blue) versus simulated UAM-1000 (black).

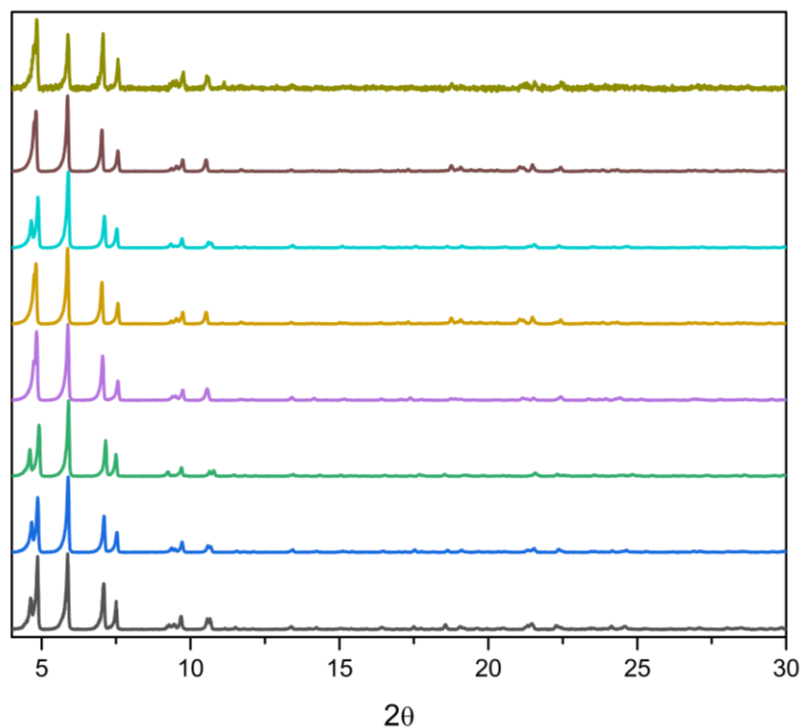


Figure II.17. Experimental PXRD plots for UAM-1000 in different solvents. Dimethylformamide (black), Acetone (dark blue), Acetonitrile (green), Methanol (purple), Tetrahydrofuran (gold), Pentane (light blue), Toluene (brown) and Dichloromethane (olive). Like other related materials with flexible linkers, the flexibility of the framework appears to cause slight shifts in the PXRD peak positions upon changes in the solvent and loss of solvent during sample preparation for PXRD.

II.III. Single Crystal X-ray Crystallography

II.III.I. General Procedures

Single crystals were mounted in Paratone-N oil on a MiTeGen micromount. Single-crystal X-ray data were typically collected at 100 K on the MX1 or MX2 beamlines of the Australian Synchrotron using the Blue-ice software interface,⁹ $\lambda = 0.71073 \text{ \AA}$. Absorption corrections were applied using multiscan methods using XDS,^{10, 11} the structures solved using SHELXS or SHELXT,^{12, 13} and refined by full-matrix least squares on F^2 by SHELXL,¹⁴ interfaced through the program X-Seed or OLEX.^{15, 16} In general, all atoms were refined anisotropically and hydrogens atoms were included as invariants at geometrically estimated positions, unless specified otherwise in additional details in supporting information. Where noted, the data was treated with the SQUEEZE routine available in Platon¹⁷ or using the solvent masking feature of Olex. Figures were produced using the software Diamond Version 4.6.8. X-ray experimental data is given in Table II.9-II.11. CIF data have been deposited with the Cambridge Crystallographic Data Centre, CCDC reference numbers CCDC 2236842 and 2236849.

II.III.II. Specific Data and Refinement Details

- **UAM-1000.** There is a mixture of OH and DMF molecules coordinated to the Zr atom that have been modelled applying RIGU, SIMU, EADP and fixing the positions of the N and a C atom of the DMF molecule.
- **UAM-1001.** The phenyl ring of the BPDC molecule was modelled in two different positions by applying DFIX, DANG, FLAT, SIMU, RIGU and EADP.
- **UAM-1001[PdCl₂].** A DMF molecule was modelled in the pores of the framework that is disordered in four different positions by applying DFIX, DANG, FLAT, SIMU, RIGU and SADI. The atoms of this DMF molecule were refined isotropically. EADP was applied to two C atoms of the phenyl ring of the BPDC molecule.
- **UAM-1001[Cu(NO₃)₂H₂O].** The nitrate anion coordinated to the Cu(II) centre was modelled applying FLAT, DFIX, SIMURIGU and SADI. EADP was also applied to the pyrazole group to stabilize the refinement.
- **UAM-1001[Rh₂(CO)₃Cl₂].** None
- **UAM-1001[Ni₂Cl₃(H₂O)₂Cl].** None
- **UAM-1001[Co₂Cl₄].** The pyrazole ring was modelled applying DFIX, DANG, FLAT, RIGU, SADI and SIMU. The two different geometries of the [Co₂Cl₄] were modelled by applying FIX XYZ, EADP to the capping chloride atoms (Cl1 and Cl6) EADP to the bridging chlorides (Cl3 and Cl5). The cobalt occupancies were fixed to 0.8 in consistency with the EDX data.
- **UAM-1001[Cu₂Cl₄].** None

II.III.III. Thermal ellipsoid plots for all structures at the 50% probability level

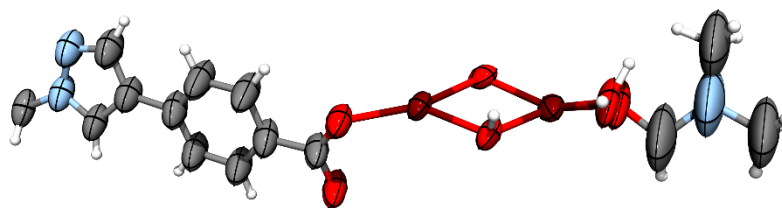


Figure II.18. Asymmetric unit of UAM-1000, with all non-hydrogen atoms represented by ellipsoids at the 50% probability level (C, grey; H, white; N, light blue; O, red; Zr, dark red).

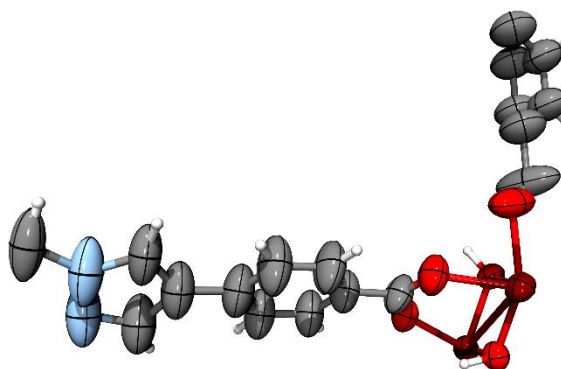


Figure II.19. Asymmetric unit of UAM-1001, with all non-hydrogen atoms represented by ellipsoids at the 50% probability level (C, grey; H, white; N, light blue; O, red; Zr, dark red).

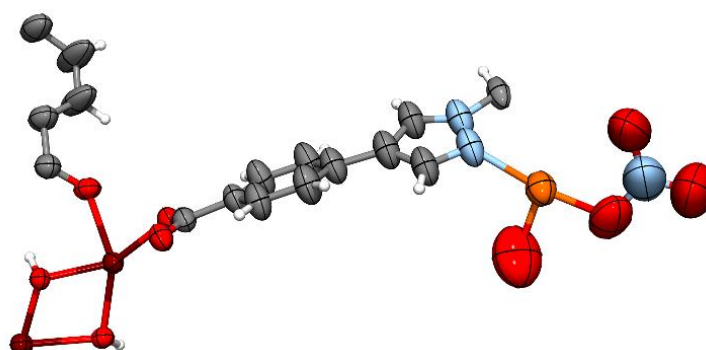


Figure II.20. Asymmetric unit of UAM-1001[Cu(NO₃)₂H₂O], with all non-hydrogen atoms represented by ellipsoids at the 50% probability level (C, grey; H, white; N, light blue; O, red; Cu, green; Zr, dark red; I, purple).

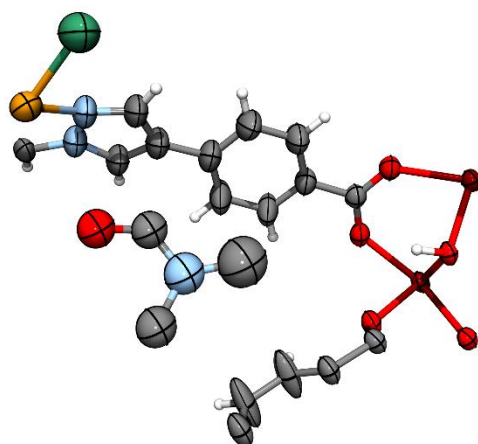


Figure II.21. Asymmetric unit of UAM-1001[PdCl₂], with all non-hydrogen atoms represented by ellipsoids at the 50% probability level (C, grey; H, white; N, light blue; O, red; Pd, light orange; Zr, dark red; Cl, green).

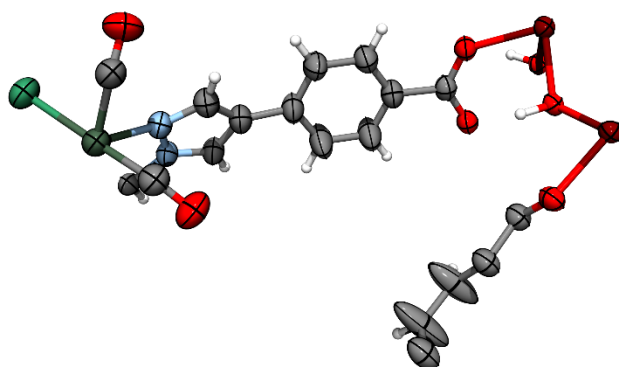


Figure II.22. Asymmetric unit of UAM-1001[Rh₂(CO)₃Cl₂], with all non-hydrogen atoms represented by ellipsoids at the 50% probability level (C, grey; H, white; N, light blue; O, red; Rh, dark green; Zr, dark red; Cl, green).

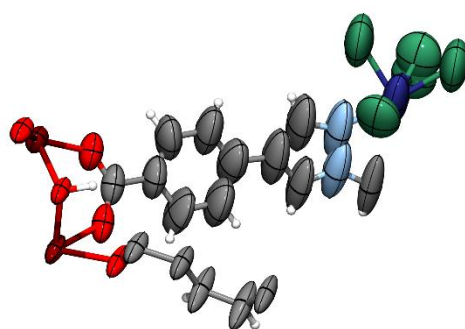


Figure II.23. Asymmetric unit of UAM-1001[Co₂Cl₄], with all non-hydrogen atoms represented by ellipsoids at the 50% probability level (C, grey; H, white; N, light blue; O, red; Co, dark blue; Zr, dark red; Cl, green).

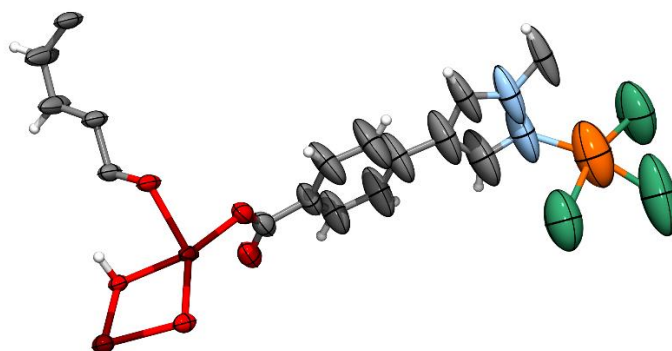


Figure II.24. Asymmetric unit of UAM-1001[CuCl₄], with all non-hydrogen atoms represented by ellipsoids at the 50% probability level (C, grey; H, white; N, light blue; O, red; Cu, orange; Zr, dark red; Cl, green).

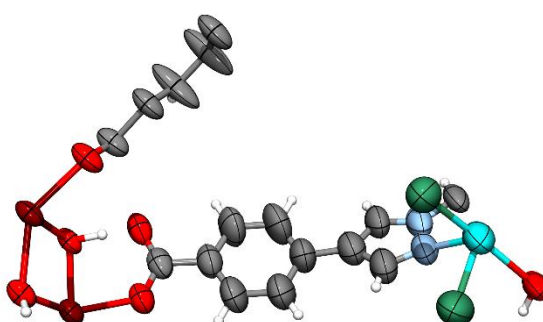


Figure II.25. Asymmetric unit of UAM-1001[NiCl₃(H₂O)₂]Cl, with all non-hydrogen atoms represented by ellipsoids at the 50% probability level (C, grey; H, white; N, light blue; O, red; Ni, light blue; Zr, dark red; Cl, green).

II.III.IV. Crystallographic Representations

UAM-1000

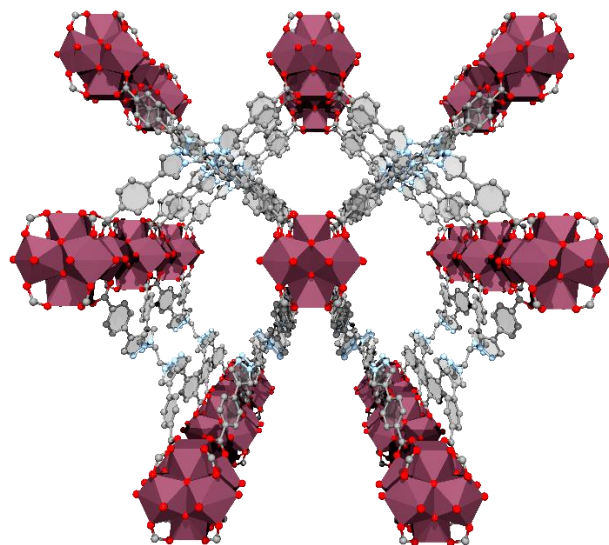


Figure II.26. Crystallographic representation of UAM-1000 viewed along the *a* axis. (C, grey; N, light blue; O, red; Zr, cyan). Hydrogens have been hidden for clarity.

UAM-1001

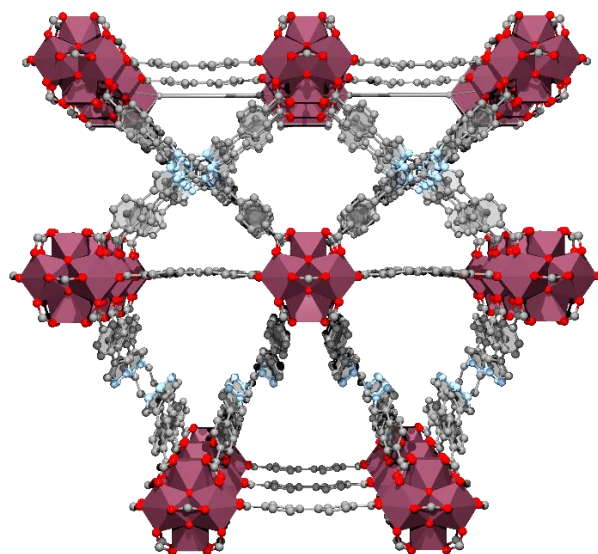


Figure II.27. Crystallographic representation of UAM-1001 viewed along the *a* axis. (C, grey; N, light blue; O, red; Zr, cyan). Hydrogens have been hidden for clarity.

II.III.V. Tables of X-ray crystallography data collection and refinement parameters

Table II.9. Crystallographic data collection and refinement parameters for UAM-1000, UAM-1001 and UAM-1001[Cu(NO₃)₂H₂O].

Sample	UAM-1000	UAM-1001	UAM-1001 [Cu(NO ₃) ₂ H ₂ O]
Crystallographic Parameter			
Formula	C _{11.7} H ₁₁ N _{2.4} O ₄ Zr _{0.75}	C ₁₄ H ₉ N ₂ O ₄ Zr _{0.75}	C ₁₄ H _{9.5} Cu _{0.25} N _{2.5} O _{5.75} Zr _{0.75}
FW	317.64	337.65	389.04
T, K	100(2)	100(2)	100(2)
Crystal system	tetragonal	tetragonal	tetragonal
Crystal system, space group	<i>I</i> ₄ / <i>amd</i>	<i>I</i> ₄ / <i>amd</i>	<i>I</i> ₄ / <i>amd</i>
a, Å	17.864(3)	18.928(2)	19.005(3)
b, Å	17.864(3)	18.928(2)	19.005(3)
c, Å	78.772(16)	72.273(15)	71.779(14)
α, °	90	90	90
β, °	90	90	90
γ, °	90	90	90
V, Å ³	25138(9)	25893(8)	25927(9)
Z	32	32	32
d _{calc} , g/cm ³	0.671	0.693	0.797
Absorption coefficient, mm ⁻¹	0.276	0.27	0.438
F(000)	5120	5408	6216
Crystal size, mm ³	0.062 × 0.052 × 0.044	0.051 × 0.045 × 0.038	0.055 × 0.048 × 0.041
Radiation	Sync. (λ = 0.71073)	Sync. (λ = 0.71073)	Sync. (λ = 0.71073)
2θ range for data collection	2.068 to 57.336	2.224 to 58.412	2.216 to 57.1
Index range	-23 ≤ h ≤ 23, -21 ≤ k ≤ 22, -96 ≤ l ≤ 96	-22 ≤ h ≤ 22, -23 ≤ k ≤ 23, -79 ≤ l ≤ 81	-23 ≤ h ≤ 23, -25 ≤ k ≤ 25, -95 ≤ l ≤ 93
Reflections collected	146083	170694	153971
Independent reflections	7751 [R _{int} = 0.1090, R _{sigma} = 0.0312]	7658 [R _{int} = 0.0592, R _{sigma} = 0.0166]	8020 [R _{int} = 0.0450, R _{sigma} = 0.0136]
Data/restraints/parameters	7751/75/185	7658/78/191	8020/46/221
GOF on F ²	1.221	1.078	1.05
Largest diff. peak and hole, eÅ ⁻³	1.40/-1.38	1.15/-1.06	0.59/-1.08
R ₁ , [I > 2σ(I)]	0.1040	0.0816	0.0700
wR ₂ , all data	0.3271	0.2834	0.2294
CCDC Number	2236842	2236843	2236845

Table II.10. Crystallographic data collection and refinement parameters for UAM-1001[PdCl₂], UAM-1001[Cu₂Cl₄] and UAM-1001[Rh₂CO₃Cl₂].

Sample	UAM-1001[PdCl ₂]	UAM-1001 [Cu ₂ Cl ₄]	UAM-1001[Rh ₂ CO ₃ Cl ₂]
Crystallographic Parameter			
Formula	C _{14.62} H ₉ Cl _{0.5} N _{2.25} O _{4.12} Pd _{0.25} Zr _{0.75}	C ₁₄ H ₉ ClCu _{0.5} N ₂ O ₄ Zr _{0.75}	C _{14.75} H _{9.5} Cl _{0.5} N ₂ O _{4.75} Rh _{0.5} Zr _{0.75}
FW	394.98	405.37	428.34
T, K	100(2)	100(2)	100(2)
Crystal system	tetragonal	tetragonal	tetragonal
space group	<i>I</i> 4 ₁ / <i>amd</i>	<i>I</i> 4 ₁ / <i>amd</i>	<i>I</i> 4 ₁ / <i>amd</i>
a, Å	19.031(3)	19.003(3)	19.066(3)
b, Å	19.031(3)	19.003(3)	19.066(3)
c, Å	71.695(14)	70.998(14)	70.971(14)
α, °	90	90	90
β, °	90	90	90
γ, °	90	90	90
V, Å ³	25966(9)	25637(9)	25799(10)
Z	32	32	32
<i>d</i> _{calc} , g/cm ³	0.808	0.84	0.882
Absorption coefficient, mm ⁻¹	0.448	0.681	0.565
<i>F</i> (000)	6256	6432	6752
Crystal size, mm ³	0.055 × 0.052 × 0.045	0.025 × 0.02 × 0.01	0.043 × 0.039 × 0.031
Radiation	Sync. (λ = 0.71073)	Sync. (λ = 0.71073)	Sync. (λ = 0.71073)
2θ range for data collection	2.214 to 57.346	2.218 to 57.792	2.212 to 57.376
Index range	-25 ≤ <i>h</i> ≤ 25, -25 ≤ <i>k</i> ≤ 25, -95 ≤ <i>l</i> ≤ 94	-22 ≤ <i>h</i> ≤ 21, -24 ≤ <i>k</i> ≤ 24, -83 ≤ <i>l</i> ≤ 83	-25 ≤ <i>h</i> ≤ 25, -24 ≤ <i>k</i> ≤ 24, -83 ≤ <i>l</i> ≤ 83
Reflections collected	157495	162238	153020
Independent reflections	7783 [R _{int} = 0.0602, R _{sigma} = 0.0181]	7989 [R _{int} = 0.0684, R _{sigma} = 0.0224]	7730 [R _{int} = 0.0586, R _{sigma} = 0.0172]
Data/restraints/parameters	7783/13/204	7989/0/226	7730/0/231
GOF on F ²	1.079	1.074	1.123
Largest diff. peak and hole, eÅ ⁻³	0.83/-1.22	1.18/-1.93	1.52/-1.59
R ₁ , [>2σ(<i>I</i>)]	0.0620	0.0693	0.0531
wR ₂ , all data	0.2099	0.2318	0.1862
CCDC Number	2236849	2236846	2236847

Table II.11. Crystallographic data collection and refinement parameters for UAM-1001[Ni₂Cl₃(H₂O)₂]Cl and UAM-1001[Co₂Cl₄].

Sample	UAM-1001[Ni ₂ Cl ₃ (H ₂ O) ₂]Cl	UAM-1001[Co ₂ Cl ₄]
Crystallographic Parameter		
Formula	C ₁₄ H ₁₀ ClN ₂ Ni _{0.5} O _{4.5} Zr _{0.75}	C ₁₄ H ₉ Cl _{0.8} Co _{0.4} N ₂ O ₄ Zr _{0.75}
FW	411.46	389.58
T, K	100(2)	100(2)
Crystal system	tetragonal	tetragonal
Crystal system, space group	<i>I</i> ₄ / <i>amd</i>	<i>I</i> ₄ / <i>amd</i>
a, Å	19.045(3)	18.976(3)
b, Å	19.045(3)	18.976(3)
c, Å	70.356(14)	70.395(14)
α, °	90	90
β, °	90	90
γ, °	90	90
V, Å ³	25519(9)	25350(9)
Z	32	32
<i>d</i> _{calc.} , g/cm ³	0.857	0.817
Absorption coefficient, mm ⁻¹	0.648	0.547
<i>F</i> (000)	6560	6189
Crystal size, mm ³	0.028 × 0.02 × 0.01	0.025 × 0.02 × 0.01
Radiation	Sync. (λ = 0.71073)	Sync. (λ = 0.71073)
2θ range for data collection	2.216 to 57.838	2.222 to 57.716
Index range	-24 ≤ <i>h</i> ≤ 24, -23 ≤ <i>k</i> ≤ 22, -87 ≤ <i>l</i> ≤ 87	-21 ≤ <i>h</i> ≤ 22, -22 ≤ <i>k</i> ≤ 22, -89 ≤ <i>l</i> ≤ 89
Reflections collected	159381	159109
Independent reflections	8101 [R _{int} = 0.0459, R _{sigma} = 0.0152]	7915 [R _{int} = 0.0488, R _{sigma} = 0.0153]
Data/restraints/parameters	8101/0/221	7915/74/221
GOF on F ²	1.08	1.07
Largest diff. peak and hole, eÅ ⁻³	1.60/-1.54	0.51/-1.01
R ₁ , [I > 2σ(I)]	0.0779	0.0654
wR ₂ , all data	0.2776	0.2244
CCDC Number	2236848	2236844

II.IV. References

1. Baker, M. V., Brown, D. H., Skelton, B. W. and White, A. H. *Aust. J. Chem.*, **2002**, *55*, 655-660.
2. Heaton, B. T., Jacob, C. and Sampanthar, J. T. *Dalton Trans.*, **1998**, *8*, 1403-1410.
3. Torres, J. F., Bello-Vieda, N. J., Macías, M. A., Muñoz-Castro, A., Rojas-Dotti, C., Martínez-Lillo, J. and Hurtado, J. *Eur. J. Inorg. Chem.*, **2018**, *2018*, 3644-3651.
4. Mohr, F., Cerrada, E. and Laguna, M. *Dalton Trans.*, **2006**, *47*, 5567-5573.
5. Jones, M. W., Adlington, R. M., Baldwin, J. E., Le Pevelen, D. D. and Smiljanic, N. *Inorganica Chimica Acta*, **2010**, *363*, 1097-1101.
6. Muñoz, S., Pons, J., García-Antón, J., Solans**, X., Font-Bardia, M. and Ros, J. *J. Coord. Chem.*, **2010**, *62*, 3940-3950.
7. Janet, Thomas, Gary and Christopher. *Eur. J. Inorg. Chem.*, **2004**, *2004*, 1073-1080.
8. Potapov, A. S., Nudnova, E. A., Khlebnikov, A. I., Ogorodnikov, V. D. and Petrenko, T. V. *Inorg. Chem. Commun.*, **2015**, *53*, 72-75.
9. McPhillips, T. M., McPhillips, S. E., Chiu, H. J., Cohen, A. E., Deacon, A. M., Ellis, P. J., Garman, E., Gonzalez, A., Sauter, N. K., Phizackerley, R. P., Soltis, S. M. and Kuhn, P. *J. Synchrotron Radiat.*, **2002**, *9*, 401-406.
10. Cowieson, N. P., Aragao, D., Clift, M., Ericsson, D. J., Gee, C., Harrop, S. J., Mudie, N., Panjikar, S., Price, J. R., Riboldi-Tunnicliffe, A., Williamson, R. and Caradoc-Davies, T. *J. Synchrotron Radiat.*, **2015**, *22*, 187-190.
11. Aragao, D., Aishima, J., Cherukuvada, H., Clarken, R., Clift, M., Cowieson, N. P., Ericsson, D. J., Gee, C. L., Macedo, S., Mudie, N., Panjikar, S., Price, J. R., Riboldi-Tunnicliffe, A., Rostan, R., Williamson, R. and Caradoc-Davies, T. *J. Synchrotron Radiat.*, **2018**, *25*, 885-891.
12. Sheldrick, G. M. *Acta Crystallogr. Sect. A: Found. Crystallogr.*, **2008**, *64*, 112-122.
13. Sheldrick, G. M. *Acta Crystallogr. Sect. A: Found. Crystallogr.*, **2015**, *71*, 3-8.
14. Sheldrick, G. M. *Acta Crystallogr. Sect. C: Cryst. Struct. Commun.*, **2015**, *71*, 3-8.
15. Barbour, L. J. *Supramol. Chem.*, **2001**, *1*, 189-191.
16. Dolomanov, O. V., Bourhis, L. J., Gildea, R. J., Howard, J. A. K. and Puschmann, H. *J. Appl. Crystallogr.*, **2009**, *42*, 339-341.
17. Spek, A. L. *Acta Crystallogr. Sect. C: Cryst. Struct. Commun.*, **2015**, *71*, 9-18.

III. Appendix 3: Supplementary Information for Chapter 4

III.I. Main text supporting data

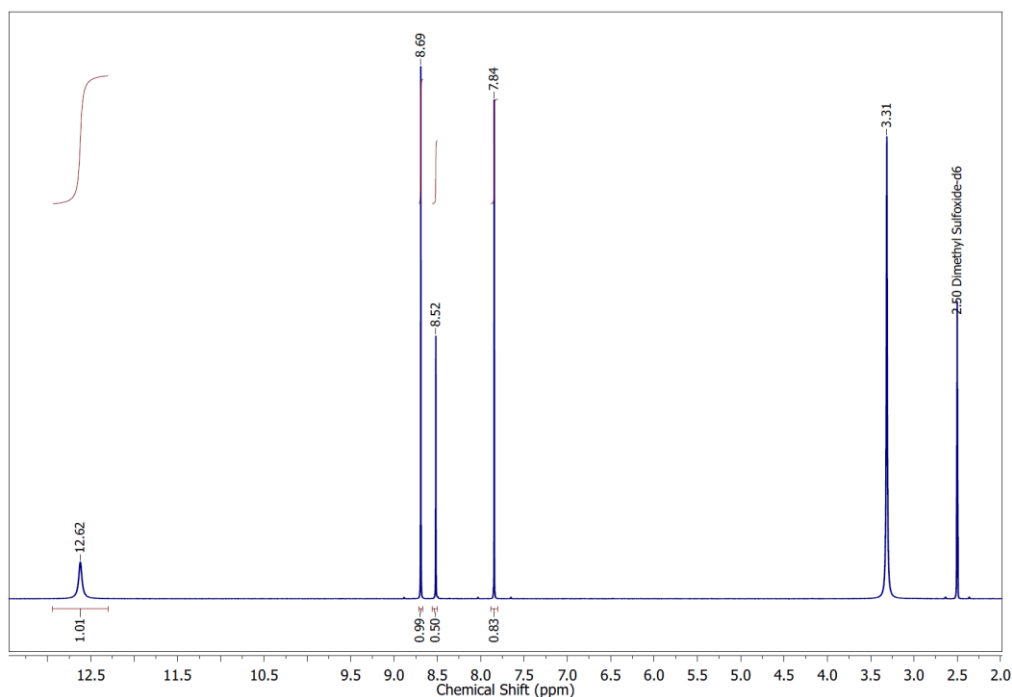


Figure III.1. $^1\text{H-NMR}$ spectrum of L1H_4 (500 MHz, DMSO-d_6): 12.62 (s, 4H, COOH), 8.69 (s, 4H, CH_2 pyrazole), 8.52 (s, 2H, N-CH-N), 7.84 (s, 4H, CH_2 pyrazole).

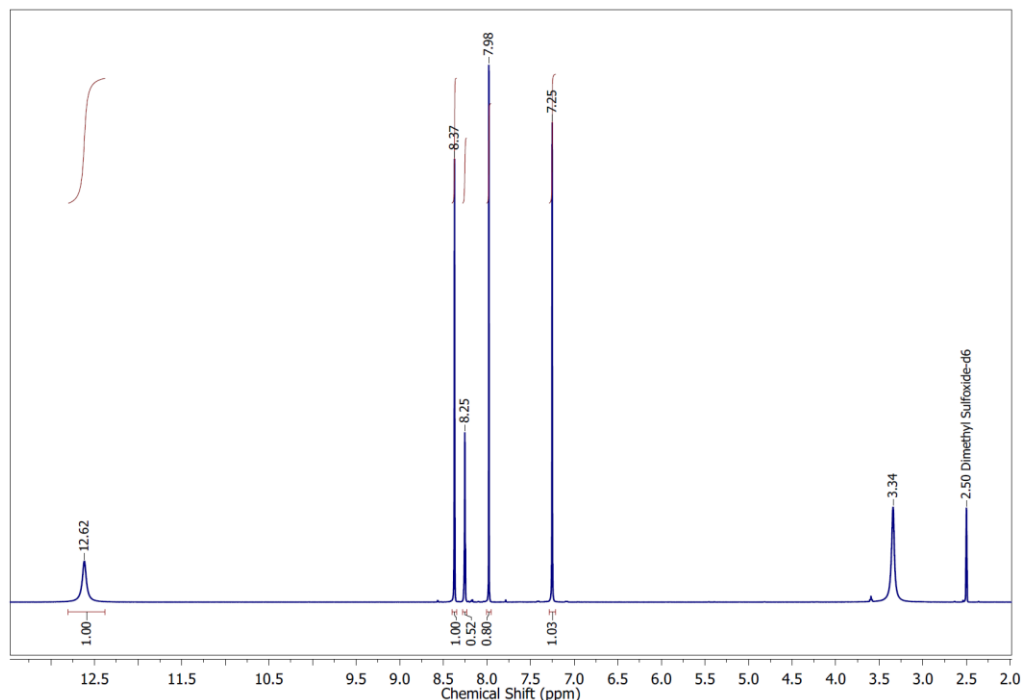


Figure III.2. $^1\text{H-NMR}$ spectrum of L2H_4 (500 MHz, DMSO-d_6): 12.62 (s, 4H, COOH), 8.37 (s, 4H, CH_2 pyrazole), 8.25 (s, 2H, N-CH-N), 7.98 (s, 4H, CH_2 pyrazole), 7.25 (s, 4H, CH phenyl).

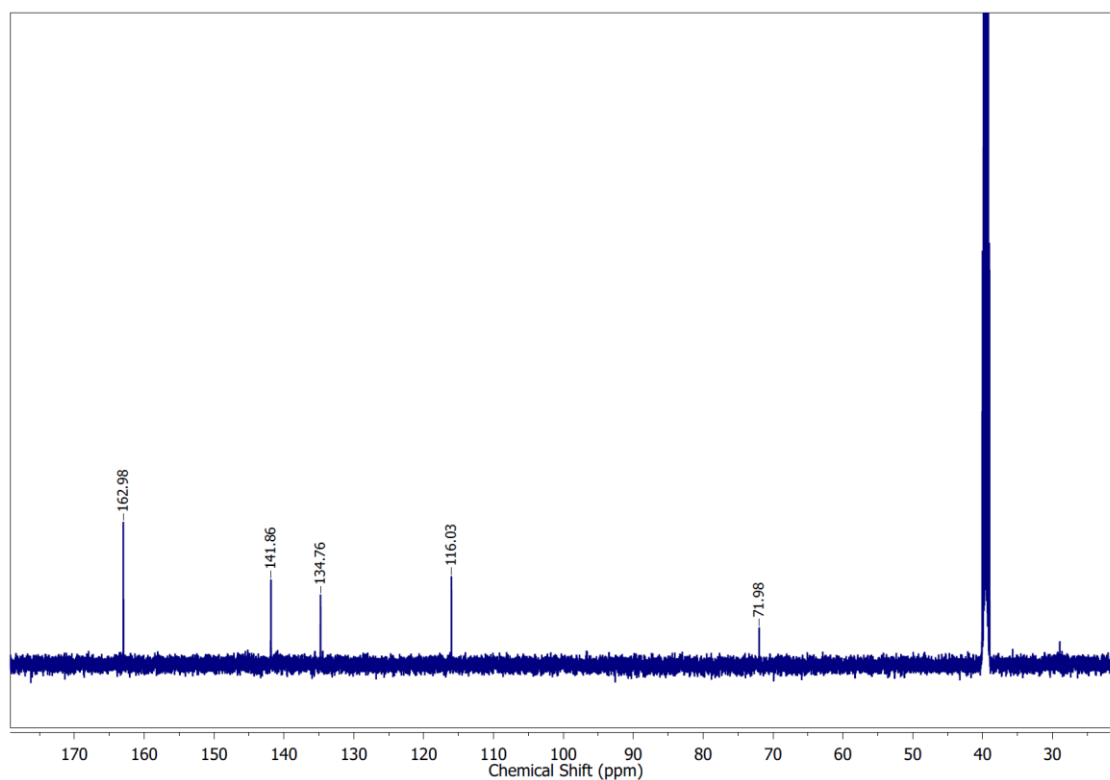


Figure III.3. ^{13}C -NMR spectrum of L1H_4 (500 MHz, DMSO-d_6): 162.98 (COOH), 141.86 (C pyr), 134.76 (C pyr), 116.03 (C py), 71.98 (C- sp^3).

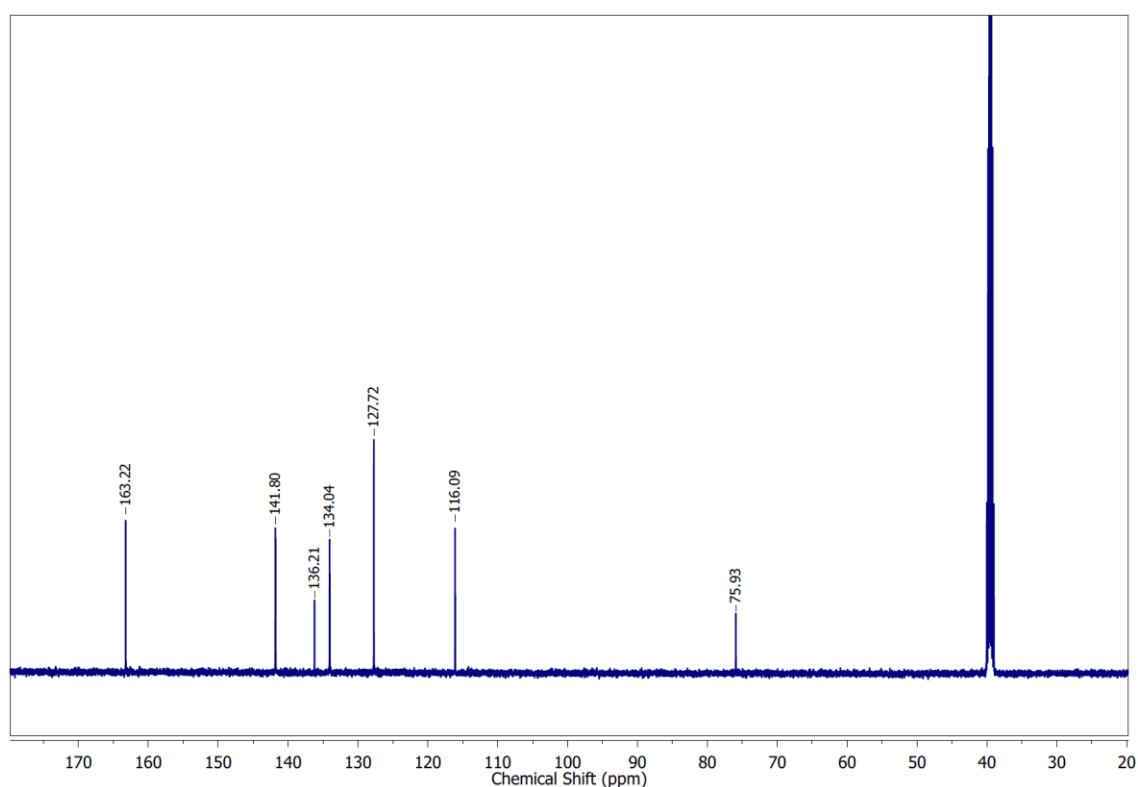


Figure III.4. ^{13}C -NMR spectrum of L2H_4 (500 MHz, DMSO-d_6): 163.22 (COOH), 141.80 (COOH), 136.21 (C pyr), 134.04 (C pyr), 127.72 (C pheyl), 116.09 (s, 4H, C pyr), 75.93 (C- sp^3).

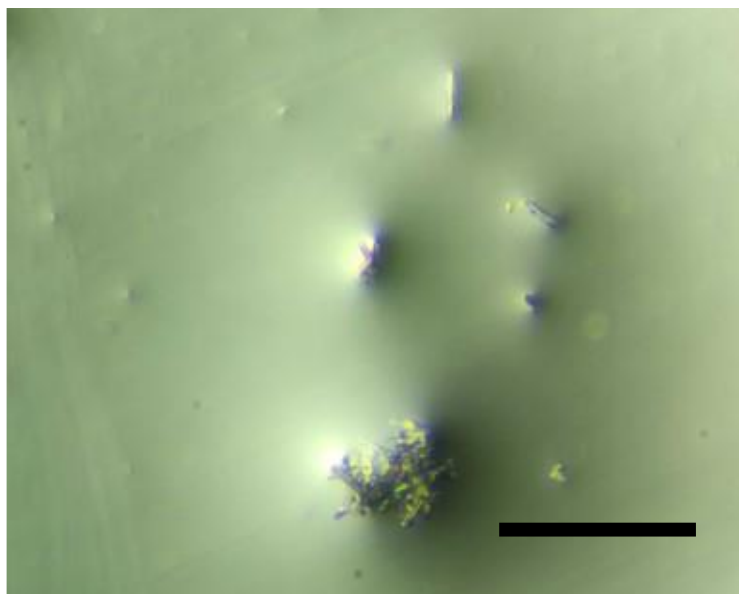


Figure III.5. Photograph down the optical microscope of the UAM-10 crystals. Scale bar = 500 μm .

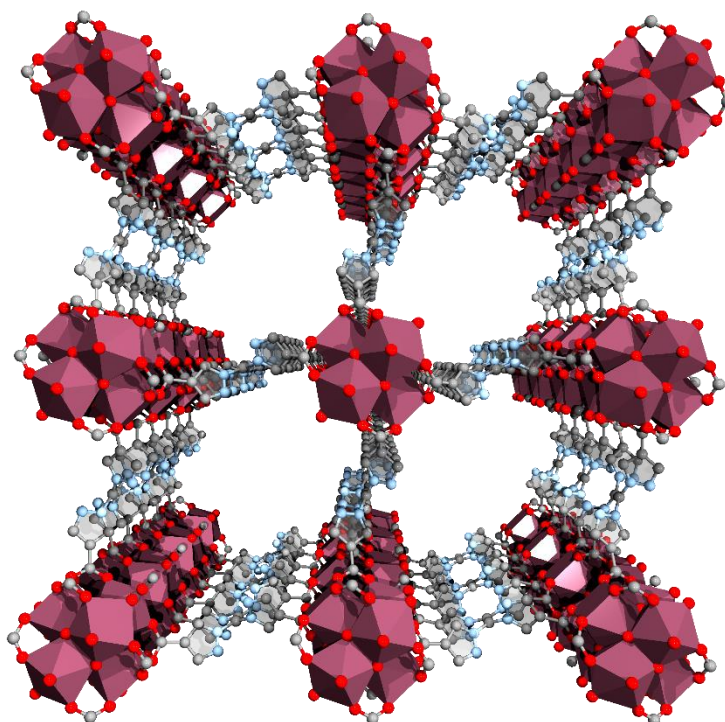


Figure III.6. Representation of the structure of UAM-10 along the c axis (C, grey; N, light blue; O, red; Zr, dark red). Hydrogens have been omitted for clarity.

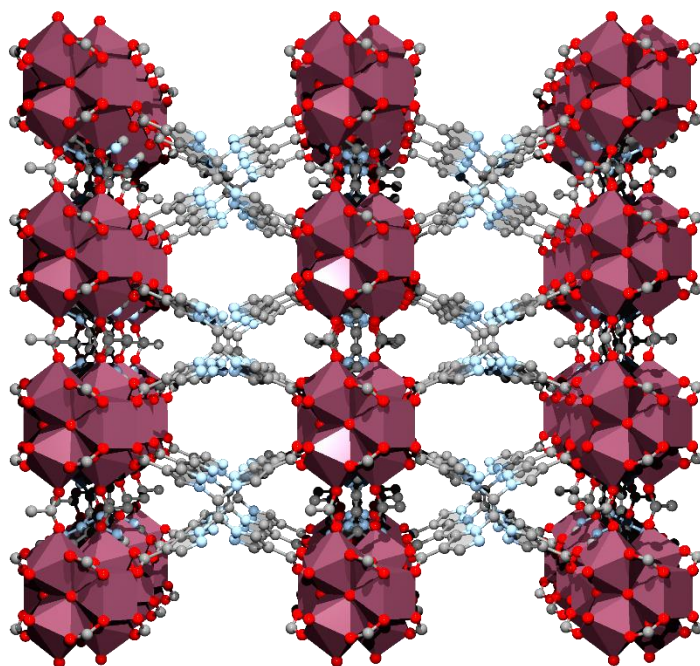


Figure III.7. Representation of the structure of UAM-10 along the *a* axis (C, grey; N, light blue; O, red; Zr, dark red). Hydrogens have been omitted for clarity.

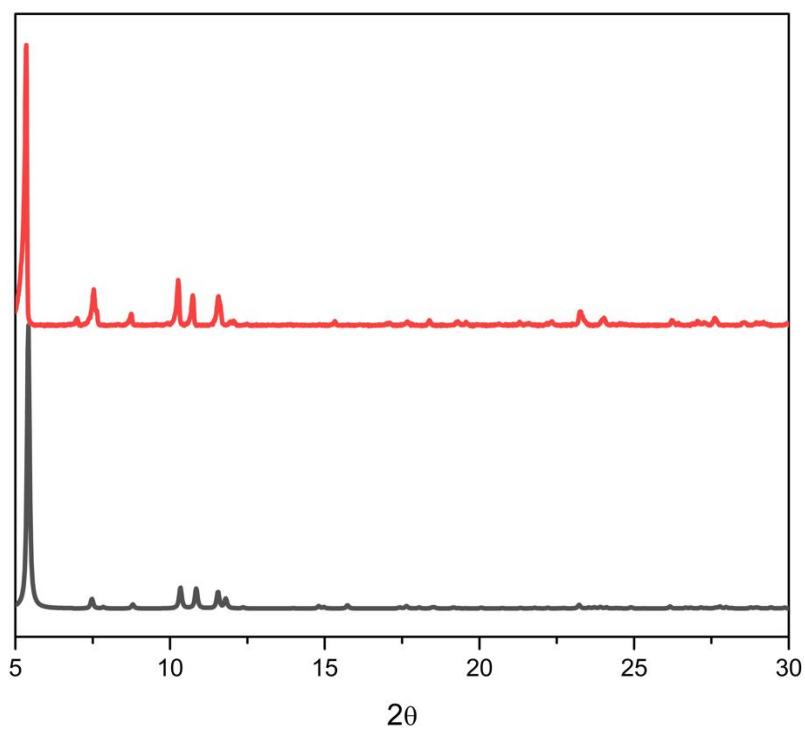


Figure III.8. PXRD plots for UAM-10 as made (red) versus simulated UAM-10 (black).

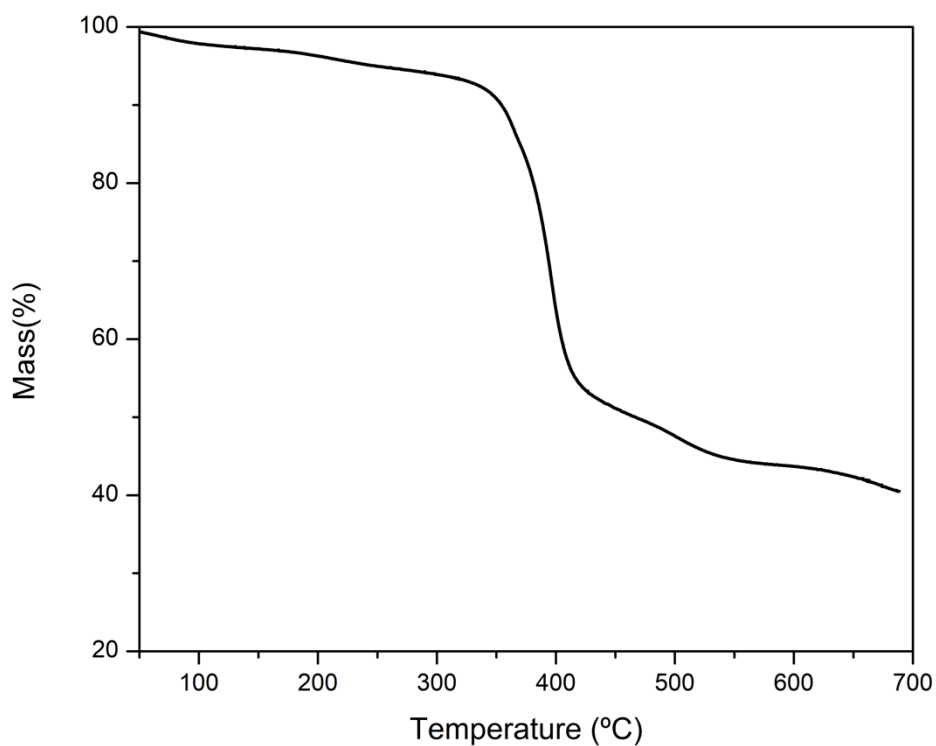


Figure III.9. Thermogravimetric analysis plot for UAM-10. Analysis conditions: 50 °C – 700 °C at 5 °C/min, under an oxidising (air) atmosphere.

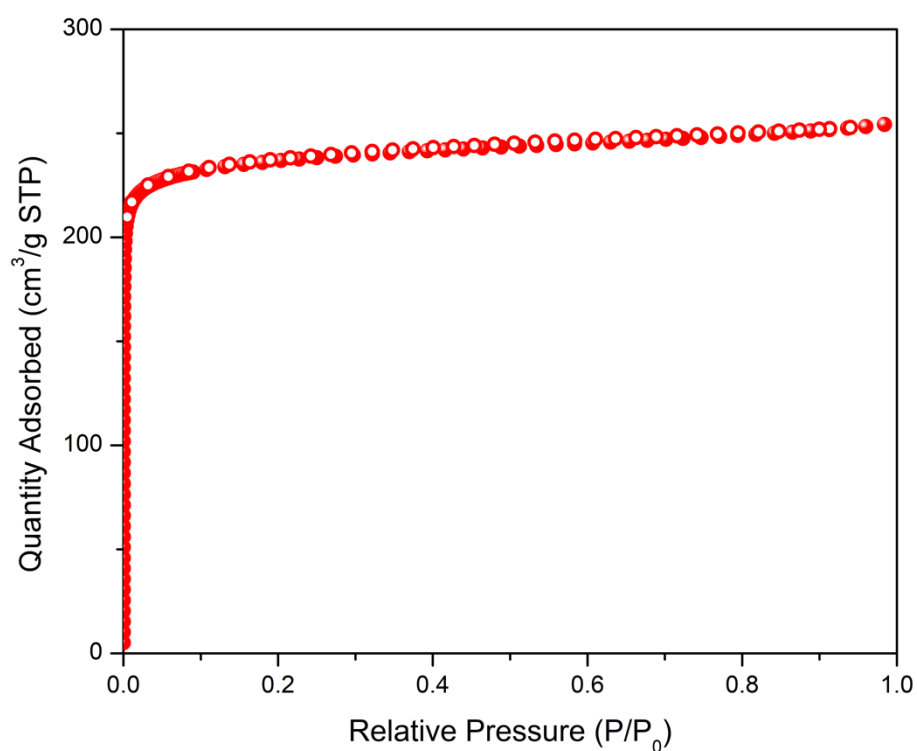


Figure III.10. 77 K N₂ isotherm data of UAM-10 after activation from acetone at 120 °C for 3 h. Filled circles represent adsorption; open circles represent desorption.

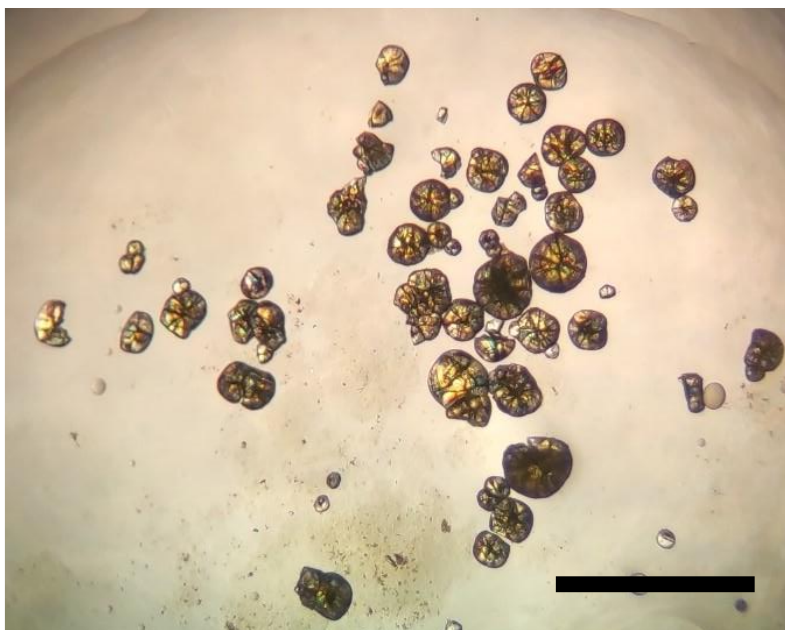


Figure III.11. Optical image of UAM-11 crystals. Structure determination was conducted on crystals excised from the clumps. Scale bar = 500 μm .

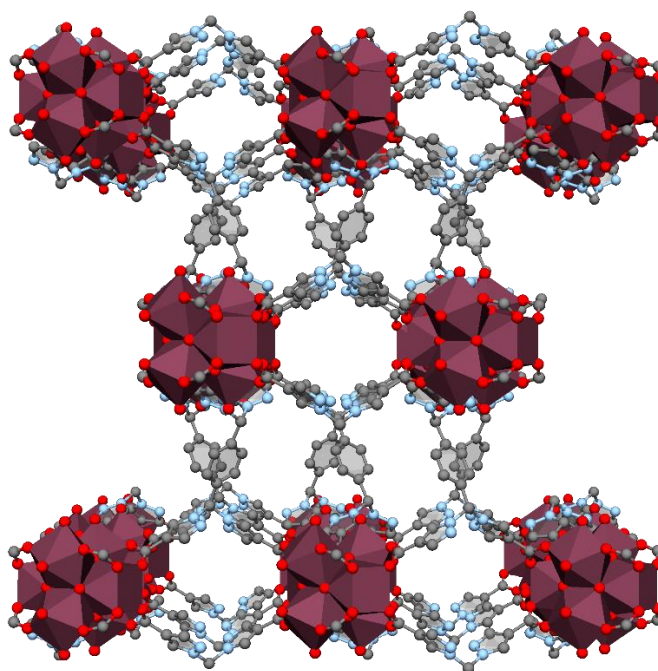


Figure III.12. Representation of the structure of UAM-11 along the (0,1,1) axis (C, grey; N, light blue; O, red; Cu, green; Zr, dark red; I, pink). Hydrogens have been omitted for clarity.

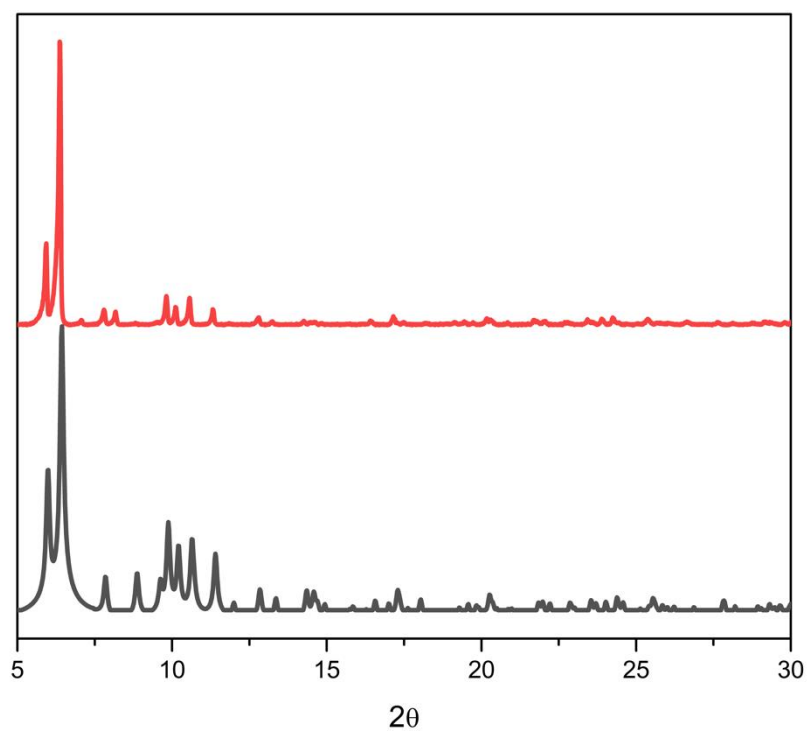


Figure III.13. PXRD plots for UAM-11 as made (red) versus simulated UAM-11 (black).

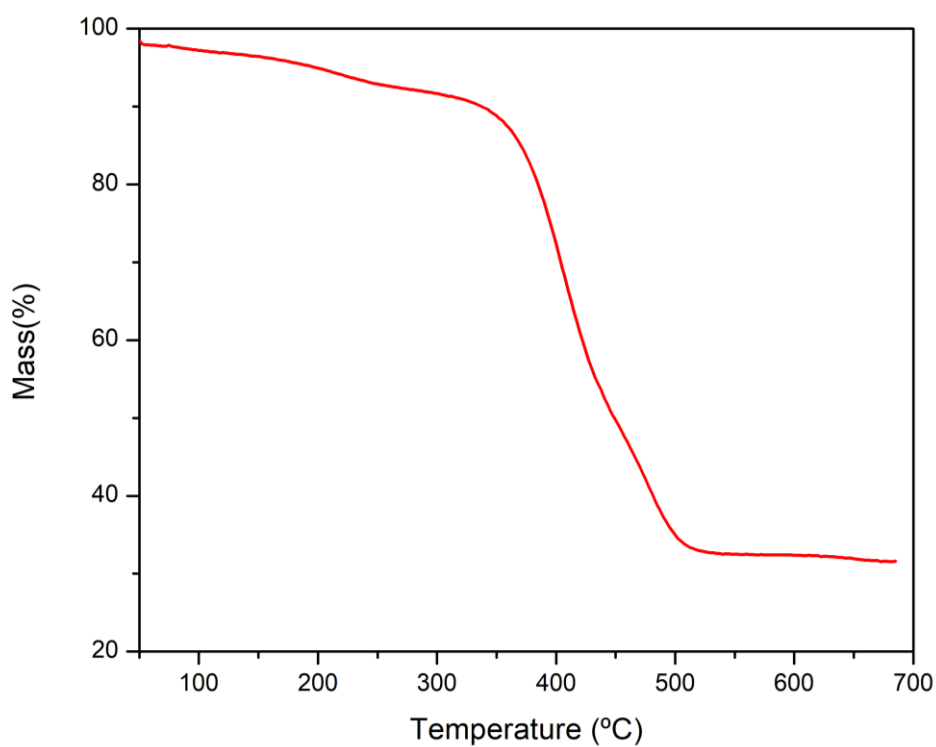


Figure III.14. Thermogravimetric analysis plot of UAM-11. Analysis conditions: 50 °C – 700 °C at 5 °C/min, under an oxidising (air) atmosphere.

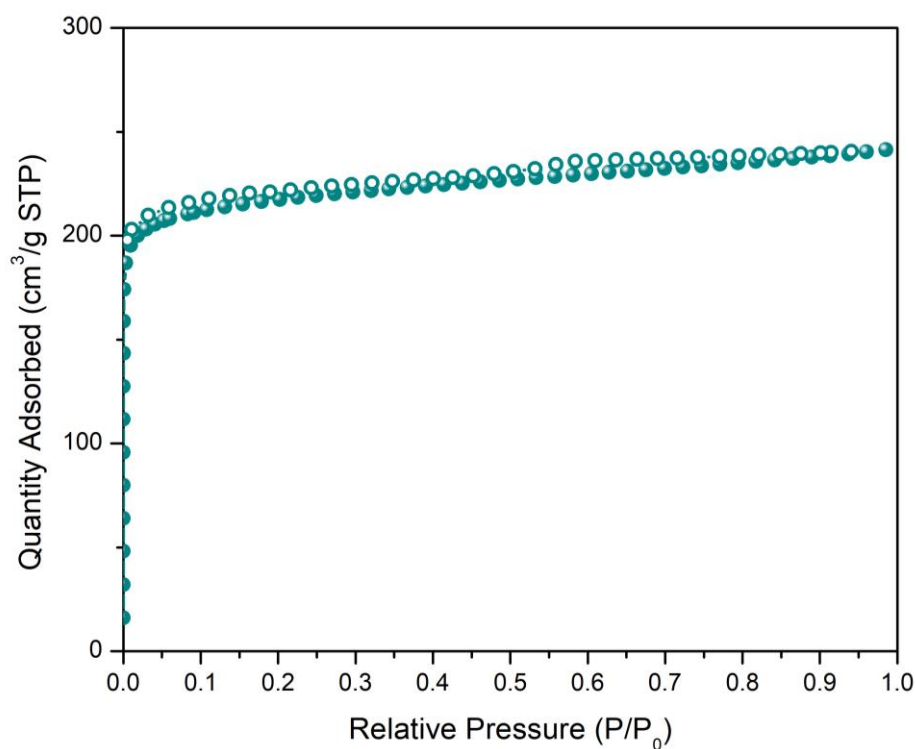


Figure III.15. 77 K N_2 isotherm data of UAM-11 after activation from acetone at 120 °C for 3 h. Filled circles represent adsorption; open circles represent desorption.

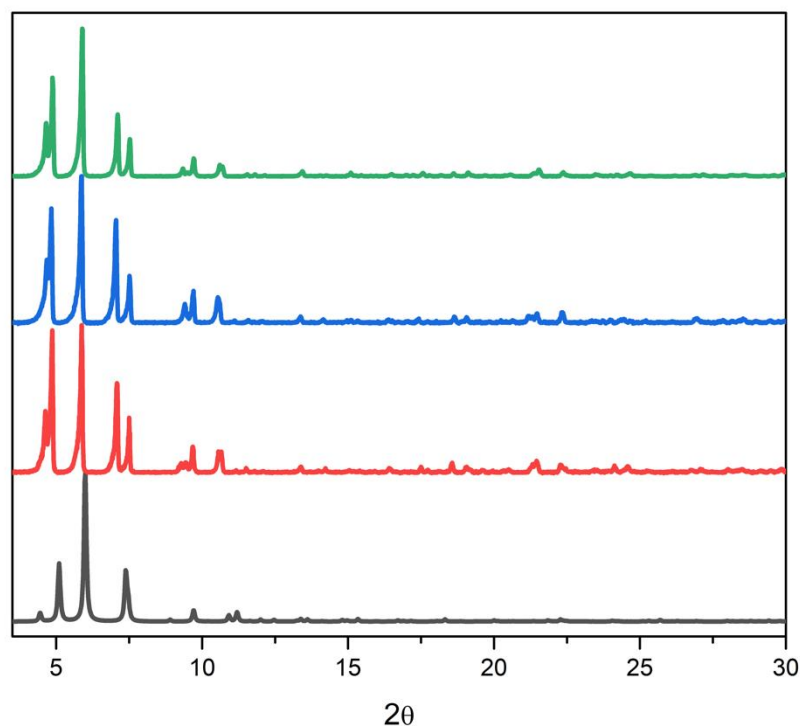


Figure III.16. PXRD plots for UAM-1000-BA as made (red), UAM-1000-AA as made (blue) and UAM-1000-TFA as made (green) versus simulated UAM-1000 (black). BA = benzoic acid, AA = acetic acid and TFA = trifluoroacetic acid.

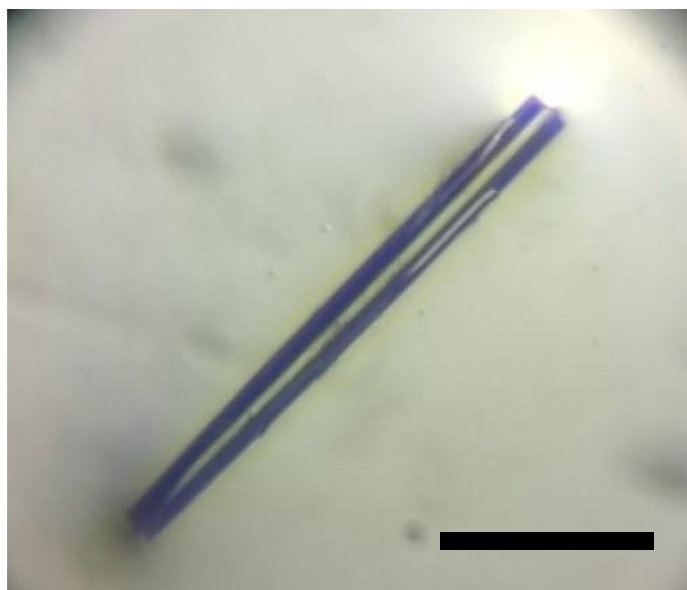


Figure III.17. An image of a UAM-1002 crystal. Scale bar = 1 mm.

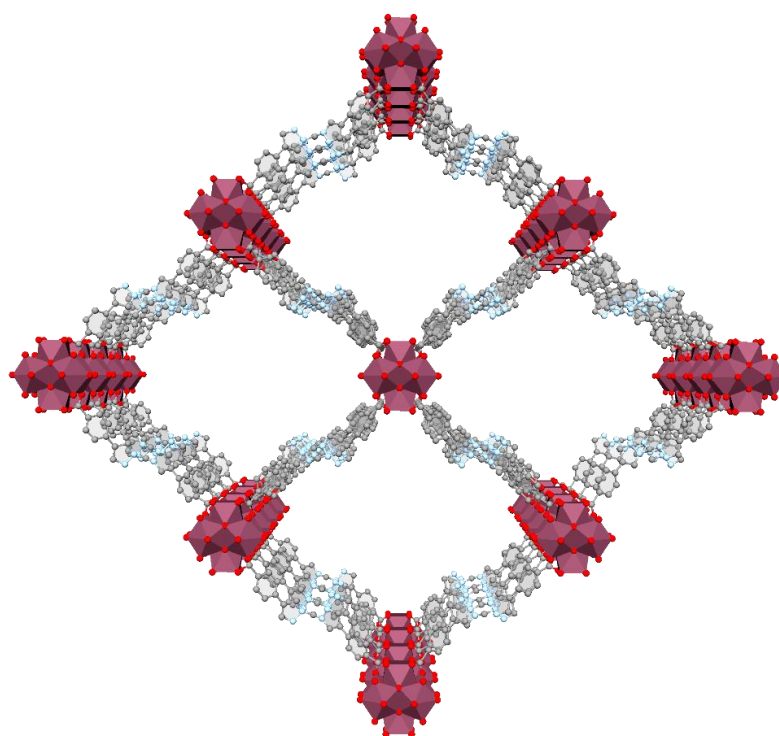


Figure III.18. Representation of the structure of UAM-1002 in the *ac* plane (C, grey; N, light blue; O, red; Cu, green; Zr, dark red; I, pink). Hydrogens have been omitted for clarity.

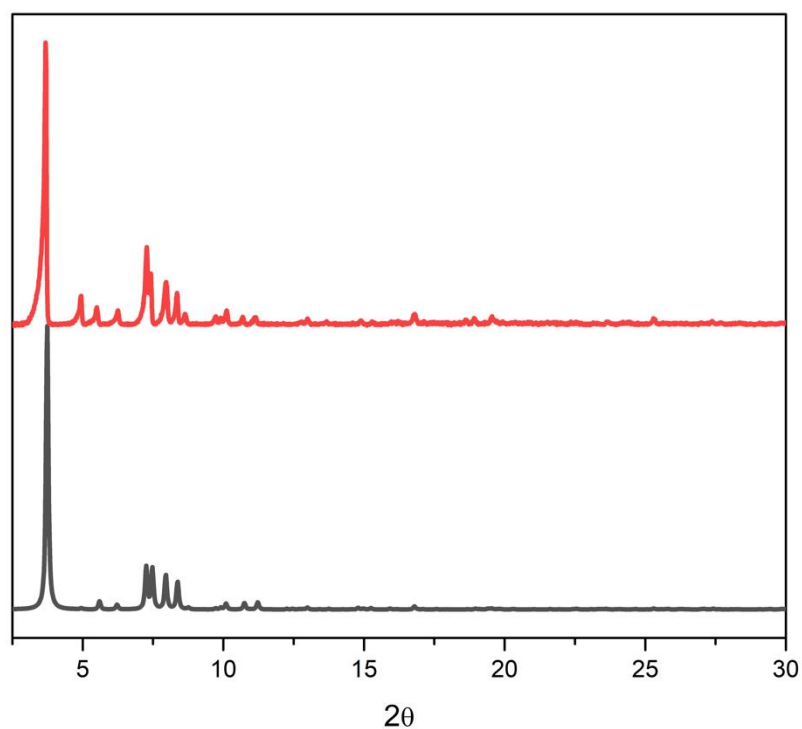


Figure III.19. PXRD plots for UAM-1002 as made (red) versus simulated UAM-1002 (black).

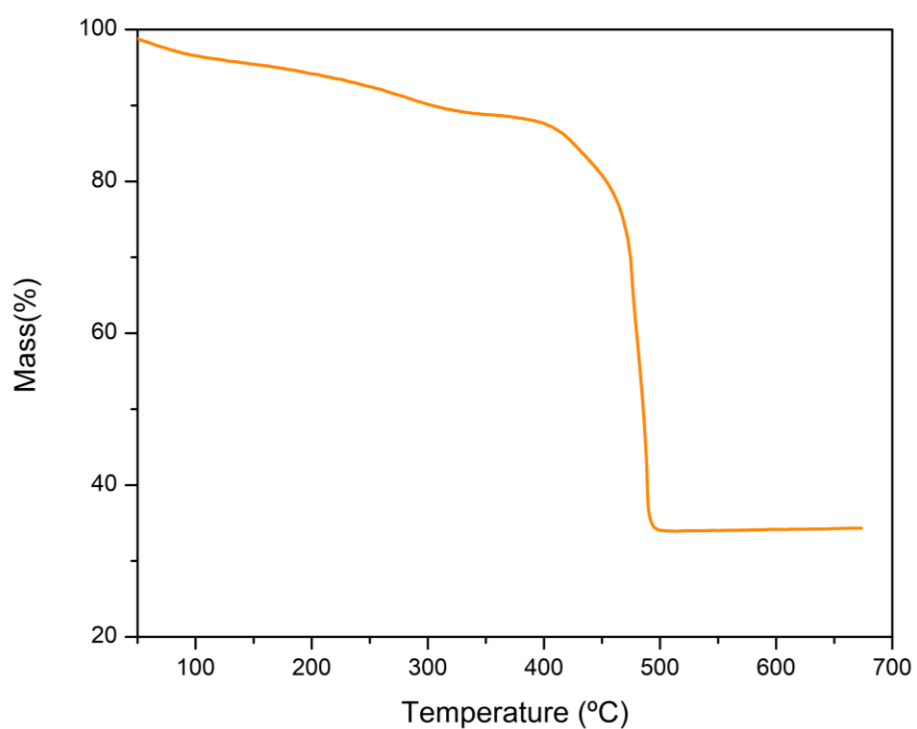


Figure III.20. Thermogravimetric analysis spectrum of UAM-1002 (black). Analysis conditions: 50 °C – 700 °C at 5 °C/min, under an oxidising (air) atmosphere.

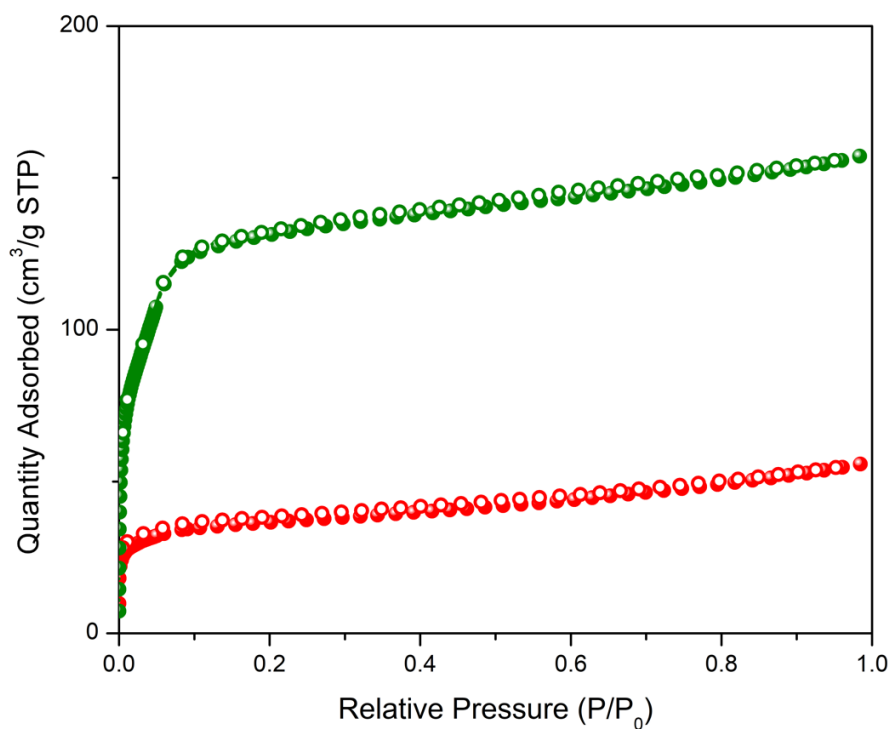


Figure III.21. 77 K N_2 isotherm data of UAM-1002 after activation from acetone at 120 °C for 3 h (red) and after activation under supercritical CO_2 (green). Filled circles represent adsorption, open circles represent desorption.

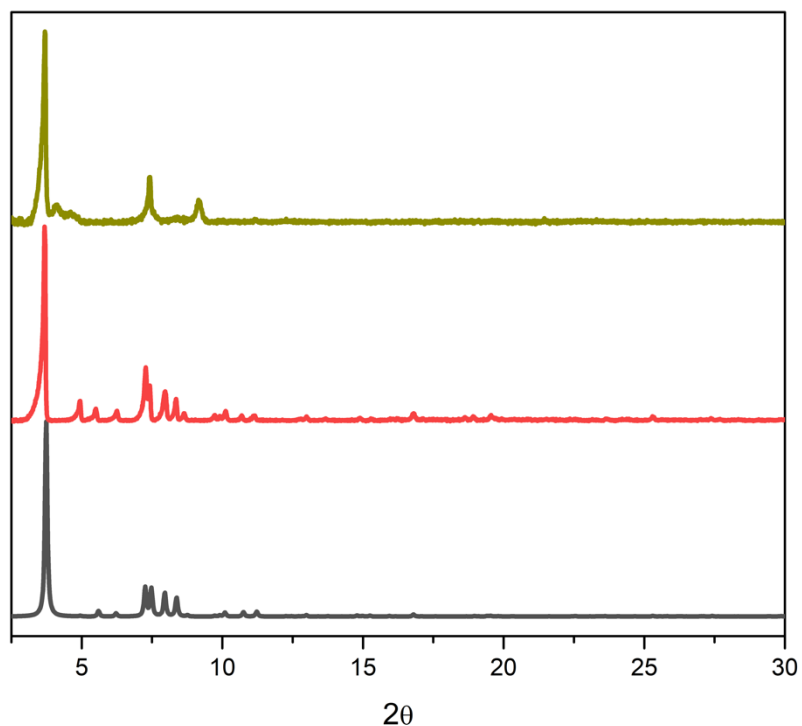


Figure III.22. PXRD plots for UAM-1002 as made (red) and UAM-1002-activated (green) versus simulated UAM-1002 (black).

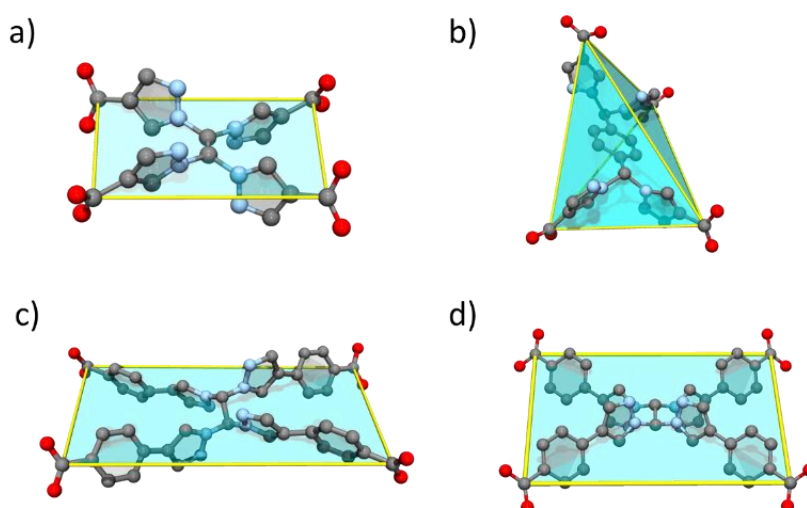


Figure III.23. Representations of the organic linkers in their respective MOF structures. a) L1 in UAM-10, b) L2 in UAM-11, c) L3 in UAM-1002 and d) L3 in UAM-1000.

Table III.1. Summary of the properties computed for the hypothetical frameworks formed with L1, L2 and TCPE. In Blue are highlighted MOFs reported experimentally in this work.

Ligand	Topology	DFT energy [eV/atom]	Density (g/ cm ³)	Accessible pore volume (cm ³ /g)	Accessible surface area (m ² /g)
L1	csq	-255.275	0.853	0.516	1444
L1	flu	-255.263	1.075	0.260	1544
L1	scu	-255.146	1.927	0.018	0
L1	sqc	-255.270	1.304	0.122	880
L2	csq	-233.897	0.600	0.945	2220
L2	flu	-233.883	0.936	0.349	1996
L2	scu	-233.900	1.267	0.172	1190
L2	sqc	-233.718	1.358	0.092	546
TCPE	csq	-194.683	0.393	1.691	3626
TCPE	flu	-194.681	0.513	1.085	3683
TCPE	scu	-194.678	0.473	1.236	3648
TCPE	sqc	-194.679	1.298	0.126	905

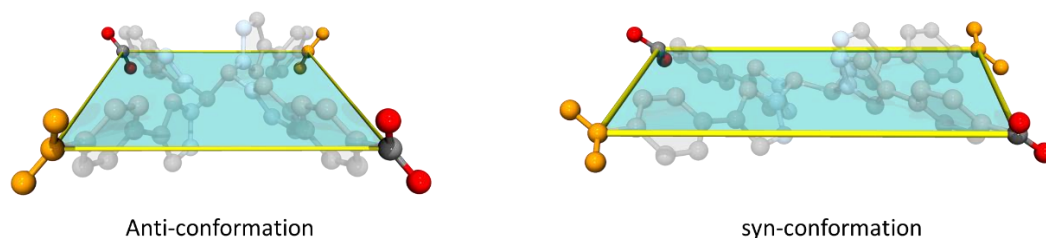


Figure III.24. Representations of TCPE in UAM-1002 (left) with its anti-conformation of the bis-pyrazole groups and UAM-1000 (right) in its syn conformation. The carboxylates that change orientation are highlighted in orange.

Table III.2. Relative UFF energies (kJ/mol per atom) for L1 and TPCE for different ligand conformations.

ligand	Topology	syn-syn	anti-anti
1	csq	0.821	1.459
1	flu	3.489	1.875
1	scu	0.000	1.100
1	sqc	2.544	2.759
TCPE	csq	0.000	0.571
TCPE	flu	-	0.688
TCPE	scu	0.219	0.634
TCPE	sqc	0.090	2.359

Table III.3. Energy-dispersive X-ray (EDX) data for Pd and Cl before and after metalation of **UAM-10**, **UAM11** and **UAM1002**. The % occupancy in the bis(pyrazolyl)methane coordinating sites was determined by measuring Zr:Pd and Pd:Cl ratios.

Sample	Pd (% occupancy) ^{a,b}	Cl (% occupancy) ^{a,b}
UAM-10·PdCl ₂	23.2 ± 10	59.4 ± 14
UAM-11·PdCl ₂	10.0 ± 9	22.3 ± 14
UAM-1002·PdCl ₂	98.5 ± 3	200 ± 3

^a Average atomic% obtained from three areas of three different crystals.

^b Relative to full occupancy of the bis(pyrazolyl)methane sites in the corresponding MOF (Zr:M = 3:2).

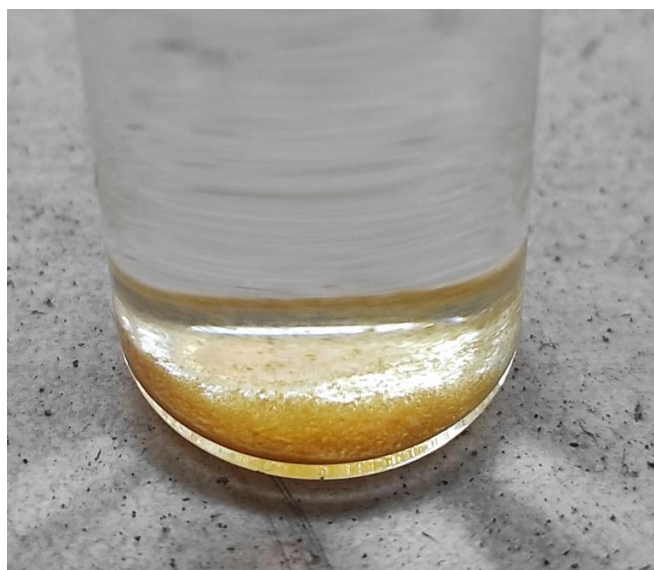


Figure III.25. Image of bulk UAM-1002[PdCl₂] showing the orange coloration of the crystals.

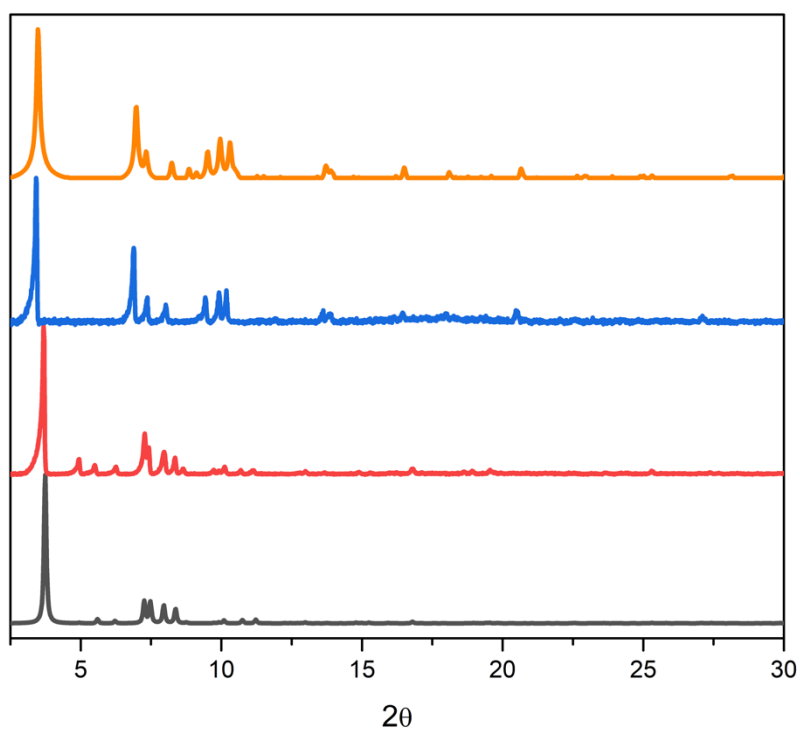


Figure III.26. PXRD plots for UAM-1002 as made (red) versus simulated UAM-1002 (black) and UAM-1002[PdCl₂] as made (blue) versus simulated UAM-1002[PdCl₂] (orange).

III.II. Fourier Transform Infrared Spectroscopy (FTIR) spectra

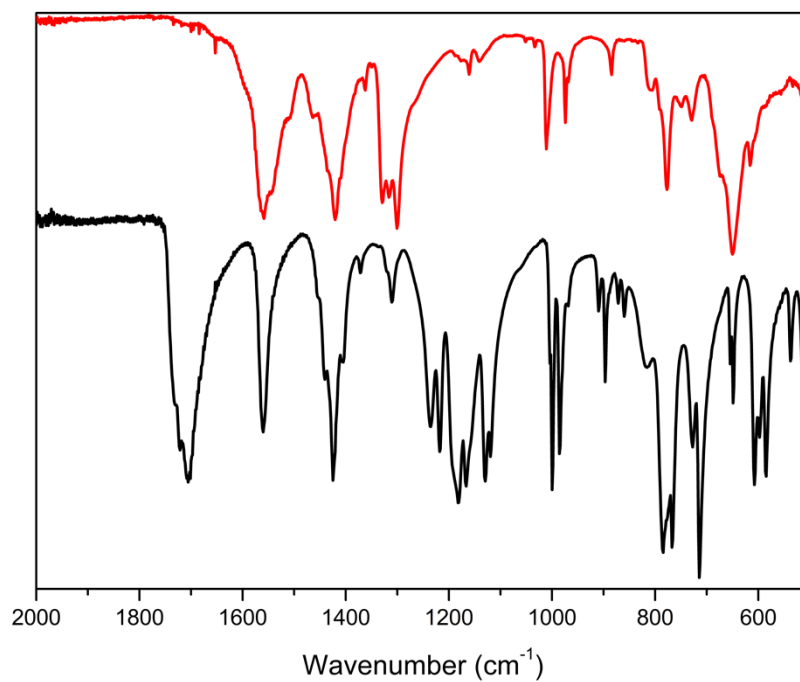


Figure III.27. FTIR spectra of L1H₄ (black) and UAM-10 as made (red).

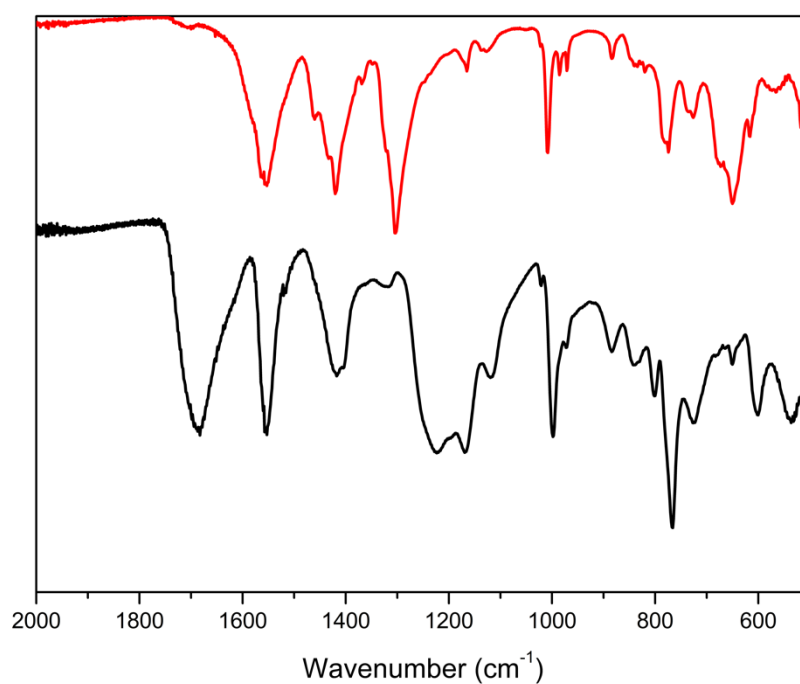


Figure III.28. FTIR spectra of L2H₄ (black) and UAM-11 as made (red).

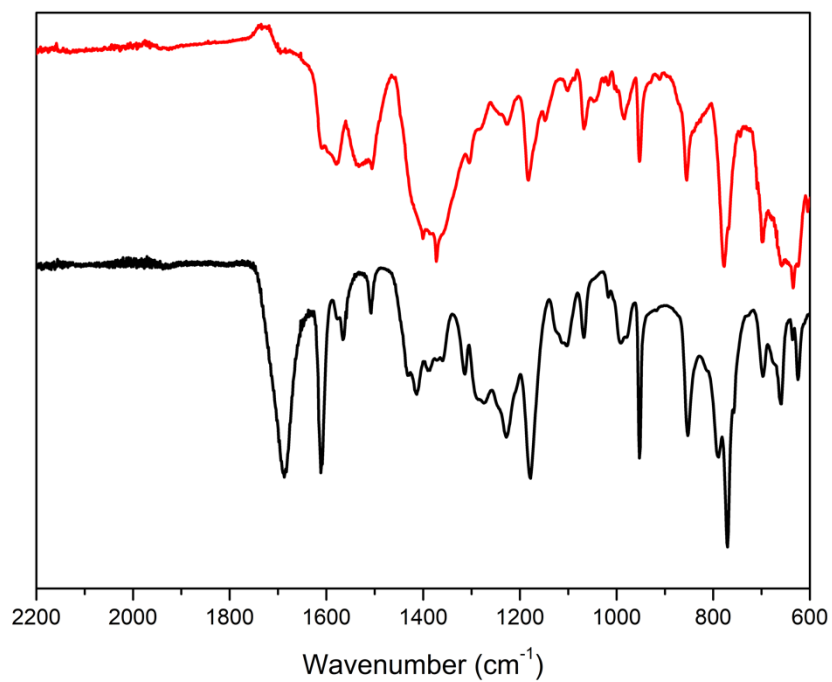


Figure III.29. FTIR spectra of TCPE (black) and UAM-1002 as made (red).

III.III. Adsorption experiments

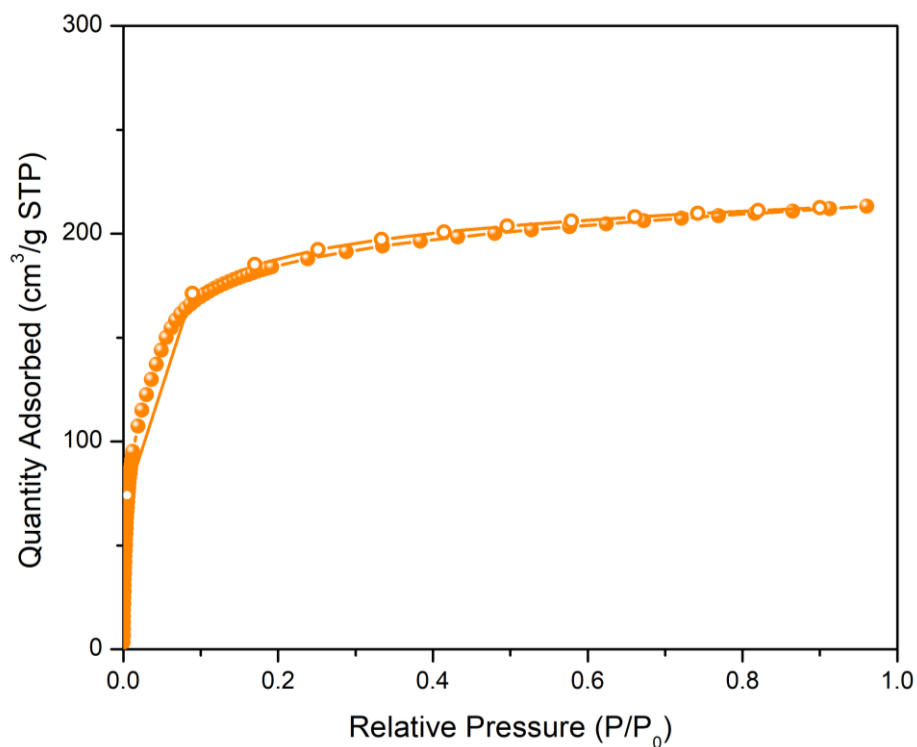


Figure III.30. 195 K CO_2 isotherm of UAM-10 after activation from acetone at 120 °C for 3 h. Filled circles represent adsorption; open circles represent desorption.

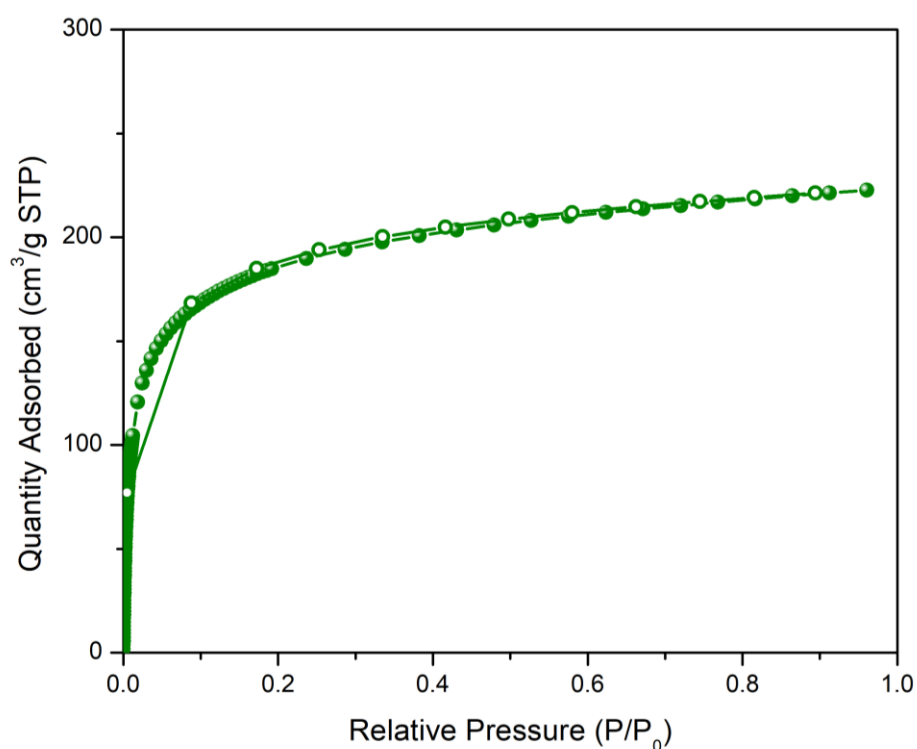


Figure III.31. 195 K CO_2 isotherm of UAM-11 after activation from acetone at 120 °C for 3 h. Filled circles represent adsorption; open circles represent desorption.

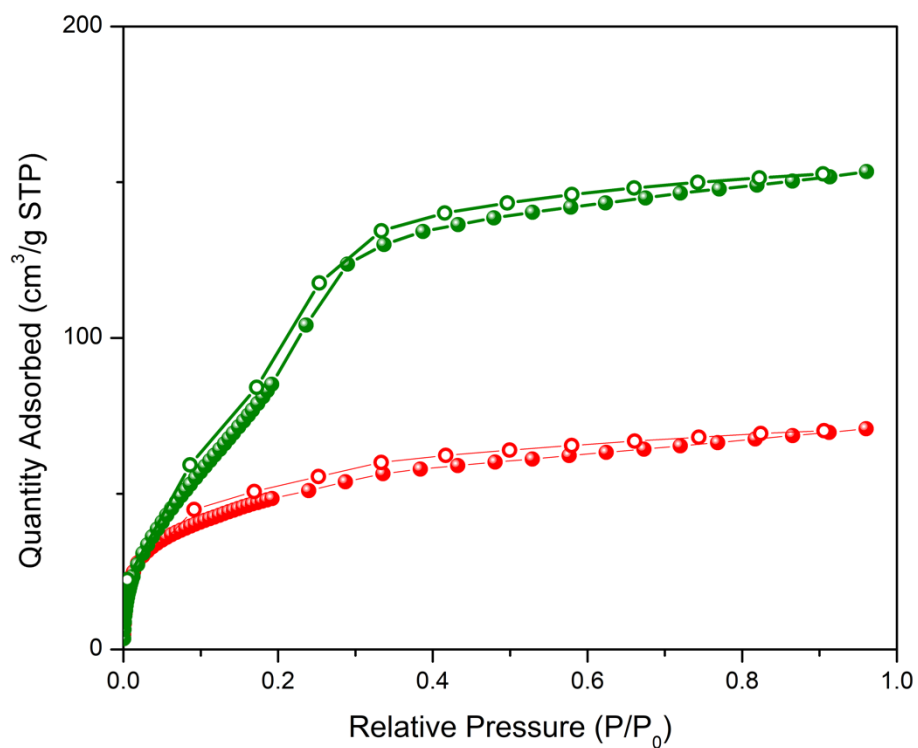


Figure III.32. 195 K CO_2 isotherm of UAM-1002 after activation from acetone at 120 °C for 3 h (red) and after activation under supercritical CO_2 (green). Filled circles represent adsorption; open circles represent desorption.

III.IV. Single crystal X-ray crystallography

III.IV.I. Specific Data and Refinement Details

- **UAM-10.** The pyrazole rings were modelled by adding them as a fragment. The atoms corresponding to the DMF molecule in the pore were left isotropic as they are too disordered to allow anisotropic refinement.
- **UAM-11.** No special refinement details.
- **UAM-1002.** The phenyl and pyrazole rings were modelled with AFIX restraints due to the crystallographic disorder.
- **UAM-1002[PdCl₂].** Some of the atoms of the pyrazole rings had to be modelled with EADP restraints due to the close proximity of the atoms arising from crystallographic disorder of the pyrazole rings.

III.IV.II. Thermal ellipsoid plots for all structures at the 50% probability level

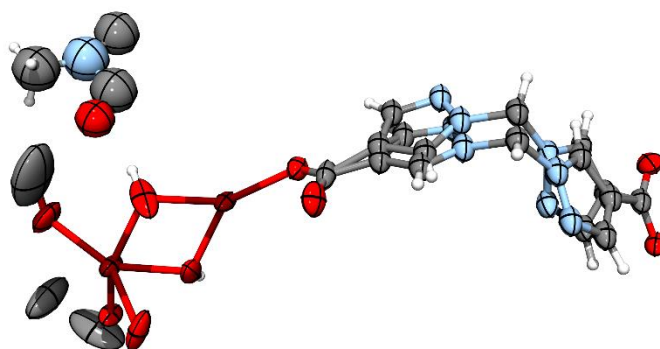


Figure III.33. Asymmetric unit of UAM-10, with all non-hydrogen atoms represented by ellipsoids at the 50% probability level (C, grey; H, white; N, light blue; O, red; Zr, dark red).

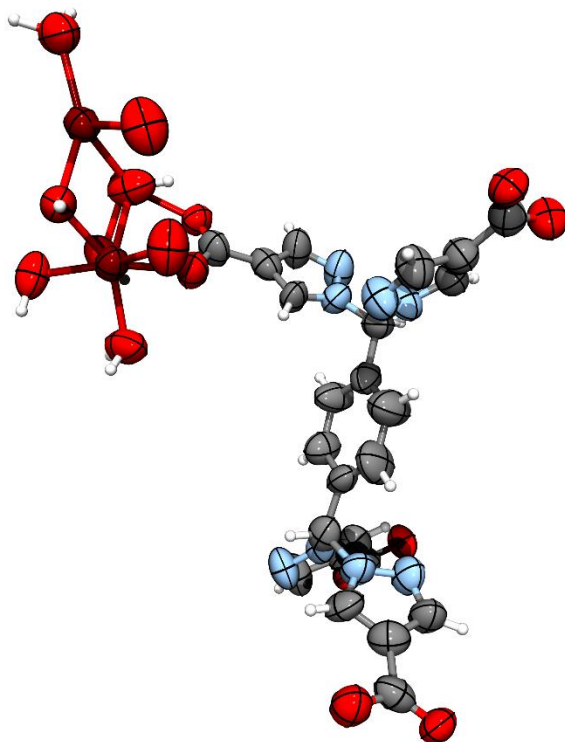


Figure III.34. Asymmetric unit of UAM-11, with all non-hydrogen atoms represented by ellipsoids at the 50% probability level (C, grey; H, white; N, light blue; O, red; Zr, dark red).

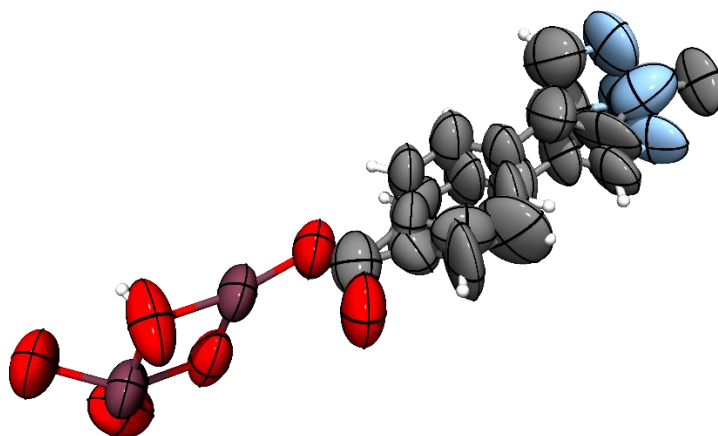


Figure III.35. Asymmetric unit of UAM-1002, with all non-hydrogen atoms represented by ellipsoids at the 50% probability level (C, grey; H, white; N, light blue; O, red; Zr, dark red).

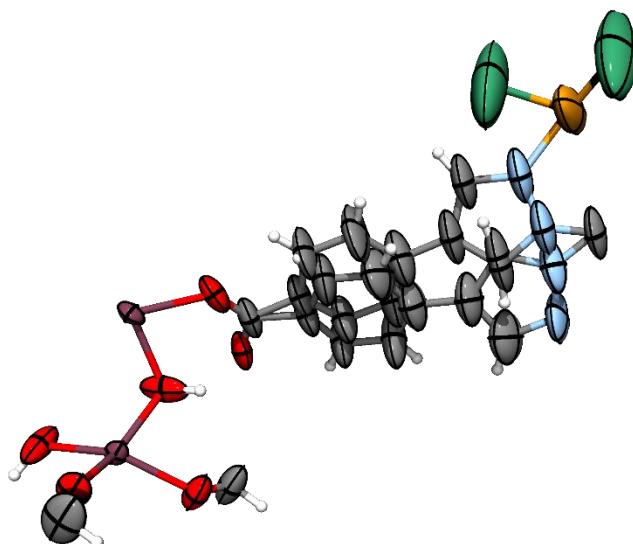


Figure III.36. Asymmetric unit of UAM-1002[PdCl₂], with all non-hydrogen atoms represented by ellipsoids at the 50% probability level (C, grey; H, white; N, light blue; O, red; Zr, dark red; Pd, orange; Cl, chlorine).

III.IV.III. Tables of X-ray crystallography data collection and refinement parameters

Table III.4. Crystallographic data collection and refinement parameters for UAM-10, UAM-11, UAM-1002 and UAM-1002[PdCl₂].

Sample	UAM-10	UAM-11	UAM-1002	UAM-1002[PdCl ₂]
Crystallographic Parameter				
Formula	C ₁₂ H ₈ N _{4.5} O _{8.5} Zr _{1.5}	C ₁₂ H ₁₁ N ₄ O ₈ Zr _{1.5}	C _{10.5} H ₇ N ₂ O ₄ Zr _{0.75}	C ₁₁ H _{7.5} ClN ₂ O ₄ Pd _{0.5} Zr _{0.75}
FW	488.06	476.08	293.6	388.75
T, K	100(2)	100(2)	100(2)	100(2)
Wavelength, Å	monoclinic	orthorhombic	orthorhombic	orthorhombic
Crystal system, space group	C2/m	Cmce	Cmmm	Cmmm
Z	22.511(5)	29.301(7)	33.273(7)	33.4742(5)
a, Å	23.641(5)	22.313(8)	35.780(7)	38.7659(6)
b, Å	10.046(2)	21.132(4)	12.220(2)	9.98330(10)
c, Å	90	90	90	90
α°	90.01(3)	90	90	90
β, °	90	90	90	90
γ°	5346.3(18)	13816(7)	14548(5)	12954.9(3)
V, Å ³	8	16	16	16
dcalc, g/cm ³	1.213	0.916	0.536	0.797
Absorption coefficient, mm ⁻¹	0.63	0.485	0.236	5.14
F(000)	1916	3760	2336	3032
Crystal size, mm ³	0.104 × 0.063 × 0.02	0.04 × 0.035 × 0.028	0.197 × 0.031 × 0.027	0.174 × 0.042 × 0.03
Radiation	Synchrotron (λ = 0.71073)	Synchrotron (λ = 0.71073)	Synchrotron (λ = 0.71073)	Cu Kα (λ = 1.54184)
2θ range for data collection	2.498 to 57.294	2.78 to 57.368	1.672 to 57.364	5.28 to 152.882
Index range	-30 ≤ h ≤ 29, -29 ≤ k ≤ 29, -13 ≤ l ≤ 13	-38 ≤ h ≤ 39, -29 ≤ k ≤ 29, -25 ≤ l ≤ 25	-43 ≤ h ≤ 43, -47 ≤ k ≤ 46, -16 ≤ l ≤ 16	-40 ≤ h ≤ 38, -48 ≤ k ≤ 39, -12 ≤ l ≤ 9
Reflections collected	33666	84271	86300	34370
Independent reflections	5477 [Rint = 0.0732, Rsigma = 0.0435]	7571 [Rint = 0.2390, Rsigma = 0.1079]	8298 [Rint = 0.1189, Rsigma = 0.0614]	6887 [Rint = 0.0392, Rsigma = 0.0307]
Data/restraints/parameters	5477/87/220	7571/0/235	8298/0/236	6887/0/222
GOF on F ²	1.06	0.878	0.936	1.134
Largest diff. peak and hole, eÅ ⁻³	1.33/-0.74	0.52/-0.89	0.44/-1.00	0.86/-1.28
R ₁ , [I > 2σ(I)]	0.0560	0.0716	0.1144	0.0488
wR ₂ , all data	0.1705	0.2304	0.3759	0.1507
CCDC Number				